

---

# Hybrid Exciton Thermalization in Atomically-Thin Semiconductors

---

Dissertation  
zur  
Erlangung des Doktorgrades  
der Naturwissenschaften  
(Dr. rer. nat.)

dem

Fachbereich Physik  
der Philipps-Universität Marburg

*vorgelegt von*

**Giuseppe Meneghini**

aus

Padova

Marburg, 2024

Hybrid Exciton Thermalization in Atomically-Thin Semiconductors by Giuseppe Meneghini is licensed under CC BY 4.0. To view a copy of this license, visit <https://creativecommons.org/licenses/by/4.0/>

Vom Fachbereich Physik der Philipps-Universität als Dissertation angenommen am:

Erstgutachter/in: Prof. Dr. Ermin Malic  
Zweitgutachter/in: Prof. Dr. Florian Gebhard

Tag der mündlichen Prüfung: 21. März 2024

Hochschulkenziffer: 1180

Hiermit versichere ich, Giuseppe Meneghini, dass ich meine Dissertation *Hybrid Exciton Thermalization in Atomically-Thin Semiconductors* selbständig ohne unerlaubte Hilfe angefertigt habe, mich dabei keiner anderen als der von mir ausdrücklich bezeichneten Quellen und Hilfen bedient und alle vollständigen oder sinngemäß übernommenen Zitate als solche gekennzeichnet habe. Die Dissertation wurde in der jetzigen oder einer ähnlichen Form noch bei keiner anderen Hochschule eingereicht und hat noch keinen sonstigen Prüfungszwecken gedient.



---

# Abstract

---

In the last few years, a new class of atomically thin semiconductors has garnered great interest across the scientific community: the transition metal dichalcogenides (TMDs). These materials, formed by a layer of metal atoms sandwiched between two layers of chalcogen atoms, show fascinating optical properties. Due to the reduced dielectric screening, tightly bound electron-hole pairs (excitons) dominate the optical response and the dynamics in these materials even at room temperature. This has been demonstrated in absorption, emission, photoluminescence and angle-resolved photoemission spectroscopy (ARPES) spectra as well as transport experiments. Furthermore, the possibility of vertically stacking two TMD layers into a heterostructure results in fascinating exciton phenomena, including the emergence of spatially separated bound charge complexes and layer-hybridized excitonic states. In addition, the twist angle between the layers appears as a new degree of freedom and offers an unprecedented tool to significantly change excitonic properties, from the creation of moiré-trapped excitons to delocalized exciton distributions.

Several experiments have recently demonstrated the existence of moiré excitons as well as the possibilities to tune them with the twist angle. In spite of a continuous progress, crucial aspects of exciton physics in twisted van der Waals heterostructures have still remained poorly understood. Charge transfer processes have been measured to occur at sub-picosecond timescales, but it is not clear why this happens so fast considering the relatively small wave function overlap between the layers. Recent experiments show unexpectedly large lifetimes and photoemission of excited moiré exciton states and also here, the microscopic origin of this phenomenon is not clear.

The aim of this thesis is to close this knowledge gap and to provide a microscopic understanding of interface exciton physics in TMD heterostructures. Adopting the density matrix formalism, we develop a microscopic many-particle model to describe exciton optics and dynamics in these materials. Solving the generalized Wannier equation allows us to calculate the twist-angle-dependent exciton energy landscape and the solution of the Boltzmann-scattering equations allows us to analyze the efficiency of possible phonon-driven scattering channels. With this material-specific and predictive approach, we could explain the measured ultrafast charge transfer process occurring in TMD bilayers and trace it back to a two-step phonon-mediated relaxation via momentum-dark hybrid exciton states. In joint theory-experiment studies with our collaboration partners from Göttingen, we could clearly confirm this phonon-driven charge transfer in ARPES. We could also

---

show that although the latter technique measures photo-ejected electrons, we can still track even a hole transfer process. We find both in theory and experiment a surprising and non-intuitive electron energy blue shift during the thermalization process. We can explain this by the correlated character of the measured electrons, which still maintain information about the energy and momentum of the remaining hole. Furthermore, we have predicted pronounced ARPES signatures for identifying hybrid excitons via the emergence of a characteristic double peak structure reflecting the hybrid character of electrons or holes.

Finally, we have simulated the phonon-driven relaxation cascade of hot interlayer excitons in a twisted TMD heterostructure. We demonstrate that at low temperatures and small twist angles resulting in flat exciton bands, a pronounced relaxation bottleneck appears, i.e. excitons cannot scatter down to the energetically lowest states resulting in a non-thermal exciton distribution. We trace this back to the flatness of the moiré exciton bands and their energetic separation making scattering with optical and acoustic phonons very inefficient. A direct consequence of the non-thermal distribution are long lifetimes and high emission intensity of excited exciton states – in excellent agreement with experimental findings.

Overall, this work provides new microscopic insights into many-particle processes governing optics and dynamics of excitons in TMD heterostructures, shedding light on intriguing experimental observations and paving the way towards promising future optoelectronic devices.

---

# Zusammenfassung

---

In den letzten Jahren hat eine neue Klasse atomar dünner Halbleiter großes Interesse in der wissenschaftlichen Gemeinschaft geweckt: die Übergangsmetall-Dichalkogenide (TMDs). Diese Materialien, die aus einer Schicht von Metallatomen zwischen zwei Schichten von Chalkogenatomen bestehen, zeigen faszinierende optische Eigenschaften. Aufgrund der reduzierten dielektrischen Abschirmung dominieren eng gebundene Elektron-Loch-Paare (Exzitonen) selbst bei Raumtemperatur die optische Antwort und die Dynamik dieser Materialien. Dies wurde in Absorptions-, Emissions-, Photolumineszenz- und winkel aufgelösten Photoemissionsspektroskopie (ARPES) -Spektren sowie in Transportexperimenten nachgewiesen. Darüber hinaus führt die Möglichkeit, zwei TMD-Schichten vertikal zu stapeln, zu faszinierenden Exzitonphänomenen, einschließlich dem Auftreten räumlich getrennter gebundener Ladungskomplexe und schicht-hybridisierter exzitonischer Zustände. Zusätzlich erscheint der Drehwinkel zwischen den Schichten als ein neuer Freiheitsgrad und bietet ein beispielloses Werkzeug, um die exzitonischen Eigenschaften signifikant zu verändern, von der Erzeugung von Moiré-gefangenen Exzitonen bis zu delokalisierten Exzitonverteilungen.

Mehrere Experimente haben kürzlich die Existenz von Moiré-Exzitonen sowie die Möglichkeiten, sie mit dem Drehwinkel einzustellen, nachgewiesen. Trotz kontinuierlicher Fortschritte sind entscheidende Aspekte der Exzitonphysik in verdrehten van-der-Waals-Heterostrukturen immer noch nicht richtig verstanden. Ladungstransferprozesse wurden gemessen und erfolgen in Zeitskalen von unter einer Pikosekunde, es ist aber nicht klar, warum dies so schnell geschieht, wenn man die relativ geringe Überlappung der Wellenfunktionen zwischen den Schichten berücksichtigt. Aktuelle Experimente zeigen unerwartet lange Lebensdauern und Photoemission von angeregten Moiré-Exzitonenzuständen, und auch hier ist der mikroskopische Ursprung dieses Phänomens nicht klar.

Das Ziel dieser Arbeit ist es, diese Wissenslücke zu schließen und ein mikroskopisches Verständnis der Exzitonphysik an TMD-Heterostrukturen zu liefern. Unter Verwendung des Dichtematrix-Formalismus entwickeln wir ein mikroskopisches Vielteilchenmodell, um Exzitonoptik und -dynamik in diesen Materialien zu beschreiben. Die Lösung der verallgemeinerten Wannier-Gleichung ermöglicht es uns, die drehwinkelabhängige Exzitonenergielandschaft zu berechnen, und die Lösung der Boltzmann-Streuungsgleichungen ermöglicht es uns, die Effizienz möglicher phononengesteuerter Streukanäle zu analysieren. Mit diesem materialspezifischen und prädiktiven Ansatz konnten wir den gemessenen

---

ultraschnellen Ladungstransferprozess in TMD-Bilayern erklären und ihn auf eine zweistufige phononengesteuerte Relaxation über Impuls-dunkle hybridisierte Exzitonzustände zurückführen. In gemeinsamen Theorie-Experiment-Studien mit unseren Kooperationspartnern aus Göttingen konnten wir diese phononengesteuerte Ladungsübertragung in ARPES eindeutig bestätigen. Wir konnten auch zeigen, dass, obwohl diese Technik photoausgelöste Elektronen misst, wir dennoch sogar einen Loch-Transferprozess verfolgen können. Sowohl in Theorie als auch in Experiment konnten wir eine überraschende und nicht intuitive Blauverschiebung der Elektronenenergie während des Thermalisierungsprozesses finden. Dies lässt sich durch den korrelierten Charakter der gemessenen Elektronen erklären, die weiterhin Informationen über die Energie und den Impuls des verbleibenden Lochs bewahren. Darüber hinaus haben wir ausgeprägte ARPES-Signaturen vorhergesagt, um hybridisierte Exzitonen durch das Auftreten einer charakteristischen Doppelpieksstruktur zur Identifizierung von Elektronen oder Löchern nachzuweisen.

Schließlich haben wir die phononengesteuerte Relaxationskaskade heißer Interlayer-Exzitonen in einer verdrehten TMD-Heterostruktur simuliert. Wir konnten zeigen, dass bei niedrigen Temperaturen und kleinen Drehwinkeln, was zu flachen Exzitonbändern führt, ein ausgeprägter Relaxationsengpass auftritt, d. h. Exzitonen können nicht zu den energetisch niedrigsten Zuständen streuen, was zu einer nicht-thermischen Exzitonverteilung führt. Wir führen dies auf die Flachheit der Moiré-Exzitonbänder und ihre energetische Trennung zurück, was Streuungen mit optischen und akustischen Phononen sehr ineffizient macht. Eine direkte Konsequenz der nicht-thermischen Verteilung sind lange Lebensdauern und hohe Emissionsintensität angeregter Exzitonzustände - in ausgezeichneter Übereinstimmung mit experimentellen Befunden.

Insgesamt liefert diese Arbeit neue mikroskopische Einblicke in Vielteilchenprozesse, die Optik und Dynamik von Exzitonen in TMD-Heterostrukturen steuern, beleuchtet faszinierende experimentelle Beobachtungen und ebnet den Weg zu vielversprechenden zukünftigen optoelektronischen Geräten.

---

# List of Publications

---

This thesis consist of a detailed introduction and the following papers:

1. **Ultrafast phonon-driven charge transfer in van der Waals heterostructures**,  
**G. Meneghini**, S. Brem and E. Malic.  
Natural Sciences 2.4 (2022): e20220014.
2. **Formation of moiré interlayer excitons in space and time**,  
D. Schmitt, J. P. Bange, W. Bennecke, A. AlMutairi, **G. Meneghini**, K. Watanabe,  
T. Taniguchi, D. Steil, D. R. Luke, R. T. Weitz, S. Steil, G. S. M. Jansen, S. Brem,  
E. Malic, S. Hofmann, M. Reutzel and S. Mathias.  
Nature 608.7923 (2022): 499-503.
3. **Probing electron-hole Coulomb correlations in the exciton landscape of a  
twisted semiconductor heterostructure**,  
J. P. Bange, D. Schmitt, W. Bennecke, **G. Meneghini**, A. AlMutairi, K. Watanabe,  
T. Taniguchi, D. Steil, S. Steil, R. T. Weitz, G. S. M. Jansen, S. Hofmann, S. Brem,  
E. Malic, M. Reutzel, S. Mathias.  
Sci. Adv.10,eadi1323 (2024).
4. **Hybrid Exciton Signatures in ARPES Spectra of van der Waals Materials**,  
**G. Meneghini**, M. Reutzel, S. Mathias, S. Brem, and E. Malic.  
ACS Photonics 10.10 (2023): 3570-3575.
5. **Excitonic thermalization bottleneck in twisted TMD heterostructures**,  
**G. Meneghini**, S. Brem and E. Malic.  
Nano Lett. 2024, 24, 15, 4505–4511.

## My contribution to the listed publications

As first author in papers 1 and 4-5, I developed the microscopic model, performed the numerical simulations, analyzed the results and wrote the manuscripts, with the supervision of Dr. Samuel Brem and Prof. Dr. Ermin Malic. In papers 2 and 3, I developed the microscopic model, performed the numerical simulations and analyzed the results as the leading theory author.

---

Publications not appended to this thesis:

6. **Ultrafast dynamics of bright and dark excitons in monolayer WSe<sub>2</sub> and heterobilayer WSe<sub>2</sub>/MoS<sub>2</sub>,**  
J. P. Bange, P. Werner, D. Schmitt, W. Bennecke, **G. Meneghini**, A. AlMutairi, M. Merboldt, K. Watanabe, T. Taniguchi, S. Steil.  
2D Materials, 10 035039 (2023).
7. **Ultrafast nano-imaging of dark excitons,**  
D. Schmitt, J. P. Bange, W. Bennecke, **G. Meneghini**, A. AlMutairi, M. Merboldt, J. Pöhls, K. Watanabe, T. Taniguchi, S. Steil, D. Steil, R. T. Weitz, S. Hofmann, S. Brem, G. S. M. Jansen, E. Malic, S. Mathias, M. Reutzel.  
arXiv preprint arXiv:2303.17886 (2023).
8. **Exciton transport in a moiré potential: From hopping to dispersive regime,**  
W. Knorr, S. Brem, **G. Meneghini**, and E. Malic.  
Phys. Rev. Materials 6, 124002 (2022).
9. **Polaron-induced changes in moiré exciton propagation in twisted van der Waals heterostructures,**  
W. Knorr, S. Brem, **G. Meneghini** and Ermin Malic.  
Nanoscale (2024), doi: 10.1039/D4NR00136B”.

---

# Liste der Publikationen

---

Diese Arbeit besteht aus einer ausführlichen Einleitung und den folgenden Arbeiten:

1. **Ultrafast phonon-driven charge transfer in van der Waals heterostructures**,  
**G. Meneghini**, S. Brem and E. Malic.  
Natural Sciences 2.4 (2022): e20220014.
2. **Formation of moiré interlayer excitons in space and time**,  
D. Schmitt, J. P. Bange, W. Bennecke, A. AlMutairi, **G. Meneghini**, K. Watanabe,  
T. Taniguchi, D. Steil, D. R. Luke, R. T. Weitz, S. Steil, G. S. M. Jansen, S. Brem,  
E. Malic, S. Hofmann, M. Reutzler and S. Mathias.  
Nature 608.7923 (2022): 499-503.
3. **Probing electron-hole Coulomb correlations in the exciton landscape of a  
twisted semiconductor heterostructure**,  
J. P. Bange, D. Schmitt, W. Bennecke, **G. Meneghini**, A. AlMutairi, K. Watanabe,  
T. Taniguchi, D. Steil, S. Steil, R. T. Weitz, G. S. M. Jansen, S. Hofmann, S. Brem,  
E. Malic, M. Reutzler, S. Mathias.  
Sci. Adv.10,eadi1323 (2024).
4. **Hybrid Exciton Signatures in ARPES Spectra of van der Waals Materials**,  
**G. Meneghini**, M. Reutzler, S. Mathias, S. Brem, and E. Malic.  
ACS Photonics 10.10 (2023): 3570-3575.
5. **Excitonic thermalization bottleneck in twisted TMD heterostructures**,  
**G. Meneghini**, S. Brem and E. Malic.  
Nano Lett. 2024, 24, 15, 4505–4511.

## Mein Beitrag zu den aufgeführten Veröffentlichungen

Als Erstautor in den Arbeiten 1 und 4-5 habe ich das mikroskopische Modell entwickelt, die numerischen Simulationen durchgeführt, die Ergebnisse analysiert und die Manuskripte verfasst, unter der Aufsicht von Dr. Samuel Brem und Prof. Dr. Ermin Malic. In den

---

Arbeiten 2 und 3 habe ich das mikroskopische Modell entwickelt, die numerischen Simulationen durchgeführt und die Ergebnisse als führender Theorieautor analysiert.

Nicht an dieser Arbeit angehängte Veröffentlichungen:

6. **Ultrafast dynamics of bright and dark excitons in monolayer WSe2 and heterobilayer WSe2/MoS2**,  
J. P. Bange, P. Werner, D. Schmitt, W. Bennecke, **G. Meneghini**, A. AlMutairi, M. Merboldt, K. Watanabe, T. Taniguchi, S. Steil.  
2D Materials, 10 035039 (2023).
7. **Ultrafast nano-imaging of dark excitons**,  
D. Schmitt, J. P. Bange, W. Bennecke, **G. Meneghini**, A. AlMutairi, M. Merboldt, J. Pöhls, K. Watanabe, T. Taniguchi, S. Steil, D. Steil, R. T. Weitz, S. Hofmann, S. Brem, G. S. M. Jansen, E. Malic, S. Mathias, M. Reutzler.  
arXiv preprint arXiv:2303.17886 (2023).
8. **Exciton transport in a moiré potential: From hopping to dispersive regime**,  
W. Knorr, S. Brem, **G. Meneghini**, and E. Malic.  
Phys. Rev. Materials 6, 124002 (2022).
9. **Polaron-induced changes in moiré exciton propagation in twisted van der Waals heterostructures**,  
W. Knorr, S. Brem, **G. Meneghini** and Ermin Malic.  
Nanoscale (2024), doi: 10.1039/D4NR00136B”.

---

# Contents

---

<b>Abstract</b>	
<b>Zusammenfassung</b>	<b>iii</b>
<b>List of Publications</b>	<b>v</b>
<b>Liste der Publikationen</b>	<b>vii</b>
<b>1 Introduction</b>	<b>1</b>
<b>2 Theoretical framework</b>	<b>7</b>
2.1 Electronic Hamiltonian . . . . .	7
2.2 Many-Body Dynamics . . . . .	13
2.3 Semiconductor Bloch Equation . . . . .	15
2.4 Exciton formalism . . . . .	16
2.5 Generalizing to bilayers . . . . .	18
2.6 Exciton Hybridization . . . . .	22
2.7 Introducing the twist angle . . . . .	25
2.8 Exciton Dynamics . . . . .	28
2.9 Beyond the second order Born-Markov approximation . . . . .	31
2.10 Hybrid exciton ARPES signal . . . . .	31
<b>3 Hybrid exciton thermalization</b>	<b>35</b>
3.1 Energy landscape . . . . .	35
3.2 Two-step phonon mediated charge transfer . . . . .	36
3.3 Temperature and stacking dependence . . . . .	38
3.4 Formation of interlayer excitons . . . . .	39
<b>4 Hybrid exciton signatures</b>	<b>45</b>
4.1 Energy landscape and hybrid exciton dynamics . . . . .	45
4.2 Double peak ARPES signal . . . . .	46

<b>5</b>	<b>Moiré exciton thermalization</b>	<b>49</b>
5.1	Energy landscape and moiré exciton dynamics . . . . .	49
5.2	Time resolved photoluminescence . . . . .	52
5.3	Characteristic relaxation time . . . . .	53
5.4	Real space equilibrium distribution . . . . .	53
5.5	Initial conditions . . . . .	55
5.6	Large twist angle limit . . . . .	56
<b>6</b>	<b>Conclusions</b>	<b>59</b>
	<b>Acknowledgements</b>	<b>61</b>
	<b>Bibliography</b>	<b>62</b>
<b>7</b>	<b>Paper 1</b>	<b>71</b>
<b>8</b>	<b>Paper 2</b>	<b>87</b>
<b>9</b>	<b>Paper 3</b>	<b>119</b>
<b>10</b>	<b>Paper 4</b>	<b>153</b>
<b>11</b>	<b>Paper 5</b>	<b>167</b>

# Introduction

---

The advent of graphene, after its first isolation and characterization in 2004 [1], represented a new great possibility for scientific and industrial progress. The exfoliation of single layers of graphite demonstrated that it is possible to have stable atomic crystals of low dimensionality, which as a consequence, leave field for the existence of many-body and strongly correlated effect that are difficult or impossible to observe in bulk systems [2–4]. On the trend of these studies, researchers found other classes of stable atomically thin materials, and between them a very promising class has stood up for the future of

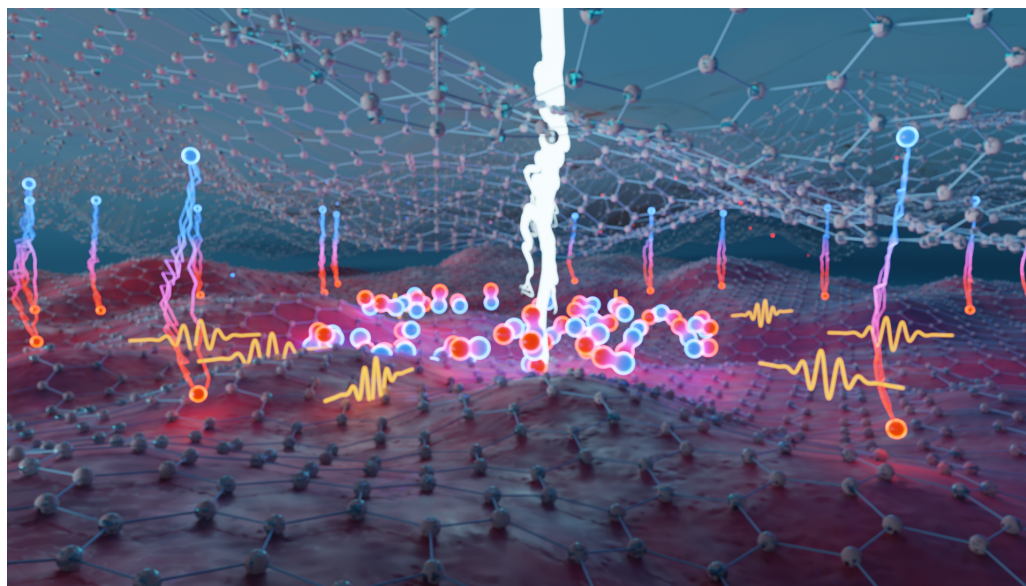


Figure 1.1: Artistic representation of a charge transfer process in 2D materials. After an optical excitation of excitons in one layer, a population of intralayer excitons is created. Thanks to phonon-mediated scattering, the intralayer excitons relax to the most energetically favorable state, which for a heterostructure is an interlayer exciton.

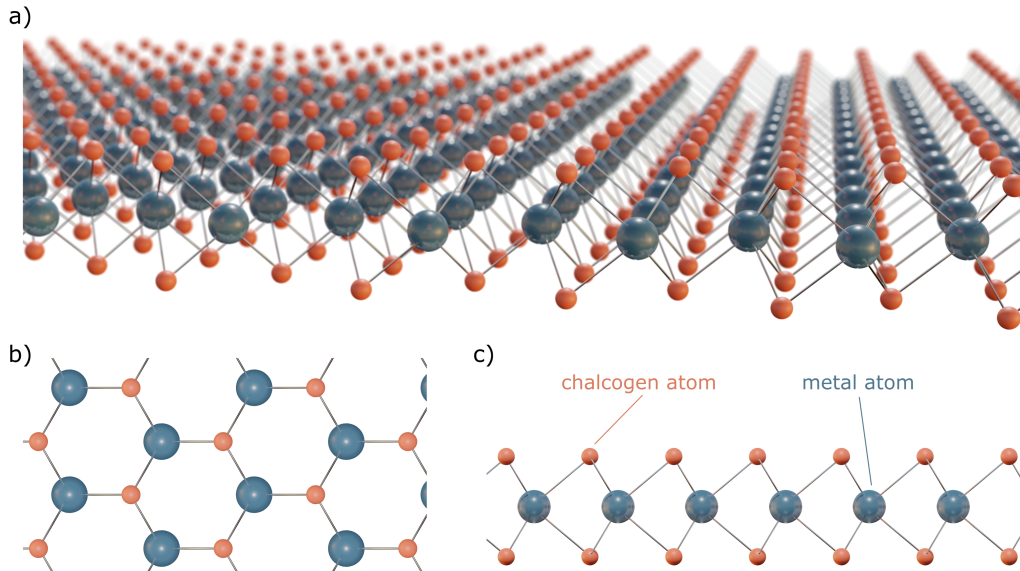


Figure 1.2: a) Three dimensional model of a TMD monolayer. We show the characteristic hexagonal pattern (top view b)), and highlight from the side view (c) its composition, i.e. a metal atom (M) sandwiched between two chalcogen atoms (X). The usual notation for TMD monolayers is  $\text{MX}_2$ .

optoelectronic devices, the transition Metal Dichalcogenides (TMDs) [5–8]. These materials are formed by a layer of metal atoms, sandwiched between two layers of chalcogen atoms (see figure 1.2), and, for simplicity, they are often denoted by the notation  $\text{MX}_2$ , where M represents the metal atom and X the chalcogen atom. The similarities with graphene are not limited to the very low dimensionality, in fact they are characterized by the same spatial periodicity, which can be described in terms of an hexagonal lattice. The significant interest in TMDs within the scientific community arises from their response to optical excitations, governed by correlations involving only few particles [9–14]. To comprehend this statement, we can briefly introduce the key ideas behind an optical excitation of a solid. The usual framework used in solid state physics for describing electronic states in the system is the band theory, where the energy landscape accessible to electrons in the system can be represented as in the schematic figure 1.3, where non excited electrons fill up to the higher valence band state. In this context, shining light on these materials triggers an excitation of valence electrons, which in the case of a direct band gap prompts the transition of these electrons to the conduction band. Generally, this state of the system can be theoretically described within the electron-hole formalism: here, the vacancies in the valence band left by promoted electrons are described as holes, possessing opposite charge and momentum compared to the missing electrons. Due to the charge difference between holes and electrons, they naturally tend to attract each other (1.3 a)). In conventional semiconductors, this effect can be approximately neglected due to the substantial screening effect of the surrounding medium. However this doesn't apply to TMDs: their reduced dimensionality leads to a diminished screening effect (1.3 b)), increasing the Coulomb attraction between holes and electrons. The strength of their interaction is such that

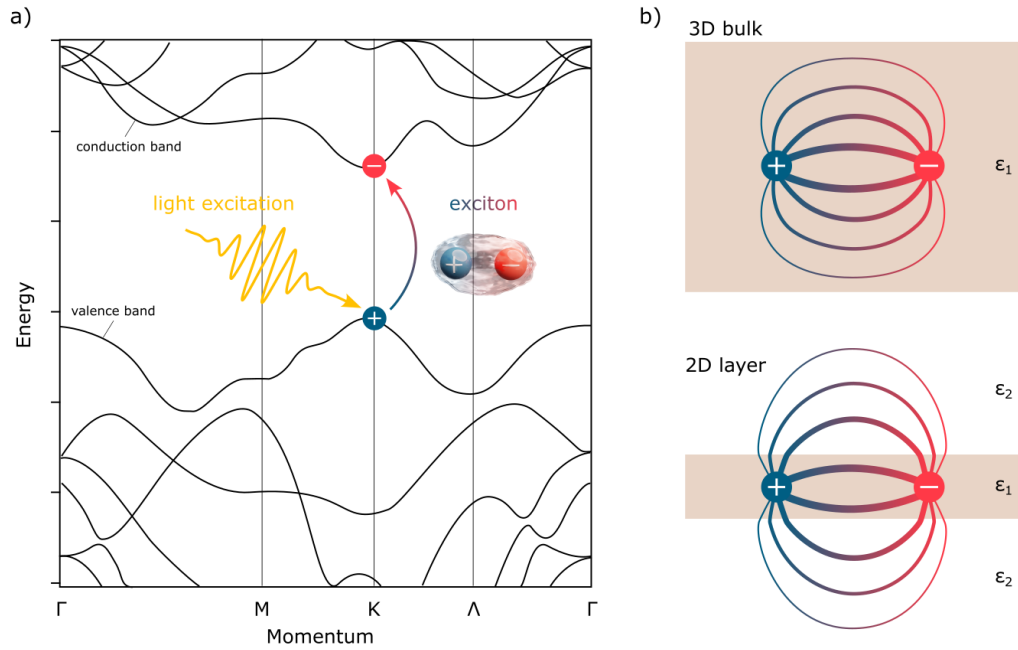


Figure 1.3: a) Sketch of a typical monolayer TMD bandstructure. After an optical excitation of an electron from the valence band to the conduction band, the left behind hole and the electron form a bound state due to the strong Coulomb interaction. b) In the monolayer case the change of dielectric constant of the surroundings ( $\epsilon_2 < \epsilon_1$ ) results in an enhancement of the electron-hole interaction, leading to a strong bound state, described in terms of q quasi-particle, called exciton.

it creates bound states, described in terms of quasi-particles known as excitons, with binding energies of hundreds of meV. Excitons are thus responsible for large absorption and emission in TMDs, making these class of materials very promising for realization of optoelectronic devices such as photodetectors, solar cells or even for light sources generation devices, as for example single photon emitters [10–12, 15–18]. In this context the possibility of stacking several layers of this materials on top of each other, while still remaining away from the bulk limit, has shown lately great possibilities increasing electronic and optical properties of monolayers [19–34], and offering different tools of tuning the excitations, tunability that is a key feature for applications in devices. Focusing in particular on bilayer systems, in addition to strain, dielectric background, electric fields, usual tools to manipulate light excitations dynamics and transport in monolayers bilayers [35–42], the stacking twist angle (figure 1.4) and the type two band alignment offset are new and valuable instruments to investigate TMD heterostructures [43–48]. Recent experiments have shown that considering different TMD heterostructures and photoexciting only one of the two layers, results in a ultrafast electron transfer between the layers [49–54]. The timescales of the process are below the hundred femtoseconds limit, showing a great potential for terahertz emissions implementations. On the other hand, in contrast to the ultrafast dissipation of energy during the thermalization described above, experiments have shown that in the presence of small twist angles, where flat bands appear, the energy

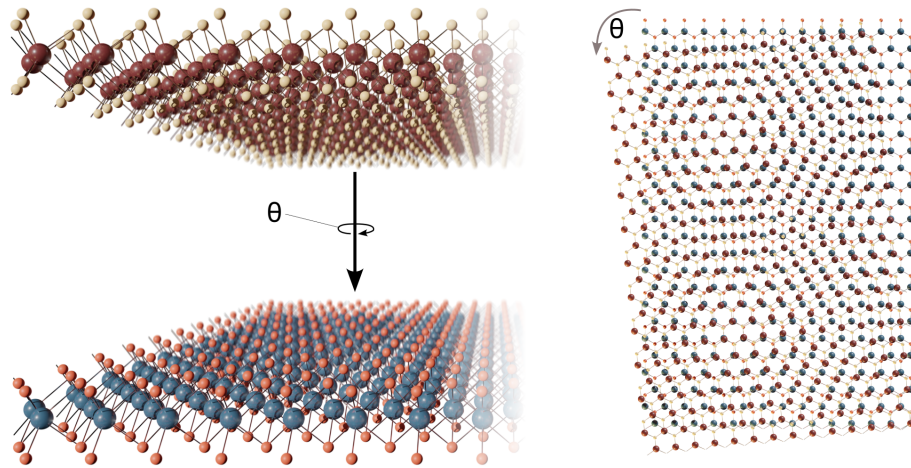


Figure 1.4: Representation of the stacking of two different TMD monolayers to form a bilayer heterostructure. Important quantity for heterostructures properties is the twist angle ( $\theta$  in the picture). Small twist angles can bring the arising of a new periodicity in the system, characterized by the so called moiré pattern.

can not be completely dissipated, inducing long-living low excitations [27, 55, 56]. These experiments show that the speed and energy scales involved in the thermalization process are heavily affected by the choice of the materials, distance between the layers, dielectric environment and twist angle between the layers. For this reason a deep understanding and a microscopic model of how excitons are formed and how they dissipate thermal energy in these systems is required to be able of effectively control these huge amount of parameters. Latest experiments have shown in addition the possibility of observing excitonic signature with Angle-Resolved Photo-Emission (ARPES) spectroscopy [53, 57–60], providing access to the momentum-energy map of excitons within the Brillouin zone. This offers a great opportunity for experiments-theory development giving direct experimental access to the momentum space in which excitonic quantities are usually theoretically described, and which are not directly accessible in PL or absorption measurements. Studies of excitonic signatures in ARPES experiments for monolayer systems have already been conducted. However a detailed study for bilayer systems, where exciton hybridization and moire effects become prominent, is still missing in literature but required to have direct access to exciton features in heterostructures and deepen our understanding of the physics behind experimental observations.

In this thesis we address these open questions with the aim of providing microscopic insights on the impact of thermalization dynamics of excitons in TMD heterostructures. By developing a theoretical model based on the density matrix formalism, we identify in the layer and momentum hybridization of excitonic states a key to unveil a deep understanding of this kind of systems. In the following chapters we will introduce the basic concepts building the theory, showing the main equations giving access to simulations and computation of observables needed for understanding experimental results. From

---

this we will introduce in detail the main effects resulting from light excitations of TMD heterostructures, decomposing the exciton relaxation cascade in two main pictures. First an initial fast dissipation of energy after an optical excitation of one of the TMD layers. This is driven by a significant hybridization between layers, enabling the charge transfer mechanism. Second, a subsequent final step of the dynamics, where the presence of the twist angle becomes predominant. Here we reveal the presence of long-living excited states, explained in terms of a twist angle and temperature dependent bottleneck effect. We will follow the complex process of exciton energy relaxation dynamics, comparing with ARPES experiments and providing new microscopic insights into exciton dynamics in TMD heterostructures.

The main results of this thesis are listed and summarized below:

- Paper 1.** Following the intriguing experimental observations of ultrafast charge transfer observed in TMD heterostructures, we provide a theoretical description of the system under study and show that a phonon-driven two-step charge transfer process via hybridized dark exciton states can predict correctly and explain the experimental observations. We characterize the charge transfer mechanism by conducting a stack dependent and temperature dependent study.
- Paper 2.** We investigate the formation time of interlayer excitons and excitons relaxation cascade in  $\text{WSe}_2\text{-MoS}_2$  in an experiment-theory collaboration. We follow how the light excitations forming layer localized excitons, during the ultrafast time evolution of the system the interlayer excitonic signal, occurring due to the electron transfer between the layers. Our prediction of the two-step charge transfer process is experimentally confirmed, proving the fundamental importance of momentum-dark highly-hybridized states in the thermalization process of light excitations, showing results that can be extended to other van der Waals heterostructures.
- Paper 3.** We simulate and predict a slower dynamics for the case of hole transfer in  $\text{WSe}_2\text{-MoS}_2$ . We predict the presence of an unexpected blue-shift of the electronic photoemitted ARPES signal, tracing it back to the correlated nature of the electron-hole pair, with electron carrying residual information about the hole state.
- Paper 4.** We investigate the characteristic momentum-energy fingerprint of highly hybridized states, predicting a characteristic double peak ARPES signal, with which hybridization can be visualized in ARPES experiments.
- Paper 5.** Focusing on the twist angle dependent thermalization, we focus on studying the low excitation regime in the presence of a moiré potential arising from

---

the spatial periodicity arising from the twist angle. Excitons already relaxed to the lowest energy state, try to dissipate the excessive energy by relaxing to the ground state, but interestingly, we find a bottleneck effect in the low twist angle and temperature regime, explaining experimental observations of long living first excited moiré exciton states with brighter PL signals.

---

## Theoretical framework

---

In this chapter we introduce the main framework of our theory. Starting from the main Hamiltonian used in solid state physics for describing electrons in solids, we will then introduce the Semiconductor Bloch equation, necessary to study the time evolution of light excitation in a semiconductor, and move to the introduction of the Wannier equation, in the case of two dimensional systems. We will then introduce the change of basis required to derive the exciton formalism, and apply it to derive the exciton Hamiltonian for a monolayer system. Finally, we will generalize the results to bilayer systems, introducing the readers to the concept of hybrid excitons. As last step we will include the twist angle dependence in our equation and introduce the concept of moiré excitons.

### 2.1 Electronic Hamiltonian

Since our main goal is describing systems of interacting many-particle, an effective way of treating this problem is writing the total Hamiltonian of the system in second quantization, giving access to the time evolution, thus the particles dynamics, by solving the Heisenberg equation of motion for interesting physical observables, as for example the electron density or the polarization.

In second quantization formalism, each many-body state can be represented in the Fock space in terms of its occupation. Starting from the vacuum state, each other many-particle states can be represented by the application of set of creation  $d_i^\dagger$  and annihilation  $d_i$  operators, acting on specific single particle states, labeled by the quantum number  $i$ . The power of this formalism is the generality of the treatment, independent on the bosonic or fermionic nature of the particles, which is taken into account thanks to the different commutation relations

$$[d_i, d_j]_{\pm} = [d_i^\dagger, d_j^\dagger]_{\pm} = 0 \quad \text{and} \quad [d_i, d_j^\dagger]_{\pm} = \delta_{i,j} \quad (2.1)$$

where  $\pm$  refers to the commutator (-) for bosons or anticommutator (+) for fermions. In general starting from any observable described with a single particle ( $o_1$ ) or two particles

( $o_2$ ) operator in first quantization, we can obtain its many-particle second quantized representation through its expectation value as follows

$$\begin{aligned}\hat{O}_1 &= \sum_{ij} \langle o_1 \rangle_{ij} d_i^\dagger d_j \\ \hat{O}_2 &= \frac{1}{2} \sum_{ijklm} \langle o_2 \rangle_{ijklm} d_i^\dagger d_j^\dagger d_l d_m\end{aligned}\tag{2.2}$$

where we use the compact notation  $\langle o \rangle_{i\dots j} = \langle i\dots | o | \dots j \rangle$  to express the expectation value computed through the integral of single particle states wavefunctions. The reader is referred to the following texts for further information [61–65]. Using second quantization, we can write the general many-body Hamiltonian of a system of electrons in a solid, considering relevant interaction terms with light and lattice vibrations (phonons), as follows

$$H = H_e + H_{phon} + H_{light} + H_{e-e} + H_{e-phon} + H_{e-light}\tag{2.3}$$

where the first terms describe free Hamiltonians in a crystal lattice for electrons ( $H_e$ ), phonons ( $H_{phon}$ ) and light ( $H_{light}$ ), followed by interaction terms, electron-electron ( $H_{e-e}$ ), electron-phonons ( $H_{e-phon}$ ) and electron-light ( $H_{e-light}$ ).

We will now proceed in analyzing each single contribution entering the total Hamiltonian.

## Free electrons

The general approach in solid state physics to describe electrons in a crystal is to use the Born-Oppenheimer approximation, i.e. considering quasi free electrons interacting with a static potential arising from a lattice of positive charged ions. In this picture, energies accessible to electrons in the system are then described by a set  $E_{\lambda\mathbf{k}}$  of single particle energies, forming the energetic band structure, where  $\lambda$  refers to the band index and  $\mathbf{k}$  to the momentum. Although in principle the spin splitting of the bands plays a role, in our work we will not consider spin flipping processes, thus we fix the spin configuration to the one corresponding to the minimum/maximum of the conduction/valence band direct gap, relevant for the optical excitations. The electronic band structure is material specific and can be obtained from first principles calculations. In the case of TMDs, the bandstructure can be sketched along a meaningful symmetry path as shown in figure (2.1). Highlighted we show the so called valleys, high symmetry points in which the electronic dispersion of conduction and valence band presents stationary points. Of great importance for our study are maxima and minima of the band structure. This is because optical excitations consist of promotion of electrons from the valence band to the conduction band, and this usually occurs with a direct gap in correspondence of a valence band maximum with a conduction band minimum. In the case of thermal distributions of optically excited conduction band electrons, these will occupy minima in the conduction band (or in the holes case, maxima of the valence band). For this reason, having in mind the aim of describing excitons, it is useful to introduce an effective mass approximation around maxima and minima of the band structure. This can be easily incorporated in our equations by splitting the total

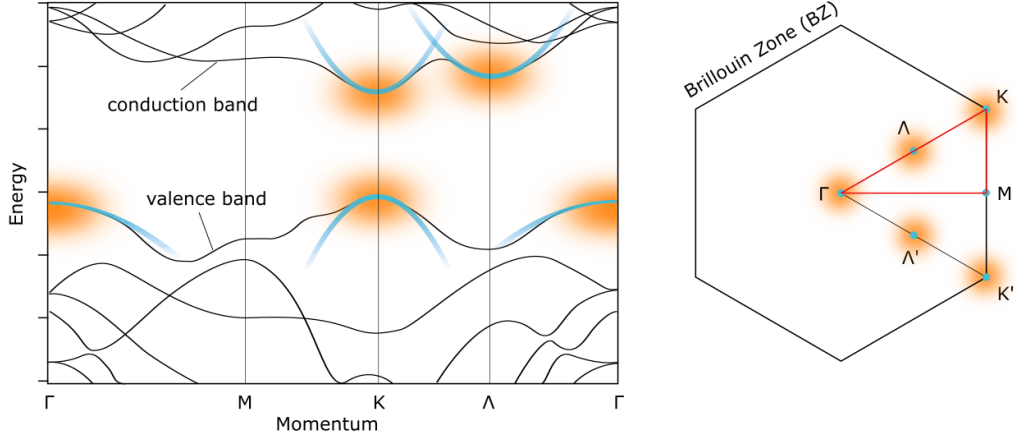


Figure 2.1: Sketch of a typical monolayer TMD bandstructure along a high-symmetry path in the Brillouin zone (red line), where we highlight in orange important high symmetry points (valleys), also marked with the same color in the 2D Brillouin zone of the system. We highlight in blue the effective mass approximation adopted, with which each maxima and minima of the bandstructure is treated within a parabolic approximation.

momentum  $\mathbf{k}^* \in BZ$  (Brillouin zone) into the sum of a valley local momentum coordinate and a valley momentum  $\zeta$  (which can be treated as a separate quantum number), i.e.  $\mathbf{k}^* = \mathbf{k} + \zeta$ . We can then split the total momentum quantum number in  $\mathbf{k}, \zeta$  and the electron dispersion can be written as  $\varepsilon_{\lambda\mathbf{k}^*} \rightarrow \varepsilon_{\lambda\zeta\mathbf{k}} = \varepsilon_{\lambda\zeta} + \sigma_{\lambda}\hbar^2\mathbf{k}^2/(2m_{\zeta}^{\lambda})$ , with effective mass  $m_{\zeta}^{\lambda}$  reflecting the parabolic curvature approximating the band  $\lambda$  around valley  $\zeta$ , and  $\sigma_{\lambda} = \pm 1$ , positive for conduction bands and negative for valence bands. Throughout our work we will use this valley local approximation, with all the TMDs effective masses and relative energies are extracted from DFT calculations [66]. With this considerations, we can finally write the free electron Hamiltonian  $H_e$  in the effective mass approximation as follows

$$H_e = \sum_{\lambda\zeta\mathbf{k}} \varepsilon_{\lambda\zeta\mathbf{k}} a_{\lambda\zeta\mathbf{k}}^{\dagger} a_{\lambda\zeta\mathbf{k}} \quad (2.4)$$

with  $a_{\lambda\zeta\mathbf{k}}^{(\dagger)}$  fermionic annihilation (creation) operators, destroying (creating) an electron in state  $|\lambda\zeta\mathbf{k}\rangle$ .

## Phonons

Following from the Born-Oppenheimer approximation, the motion of atoms in the crystal and how this affects the energy of electrons in the system is taken into account by the introduction of quasi-particles, describing the quantized collective harmonic oscillations of the ion lattice. This quasi-particles, called phonons, play a crucial role in the electron dynamics, since the thermalization of electrons in the system can be described, in this picture, as an electron-phonon scattering process. We can use the following Hamiltonian

to describe free phonons in the system [61, 62]

$$H_{phon} = \sum_{\kappa\mathbf{q}} \hbar\Omega_{\kappa\mathbf{q}} \left( b_{\kappa\mathbf{q}}^\dagger b_{\kappa\mathbf{q}} + \frac{1}{2} \right) \quad (2.5)$$

with  $\hbar\Omega_{\kappa\mathbf{q}}$  phonon energy and  $b_{\kappa\mathbf{q}}^{(\dagger)}$  bosonic annihilation (creation) operators, destroying (creating) a phonon in state  $|\kappa\mathbf{q}\rangle$  described by the phonon mode  $\kappa$  and momentum  $\mathbf{q}$ . Phonon energies are eigenvalues derived from the diagonalization of the dynamical matrix, taking into account all the repulsive forces arising from the nuclei in the lattice and screened by the core and valence electrons [67, 68]. As for the electron dispersion, the phonon dispersion is material specific and computed through first principles calculations, however we can represent its general form along the usual symmetry path as in figure 2.1. Of great importance for TMDs are transitions between valleys, thus the highlighted areas in 2.1. For this reason it is useful to introduce, also in the case of phonons, an approximation to describe the dispersion around main symmetry points, splitting the phonon momentum in a local coordinate and a momentum valley index. Following the Debye and Einstein approach we split the total dispersion of acoustic phonons in a linear part  $\Omega_{\zeta=\Gamma,\mathbf{q}} = v|\mathbf{q}|$  around the  $\Gamma$  valley, with  $v$  sound velocity, and a constant contribution around  $M, K$ , i.e.  $\Omega_{\zeta=M/K,\mathbf{q}} = \Omega_{\zeta=M/K}$ , and with constant energies around  $\Gamma, M, K$ ,  $\Omega_{\zeta=\Gamma/M/K,\mathbf{q}} = \Omega_{\zeta=\Gamma/M/K}$ , for optical phonons. Throughout this work we include longitudinal and transverse acoustic modes (LA,TA), as well as the corresponding optical modes (LO, TO) and the out-of-plane optical mode (A1), and take sound velocities and energies from DFPT calculations in [69].

## Light

To obtain a quantized theory of the electromagnetic field in Coulomb gauge, the usual procedure is starting from the vector potential  $\mathbf{A}$ , transforming it to an operator

$$A(\mathbf{r}, t) \rightarrow \hat{A}(\mathbf{r}, t) = \sum_{\sigma,\mathbf{k}} \sqrt{\frac{\hbar}{2\epsilon_0 L^3 \omega_k}} \mathbf{e}_{\sigma,\mathbf{k}} c_{\sigma,\mathbf{k}}(t) e^{i\mathbf{k}\mathbf{r}} + h.c. \quad (2.6)$$

where  $c_{\sigma,\mathbf{k}}^{(\dagger)}$  annihilation(creation) operator (fulfilling bosonic commutation relations) for a photon in mode  $\sigma$  and wavevector  $\mathbf{k}$ . With this transformation the Hamiltonian of the electromagnetic field obtains the convenient form

$$H_{light} = \sum_{\sigma\mathbf{k}} \hbar\omega_{\mathbf{k}} \left( c_{\sigma\mathbf{k}}^\dagger c_{\sigma\mathbf{k}} + \frac{1}{2} \right) \quad (2.7)$$

where each mode of the electromagnetic field is interpreted as an harmonic oscillator with quantized energy  $\hbar\omega_{\mathbf{k}}$ , with photon dispersion  $\omega_{\mathbf{k}} = c|\mathbf{k}|$  (light cone) determined by the light velocity  $c$ .

## Electron-electron interaction

Being electrons and holes charged particles, of great importance for the description of our problem is the Coulomb interaction. The non-local two-particles second quantized

operator describing the Coulomb interaction in a many-body system can be written in the momentum space as

$$H_{e-e} = \frac{1}{2} \sum_{ijmn} V_{mn}^{ij} a_i^\dagger a_j^\dagger a_m a_n \quad (2.8)$$

where  $V_{mn}^{ij} = \langle ij | V(\mathbf{r}-\mathbf{r}') | mn \rangle = \sum_{\mathbf{q}} V_{\mathbf{q}} \mathcal{F}_{in}(\mathbf{q}) \mathcal{F}_{jm}(-\mathbf{q})$ , where in the second step we used the Fourier transformed Coulomb matrix element  $V(\mathbf{r}-\mathbf{r}') = \sum_{\mathbf{q}} V_{\mathbf{q}} e^{i\mathbf{q}\cdot\mathbf{r}}$  and  $\mathcal{F}_{in}(\mathbf{q}) = \langle i | e^{i\mathbf{q}\cdot\mathbf{r}} | n \rangle$ . By using the Bloch theorem we can obtain a simplified form for our Coulomb matrix element, in fact  $\mathcal{F}_{in}(\mathbf{q}) = \delta_{\mathbf{k}_n - \mathbf{k}_i, \mathbf{q}} \langle u_{\mathbf{k}_i + \mathbf{q}}^* | u_{\mathbf{k}_n} \rangle \approx \delta_{\mathbf{k}_n - \mathbf{k}_i, \mathbf{q}}$ , with Bloch functions  $u_{\mathbf{k}}$  where in the last step we used that Bloch functions are approximately constant in proximity of high symmetry points. Thus we obtain

$$H_{e-e} = \frac{1}{2} \sum_{\substack{\mathbf{k} \ \mathbf{p} \ \mathbf{q} \\ \lambda \lambda' \zeta \zeta'}} V_{\mathbf{q}} a_{\lambda \zeta \mathbf{k} + \mathbf{q}}^\dagger a_{\lambda' \zeta' \mathbf{p} - \mathbf{q}}^\dagger a_{\lambda' \zeta' \mathbf{p}} a_{\lambda \zeta \mathbf{k}} \quad (2.9)$$

where we already introduced a valley local coordinate system, and restrict to consider only intra-valley and band conserving Coulomb processes, neglecting terms related to higher order processes for the electron-hole bound states we aim to describe. We will consider in the following sections the non trivial dielectric environment of the system and the specific dimensionality of the problem, providing a specific form for the coulomb matrix element of a two dimensional layer TMD, with a specific dielectric constant  $\epsilon_0$ , embedded into a three dimensional space (characterized by a different dielectric constant), given by

$$V_{\mathbf{q}} = \frac{e_0^2}{2\epsilon_0 A \epsilon_s(q) q} \quad (2.10)$$

with  $\epsilon_s(q) = v_{TMD} \operatorname{th} \left( \frac{1}{2} \left[ dq \alpha_{TMD} - \ln \left( \frac{v_{TMD} - v_{bg}}{\kappa_{TMD} + v_{bg}} \right) \right] \right)$

with  $e_0$  electron charge,  $A$  area of the layer,  $v = \sqrt{\epsilon_{\parallel} \epsilon_{\perp}}$ ,  $\alpha = \sqrt{\epsilon_{\parallel} / \epsilon_{\perp}}$ , functions of the transversal and longitudinal dielectric constant, and  $d$  the thickness of the layer, using subscripts TMD/bg differentiating between the TMD/back ground values. Additional details on the derivation can be found in [70–72].

## Electron-phonon interaction

Following the Born-Oppenheimer approximation, the interaction between electrons and the lattice vibrations can be derived as an electron-phonon interaction Hamiltonian. In this case given the two different regimes of motions for electrons and atoms in the lattice, the small lattice deformation deriving from vibrations of atoms around their equilibrium position can be taken into account starting from the unperturbed lattice potential  $V_{lattice}^0(\mathbf{r}) = \sum_i v_{atom}(\mathbf{r} - \mathbf{R}_i)$ , Taylor expanding up to the first order for a small time dependent displacement around the equilibrium position of each atom, i.e.  $V_{lattice}(\mathbf{r}, t) = V_{lattice}^0(\mathbf{r}) - \sum_i \nabla v_{atom}(\mathbf{r} - \mathbf{R}_i) \cdot \mathbf{u}_i(t)$ , where we consider the vector  $\mathbf{u}_i$  representing the small displacement vector for the  $i$ -th atom. Whereas the constant term is already included in the eigenenergies deriving from eq. 2.5, the second part, using the

general procedure to obtain operators in second quantization, by expanding  $u_i$  in terms of phonons, let us derive the general electron-phonon interaction contribution

$$H_{e-phon} = \sum_{\kappa\lambda\zeta\zeta'\mathbf{k}\mathbf{q}} \mathcal{G}_{\zeta-\zeta',\mathbf{q}}^{\kappa\lambda} a_{\lambda\zeta\mathbf{k}+\mathbf{q}}^\dagger a_{\lambda\zeta'\mathbf{k}} \left( b_{\kappa,\zeta-\zeta',\mathbf{q}} + b_{\kappa,\zeta'-\zeta,-\mathbf{q}}^\dagger \right) \quad (2.11)$$

with  $\mathcal{G}_{\zeta-\zeta',\mathbf{q}}^{\kappa\lambda} \simeq \sqrt{\frac{\hbar}{2\rho A\Omega_j\mathbf{q}}} \tilde{\mathcal{G}}_{\zeta-\zeta',\mathbf{q}}^{\kappa\lambda}$

expressing scattering processes with emission ( $b_l^\dagger$ ) or absorption ( $b_l$ ) of phonon, where we restrict again to band conserving processes, major contributions in our approximations. The electron-phonon couplings  $\mathcal{G}_{\zeta-\zeta',\mathbf{q}}^{\kappa\lambda}$  are obtain from ref [69], by applying a deformation potential approximation, corresponding to a zeroth/first order Taylor expansion of the full electron-phonon coupling element obtained from DFPT calculations, where  $A$  is the area of the system,  $\rho$  the surface mass density of the material, and  $\tilde{\mathcal{G}}_{\zeta-\zeta',\mathbf{q}}^{\kappa\lambda}$  is the scattering potential, containing information about electron-atoms interaction and polarization vector of the phonon mode.

### Electron-light interaction

A final important interaction we have to introduce in our description is the electron-light interaction. This interaction, is in fact responsible for the creation of optical excited states, seen as an interband flux of electrons, which from the valence band are promoted to the conduction band. This interaction is also responsible for general changes in number of excitons, since after being excited, excitons can radiatively recombine by emitting photons. Depending on the process to describe, it is possible to choose between a semi-classical description, in the case in which the external electromagnetic field can be interpreted directly as a time dependent perturbation injecting excitons in the system; or a fully quantum mechanical approach, in the case in which an equivalent classical description is not possible, as in the case of recombination through spontaneous emission. In our work, given our interest in the fast dynamics occurring in the system, we will use a semiclassical description, neglecting processes occurring at much longer timescales, that in contrast would require a full quantum-mechanical description, like exciton recombination. Recombination processes occur at picosecond timescales, and thus negligible for the dynamics on the hundreds of femtoseconds scale. In the semiclassical description of the electron-light interaction one treats the light as a classical electromagnetic field, and express the interaction with the minimal coupling Hamiltonian [73]

$$H_{e-light} = \frac{e_0}{m_0} \sum_{ij\sigma} \mathbf{M}_\sigma^{ij} \cdot \mathbf{A}(t) a_i^\dagger a_j \quad (2.12)$$

where  $\mathbf{M}_\sigma^{ij} = \langle i | \mathbf{P} | j \rangle$  is the optical matrix element for polarization  $\sigma$ , with momentum operator  $\mathbf{P}$ , and the electromagnetic vector potential  $\mathbf{A}(t)$ , electron charge  $e_0$  and mass  $m_0$ , and can be calculated from first principle methods. To obtain this Hamiltonian we have to choose the Coulomb gauge and neglect terms proportional to  $\mathbf{A}^2$ . In addition we apply the dipole approximation, assuming that the vector potential variation is weakly varying on the timescales of variation of the electronic wavefunction.

## 2.2 Many-Body Dynamics

### Density Matrix Formalism

With the introduction of the full Hamiltonian, we are ready to move to the derivation of equations of motion, with which we can study the electron dynamics in the system. In particular, using the Heisenberg picture, the dynamics of the system can be describe in terms of time-dependent operators, which time evolution is governed by the Heisenberg equation, that for an observable  $\hat{O}$  reads  $i\hbar \frac{d\hat{O}}{dt} = [\hat{O}, H]$ . Throughout our work, we apply the density matrix theory formalism to describe particles in solid. Within this framework, expectation values of observables,  $\langle \hat{O} \rangle$ , are accessible exploiting the density matrix of the system, which in general contains information about populations and correlations of the states accessible to the system. By introducing the density matrix  $\hat{\rho} = \sum_i p_i |\psi_i\rangle \langle \psi_i|$ , where each quantum state  $\psi_i$  can occur with probability  $p_i$ , we can compute expectation values as  $\langle \hat{O} \rangle = \text{Tr}(\hat{\rho}\hat{O})$ , where  $\text{Tr}()$  indicates the trace. The time evolution of this expectation value can then be computed through the Heisenberg equation of motion

$$i\hbar \frac{d\langle \hat{O} \rangle}{dt} = \langle [\hat{O}, H] \rangle. \quad (2.13)$$

In our study we will be interested in particular in the time evolution of the following expectation values, as electron occupation  $\rho_{\lambda\mathbf{k}} = \langle a_{\lambda\mathbf{k}}^\dagger a_{\lambda\mathbf{k}} \rangle$ , microscopic polarization  $p_{\mathbf{k}\mathbf{k}'} = \langle a_{c\mathbf{k}}^\dagger a_{v\mathbf{k}'} \rangle$  (where  $c$  stands for conduction and  $v$  for valence band), and phonon number  $n_{j\mathbf{q}} = \langle b_{j\mathbf{q}}^\dagger b_{j\mathbf{q}} \rangle$ . A detailed derivation of how to derive the equations of motions within the density matrix formalism can be found in Ref. [74].

### Hierarchy Problem and Cluster Expansion

A known problem arising when solving the Heisenberg equation for a generic N-particle operator, is deriving from the presence of many-particle interactions in the Hamiltonian, which induces a coupling to an (N+1)-particle operator. The dynamics of an N-particle operator results thus linked to the time evolution of a (N+1)-particle operator, and in order to proceed with finding the equation of motion for the starting operator, we would need to solve a separate Heisenberg equation for the (N+1)-particle operator. Continuing, if we would try to solve the Heisenberg equation for the (N+1)-particle operator, this would be coupled to the time evolution of a (N+2)-particle operator. This procedure leads to an infinite hierarchy of coupled equations. For example, if we want to compute the time evolution of the electron occupation  $\rho_{\lambda\mathbf{k}}$  using equation 2.13, we would obtain terms of the form  $\langle a_i^\dagger a_j^\dagger a_k a_l \rangle$ , meaning that one requires the solution of equation 2.13 for this operator to obtain the time evolution of the electron occupation, which then couples to three-particle operators and so on. To solve this problem one can use the cluster expansion and expand the (N+1)-particle operator in terms of a sum of products of single-particle operators (singlets), where the sum is performed over all the possible permutations, plus

terms containing correlations, i.e.

$$\begin{aligned}
 \langle \hat{O}_2 \rangle &= \sum_i \sigma^i P_i \{ \langle \hat{O}_1 \rangle \langle \hat{O}_1 \rangle \} + \Delta \langle \hat{O}_2 \rangle \\
 \langle \hat{O}_3 \rangle &= \sum_i \sigma^i P_i \{ \langle \hat{O}_1 \rangle \langle \hat{O}_1 \rangle \langle \hat{O}_1 \rangle \} + \sum_i \sigma^i P_i \{ \langle \hat{O}_1 \rangle \Delta \langle \hat{O}_2 \rangle \} + \Delta \langle \hat{O}_3 \rangle \\
 &\vdots \\
 \langle \hat{O}_N \rangle &= \mathcal{F} \left( \langle \hat{O}_1 \rangle, \Delta \langle \hat{O}_2 \rangle, \dots, \Delta \langle \hat{O}_N \rangle \right)
 \end{aligned} \tag{2.14}$$

Where  $P$  is the permutation operation, with  $\sigma = 1$  for bosons and  $\sigma = -1$  for fermions,  $\Delta$  refers to the pure correlation part, and  $\mathcal{F}(\dots)$  is a function obtained recursively [75]. In this way we are not performing any approximation but just rewriting the equation in terms of correlations. The approximations, which lead to an effective simplification of the problem, are then performed on these correlation terms. An example of this procedure is the Hartree-Fock approximation, where starting from  $\langle a_i^\dagger a_j^\dagger a_k a_l \rangle$ , we obtain an expansion into products of singlets plus a correlation term that is neglected in a mean field approach, i.e.  $\langle a_i^\dagger a_j^\dagger a_k a_l \rangle = \langle a_j^\dagger a_k \rangle \langle a_i^\dagger a_l \rangle + \langle a_j^\dagger a_l \rangle \langle a_i^\dagger a_k \rangle + \Delta \langle a_i^\dagger a_j^\dagger a_k a_l \rangle$ . By applying this procedure, we have a systematic and controlled way of truncating the infinite hierarchy to a precise order.

## Markov Approximation

Another problem arising from the solution of equation 2.13, is deriving from the complex temporal dependence of correlation terms in its solution. The Heisenberg equation of motion for  $S$ , deriving from solving 2.13, reads

$$\dot{S}(t) = (i\omega - \gamma)S(t) + C(t) \tag{2.15}$$

where  $C(t)$  is the source of correlations term, with  $\omega$  and  $\gamma$  characteristic frequency and decay rate of the specific quantity under exam. The analytical solution of the previous equation, assuming a fast decay of the initial value of  $S(t)$ , is

$$S(t) = \int_0^\infty d\tau e^{(i\omega - \gamma)\tau} C(t - \tau). \tag{2.16}$$

A simplification to this solution can be introduced within the Markov approximation [63, 65]. Here quantum memory effects, taken into account by the full time dependent integral and resulting in non-linear terms, are neglected to obtain solutions describing energy conserving scattering. In this case the source of correlations is then approximated to be independent from past values and approximated to  $C(t - \tau) \simeq C(t)e^{-i\omega_0\tau}$ . With this approximation we neglect the memory effects in  $C$ , but assume that its time dependence can be well captured by a characteristic frequency  $\omega_0$ . With this approximation the solution of equation 2.15 becomes

$$S(t) = -i \frac{C(t)}{(\omega - \omega_0) - i\gamma}, \tag{2.17}$$

that in the limit of decay going to zero, by applying the Sokhotski–Plemelj theorem, leads to

$$S(t) = \pi C(t)\delta(\omega - \omega_0) - iP \left( \frac{C(t)}{\omega - \omega_0} \right), \quad (2.18)$$

where  $P$  is the principal value. By plugging  $S(t)$  back in the equation of motion for the corresponding single-particle quantity, the first term leads to energy conserving scattering events, characterized by sharp energy requirements (zeros of the  $\delta$  function), while the second term is related to many-particle induced energy-renormalizations, which are usually divergent and require a self-consistent treatment. For most of our work we will neglect the influence of the second term, leading to small corrections within our approximations. However this term has to be taken into account when dealing with phonon dephasing in the presence of peculiar band topology, where the importance of the temperature dependent self-consistent broadening of the decay rate can lead to suppression or activation of specific scattering channels. This is the case for Paper 5, where the appearance of flat bands require a more sophisticated treatment and will be described in following sections.

## 2.3 Semiconductor Bloch Equation

Having introduced the basics elements of the theory, we can now introduce the main equations that will allow us to switch to an excitonic formalism. The key quantity in this context is the microscopic polarization,  $p_{\mathbf{k}\mathbf{k}'} = \langle a_{\mathbf{c}\mathbf{k}}^\dagger a_{\mathbf{v}\mathbf{k}'} \rangle$ . If we apply equation 2.13 to study its time-evolution, we obtain the *Semiconductor Bloch equations* [64, 74]. In our theoretical framework we will always restrict to the case of low light excitations, meaning that changes in valence and conduction band occupations induced by the laser pulse and occupation induced energy renormalizations can be neglected. In the low density regime the Semiconductor Bloch equation can be written in the following form

$$i\hbar\partial_t p_{\mathbf{k}\mathbf{k}'} = - \sum_{\mathbf{q}} \tilde{V}_{\mathbf{k}\mathbf{k}'\mathbf{q}} p_{\mathbf{k}+\mathbf{q},\mathbf{k}'+\mathbf{q}} - \frac{e_0}{m_0} \mathbf{M}_{\mathbf{k}}^{cv} \cdot \mathbf{A} \delta_{\mathbf{k}\mathbf{k}'} \quad (2.19)$$

$$\tilde{V}_{\mathbf{k}\mathbf{k}'\mathbf{q}} = (\varepsilon_{\mathbf{c}\mathbf{k}} - \varepsilon_{\mathbf{v}\mathbf{k}'}) \delta_{\mathbf{q},\mathbf{0}} - V_{\mathbf{q}},$$

equation that describes how the optical excitation, promoting electrons from the valence to the conduction band changes the optical property of the system. If we now consider the homogeneous part of this equation, i.e. without including the electromagnetic field coupling driving the transition, we can derive the energy landscape accessible to light excitations of the system by solving the related eigenvalue problem related, i.e.

$$(\varepsilon_{\mathbf{c}\mathbf{k}} - \varepsilon_{\mathbf{v}\mathbf{k}'}) \phi(\mathbf{k}, \mathbf{k}') - \sum_{\mathbf{q}} V_{\mathbf{q}} \phi(\mathbf{k} + \mathbf{q}, \mathbf{k}' + \mathbf{q}) = E_{\mathbf{k},\mathbf{k}'} \phi(\mathbf{k}, \mathbf{k}') \quad (2.20)$$

which can be seen as a two-particle Schrödinger equation for an electron and a hole, and it is called in literature *Wannier equation*. By solving numerically this equation for TMD systems, one finds strongly bound electron-hole states, with bounding energies of hundreds of meV and strongly localized wavefunctions in momentum space (translated into real space means large radii compared to the unit cell). This bound states are usually described as

quasi-particles called excitons. With this clarification, the previously introduced notation and effective mass approximation around maxima/minima of the BZ, can be used to express the problem in a more suitable form, obtaining a set of equations, one for each pair of electron-hole valleys.

In an hydrogen-like atom approach, one can separate the motion of electrons and holes in terms of center of mass (CoM) momentum  $\mathbf{Q}$  and relative momentum  $\mathbf{k}$ , obtaining energies

$$\begin{aligned} \varepsilon_{c\zeta\mathbf{k}_e} - \varepsilon_{v\zeta'\mathbf{k}_h} &= \frac{\hbar^2\mathbf{k}_e^2}{2m_\zeta^e} - \frac{\hbar^2\mathbf{k}_h^2}{2m_{\zeta'}^h} + E_{gap} = \frac{\hbar^2\mathbf{k}^2}{2\tilde{m}_{\zeta\zeta'}} + \frac{\hbar^2\mathbf{Q}^2}{2M_{\zeta\zeta'}} + E_{gap} \\ \text{with } \mathbf{k} &= \frac{m_\zeta^e}{M_{\zeta\zeta'}}\mathbf{k}_e + \frac{m_{\zeta'}^h}{M_{\zeta\zeta'}}\mathbf{k}_h \quad \text{and} \quad \mathbf{Q} = \mathbf{k}_e - \mathbf{k}_h \end{aligned} \quad (2.21)$$

where we introduced  $E_{gap} = \varepsilon_{c\zeta} - \varepsilon_{v\zeta'}$ , reduced mass  $\tilde{m}_{\zeta\zeta'} = (m_\zeta^e m_{\zeta'}^h)/(m_\zeta^e + m_{\zeta'}^h)$  and total mass  $M_{\zeta\zeta'} = m_\zeta^e + m_{\zeta'}^h$ , with effective electron and hole masses around each valley  $m_{e/h}^\zeta$ . In addition, given that the interaction term only depends on the relative coordinate, we can assume a separation ansatz for the total wavefunction, i.e.  $\phi(\mathbf{k}, \mathbf{Q}) = \psi(\mathbf{k})\mathcal{Y}(\mathbf{Q})$ . With this we can rewrite the Wannier equation for the relative momentum component

$$\frac{\hbar^2\mathbf{k}^2}{2\mu_\alpha}\psi^\alpha(\mathbf{k}) - \sum_{\mathbf{q}} V_{\mathbf{q}}\psi^\alpha(\mathbf{k} + \mathbf{q}) = E_b^\alpha\psi^\alpha(\mathbf{k}) \quad (2.22)$$

with which we can obtain the binding energies for each excitonic state  $\alpha$ , where we introduced the new quantum number  $\alpha = (n, \zeta_e, \zeta_h)$ , containing the quantum number describing the Rydberg-like series of excitonic states and the electron and hole valley indexes. The total energy of the exciton is computed as  $E_{\mathbf{Q}}^\alpha = \frac{\hbar^2\mathbf{Q}^2}{2M_\alpha} + E_b^\alpha + E_{gap}$ . We note that since the excitons are now identified by two valley indices, one for the hole and one for the electron, in the following we will refer to the *exciton valley* for exciton labeled by  $\alpha$  with  $\zeta^\alpha = \zeta_h \zeta_e$  (for example  $\zeta^\alpha = \text{KK}, \text{K}\Lambda, \text{K}\Gamma$ ) and use  $\zeta_{e/h}^\alpha$  to refer to the electron/hole substructure of the exciton indices. We will use the same notation for all other excitonic quantities, for example we will call electron/hole masses of exciton  $\alpha$  with  $m_{e/h}^\alpha$ , and so on.

## 2.4 Exciton formalism

In the previous section we saw that the presence of strongly interacting electron and holes, creating strongly bound states, changes the optical response of the material, change that is described by equation 2.19. For non-interacting electrons, the interband transition energies are simply given by the band gap at the respective momentum. However the strong Coulomb interaction between electron and holes, couples polarizations at different momenta, and decreases the energy needed for an optical excitation restructuring the energy landscape accessible to optical excitations. In this context, becomes useful the introduction of a formalism based on the existence of excitons. The introduction of this formalism is conceptually justified by the considerations above, however we will provide in

the following a mathematical justification and the required change of basis, moving from an electronic to an excitonic picture. The advantage of changing picture, by introducing a change of basis directly in our Hamiltonians, brings to a simplification in the derivation of all the equation of motion. In principle all the equations that will be shown in the following chapters, can be derived from an electronic picture and applying an Hartree-Fock approximation in the cluster expansion. However applying the change of basis from the beginning, decreases drastically the amount of operators involved and helps with the interpretation of higher order interaction processes as for the exciton-phonon interaction.

The first step in this procedure is introducing the pair operator  $P_{\mathbf{k}\mathbf{k}'}^\dagger = a_{c\mathbf{k}}^\dagger a_{v\mathbf{k}'}$ , describing the creation and annihilation of electron-hole pairs. For this first introduction part we will neglect the valley index, that can be later reintroduce as part of the exciton quantum number. The commutation relations for the pair operators are

$$\begin{aligned} [P_{ij}, P_{kl}^\dagger] &= \delta_{ik}\delta_{jl} - F_{ijkl} \\ \text{with } F_{ijkl} &= a_{vl}^\dagger a_{vj}^\dagger \delta_{ik} + a_{ck}^\dagger a_{ci}^\dagger \delta_{jl} \end{aligned} \quad (2.23)$$

here the operator  $F_{ijkl}$  represents the fermionic substructure of the pair operator, and is responsible for terms including the Pauli blocking. The key of our derivation is now to approximate these commutator to be a fully bosonic commutator, by setting  $F_{ijkl} \approx 0$ , approximation valid in the low excitation limit. To transform Hamiltonian 2.3 in terms of pair operators, we need as well to express electron intraband contributions into combination of pair operators [76]

$$\begin{aligned} a_{ci}^\dagger a_{cj} &\rightarrow \sum_l P_{il}^\dagger P_{jl} \\ a_{vi}^\dagger a_{vj} &\rightarrow \sum_l P_{li}^\dagger P_{lj}. \end{aligned} \quad (2.24)$$

The electronic part of Hamiltonian 2.3, can now be written as

$$H_e + H_{e-e} \rightarrow \sum_{\mathbf{k}_e \mathbf{k}_h} \left[ (\varepsilon_{c\mathbf{k}_e} - \varepsilon_{v\mathbf{k}_h}) P_{\mathbf{k}_e \mathbf{k}_h}^\dagger - \sum_{\mathbf{q}} V_{\mathbf{q}} P_{\mathbf{k}_e + \mathbf{q}, \mathbf{k}_h + \mathbf{q}}^\dagger \right] P_{\mathbf{k}_e \mathbf{k}_h} \quad (2.25)$$

and by performing an expansion of pair operator into excitonic eigenmodes, by separating into relative and CoM momenta, i.e.  $P_{\mathbf{k}_e \mathbf{k}_h}^\dagger = \sum_{\alpha} X_{\alpha, \mathbf{k}_e - \mathbf{k}_h}^\dagger \psi^{\alpha}(m_e^{\alpha}/M_{\alpha} \mathbf{k}_h + m_h^{\alpha}/M_{\alpha} \mathbf{k}_e) = \sum_{\alpha} X_{\alpha \mathbf{Q}}^\dagger \psi^{\alpha}(\mathbf{k})$ , with  $\psi^{\alpha}$  obtained from the Wannier equation 2.22, we arrive at the diagonal free exciton Hamiltonian

$$H_{X,0} \approx \sum_{\alpha \mathbf{Q}} E_{\mathbf{Q}}^{\alpha} X_{\alpha \mathbf{Q}}^\dagger X_{\alpha \mathbf{Q}} \quad (2.26)$$

It is important to note that Hamiltonian 2.26, describing the energy of free excitons as single-particle operators, contains within the effective single-particle exciton treatment the Coulomb interaction. In the electron picture (Hamiltonian 2.3) the Hamiltonian contained many-particle interactions, that in the equation of motion leads to the hierarchy problem in Coulomb correlations, as discussed in the previous sections. The Hartree-Fock approximation to cut the hierarchy problem in that case, it is now fully contained in the negligence of the fermionic correction term  $F_{ijkl}$  in the commutator of the pair

operator 2.23, and produced an effective single particle problem within the same order of approximations. By performing the same change of basis in all the other terms of 2.3 we obtain the full exciton Hamiltonian, including exciton-phonon and exciton-light interactions [77]

$$\begin{aligned}
 H_X &= \sum_{\alpha\mathbf{Q}} E_{\mathbf{Q}}^{\alpha} X_{\alpha\mathbf{Q}}^{\dagger} X_{\alpha\mathbf{Q}} + \sum_{\substack{\alpha\beta j \\ \mathbf{q}\mathbf{Q}}} G_{j\mathbf{q}}^{\alpha\beta} X_{\alpha\mathbf{Q}+\mathbf{q}}^{\dagger} X_{\beta\mathbf{Q}} \left( b_{j,\mathbf{q}} + b_{j,-\mathbf{q}}^{\dagger} \right) + \sum_{\sigma\alpha\mathbf{q}} \tilde{M}_{\sigma\mathbf{q}}^{\alpha} \cdot \mathbf{A} X_{\alpha\mathbf{q}}^{\dagger} \\
 &\text{with } G_{j\mathbf{q}}^{\alpha\beta} = \mathcal{G}_{\zeta_e^{\alpha}\zeta_e^{\beta}\mathbf{q}}^{jc} \delta_{\zeta_{ph},\zeta_e^{\beta}-\zeta_e^{\alpha}} \delta_{\zeta_h^{\beta}\zeta_h^{\alpha}} \mathcal{F}_{\alpha\beta} \left( \frac{m_h^{\beta}}{M_{\beta}} (\mathbf{q} + s_{\beta\alpha}\mathbf{Q}) \right) + \\
 &\quad - \mathcal{G}_{\zeta_h^{\alpha}\zeta_h^{\beta}\mathbf{q}}^{jv} \delta_{\zeta_{ph},\zeta_h^{\beta}-\zeta_h^{\alpha}} \delta_{\zeta_e^{\beta}\zeta_e^{\alpha}} \mathcal{F}_{\alpha\beta} \left( -\frac{m_e^{\beta}}{M_{\beta}} (\mathbf{q} + s_{\beta\alpha}\mathbf{Q}) \right) \\
 &\quad \text{and } \tilde{M}_{\sigma\mathbf{q}}^{\alpha} = \delta_{\zeta^{\alpha},\mathbf{K}\mathbf{K}} M_{\sigma\mathbf{Q}}^{cv} \sum_{\mathbf{k}} \psi^{\alpha*}(\mathbf{k})
 \end{aligned} \tag{2.27}$$

where the phonon quantum number has been redefined into a superindex  $j = (\kappa, \zeta_{ph})$  containing the phonon mode and the phonon valley, form factors with respect to exciton wavefunctions  $\mathcal{F}_{\alpha\beta}(\mathbf{q}) = \sum_{\mathbf{k}} \psi^{\alpha}(\mathbf{k} + \mathbf{q})^* \psi^{\beta}(\mathbf{k})$ ,  $s_{\alpha\beta} = 1 - M_{\alpha}/M_{\beta}$ , and the new exciton-phonon and exciton-light couplings are defined starting from equations 2.11, 2.12. We note that the hermitian conjugate of the exciton-light term, responsible of spontaneous recombination of exciton, is not consider in our study, term that would bring a loss of excitons negligible in the timescales under study (ultrafast exciton dynamics). The full exciton Hamiltonian 2.27 contains the main elements to describe, through equation 2.13, the time evolution of exciton densities  $N_{\mathbf{Q}}^{\alpha} = \langle X_{\alpha\mathbf{Q}}^{\dagger} X_{\alpha\mathbf{Q}} \rangle$ , following the thermalization of excitons after an optical excitation of a TMD monolayer [77, 78].

## 2.5 Generalizing to bilayers

Having introduced the basic effective exciton Hamiltonian for a monolayer system, we can now move to generalize the previous equations to the bilayer case.

Our work will focus on deriving microscopic based equations and numerically solve them, to investigate mainly two interesting and unusual experimental results: i) ultrafast charge transfer in TMD heterostructures and ii) long living and PL brighter signal of hot exciton states. The general problem of the thermalization of excitons in TMD heterostructures can be split in two main steps: i) a rapid thermal dissipation to the ground state and ii) reaching of a Boltzmann-like distribution around the minimum of the ground state. We will see that the first step of the dynamics can explain the ultrafast charge process observed in experiments, and can be study independently of the twist angle. Due to the high energies involved in the relaxation, twist angle dependent modifications of the bandstructure would impact only marginally the dynamics. For this reason to study this first thermalization step, we will restrict to only perfectly align TMD bilayers. On the other hand the specific potential induced by the twist angle cannot be neglected at low energy comparable to the moiré potential strength. For this reason to study the final equilibration process we need to include the twist angle in our model.

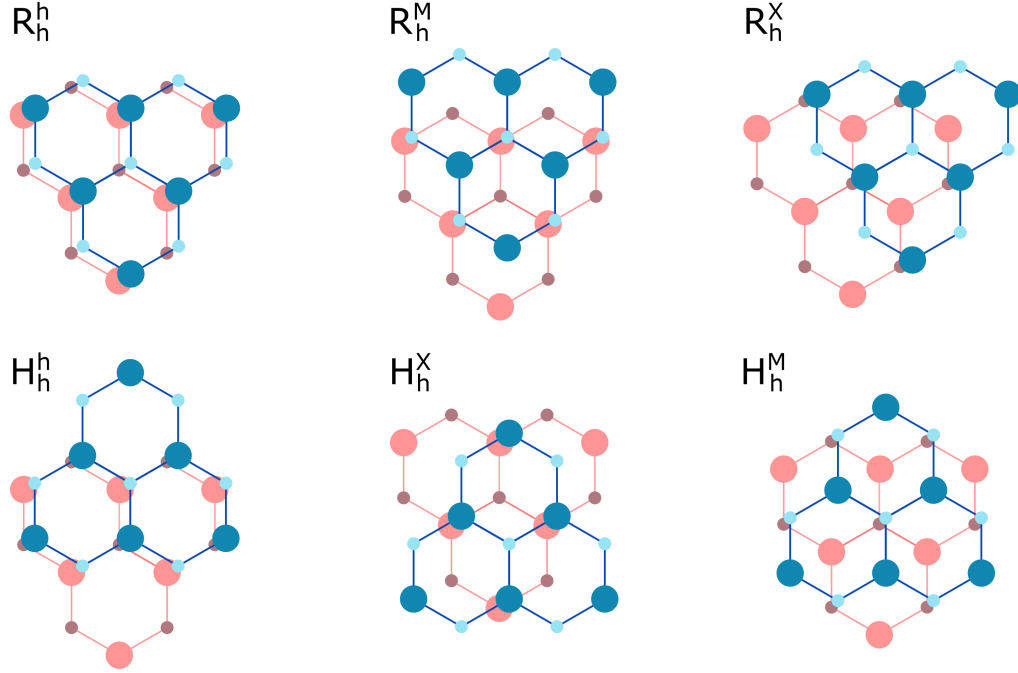


Figure 2.2: List of high-symmetry stacking geometries of two TMD layers (blue and red). Here the perfectly aligned layers are referred to as R-type stackings (with a  $0^\circ$  rotation of the layers), and H-type stackings (with a  $60^\circ$  rotation of the layers), meaning that the metal atoms of one layer are placed on top of the metal (chalcogen) atoms of the other layer, obtaining the  $R_h^h$  ( $H_h^h$ ) stacking. The other combinations result from lateral shifts of one layer along a high-symmetry line, so that a metal (M) or a chalcogen atom (X) of the upper layer is above the void (h) of the other layer, denoted by  $R_h^{M/X}$ .

Due to these two main reasons, we will first proceed with introducing a general model for perfectly aligned TMD bilayers and afterwards introduce the twist angle dependence. We will then use the two different models to describe the results in the two different cases discussed above.

We start by considering the bilayer system as prepared in a fixed stacking configuration (2.2). Here we present a short summary of the main steps leading to our bilayer Hamiltonian, for further details refer to the supplemental material of Papers 1-4 attached to this work.

## Bandstructure

Starting from the electronic bandstructure in 2.4 for a monolayer system,  $\varepsilon_{\lambda\zeta\mathbf{k}}$ , we can move to a bilayer description by adding an additional quantum number, the layer index  $l = 0, 1$  (0 for the bottom and 1 for the upper layer), i.e.

$$\varepsilon_{\lambda\zeta\mathbf{k}} \rightarrow \varepsilon_{\lambda l\zeta\mathbf{k}} = \varepsilon_{\lambda l\zeta} + \sigma_\lambda \frac{\hbar^2 \mathbf{k}^2}{2m_{l\zeta}^\lambda} \quad (2.28)$$

extension that is also applied to the electron state  $|\lambda\zeta\mathbf{k}\rangle \rightarrow |\lambda l\zeta\mathbf{k}\rangle$ , leading to the bilayer free electron Hamiltonian

$$H_e^B = \sum_{\lambda l\zeta\mathbf{k}} \epsilon_{\lambda l\zeta\mathbf{k}} a_{\lambda l\zeta\mathbf{k}}^\dagger a_{\lambda l\zeta\mathbf{k}}. \quad (2.29)$$

The valley dependent masses as well as valley relative positions strongly depend on the considered materials as well as their stacking. These have to be determined through first principles calculations or adjustments to experiments. Throughout our work we will derive the necessary parameters from DFT calculations [66, 79, 80], except for our joint experiment-theory studies (Paper 2,3) in which we use experimental data.

### Electron-electron interaction

In contrast to the bandstructure, that derives straightforwardly from the monolayer case, the electron-electron interaction needs to take into account that charges in one layer are affected by the Coulomb potential of charges in the neighbouring layer. This leads to an attraction between electrons and holes of different layers, leading to the formation of interlayer excitons, with electron and hole spatially separated in different layers, in contrast to intralayer excitons where the charges are located within the same layer. To describe the Coulomb potential of charges in a bilayer system, we need to introduce a different screening function with respect to 2.10. To do so, we solve the Poisson equation considering now two different homogeneous dielectric sheets on top of each other immerse in a background dielectric environment [55, 81]. By solving the Poisson equation we obtain an effective Coulomb potential of the following form

$$V_{\mathbf{q}}^{ll'} = \frac{e_0^2}{2\epsilon_0 A q \epsilon_{ll'}(q)} \quad \epsilon_{ll'}(q) = \begin{cases} \epsilon_{intra}^l(q), & \text{if } l = l' \\ \epsilon_{inter}(q), & \text{if } l \neq l' \end{cases} \quad (2.30)$$

where we use the layer index  $l = 0, 1$ , and introduced dielectric screenings for interlayer states  $\epsilon_{inter}(q) = v_{bg} g_q^0 g_q^1 f_q$ , intralayer states  $\epsilon_{intra}^l(q) = \frac{v_{bg} g_q^l f_q}{\text{ch}(\delta_{lq}/2) h_q^{1-l}}$ , and  $v = \sqrt{\epsilon^{\parallel} \epsilon^{\perp}}$ ,  $\delta_l = \alpha_l d_l$ ,  $\alpha = \sqrt{\epsilon^{\parallel} / \epsilon^{\perp}}$ , functions defined from the dielectric constants of the layers. Here, we have introduced the following abbreviations:

$$\begin{aligned} f_q &= 1 + \frac{1}{2} [\tilde{v}_{bg}^0 \text{th}(\delta_0 q) + \tilde{v}_{bg}^1 \text{th}(\delta_1 q) + \tilde{v}_1^0 \text{th}(\delta_0 q) \text{th}(\delta_1 q)] \\ h_q^l &= 1 + \frac{v_{bg}}{v_l} \text{th}(\delta_l q) + \frac{v_{bg}}{v_{1-l}} \text{th}(\delta_{1-l} q/2) + \frac{v_l}{v_{1-l}} \text{th}(\delta_l q) \text{th}(\delta_{1-l} q/2) \\ g_q^l &= \frac{\text{ch}(\delta_l q)}{\text{ch}(\delta_l q/2) \left[ 1 + \frac{v_{bg}}{v_l} \text{th}(\delta_l q) \right]} \end{aligned} \quad (2.31)$$

with  $\tilde{v}_\zeta^l = \left( \frac{v_l}{v_\zeta} + \frac{v_\zeta}{v_l} \right)$ , where  $\zeta = bg, 0, 1$  ( $bg$  stands for background). With this introduction we can write the new bilayer electron-electron Hamiltonian as

$$H_{e-e}^B = \frac{1}{2} \sum_{\substack{\lambda\lambda' l l' \\ \zeta\zeta' \mathbf{k}\mathbf{p}\mathbf{q}}} V_{\mathbf{q}}^{ll'} a_{\lambda l\zeta\mathbf{k}+\mathbf{q}}^\dagger a_{\lambda' l'\zeta'\mathbf{p}-\mathbf{q}}^\dagger a_{\lambda' l'\zeta'\mathbf{p}} a_{\lambda l\zeta\mathbf{k}}. \quad (2.32)$$

This approach let us treat the system as an effective 2D layer, while all the spatial details about the z-direction remain encoded into the effective screening.

### Electron-phonon and electron-light interactions

Regarding the electron-phonon interaction, in our work we will not consider any stacking induced changes in the phonon modes of the two monolayers. This approximation is justified by the weak van der Waals forces between atoms in different layers with respect to the strong intralayer bonds. For this reason also in this case the extension to a bilayer system can be easily extended within our formalism by including the phonon layer index in the superindex  $j = (l_{ph}, \kappa, \zeta_{ph})$  introduced in the previous sections. We obtain the following bilayer electron-phonon Hamiltonian

$$H_{e-phon}^B = \sum_{\substack{j\lambda l l' \\ \zeta \zeta' \mathbf{k} \mathbf{q}}} \mathcal{G}_{ll'\zeta\zeta'\mathbf{q}}^{j\lambda} a_{\lambda l \zeta \mathbf{k} + \mathbf{q}}^\dagger a_{\lambda l' \zeta' \mathbf{k}} \left( b_{j, \zeta - \zeta', \mathbf{q}} + b_{j, \zeta' - \zeta, -\mathbf{q}}^\dagger \right) \quad (2.33)$$

with  $\mathcal{G}_{ll'\zeta\zeta'\mathbf{q}}^{j\lambda} = \mathcal{G}_{\zeta\zeta'\mathbf{q}}^{j\lambda} \delta_{\zeta_{ph}, \zeta - \zeta'} \delta_{l_{ph}, l_i} \delta_{l_{ph}, l_f}$ , where we note that the choice of a decoupled basis has as main consequence that phonon-mediated scattering within different layers is forbidden, so that initial and final states have to share the same layer of the phonon. The generalization of the electron-light interaction term is performed easily by adding the additional layer quantum number to the creation and annihilation operators and to the optical matrix elements.

### Intralayer and Interlayer excitons

After introducing the layer dependence in the electronic Hamiltonian, we can use the same method illustrated in 2.4 to move to the exciton picture. Starting from the electron and hole layer-dependent Wannier equation

$$\frac{\hbar^2 \mathbf{k}^2}{2\tilde{m}_{\alpha l_e l_h}} \psi_{l_e l_h}^\alpha(\mathbf{k}) - \sum_{\mathbf{q}} V_{\mathbf{q}}^{l_e l_h} \psi_{l_e l_h}^\alpha(\mathbf{k} + \mathbf{q}) = E_b^{\alpha l_e l_h} \psi_{l_e l_h}^\alpha(\mathbf{k}) \quad (2.34)$$

we obtain a series of excitonic eigenenergies for intra- and interlayer states. For both intra- and interlayer excitons we find strongly reduced binding energies compared to the monolayer. For the intralayer exciton this results from the additional screening created by the second layer. For the interlayer exciton the binding energy is further reduced due to the distance constraints for the electron and hole. In addition we see that for heterostructures, interlayer excitons results to be the most energetically favorable states, given the type II band alignment. This will have great impact in the dynamics of charges in TMD heterostructures, and will be discussed in details in the following chapters (Papers 1,2,3). In addition, due to their i) spatially indirect character, leading to a recombination rate of orders of magnitude smaller compared to direct intralayer states, and ii) permanent electric dipole, these states promise to be technologically highly relevant for information storage and energy harvesting technologies [54, 82–84].

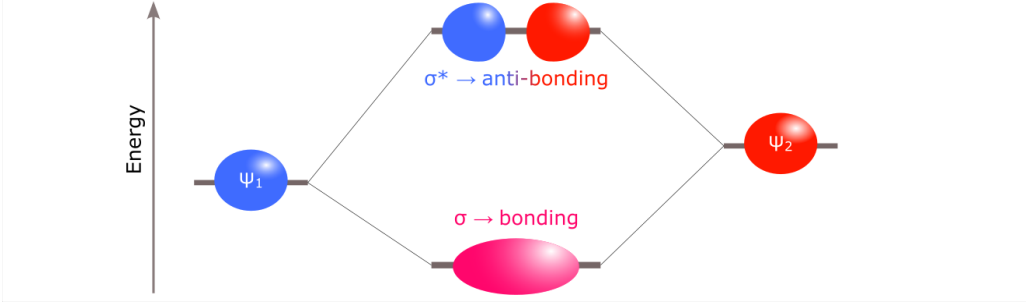


Figure 2.3: Schematic of the emergence of molecular orbitals from the two starting orbitals  $\psi_{1/2}$ . Molecular orbitals can be seen as a case of hybridization of electronic orbitals, where the new available states of the compound system, are superpositions of each single system component wavefunctions.

We can finally write the exciton Hamiltonian for a system of purely intra- or interlayer states, that introducing a new compound index to describe all the electron and hole quantum numbers entering in the exciton definition,  $\mu = (n^\mu, l_e^\mu, \zeta_e^\mu, l_h^\mu, \zeta_h^\mu)$ , reads [55]

$$H_X^B = \sum_{\mu\mathbf{Q}} X_{\mu\mathbf{Q}}^\dagger X_{\mu\mathbf{Q}} + \sum_{\substack{\mathbf{Q}\mathbf{q} \\ j\mu\nu}} \tilde{G}_{j\mathbf{q}\mathbf{Q}}^{\mu\nu} X_{\nu\mathbf{Q}+\mathbf{q}}^\dagger X_{\mu\mathbf{Q}} (b_{j,\mathbf{q}} + b_{j,-\mathbf{q}}^\dagger) + \sum_{\sigma\mathbf{Q}\mu} \tilde{\mathcal{M}}_{\sigma\mathbf{Q}}^\mu \cdot \mathbf{A} X_{\mu\mathbf{Q}}^\dagger \quad (2.35)$$

with new exciton-phonon and exciton-light matrix elements derived from the change of basis

$$\begin{aligned} \tilde{G}_{j\mathbf{q}\mathbf{Q}}^{\mu\nu} &= G_{\zeta_e^\mu \zeta_h^\nu \mathbf{q}}^{jc} \delta_{\zeta_h^\mu \zeta_h^\nu} \delta_{\zeta_e^\nu - \zeta_e^\mu, \zeta_j^{ph}} \delta_{l_e^\nu l_j^{ph}} \delta_{l_e^\nu l_e^\mu} \mathcal{F}_{\mu\nu} \left( \frac{m_h^\nu}{M_\mu} (\mathbf{q} + s_{\mu\nu} \mathbf{Q}) \right) + \\ &\quad - G_{\zeta_h^\mu \zeta_h^\nu \mathbf{q}}^{jv} \delta_{\zeta_e^\mu \zeta_e^\nu} \delta_{\zeta_h^\nu - \zeta_h^\mu, \zeta_j^{ph}} \delta_{l_h^\nu l_j^{ph}} \delta_{l_h^\nu l_h^\mu} \mathcal{F}_{\mu\nu} \left( -\frac{m_e^\nu}{M_\mu} (\mathbf{q} + s_{\mu\nu} \mathbf{Q}) \right) \\ \tilde{\mathcal{M}}_{\sigma\mathbf{Q}}^\mu &= \frac{e_0}{m_0} \delta_{\zeta_e^\mu \zeta_h^\mu, \mathbf{K}\mathbf{K}} \mathbf{M}_{\sigma\mathbf{Q}}^{c\nu} \sum_{\mathbf{k}} \psi^{\mu*}(\mathbf{k}) \end{aligned} \quad (2.36)$$

## 2.6 Exciton Hybridization

In the last section we showed that extending the exciton formalism to include intra- and interlayer excitons is straightforward using the procedure introduced in 2.4, by only adding the dependence on the new electron and hole layer quantum numbers in our exciton annihilation(creation) operator and redefining a new effective Coulomb potential to contain details on the specific dielectric screening arising from the presence of a second layer.

However this alone is not yet enough to capture completely the exciton dynamics in a bilayer system. To understand the reason behind this statement, we have to move slightly back to the electron picture. In the presence of two different layers in fact, the interlayer and intralayer contributions to the interband electronic transitions cannot be treated as decoupled. The reduced distance between the two layers creates regions of overlap between electronic orbitals around atoms of different layers, bringing to a non-negligible probability of electron tunneling between the different layers. To understand better the

physical problem we can draw an analogy to the description of two hydrogen atoms. When the two atoms are brought in close proximity, the electronic states emerging in this context are the molecular orbitals, superpositions of the single-atom problem orbitals (sketch in figure 2.3). This can be seen as an example of hybridization of electronic states, and measuring the splitting between the bonding and anti-bonding state is a direct measure for the interaction strength between the two initial states.

If we look closely to the bandstructure of TMD bilayers as in [85], we can observe also in this case the presence of splitting of bands, and the clear emergence of regions in the energy-momentum map in which the electron results delocalized between the layers, i.e. in a state that is a superposition of both layers. Similarly to the molecular orbital case, one can obtain a direct measurement of the tunneling strength emerging from the proximity of the two layers by looking at the band splitting in the electronic bandstructure.

To describe the problem correctly and obtain physical results we must then include hybridization in our description. Starting from Hamiltonian 2.29, we introduce an off-diagonal term in the layer subspace, coupling states from different layers (defining a new compound index  $i = (l_i, \zeta_i)$ )

$$H_T = \sum_{ijk\mathbf{q}\lambda} T_{ij}^\lambda(\mathbf{q}) a_{\lambda i\mathbf{k}+\mathbf{q}}^\dagger a_{\lambda j\mathbf{k}} \quad (2.37)$$

with  $T_{ij}^\lambda(\mathbf{q}) = (1 - \delta_{l_i, l_j}) \langle \lambda i\mathbf{k} + \mathbf{q} | V_0 + V_1 | \lambda j\mathbf{k} \rangle$ , where  $V_l$  (with  $l = 0, 1$ ) the electrostatic potentials generated by the two layers. Assuming tight-binding wave functions, the overlap of electronic wavefunctions is becoming rapidly very small for  $q > 0$ , and thus justifies the restriction to processes of vanishing momentum transfer  $q$ . In our effective model, we describe electrons and holes in proximity of high-symmetry points of the Brillouin zone using an effective mass approximation, thus we consider the tunneling dependent only on the valley index, allowing only valley-local tunneling terms.

We can now apply the general procedure to switch to exciton formalism 2.4, by expressing the operators in 2.37 in terms of pair operators

$$\begin{aligned} P_{i\mathbf{k}, l\mathbf{k}'}^\dagger &= a_{c i\mathbf{k}}^\dagger a_{v j\mathbf{k}'} \\ a_{c i\mathbf{k}}^\dagger a_{c i\mathbf{k}'} &\approx \sum_{h\mathbf{p}} P_{i\mathbf{k}, h\mathbf{p}}^\dagger P_{j\mathbf{k}', h\mathbf{p}} \\ a_{v i\mathbf{k}}^\dagger a_{v j\mathbf{k}'} &\approx \delta_{\mathbf{k} \mathbf{k}'}^{ij} - \sum_{h\mathbf{p}} P_{h\mathbf{p}, j\mathbf{k}'}^\dagger P_{h\mathbf{p}, i\mathbf{k}}. \end{aligned} \quad (2.38)$$

Then, by introducing the expansion in terms of exciton wavefunctions for the tunneling Hamiltonian, using  $P_{i\mathbf{k}, j\mathbf{p}}^\dagger = \sum_\mu X_{\mu\mathbf{k}-\mathbf{p}}^\dagger \psi(m_e^\mu/M_\mu \mathbf{k} + m_h^\mu/M_\mu \mathbf{p})$ , we obtain

$$H_{X,T} = \sum_{\mu\nu\mathbf{Q}} \mathcal{T}_{\mu\nu} X_{\mu\mathbf{Q}}^\dagger X_{\nu\mathbf{Q}} \quad (2.39)$$

where we have introduced the excitonic tunnelling matrix elements

$$\begin{aligned} \mathcal{T}_{\mu\nu} &= \delta_{l_h^\mu l_h^\nu} (1 - \delta_{l_e^\mu l_e^\nu}) T_{\mu\nu}^c - \delta_{l_e^\mu l_e^\nu} (1 - \delta_{l_h^\mu l_h^\nu}) T_{\mu\nu}^v \\ T_{\mu\nu}^c &= \delta_{\zeta^\mu \zeta^\nu} T_{ij}^c \mathcal{F}_{\mu\nu} \quad \text{and} \quad T_{\mu\nu}^v = \delta_{\zeta^\mu \zeta^\nu} T_{ij}^v \mathcal{F}_{\mu\nu} \end{aligned} \quad (2.40)$$

with  $\mathcal{F}_{\mu\nu}$  form factors defined in section 2.4. We note that in this description, different exciton states only directly interact via tunneling terms if they either have an electron or a hole within the same layer. Using now Hamiltonian 2.35, considering only the non-interacting part, we can include the tunneling term, introducing in this way a term of mixing between intra- and interlayer excitonic states

$$H_{X,0}^B \rightarrow H_{X,0}^B + H_{X,T} = \sum_{\mu\mathbf{Q}} E_{\mathbf{Q}}^{\mu} X_{\mu\mathbf{Q}}^{\dagger} X_{\mu\mathbf{Q}} + \sum_{\mu\nu\mathbf{Q}} \mathcal{T}_{\mu\nu} X_{\mu\mathbf{Q}}^{\dagger} X_{\nu\mathbf{Q}}. \quad (2.41)$$

The incorporation of a non-diagonal term into our Hamiltonian suggests that there is a more suitable basis for describing our problem, where available states are expressed as a superposition of pure intra- interlayer states. To do so we diagonalize Hamiltonian 2.41, by introducing a new set of hybrid excitons annihilation(creation) operators  $Y_{\eta\mathbf{Q}}^{(\dagger)} = \sum_{\mu} c_{\mu}^{\eta(*)}(\mathbf{Q}) X_{\mu\mathbf{Q}}^{(\dagger)}$ , these are operators creating or annihilating layer-hybridized states, consisting of a mixture of intra- and interlayer excitons, where the degree of mixing is express via the mixing coefficients  $c_{\mu}^{\eta}(\mathbf{Q})$ . Here the mixing coefficients satisfy orthonormality relations

$$\sum_{\mu} c_{\mu}^{\eta*}(\mathbf{Q}) c_{\mu}^{\xi}(\mathbf{Q}) = \delta_{\eta\xi} \quad \text{and} \quad \sum_{\eta} c_{\mu}^{\eta*}(\mathbf{Q}) c_{\nu}^{\eta}(\mathbf{Q}) = \delta_{\mu\nu} \quad (2.42)$$

The mixing coefficients have a key role in our description. Using the orthonormality relation we can derive that  $\sum_{\mu} |c_{\mu}^{\eta}(\mathbf{Q})|^2 = 1$ , so the contribution of each excitonic state  $\mu$  inside the hybrid state  $\eta$ , can be quantified by a number  $|c_{\mu}^{\eta}(\mathbf{Q})|^2 \in [0, 1]$  that can be interpreted as a percentage of contribution. The diagonalized Hamiltonian for free hybrid excitons reads

$$H_{Y,0} = \sum_{\eta\mathbf{Q}} \mathcal{E}_{\mathbf{Q}}^{\eta} Y_{\eta\mathbf{Q}}^{\dagger} Y_{\eta\mathbf{Q}} \quad (2.43)$$

with the corresponding hybrid-exciton energies  $\mathcal{E}_{\mathbf{Q}}^{\eta}$ , where the new quantum number  $\eta$  defines the new hybrid-exciton Rydberg like series of energy states, and inherits the valley index from  $\mu$ , due to the valley conserving tunneling. As a final remark, in our work we focus on the 1s ground state for all exciton species, as higher-energy states in the Rydberg-like series of excitons exhibit a much smaller scattering probability compared to the 1s-1s transitions [72]. This has been verified by numerically evaluating phonon-assisted scattering involving higher-energy states. To understand better the impact of the hybridization on the bilayer exciton energy landscape we show the energy landscape of the exemplary WSe<sub>2</sub>-MoS<sub>2</sub> heterostructure, that will be the focus of our study in the following chapter (study in Paper 3-4). As we can see in Figure 2.4, the tunneling creates a mixture of intra- and interlayer states, this can be seen in the picture thanks to the color scheme with which each state is colored with the corresponding different contributions of excitonic states. We note that states around K $\Lambda$  and  $\Gamma$ K valleys show a high degree of hybridization, in contrast to states in the KK valley. This can be explained in terms of electron wavefunction: for states around  $\Lambda$  and  $\Gamma$  valleys, the electronic orbital is mostly centered around the chalcogen atoms, creating a larger overlap region with the neighbouring layer; on the other hand electronic orbitals around K show a localization around the metal atom, bringing to a negligible overlap [86, 87].

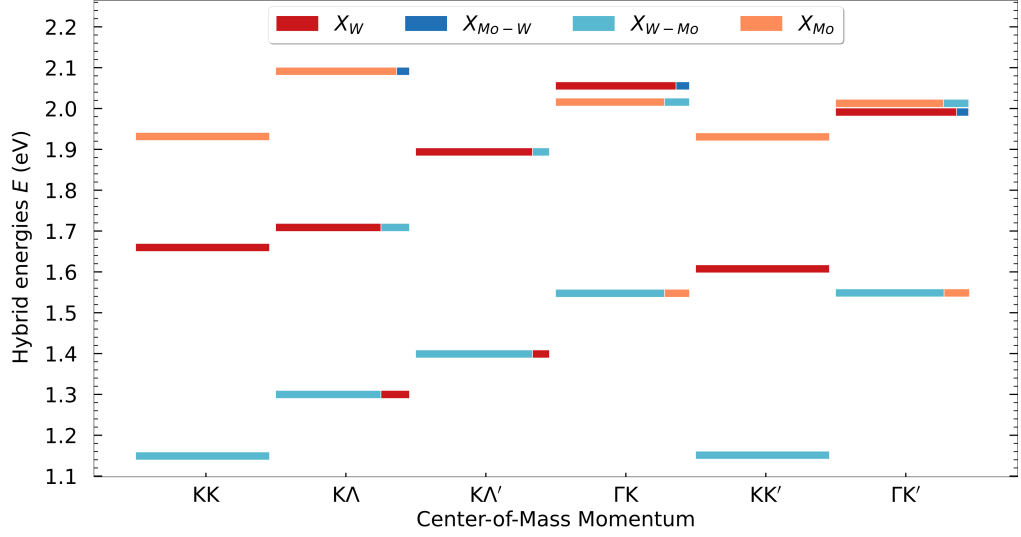


Figure 2.4: Hybrid exciton energy landscape for WSe<sub>2</sub>-MoS<sub>2</sub> heterostructure. We use different colors for depicting the four initial intra- and interlayer excitonic states named with  $X_{l_h-l_e}$  (using only one index for intralayer excitons). We highlight on each state the percentage of the involved intra- and interlayer exciton states. (Picture adapted from the supporting information of Paper 4)

We can now apply this change of basis directly to the interaction Hamiltonians, obtaining the final Hamiltonian

$$H_Y^B = \sum_{\eta\mathbf{Q}} \mathcal{E}_{\mathbf{Q}}^{\eta} Y_{\eta\mathbf{Q}}^{\dagger} Y_{\eta\mathbf{Q}} + \sum_{\substack{j\eta\xi \\ \mathbf{Q}\mathbf{q}}} \mathcal{G}_{j\mathbf{q}\mathbf{Q}}^{\eta\xi} Y_{\xi\mathbf{Q}+\mathbf{q}}^{\dagger} Y_{\eta\mathbf{Q}} (b_{j,\mathbf{q}} + b_{j,-\mathbf{q}}^{\dagger}) + \sum_{\sigma\mathbf{Q}\eta} \mathcal{M}_{\sigma\mathbf{Q}}^{\eta} \cdot \mathbf{A} Y_{\eta\mathbf{Q}}^{\dagger} \quad (2.44)$$

where the new couplings and matrix elements for hybrid-phonons and hybrid-light interactions are defined from the change of basis as

$$\begin{aligned} \mathcal{G}_{j\mathbf{q}\mathbf{Q}}^{\eta\xi} &= \sum_{\mu\nu} c_{\mu}^{\eta*}(\mathbf{Q}) c_{\nu}^{\xi}(\mathbf{Q} + \mathbf{q}) \tilde{G}_{j\mathbf{q}\mathbf{Q}}^{\mu\nu} \\ \mathcal{M}_{\sigma\mathbf{Q}}^{\eta} &= \sum_{\mu} c_{\mu}^{\eta}(\mathbf{Q}) \tilde{\mathcal{M}}_{\sigma\mathbf{Q}}^{\mu} \end{aligned} \quad (2.45)$$

We will use this Hamiltonian in combination with equation 2.13 in section 2.8 to obtain the hybrid exciton equation of motion, needed to study exciton thermalization processes in TMD heterostructures.

## 2.7 Introducing the twist angle

In the previous section we introduced the main Hamiltonian needed to describe a bilayer TMDs system, where the layers are perfectly aligned at specific high symmetry stacking configurations. We now introduce the twist angle dependence in our equations. Starting point is the decoupled Hamiltonian of a bilayer system. While the tunneling is important

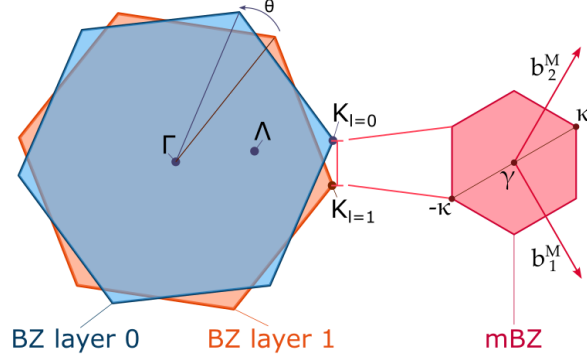


Figure 2.5: Brillouin zone (BZ) of a twisted TMD bilayer. On the left side we plot superimposed the two Brillouin zone for the separate layers. The twist angle creates a mismatch in the corners of the two BZs (shown at the K valleys of layer 0/1,  $K_{l=0/1}$ ). This results in a new BZ, called mini Brillouin zone (mBZ), with the two main reciprocal lattice vectors  $\mathbf{b}_{1/2}^M$  (right side). Here the analogue of the high-symmetry points are called with greek letters.

when the electronic bands in both layers are energetically close, for type II heterostructures and for electronic valleys with protected orbitals such as the K point, we can neglect this term. We will restrict to the specific derivation of the KK exciton valley, since the ground state of the system under study is a KK interlayer exciton state. The presence of the twist angle can be included in our model in terms of an effective potential, arising from the spatially dependent atomic local alignment [55], denoted as *moiré potential*. Starting from the electronic picture, we can write the potential felt by electrons of layer  $l = 0, 1$  generated by nuclei in layer  $1 - l$  as

$$H_M = \sum_{\lambda \mathbf{k} \mathbf{q}} \mathcal{V}_l^\lambda(\mathbf{q}, \mathbf{k}) a_{\lambda l \mathbf{k} + \mathbf{q}}^\dagger a_{\lambda l \mathbf{k}} \quad (2.46)$$

where  $\mathcal{V}_l^\lambda(\mathbf{q}, \mathbf{k}) = \langle \lambda | \mathbf{k} + \mathbf{q} | V_{1-l} | \lambda | \mathbf{k} \rangle$ . To obtain the proper information about the nuclei alignment, we have to explicitly insert our knowledge about the geometry of the problem. To do so we expand the potential in terms of lattice vectors and single atomic contributions  $V_l(\mathbf{r}) = \sum_{\mathbf{R}_l} v_l(\mathbf{r} - \mathbf{R}_l)$ . Assuming a tight binding approach for the electronic wavefunction and expanding in the reciprocal lattice vector basis of each layer  $\mathbf{G}_l = a_0 \mathbf{b}_l^0 + a_1 \mathbf{b}_l^1$  ( $a_{0/1}$  integers), we can write our potential as [55]

$$\mathcal{V}_l^\lambda(\mathbf{q}) = \sum_{\mathbf{G}_l \mathbf{G}_{1-l}} m_l^\lambda(\mathbf{G}_{1-l}) e^{i(\mathbf{G}_l + \mathbf{G}_{1-l}) \cdot \mathbf{D}_l / 2} \delta_{\mathbf{q}, K_{1-l} - K_l + \mathbf{G}_{1-l} - \mathbf{G}_l} \quad (2.47)$$

where  $m_l^\lambda(\mathbf{q}) \propto \int dz \tilde{\rho}_l^\lambda(-\mathbf{q}) \tilde{v}_l(\mathbf{q})$ , with charge density  $\rho_l^\lambda$  compute with the  $\lambda$  (conduction/valence) electronic orbitals and  $\tilde{f}(\mathbf{q}) = \int d\mathbf{r}_\parallel f(\mathbf{r}) \exp\{i\mathbf{q} \cdot \mathbf{r}_\parallel\}$  in-plane Fourier transform, and  $\mathbf{D}_l / 2 = (-1)^{1+l} \mathbf{R}_l^0$ , where we fix the coordinate system center at the junction of the two layers. By looking at the equation is important to notice that although we are focusing around the same valley  $\zeta = \text{K}$ , when including the twist angle the two K points of the different layers will be displaced from each other by a vector  $K_{1-l} - K_l$ . Now looking at the  $\mathbf{G}$ -sums, considering the van der Waals nature of the interlayer forces we

can restrict them to the first shell (and incorporate the  $\mathbf{G} = 0$  term as an electrostatic constant shift). In this way we obtain six  $\mathbf{G}$  vectors. Being these reciprocal lattice vectors  $C^6$  symmetric, we can split the  $\mathbf{G}$  vectors in two parts, and restrict the sum only to three of these, including the sum over the other three in the hermitian conjugated Hamiltonian. We thus obtain

$$H_M = \sum_{\lambda l \mathbf{k} \mathbf{q}} \mathcal{V}_l^\lambda(\mathbf{q}) a_{\lambda l \mathbf{k} + \mathbf{q}}^\dagger a_{\lambda l \mathbf{k}} + h.c. \quad (2.48)$$

$$\mathcal{V}_l^\lambda(\mathbf{q}) = m_l^\lambda \sum_{n=0}^2 \delta_{\mathbf{q} \mathbf{g}_n}$$

where we used the symmetry over the  $\mathbf{G}$  vectors and we introduced  $\mathbf{g}_n = C_3^n(\mathbf{G}_{1-l}^0 - \mathbf{G}_l^0)$ . Here  $m_l^\lambda$  can be extracted from first principle calculations, and we have set  $\mathbf{D} = 0$  (without loss of generality). The new  $\mathbf{g}_n$  vectors, define the new periodicity of our crystal and are called in literature moiré reciprocal lattice vectors and the lattice arising from this new periodicity is called superlattice. We will refer to the new Brillouin zone corresponding to the superlattice as mini Brillouin zone (mBZ). If we now transform Hamiltonian 2.48 from electronic picture into excitonic picture, exposing the layer indexes and using the delta in equation 2.48, we obtain

$$H_X^M = \sum_{\mathbf{Q} n l l'} \Theta_{\mathbf{g}_n}^{ll'} X_{ll' \mathbf{Q} + (-1)^l \mathbf{g}_n}^\dagger X_{ll' \mathbf{Q}} \quad (2.49)$$

$$\Theta_{\mathbf{g}_n}^{ll'} = m_l^c \mathcal{F}_{ll'} \left( \frac{m_h^{ll'}}{M_{ll'}} \mathbf{g}_n \right) - m_{l'}^v \mathcal{F}_{ll'}^* \left( -\frac{m_e^{ll'}}{M_{ll'}} \mathbf{g}_n \right)$$

with the usual definition of the form factor  $\mathcal{F}$ , where  $l$  and  $l'$  are the layer indexes. Now since the moiré Hamiltonian is not mixing differet excitonic states, we can split the problem in  $N$  different Hamiltonians, one for each excitonic state and solve the eigenvalue problem separately for each excitonic state. Since we are mainly interested in the ground state interlayer exciton of the MoSe<sub>2</sub>-WSe<sub>2</sub> heterostructure, in the following we fix  $l, l'$  to match the electron and hole layer of the state under exam, and omit them in the following equations. To show the shape of the moiré potential, we plot in Figure 2.6 the real space transformed excitonic moiré potential  $\Theta^{ll'}(\mathbf{r}) = \mathcal{F}(\Theta_{\mathbf{Q}}^{ll'})$ , for the lowest interlayer ( $l = 0, l' = 1$ ) and intralayer ( $l = 0, l' = 0$ ) excitonic states of the MoSe<sub>2</sub>-WSe<sub>2</sub> heterostructure. In order to write the Hamiltonian in a more convenient form, we rewrite our operators in terms of *folded* operators by using the new moiré periodicity, splitting the sum over the total CoM momentum  $\mathbf{Q}$  into a sum of  $\mathbf{Q} + \mathbf{g}$ , with  $\mathbf{g} = s_1 \mathbf{b}_1^M + s_2 \mathbf{b}_2^M$  reciprocal moiré lattice vector and  $s_{0/1}$  as integers and  $\mathbf{Q} \in \text{mBZ}$ . Considering the free exciton term and the moiré potential term, our bilayer free moiré exciton Hamiltonian reads

$$H_{M,0}^B = H_{X,0}^B + H_M = \sum_{\mathbf{Q} \mathbf{g}} E_{\mathbf{Q} + \mathbf{g}} X_{\mathbf{Q} \mathbf{g}}^\dagger X_{\mathbf{Q} \mathbf{g}} + \sum_{\mathbf{Q} \mathbf{g} \tilde{\mathbf{g}}} \tilde{\Theta}_{\mathbf{g} \tilde{\mathbf{g}}} X_{\mathbf{Q} \mathbf{g}}^\dagger X_{\mathbf{Q} \tilde{\mathbf{g}}} \quad (2.50)$$

$$\tilde{\Theta}_{\mathbf{g} \tilde{\mathbf{g}}} = \Theta \left( \delta_{s_1, \tilde{s}_1 + (-1)^l} \delta_{s_2, \tilde{s}_2} + \delta_{s_1, \tilde{s}_1} \delta_{s_2, \tilde{s}_2 + (-1)^l} + \delta_{s_1, \tilde{s}_1 + (-1)^l} \delta_{s_2, \tilde{s}_2 + (-1)^l} \right) +$$

$$+ \Theta^* \left( \delta_{s_1, \tilde{s}_1 - (-1)^l} \delta_{s_2, \tilde{s}_2} + \delta_{s_1, \tilde{s}_1} \delta_{s_2, \tilde{s}_2 - (-1)^l} + \delta_{s_1, \tilde{s}_1 - (-1)^l} \delta_{s_2, \tilde{s}_2 - (-1)^l} \right)$$

where we exploited the excitonic wavefunction symmetry in the form factors, i.e.  $\Theta_{\mathbf{g}_n} = \Theta_{\mathbf{g}_0} = \Theta$ . As seen in the previous section, we can diagonalize this Hamiltonian to obtain a

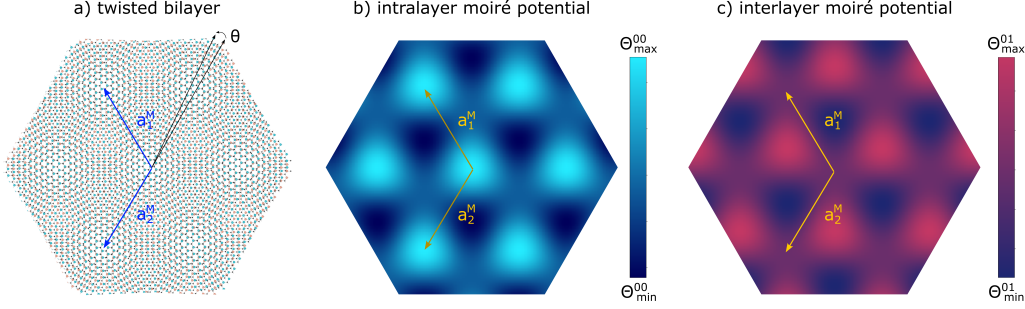


Figure 2.6: a) Twisted TMD bilayer. Recognizable in the picture the new periodicity generated from the local displacement of atoms in the two layers, called moiré lattice, where we highlight the moiré lattice vectors  $a_{1,2}^M$ . b) and c) show the effective moiré potential seen from intralayer (b)) and interlayer (c)) excitons.

new basis for our problem,  $Y_{\eta\mathbf{Q}}^{(\dagger)} = \sum_{\mathbf{g}} c_{\mathbf{g}}^{\eta(*)}(\mathbf{Q}) X_{\mathbf{Q}\mathbf{g}}^{(\dagger)}$ , where now  $\eta$  labels the new set of *minibands* periodic in the mBZ, with hybridized states formally similar to the exciton hybrids seen in the previous section, but instead of being a mixture of different excitonic states, they are a mixture in momentum shells of the same excitonic state, with  $|c_{\mathbf{g}}^{\eta}(\mathbf{Q})|^2$  quantifying the degree of contribution of each momentum shell to the specific miniband labeled by  $\eta$ . We will refer to these new hybrids as *moiré excitons*. We show in Figure 2.7 a) the solution of the eigenvalue problem for the interlayer state under exam, and plot in Figure 2.7 b) the unfolded (i.e. using  $|c_{\mathbf{g}}^{\eta}(\mathbf{Q})|^2 = |c^{\eta}(\mathbf{Q} + \mathbf{g})|^2$ ) mixing coefficients for the lowest nine minibands, showing that the lowest energy bands are localized within the first few momentum shells. We note that in general, for exciton states highly affected by tunneling or where the energy separation induces a high degree of mixture, the problem cannot be decoupled in finding the minibands separately for each exciton state, but one would need to include the tunneling Hamiltonian in 2.41 together with the moiré Hamiltonian and solve the eigenvalue problem, obtaining a set of hybridized moiré minibands.

We can now use this new set of operators to perform a change of basis in the interaction Hamiltonians arriving to

$$H_M^B = \sum_{\eta} E_{\mathbf{Q}}^{\eta} Y_{\mathbf{Q}}^{\eta\dagger} Y_{\mathbf{Q}}^{\eta} + \sum_{\substack{\eta\xi j \\ \mathbf{Q}\mathbf{Q}'\mathbf{g}}} \tilde{G}_{\mathbf{Q}\mathbf{Q}'\mathbf{g}}^{\eta\xi j} Y_{\mathbf{Q}'}^{\xi\dagger} Y_{\mathbf{Q}}^{\eta} b_{\mathbf{Q}'-\mathbf{Q}+\mathbf{g}}^j + h.c. \quad (2.51)$$

$$\tilde{G}_{\mathbf{Q}\mathbf{Q}'\mathbf{g}}^{\eta\xi j} = \sum_{\mathbf{g}'\tilde{\mathbf{g}}} \tilde{G}_{j\mathbf{Q}'-\mathbf{Q}+\mathbf{g},\mathbf{Q}\omega_{\tilde{\mathbf{g}}}^{\eta*}(\mathbf{Q})\omega_{\mathbf{g}'}^{\xi}(\mathbf{Q}')\delta_{\mathbf{g},\mathbf{g}'-\tilde{\mathbf{g}}}}$$

where we include only the exciton-phonon interaction, since in the study of Paper 5 we will not use a laser pulse to excite the system and generate excitons, but initialize the exciton distribution at a fixed energy.

## 2.8 Exciton Dynamics

After having introduced the main Hamiltonians 2.44 and 2.51, we have the necessary tools to solve the Heisenberg equation within the second-order Born-Markov approximation (i.e.

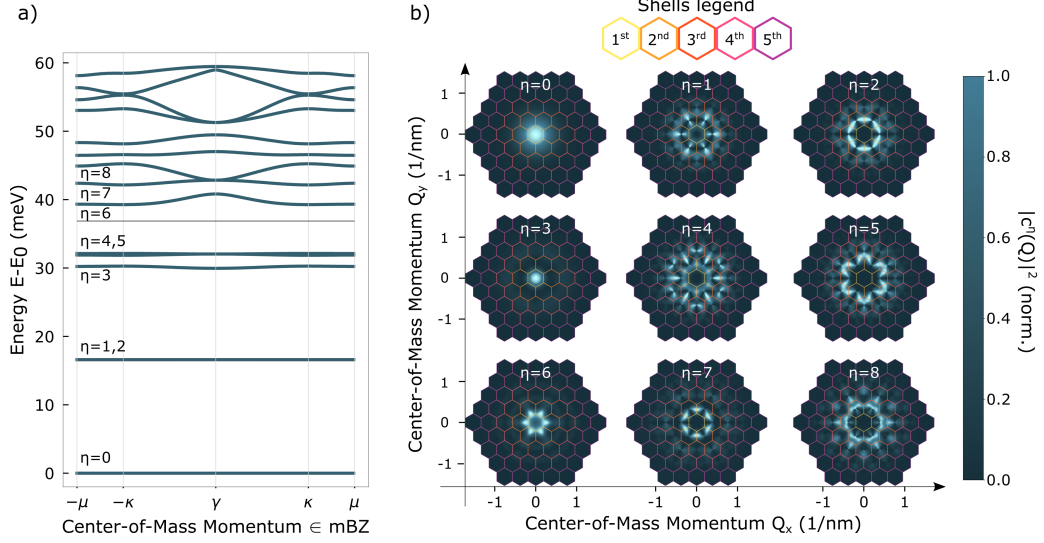


Figure 2.7: a) miniband structure for the interlayer lowest energy excitonic state of MoSe<sub>2</sub>-WSe<sub>2</sub>, shifting the  $\gamma$  mBZ to match the minimum of the lowest energy state ( $\kappa \rightarrow \gamma$ ). All the bands are plotted with respect to the lowest energy state,  $E_0$ . b) Unfolded mixing coefficients  $|c^\eta(\mathbf{Q} + \mathbf{g}^M)|^2$  of the lowest nine minibands, showing the main localization in the first few shells.

truncating the infinite hierarchy at the second order and using the Markov approximation). Key quantity for our study is the exciton occupation  $N_{\mathbf{Q}}^\eta = \langle Y_{\eta\mathbf{Q}}^\dagger Y_{\eta\mathbf{Q}} \rangle$ , with which we can track the exciton distribution in momentum and time, allowing to follow the exciton dynamics resulting in a phonon driven relaxation cascade, bringing the exciton population to its equilibrium distribution. We will in this section explain how the exciton equation of motion for  $N_{\mathbf{Q}}^\eta$  can be derived. We will show the derivation for hybrid excitons, being formally equivalent to the moiré excitons one, with the only difference contained in the specific couplings. We start by deriving the phonon-contribution to the equation of motion, including only the free and the hybrid-phonon terms of the Hamiltonian. Using the procedure described in Sec. 2.2 we truncate the many-particle hierarchy on the level of two particle correlations, obtaining the coupled equations

$$\begin{aligned} \partial_t N_{\mathbf{Q}}^\eta |_{Y-ph} &= \frac{2}{\hbar} \sum_{\xi j \mathbf{Q} \pm} \text{Im} \left( \mathcal{G}_{j\mathbf{Q}\mathbf{q}}^{\xi\eta} C_{j\mathbf{Q}\mathbf{q}}^{\eta\xi\pm} \right) \\ i\hbar \partial_t C_{j\mathbf{Q}\mathbf{q}}^{\eta\xi\pm} |_{Y-ph} &= \left( \mathcal{E}_{\mathbf{Q}-\mathbf{q}}^\xi - \mathcal{E}_{\mathbf{Q}}^\eta \mp \hbar\Omega_{j\mathbf{q}} \right) C_{j\mathbf{Q}\mathbf{q}}^{\eta\xi\pm} - \mathcal{G}_{j\mathbf{Q}\mathbf{q}}^{\xi\eta*} \left( \chi_{\mathbf{q}}^\mp N_{\mathbf{Q}-\mathbf{q}}^\xi - \chi_{\mathbf{q}}^\pm N_{\mathbf{Q}}^\eta \right) \end{aligned} \quad (2.52)$$

introducing  $C_{j\mathbf{Q}\mathbf{q}}^{\eta\xi\pm} = \langle Y_{\eta\mathbf{Q}}^\dagger Y_{\xi\mathbf{Q}-\mathbf{q}}^\dagger b_{j,\mp\mathbf{q}}^{\dagger/0} \rangle$  and  $\chi_{\mathbf{q}}^\pm = 1/2 \mp 1/2 + \langle b_{j\mathbf{q}}^\dagger b_{j\mathbf{q}} \rangle$ . It is important to note that while obtaining the latter equations, non linear terms are arising from the exciton bosonic commutator. However we remind that in our derivation, to obtain pure bosonic relations and introduce the exciton formalism, we restricted to the case of low density. In this limit linear terms dominate, allowing us to neglect all non-linear terms. Using the Markov approximation on the correlation term, i.e.

$$C_{j\mathbf{Q}\mathbf{q}}^{\eta\xi\pm} \approx i\pi \mathcal{G}_{j\mathbf{Q}\mathbf{q}}^{\xi\eta*} \left( \chi_{\mathbf{q}}^\mp N_{\mathbf{Q}-\mathbf{q}}^\xi - \chi_{\mathbf{q}}^\pm N_{\mathbf{Q}}^\eta \right) \delta \left( \mathcal{E}_{\mathbf{Q}-\mathbf{q}}^\xi - \mathcal{E}_{\mathbf{Q}}^\eta \mp \hbar\Omega_{j\mathbf{q}} \right) \quad (2.53)$$

brings us to a Boltzmann scattering equation for excitonic densities

$$\begin{aligned} \partial_t N_{\mathbf{Q}}^\eta &= \sum_{\xi \mathbf{Q}'} \left( \mathcal{W}_{\mathbf{Q}'\mathbf{Q}}^{\xi\eta} N_{\mathbf{Q}'}^\xi - \mathcal{W}_{\mathbf{Q}\mathbf{Q}'}^{\eta\xi} N_{\mathbf{Q}}^\eta \right) \\ \mathcal{W}_{\mathbf{Q}\mathbf{Q}'}^{\eta\xi} &= \sum_{j\pm} \left| \mathcal{G}_{j\mathbf{Q}-\mathbf{Q}'}^{\eta\xi} \right|^2 \left( \frac{1}{2} \pm \frac{1}{2} + n_{j\mathbf{Q}'-\mathbf{Q}}^B \right) \delta \left( \mathcal{E}_{\mathbf{Q}'}^\xi - \mathcal{E}_{\mathbf{Q}}^\eta \pm \hbar \Omega_{j\mathbf{Q}'-\mathbf{Q}} \right) \end{aligned} \quad (2.54)$$

where  $n_{j\mathbf{Q}'-\mathbf{Q}}^B$  is the Bose-Einstein distribution for phonons with the mode  $j$ , the momentum  $\mathbf{Q}' - \mathbf{Q}$ , and the energy  $\Omega_{j\mathbf{Q}'-\mathbf{Q}}$ . This equations can be interpreted as a microscopically based master equation, where the transition probability rates to scatter from a state  $|\eta\mathbf{Q}\rangle$  to a state  $|\xi\mathbf{Q}'\rangle$  are contained in the tensor  $\mathcal{W}_{\mathbf{Q}\mathbf{Q}'}^{\eta\xi}$ , which contains fixed energy conservation resonances, resembling the Fermi golden rule. An important quantity related to  $\mathcal{W}_{\mathbf{Q}\mathbf{Q}'}^{\eta\xi}$ , is the dephasing rate  $\Gamma$ , i.e. inverse of the coherence lifetime, that can be computed as  $\Gamma = \hbar/2 \sum_{\xi\mathbf{Q}'} \mathcal{W}_{\mathbf{Q}\mathbf{Q}'}^{\eta\xi}$ .

Equation 2.54 describes the phonon driven dynamics of hybrid exciton. However to be able of describing the optical excitation of the system, responsible of injecting excitons in our system, we need to solve the hybrid exciton-light part of the Heisenberg equation. For our purpose we want to mimic an excitation of the system with a short laser pulse, which is described by a coherent light pulse, and thus creating a coherent population of excitons. This consideration brings us to split the exciton occupation in a coherent and a non-coherent part  $N_{\mathbf{Q}}^\eta = \langle Y_{\eta\mathbf{Q}}^\dagger Y_{\eta\mathbf{Q}} \rangle = \langle Y_{\eta\mathbf{Q}}^\dagger \rangle \langle Y_{\eta\mathbf{Q}} \rangle + \Delta N_{\mathbf{Q}}^\eta$ , where we will refer to  $\langle Y_{\eta\mathbf{Q}}^\dagger \rangle = P_{\mathbf{Q}}^\eta$  as coherent population and to  $\Delta N_{\mathbf{Q}}^\eta$  as incoherent population. With this specification, we can write the part of the dynamics driven by the laser field of  $\sigma$ -polarized light, reflecting the creation of coherent hybrid excitons, as

$$\partial_t N_{\mathbf{Q}}^\eta |_{Y-l} = \frac{2}{\hbar} \text{Im} \left( \frac{e_0}{m_0} \mathcal{M}_{\sigma\mathbf{Q}}^\eta \cdot \mathbf{A} \right) \delta_{\mathbf{Q},0} \quad (2.55)$$

where we approximate the light cone to be a fixed delta condition.

In the light of this result, we recompute the phonon driven scattering equations in terms of coherent and incoherent population obtaining the final result

$$\begin{aligned} i\hbar \partial_t P^\eta &= - \left( \mathcal{E}_{\mathbf{Q}}^\eta + i\Gamma_{\mathbf{Q}=0} \right) P^\eta - \frac{e_0}{m_0} \mathcal{M}_{\sigma\mathbf{Q}=0}^\eta \cdot \mathbf{A} \\ \partial_t \Delta N_{\mathbf{Q}}^\eta &= \sum_{\xi} \mathcal{W}_{\delta\mathbf{Q}}^{\xi\eta} |P^\xi|^2 + \sum_{\xi\mathbf{Q}'} \left( \mathcal{W}_{\mathbf{Q}'\mathbf{Q}}^{\xi\eta} \Delta N_{\mathbf{Q}'}^\xi - \mathcal{W}_{\mathbf{Q}\mathbf{Q}'}^{\eta\xi} \Delta N_{\mathbf{Q}}^\eta \right) \end{aligned} \quad (2.56)$$

where we used  $P^\eta = P_{\mathbf{Q}=0}^\eta$  and  $\mathcal{W}_{\mathbf{Q}\mathbf{Q}'}^{\eta\xi}$  has been defined in eq. 2.54. With this equation we are able of tracking the main steps of the hybrid excitons lifetime. Starting from the coherent excitation, we can follow the phonon mediated scatterings between the exciton states leading to the thermal equilibration of the system. From the scattering tensor we can define an additional quantity, the density of in-scattering states for the specific exciton state  $\eta$ , in order to quantify the density of states contributing the most to the exciton influx to the specific state  $\eta$ . This reads

$$\text{DOI}_{in}^\eta(E) = \sum_{\xi\mathbf{Q}'} \mathcal{W}_{\mathbf{Q}'\mathbf{Q}=0}^{\xi\eta} \delta \left( E - E_{\mathbf{Q}'}^\xi \right). \quad (2.57)$$

## 2.9 Beyond the second order Born-Markov approximation

Equation (2.54) is derived by using a second-order Born-Markov approximation [64, 77, 78, 88], thus obtaining fixed resonances from the energy conservation described by the delta function. However, in the presence of peculiar topology of the energy band structure, the quantity  $\Gamma_{\mathbf{Q}}^{\eta}$  can diverge due to Van Hove singularities. In this case, to solve the problem and obtain a finite dephasing we need to go one step further in the infinite correlation hierarchy. By continuing the correlation expansion taking into account two-particle correlations and considering only the imaginary part of the self-energy (neglecting polaron renormalization terms) [89] we can include a self-consistent temperature-dependent broadening of the dephasing, solving the divergence problem. Considering only the phonon contribution, we can define the dephasing rate as follows

$$\Gamma_{\mathbf{Q}}^{\eta\xi} = \frac{\hbar}{2} \sum_{j \pm \mathbf{Q}'_{\mathbf{g}}} |\tilde{\mathcal{D}}_{\mathbf{Q}'_{\mathbf{g}}}^{\eta\xi j}|^2 \left( \frac{1}{2} \pm \frac{1}{2} + n_{j\mathbf{Q}'-\mathbf{Q}}^B \right) \mathcal{L}_{\Gamma_{\mathbf{Q}}^{\eta} + \Gamma_{\mathbf{Q}'}^{\xi}} \left( \Delta_{\mathbf{Q}\mathbf{Q}'}^{\eta\xi \pm} \right) \quad (2.58)$$

where we introduced  $\Delta_{\mathbf{Q}\mathbf{Q}'}^{\eta\xi \pm} = E_{\mathbf{Q}'}^{\xi} - E_{\mathbf{Q}}^{\eta} \pm \Omega_{j\mathbf{Q}'-\mathbf{Q}}$ . This consist of a system of coupled equations that can be solved self-consistently. Here,  $\mathcal{L}_{\Gamma}$  corresponds to the Cauchy/Lorentz distribution with the width  $\Gamma$ . We can notice that the equation is formally equivalent to the dephasing derived within the second-order Born-Markov approximation, with the only difference that instead of having fixed energy resonance, these result in being softened by a Lorentzian function.

## 2.10 Hybrid exciton ARPES signal

In Paper 4, we introduce new theoretical tools, required to describe excitonic signature of hybrid states in ARPES experiments. While the main results and study will be discussed in Chapter 4, we introduce here the main derivation to derive the equation for describing the ARPES signal in the hybrid exciton basis.

Starting from a three step model to describe the photoemission of electrons [90], the intensity of the ARPES signal can be derived from the Fermi-Golden rule

$$\mathcal{I}(\mathbf{k}, h\nu; t) \propto \sum_{i,f} |\langle f\mathbf{k} | H_{int} | i \rangle|^2 N_i(t) \delta(E_{f\mathbf{k}} - E_i - h\nu) \quad (2.59)$$

where  $|i/f\rangle$  are the initial/final state of the system where we consider eigenstates of the two-body Hamiltonian with initial/final eigenenergies  $E_{i/f}$ . The energy of the photon is denoted by  $h\nu$  and the initial state occupation by  $N_i(t)$ . The key idea behind the procedure is expressing the initial and final states in the expectation value above into electronic picture, using a pure monolayer eigenstates basis.

The final state  $|f\rangle$ , can be described by the product of a free electron and a hybrid hole, where the latter is obtained by solving the eigenvalue problem for the bilayer Hamiltonian  $H_e^B + H_T$  (equations 2.29,2.37). The solution of the eigenvalue problem leads to a set

of hybridized electronic valence and conduction bands, that reads as function of the two decoupled layer energies  $\varepsilon_{\lambda 0 \zeta \mathbf{k}}$ ,  $\varepsilon_{\lambda 1 \zeta \mathbf{k}}$

$$E_{\mathbf{k}\gamma}^{\lambda} = \frac{1}{2} (\varepsilon_{\lambda 0 \zeta \mathbf{k}} + \varepsilon_{\lambda 1 \zeta \mathbf{k}}) \pm \frac{1}{2} \sqrt{(\varepsilon_{\lambda 0 \zeta \mathbf{k}} - \varepsilon_{\lambda 1 \zeta \mathbf{k}})^2 + 4|\mathcal{T}_{01}^{\lambda}|^2} \quad (2.60)$$

with  $\gamma = (\pm, \xi)$  labeling the two new states ( $\pm$  solutions) and the valley index  $\xi$ . The corresponding eigenvectors are obtained from the same  $2 \times 2$  eigenvalue problem which we write as a superposition of the old monolayer states as

$$|\gamma \lambda \mathbf{p}\rangle = \sum_l g_l^{\gamma} a_{\lambda l \mathbf{p} \xi}^{\dagger} |0\rangle$$

with the mixing coefficients  $g_l^{\gamma}$ . Since the final state is composed by two unbound particles, we can use as final state the tensor product of a free electron state and the above derived hybrid hole,

$$|f\rangle = |\mathbf{k}, \gamma v \mathbf{p}\rangle = \sum_l g_l^{\gamma} a_{l \mathbf{p}}^{\dagger} a_{v l \mathbf{p} \xi_h}^{\dagger} |0\rangle \quad (2.61)$$

with free electron operator  $a_{l \mathbf{k}}^{\dagger}$ .

The initial state  $|i\rangle$ , on the other hand, is represented by a hybrid exciton state, so we have to express it in terms of monolayer electrons. In this case, we have to proceed backward in the derivation in section 2.6, expressing the hybrid state in terms of electron operators. Starting from the hybrid exciton state  $|\eta \mathbf{Q}\rangle$ , and performing a series of backward transformations from hybrid exciton operators to exciton operators arriving finally to electron operators  $Y^{\dagger} \rightarrow X^{\dagger} \rightarrow a^{\dagger} a$ , we finally obtain

$$\begin{aligned} |i\rangle &= |\eta \mathbf{Q}\rangle = Y_{\eta \mathbf{Q}}^{\dagger} |0\rangle = \sum_{\mu} \mathbf{c}_{\mu}^{\eta*}(\mathbf{Q}) X_{\mu \mathbf{Q}}^{\dagger} |0\rangle = \\ &= \sum_{\mu \mathbf{k}} \mathbf{c}_{\mu}^{\eta*}(\mathbf{Q}) \psi^{\mu*}(\mathbf{k}) a_{c, \mathbf{k} + \tilde{m}_e \mathbf{Q}, \mu_e}^{\dagger} a_{v, \mathbf{k} - \tilde{m}_h \mathbf{Q}, \mu_h} |0\rangle \end{aligned} \quad (2.62)$$

with the compound index  $\eta = (n, \xi)$  describing the hybrid degrees of freedom,  $\mathbf{c}_{\mu}^{\eta*}(\mathbf{Q})$  excitonic mixing coefficients,  $\mu = (L, \xi)$  describing the excitonic degrees of freedom, with  $L = (l_e, l_h)$  and  $\xi = (\xi_e, \xi_h)$ , and we use the notation  $\mu_{e/h}$  to refer to the quantum numbers inside  $\mu$  labelled by  $e/h$ . Inserting the initial and final states in Eq. (2.59) we obtain

$$\mathcal{I}(\mathbf{k}, h\nu) \propto \sum_{\substack{\eta \gamma \\ \mathbf{p} \mathbf{Q}}} |\langle \mathbf{k}, \gamma v \mathbf{p} | H_{int} | \eta \mathbf{Q} \rangle|^2 \cdot N_{\mathbf{Q}}^{\eta}(t) \delta(E_{\mathbf{k}}^e - E_{\gamma, \mathbf{p}}^v - E_{\eta, \mathbf{Q}}^X - h\nu) \quad (2.63)$$

where  $\mathbf{p}$  is the hole momentum,  $N_{\mathbf{Q}}^{\eta}(t)$  denotes the hybrid exciton time-dependent occupation for the hybrid exciton state  $\eta$  at the center-of-mass momentum  $\mathbf{Q}$ , relative to the valley. Moreover,  $E_{\mathbf{k}}^e$  corresponds to the free electron energy,  $E_{\gamma, \mathbf{p}}^v$  to the hybrid valence band energy,  $E_{\eta, \mathbf{Q}}^X$  to the hybrid exciton energy.

The last ingredient missing is  $H_{int}$ . The interaction to be included here is again the hybrid electron-light interaction, that in hybridized electron bands reads

$$H_{int} = \sum_{\mathbf{p} \mathbf{k} \gamma} \mathcal{M}_{\mathbf{p} \mathbf{k} \xi_e} a_{l \mathbf{p}}^{\dagger} a_{c \mathbf{k}}^{\gamma} = \sum_{\mathbf{p} \mathbf{k} \gamma l} g_{l \mathbf{k}}^{\gamma} \mathcal{M}_{\mathbf{p} \mathbf{k} \xi_e} a_{l \mathbf{p}}^{\dagger} a_{c \mathbf{k} l \xi_e} \quad (2.64)$$

with the optical matrix element  $\mathcal{M}_{\mathbf{p}\mathbf{k}\xi_e}$  containing the optical selection rules. If we now take the expectation value, computed on the initial and final states just derived we obtain a series of selection rules, that together with conservation of the total electron momentum and neglecting all other momentum dependencies in the optical selection rule term, i.e.  $\mathcal{M}_{\mathbf{p}\mathbf{k}\xi} = \tilde{\mathcal{M}}\delta_{\mathbf{p}\parallel, \mathbf{k}+\xi}$ , let us arrive to the final equation for the ARPES signal

$$\begin{aligned} \mathcal{I}(\mathbf{k}, h\nu; t) &\propto \sum_{\eta, \gamma, \mathbf{p}} |\mathcal{G}_{\mathbf{p}\mathbf{k}}^{\eta\gamma}|^2 N_{\mathbf{k}-\mathbf{p}}^{\eta}(t) \delta\left(E_{\mathbf{k}}^e - E_{\gamma, \mathbf{p}}^v - E_{\eta, \tilde{\mathbf{k}}-\mathbf{p}}^X - h\nu\right) \\ \mathcal{G}_{\mathbf{p}\mathbf{k}}^{\eta\gamma} &= \sum_{\mu} g_{l_h \mathbf{p}}^{\gamma*} \tilde{\mathcal{M}} \mathbf{c}_{\mu}^{\eta*}(\tilde{\mathbf{k}} - \mathbf{p}) \psi^{\mu*}(\tilde{m}_e \mathbf{p} + \tilde{m}_h \tilde{\mathbf{k}}) \cdot \delta_{\xi_h^{\gamma}, \xi_h^{\mu}}. \end{aligned} \quad (2.65)$$

where we used  $\tilde{\mathbf{k}} = \mathbf{k} - \xi_e$ . The new coupling  $\mathcal{G}_{\mathbf{p}\mathbf{k}}^{\eta\gamma}$  contains the momentum dependence of the ARPES signal, i.e. superposition of the excitonic wavefunctions weighted by the mixing coefficients and the hole hybridization coefficients. Note that ARPES signals stemming from different electron valleys are additionally weighted by different photoemission matrix elements  $\mathcal{M}$ , which is neglected here.



---

## Hybrid exciton thermalization

---

Having introduced the theoretical framework for our description of optical excitations in TMD bilayers, we can now investigate in detail the thermalization process of excitons, focusing on the huge impact of hybridization on the exciton dynamics. With the tools developed in Chapter 2, we analyze in Paper 1 the details behind the thermalization process in TMD heterostructures at fixed stackings, focusing on the exemplary case of the MoSe<sub>2</sub>-WSe<sub>2</sub> heterostructure in R<sub>h</sub><sup>h</sup> stacking configuration (other stackings and a different heterostructure, MoS<sub>2</sub>-WS<sub>2</sub>, are studied in the SI), we unravel the resulting charge transfer as the consequence of a phonon-mediated two-step relaxation via highly hybridized states. In addition in Paper 2-3 we study the different charge transfer mechanisms in the WSe<sub>2</sub>-MoS<sub>2</sub> heterostructure, predicting and explaining the presence of a blue shift in the measured energetic ARPES signal of the photoejected electron.

### 3.1 Energy landscape

In the past few years, some experimental observations have shown that, exciting with a laser one of the two layers of a TMD heterostructure, i.e. resonantly to the intralayer A exciton of one of the two layers, was causing a charge transfer to the opposite layer [49–54]. Surprisingly, the charge transfer process has been measured to be on the order of sub-picoseconds timescales, thus appealing for future terahertz applications [91].

In order to have access and to understand the process we start by computing the energy landscape of the system. This is done by solving the Wannier equation in the hybrid-exciton basis (see procedure leading to equation 2.43), obtaining a set of hybrid exciton bands for each excitonic valley. By looking at the resulting hybrid exciton band structure, we plot in Figure 3.1 a) the energy minima of the hybrid exciton parabolas, choosing an energy window accessible to an optical excitation of a bright intralayer W-W state. As additional and necessary information to understand the dynamics, we quantify the contribution of each state to the new hybrid-exciton states by evaluating the mixing coefficients. We use  $|c_{\mu}^{\eta}(\mathbf{Q})|^2$  as a color tool, interpreting it as the percentage of the exciton

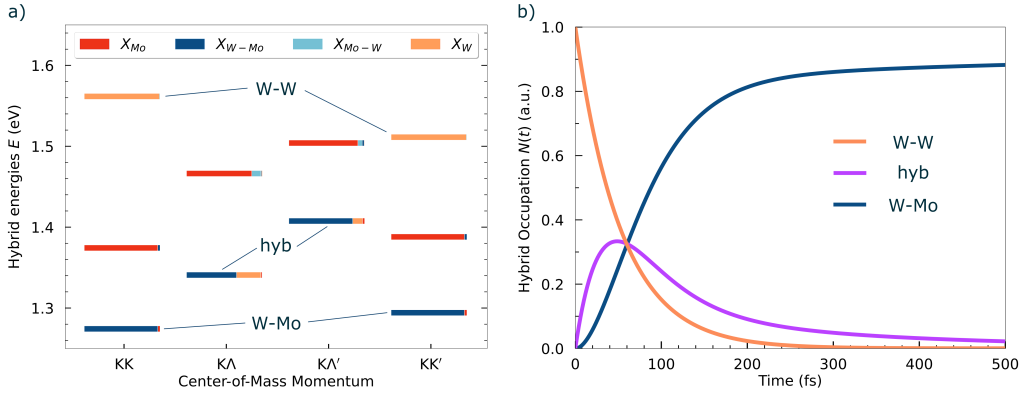


Figure 3.1: a) Hybrid exciton energy landscape for MoSe<sub>2</sub>-WSe<sub>2</sub> heterostructure. We adopt a color scheme using the mixing coefficients (coefficients of the change into hybrid basis) as percentage of the contribution of an excitonic state into a hybrid state. b) Momentum integrated hybrid exciton occupation, resolved for the different channels W-W (intralayer states), *hyb* (highly hybridized momentum-dark states, with electron probability in  $\Lambda$  smeared across both layers), and W-Mo (interlayer states). (Figure adapted from Paper 1)

state  $\mu$  inside the hybrid state  $\eta$ . We adopt a color scheme in which hybrid states of a pure intralayer or interlayer character are just red or blue, respectively. In contrast, strongly hybridized states consist of different colors. In the presence of strong tunneling, the hybrid states are heavily influenced by different excitonic species, this is the case for the momentum-dark states *hyb*. In contrast, a weak tunneling results in hybrid states that are almost purely intra- or interlayer excitons, as in the case of KK excitons. The energetically lowest states of the system are interlayer state (W-Mo), this is justified by the type II band alignment of the heterostructure. From the presented context, we can envision that an excitation resonantly to the intralayer W-W bright state will be followed by a phonon-mediated cascade, leading to the dissipation of thermal energy until reaching an equilibrium configuration. It is essential to emphasize that, for phonon-mediated scattering to occur between two states, they must partially share the same layer. This arises from the phonon selection rules encapsulated in equations 2.54,2.56. Phonons, being a local process with respect to the layer index, cannot directly mediate charge transfers between layers. In this context, the existence of highly hybridized states not only alters the energy landscape but also significantly influences relaxation dynamics by activating scattering channels through which phonons can indirectly mediate charge transfers in conjunction with tunneling.

## 3.2 Two-step phonon mediated charge transfer

This is completely manifest if we have a closer look at the time evolution of the system. To focus only on the important aspects of the dynamics, given the huge amount of states involved in the relaxation, we opt to simplify the starting condition and choose a static initialization of the system. We place an initial distribution of excitons in the bright W-W

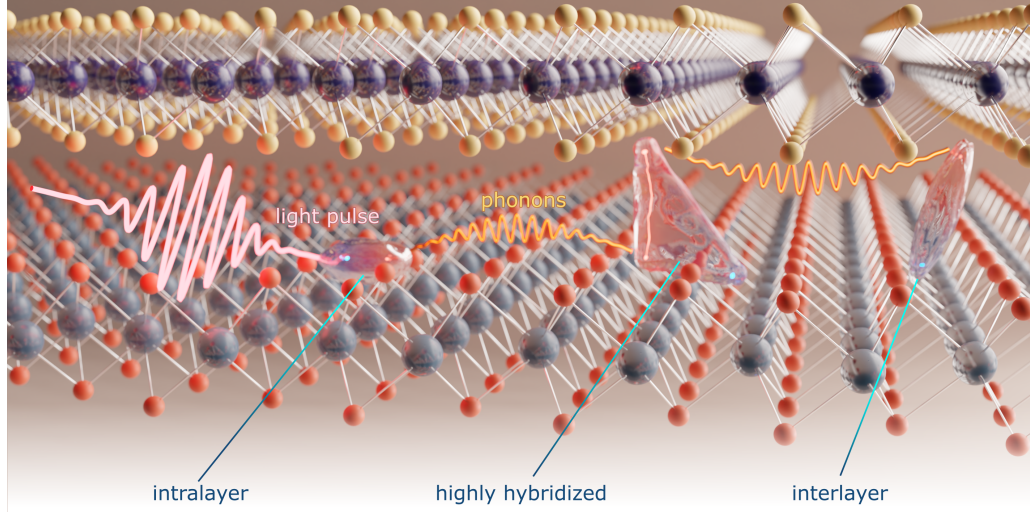


Figure 3.2: Illustration of a charge transfer process in TMD heterostructures: starting from the left, following an optical excitation of one layer, a population of intralayer excitons is excited. This population undergoes a two-step relaxation process driven by phonon-mediated scatterings. Initially, the relaxation occurs through highly hybridized states, states in which the electron and hole exist in a superposition across both layers. Subsequently, in the final step, the process leads to the formation of the most energetically favorable interlayer state.

intralayer state and use equation 2.56 to have access to the momentum and time resolve hybrid exciton occupation  $N_{\mathbf{Q}}^n$  during its time evolution. In Figure 3.1 b) we plot the momentum integrated occupation, to be able to follow the relaxation path across the different states. At 0 fs, we see the orange line at full occupation, reflecting the choice of our initial conditions. The dynamics can then be explained in terms of a two-step process: at an early stage of the dynamics (0-100 fs), excitons rapidly relax down to the highly hybridized *hyb* (purple lines), in which the hole is fixed in the excited layer and the electron is in a superposition of both layers. Once the electron has been scattered into a hybridized state, that is, into a superposition between both layers, there is a nonzero probability of further scattering into the opposite layer. This is what we see at later stage of the dynamics in which the hybrid exciton population is being transferred to interlayer states W-Mo. The latest stage of the dynamics consist finally of the thermal equilibration between the almost degenerate interlayer ground states. From this study, we can draw significant conclusions. Firstly, by incorporating tunneling and phonons into our model, the exciton dynamics in a bilayer system, following excitation in either of the two layers, occur very rapidly, on the order of hundreds of femtoseconds through a two-step process. Secondly, in the context of our description, returning to an electronic picture, the process we elucidated represents a charge transfer: electrons in one layer, due to optical excitation, form bound states with holes in the same layer. Through scattering with phonons, the electrons bound to holes acquire momentum, moving to occupy momentum-dark states. The substantial overlap between the atomic orbitals of the two layers is responsible for a strong tunneling effect, increasing the electron probability of being found in the second

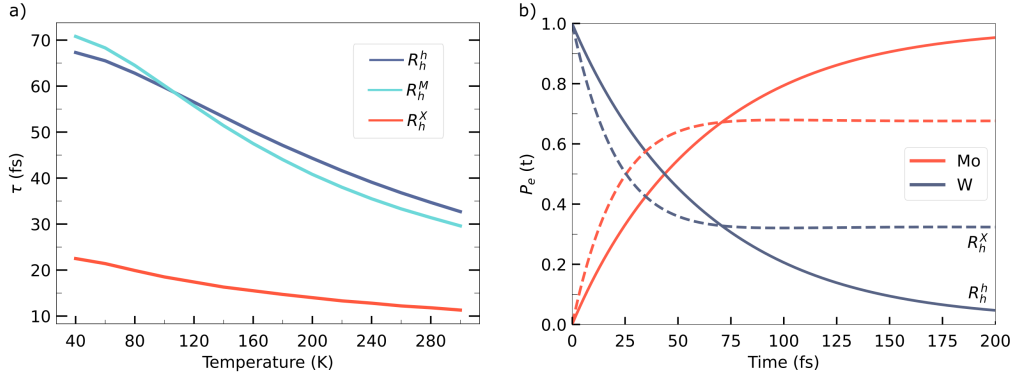


Figure 3.3: a) Characteristic electron transfer time as a function of temperature for MoSe<sub>2</sub>-WSe<sub>2</sub> in different high-symmetry stackings. The time is extracted from an exponential fit of the layer-dependent electron probability  $P_e(t)$  as shown in part b). We find a considerable decrease in the charge transfer time with temperature reflecting a more efficient exciton-phonon scattering. Interestingly, we predict a much faster transfer time for  $R_h^X$  stacking, as here the highly hybridized *hyb* states are very close to the interlayer W-Mo states (cf sI Paper 1). The faster electron transfer speed comes at the cost of a more incomplete transfer process as the stationary occupation of the *hyb* excitons is relatively high, where the electrons is delocalized between both layers.

layer. This non-negligible probability facilitates phonon scattering with the opposite layer. The phonon mediated scattering enables the relaxation to the more energetically favorable interlayer state.

Another crucial consideration is that our microscopic model successfully explains the experimentally observed ultrafast charge transfer predicting the same timescales for the overall process.

### 3.3 Temperature and stacking dependence

To further characterize the charge transfer process, we introduce the *characteristic charge transfer time*  $\tau$  to have a measurable quantity for easy comparison. We then investigate the process as a function of different stackings and temperatures. The results of this analysis are depicted in Figure 3.3, where we plot  $\tau$  against temperature, using distinct colors for the various analyzed stackings. In Figure 3.3 a), we observe that the charge transfer process, being phonon-mediated, is highly influenced by temperature regardless of the stacking. The process varies from a characteristic time around 70 fs at 40, settling between 30 and 40 fs at room temperature. This holds true for  $R_h^h$  and  $R_h^M$ , owing to the similar energetic composition of the band structure. On the other hand, the drastic convergence of hybrid states to the interlayer state and the reduced energy difference between the initial and final states in the case of  $R_h^X$  stacking lead to an increase in velocity. However, this difference is accompanied by an additional effect. By calculating the probability of finding an electron in either layer as a function of time (see SI Paper 1 for details), we can compare the difference between  $R_h^h$  and  $R_h^X$  (Figure 3.3 b)). Here, in the case of  $R_h^h$ , we observe a complete charge transfer. In contrast, for  $R_h^X$ , despite the

process being faster, we witness a partial charge transfer. This is attributed to the close energetic proximity between interlayer W-Mo and *hyb* states. Given the two states are energetically close, the equilibrium distribution predicts that the population is thermally distributed between them, with KL states where electrons overlap between the two layers, i.e. still not completely transferred to the opposite layer.

From this considerations we can understand that the charge transfer mechanism is strictly material and transfer specific, and in the additional study performed in a different heterostructure (MoS<sub>2</sub>-WS<sub>2</sub>) in the SI of Paper 1, we show that both charge transfer of electron and holes are possible depending on the specific energy landscape of the system under study.

### 3.4 Formation of interlayer excitons

The possibility of having an interlayer exciton as the ground state, characterized by a permanent electric dipole with charges spatially separated in the two layers, has proven to be an effective tool for controlling light excitation [54, 82–84, 92]. This justifies the interest in unraveling its formation process. In Paper 2 and 3 we investigate this formation process in the WSe<sub>2</sub>-MoS<sub>2</sub> heterostructure, analyzing the two different charge transfer mechanisms bringing the exciton population from the intralayer states in the two opposite layers to the ground state interlayer state. Thanks to an experiment-theory collaboration we investigate electron and hole charge transfer using time-resolved angle-resolved photoemission electron spectroscopy (trARPES). The significant advantage of ARPES experiments lies in the capability to acquire momentum-energy-time maps of photoemitted electrons after an optical excitation creating bound electron-hole pairs. This proves advantageous as the model introduced in Chapter 2 grants us direct access to the same quantity.

#### Electron transfer

For describing the physical system under examination, we had to tailor the previously introduced model to the specific case: the investigated structure features an angle of approximately 9-10 degrees. At this angle, the model initially devised to handle the twist angle via a moiré potential becomes unsuitable for describing the problem (the model was derived in the small-angle limit of 0-5°). This is because the period of the superlattice would be so small as to be comparable to the Bohr radius of excitons. On the other hand, employing the perfect stacking model wouldn't be entirely appropriate either, as the energy bands and mixing coefficients turn out to be non-isotropic in this case. Thus, we introduce an adaptation of the model in which the twist angle is incorporated as a rigid rotation of one layer's valleys relative to the other, extracting non-isotropic mixing coefficients. Subsequently, assuming that the large twist angle leads to fast intravalley equilibration through elastic co-scattering (e.g., with defects). Hence, we perform an average over the valley local angle of the exciton momentum, assuming that the population stays almost isotropic at all times. We define angle-averaged quantities  $\delta N_{\mathbf{Q}}^{\eta} \approx \delta \tilde{N}_{\mathbf{Q}}^{\eta}$  with the 1D density  $\tilde{N}_{\mathbf{Q}}^{\eta}$  depending only on the radial component of the CoM momentum. We then integrate

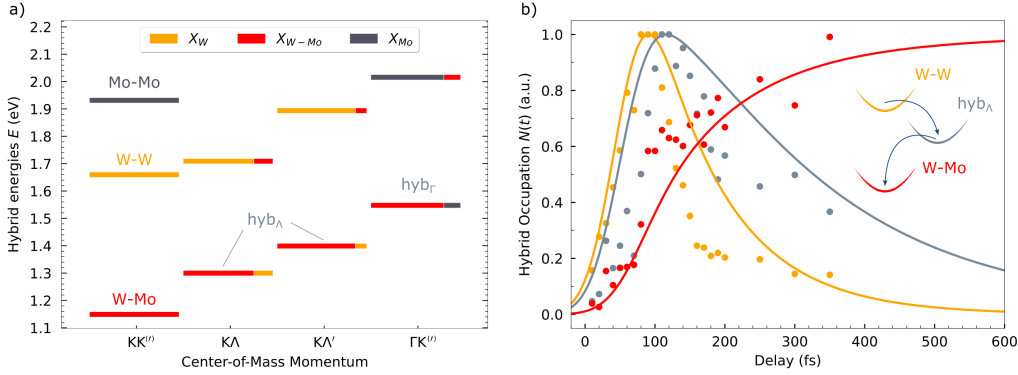


Figure 3.4: a) Hybrid energy landscape for  $\text{WSe}_2\text{-MoS}_2$ . b) Momentum integrated hybrid exciton occupation. Here we plot with solid lines the theoretical results and with dots the experimental data. Figure adapted from Papers 2-3.

equation 2.56 over the momentum to obtain averaged scattering rates  $\tilde{W}_{QQ'}^{\eta\xi} = \sum_{\theta,\theta'} W_{QQ'}^{\eta\xi}$ . After this initial clarification we can now enter in the details of the process under exam. In the two different papers we analyze the different charge transfer processes consequently to a different excitation of the system: in Paper 2 we analyze the formation of interlayer excitons after excitations resonantly to W-W, intralayer state in W-based layer, while in Paper 3 resonantly to Mo-Mo, intralayer state in Mo-based layer. These two studies show remarkably different dynamics, here we provide a detailed summary of the results. We start by computing the specific energy landscape of the heterostructure under study (Figure 3.4 a)), where we fix our parameters for band alignment and valleys offset to the experimental values (instead of the DFT parameters used for Paper 1-4-5). Adopting the same color scheme used in section 3.1, we plot the hybrid exciton states with energy accessible to both the intralayer excitations. We can see that in this specific heterostructure in addition to the strongly hybridized  $\text{hyb}_\Lambda$  states, in the case of Mo-Mo excitations also the  $\text{hyb}_\Gamma$  states lay below the excitation energy, thus will be of great importance for the time evolution of the system.

We start by analyzing the case of excitation resonantly to W-W. In this scenario, in a similar process to the one studied in Paper 1, the formation of interlayer excitons occurs through a two-step electron transfer process: by injecting excitonic population into the W-based layer (W-W exciton state), excitons rapidly dissipate their excess thermal energy, by relaxing and populating interlayer states (W-Mo state), thanks to the energetically accessible hybrid  $\text{KA}^{(\prime)}$  states ( $\text{hyb}$  states in Figure 3.4 a)). This is evident from Figure 3.4 b), where we illustrate the temporal evolution of the system, plotting the momentum integrated hybrid exciton density  $N(t)$ . The data points represent experimental results, and the solid lines the theoretical simulation results (each state is normalized to its own maximum). As observed, despite numerous approximations in the model, we manage to quantitatively reproduce the temporal scales of the ongoing charge transfer effectively.

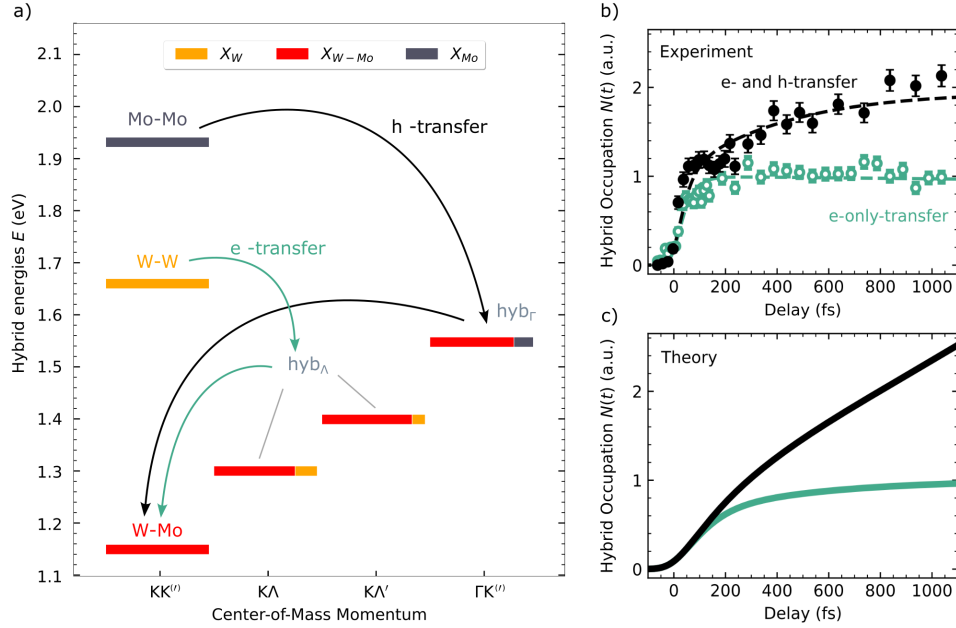


Figure 3.5: a) Hybrid energy landscape for  $WSe_2$ - $MoS_2$ . We highlight with black arrows the hole-transfer relaxation cascade and with green arrows the electron transfer relaxation cascade. b)-c) Momentum integrated hybrid exciton occupation as function of the probe delay. Here we plot in b) the experimental data and in c) the theoretical results. Figure adapted from Papers 2-3.

## Hole transfer

Now, let's delve into the case of resonant excitation at Mo-Mo energies, thus injecting excitons into the layer opposite to the one just described. In this scenario, the energies involved during relaxation are significantly higher (initial state 300-400 meV more energetic) as can be seen from Figure 3.5 a), and this profoundly impacts our model. Firstly, the effective mass approximation is valid only in the vicinity of the valleys. Therefore, considering such high energies forces us to extend the bands further, encompassing scattering that could either overestimate or underestimate contributions derived from the actual topology of the electron bands. Moreover, a second complication stems from the experimental side: exciting so intensely out of equilibrium requires very powerful lasers, causing non-resonant excitation of the opposite layer as well. Specifically, this means that in addition to injecting Mo-Mo excitons, W-W excitons are also created in a ratio of 5:1. This dual excitation must be considered in our simulations to obtain comparable results. This second point leads to an additional complication due to the large number of states involved in the process, resulting in a high numerical complexity of the simulations. Given these observations, we decide to focus more on the qualitative analysis of the process, emphasizing the differences from the process electron transfer. Now, focusing on the dynamics, we can divide it into two parts: the first part concerning resonant excitation in the Mo layer, creating excitons in the Mo-Mo state, and the second part involving non-resonant excitation in the W layer, resulting in the creation of W-W excitons. Analyzing the first part, we observe that the

states affected during relaxation are the highly hybridized  $\Gamma$ K states. These states play a role similar to the KA states analyzed in Papers 1-2, activating the hole transfer between the layers. The dynamics of this first part is substantially slower (timescales of ps compared to the hundreds of fs for electron transfer within the same heterostructure). This is due to two main reasons: i) the significant intravalley relaxation component necessary to reach energies suitable for intervalley scatterings and ii) the presence of the threefold degeneracy for  $\Lambda$  valleys in the case of the electron transfer, in contrast to the single  $\Gamma$ -based relaxation channel for the hole transfer.

The second part of the dynamics consists of the exact electron transfer process described above (Paper 2). The two parts of the dynamics are decoupled, since they occur through different relaxation channels with negligible interactions. For the hybrid exciton phonon scatterings, in fact, scattering processes  $\text{hyb}_\Lambda \leftrightarrow \text{hyb}_\Gamma$  require simultaneous phonon absorption/emission from both electron and hole, being this scattering process of higher order, it can be safely neglected. Although occurring through different channels, both processes (e-transfer and h-transfer) lead to the final population of energetically favorable states, i.e., interlayer W-Mo. In Figure 3.5, we can observe the comparison of these two parts of the dynamics. In both figures, representing (b) experimental data and (c) theoretical simulations, we observe the same trends with good qualitative agreement. When considering the electron-only transfer process (green symbols 3.5(b)), the interlayer exciton signal increases rapidly with pump-probe delay and saturates on the sub-200 fs timescale. In contrast, the joint build-up of interlayer W-Mo excitons via electron- and hole-transfer processes after 1.9 eV excitation, saturates on the 1 ps timescale for experimental data (black symbols 3.5(b)). The huge difference notable between experiment and theory is a combination of the considerations we have introduced before about the limits of our model, and, in addition, due to the not included recombination processes, that on timescales of ps should impact more on the exciton occupation. Despite predicting a similar order of magnitude for the transfer (experiments 1 ps and theory 4 ps for the saturation of the interlayer via electron- and hole-transfer signal) we can not obtain a quantitative comparison. Both experimental and simulated data suggest that the interlayer hole-transfer mechanism across the  $\text{WSe}_2\text{-MoS}_2$  heterointerface is substantially slower compared to the electron-transfer mechanism.

The most surprising result of this experiment, however, comes from the analysis of the energy-time map of the ARPES signal. As seen in Figure 3.6, the ARPES signal is completely different from that analyzed in the case of electron transfer. While there, the energy relaxation of excitons was accompanied by energy relaxation of the photo-emitted electron, here the final signal is at a higher energy than the initial excitation. Despite this seemingly inexplicable blue shift, an explanation can be found by considering the electron-hole complex. The ARPES-derived signal, in fact, only partially accounts for energy exchanges in the system, capturing information related to electrons only. In contrast, the excitonic system before the breakdown through light pulse is a bound electron-hole system, so the energy of the system is conserved only in this picture. This has already been discussed when deriving equation 2.65, the delta function appearing there, in fact, fixes energy conservation for the system. Generally, for the excitonic signal in a monolayer, the

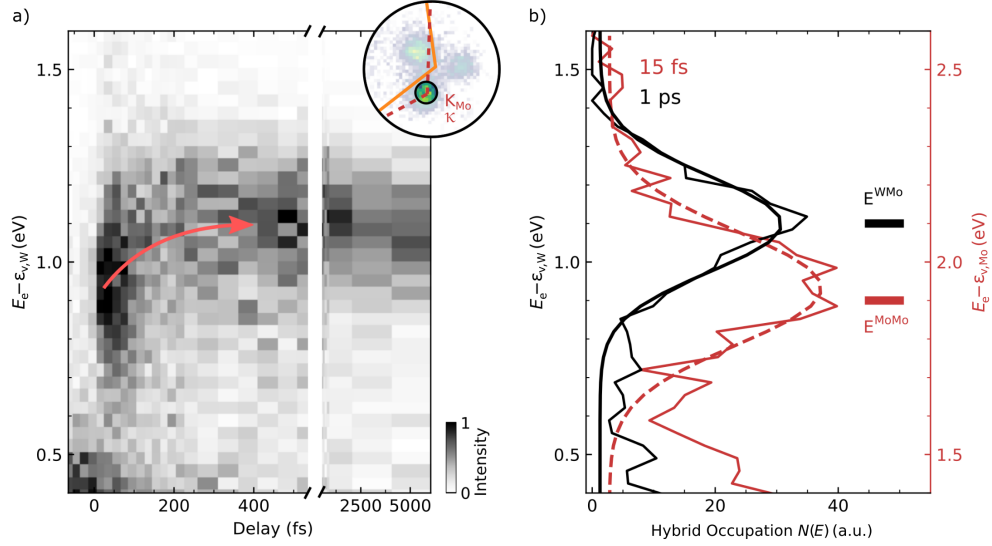


Figure 3.6: a) Energy-time map of the ARPES intensity. b) Hybrid exciton occupation as function of energy, using respectively as zero: in black the W-valence band, and in red the Mo-valence band. Figure adapted from Paper 3.

reference energy is the valence band, with the excitonic signal appearing a binding energy below the conduction band, i.e.,  $E_e = \varepsilon_{v,l} + E^X = \varepsilon_{c,l} - E_b$ , where  $E_e$  is the energy of the photo-ejected electron,  $\varepsilon_{v/c,l}$  valence/conduction band energy maximum/minimum for layer  $l$ ,  $E_b$  binding energy and  $E^X$  total energy of the exciton state. In our case, however, in the presence of a bilayer, we have two valence bands. This has two main consequences: i) we cannot define uniquely a binding energy for an hybrid state, ii) the excitonic signal must be referenced to the valence band corresponding to the layer of the hole forming the excitonic state. In the examined case, since there is a layer exchange for the hole, the photo-emitted electron's energy at the beginning of the process is  $E_e^i = \varepsilon_{v,Mo} + E^{Mo-Mo} + \hbar\omega$  and at the end  $E_e^f = \varepsilon_{v,W} + E^{W-Mo} + \hbar\omega$ , where we use  $i/f$  refer to the initial/final stage of the process, and  $\varepsilon_{\lambda,l}$  usual notation for electron energy in a state labeled by band index  $\lambda$  and layer  $l$ . This layer exchange of the hole leads to an energy gain for the electrons due to the relative difference between excitonic energies and reference valence bands, i.e.  $\Delta E_e = \Delta\varepsilon_v + \Delta E^X \approx 0.17$  eV. Despite the energy gain of the electron, the hole+electron system has followed the normal energy relaxation process. With this result we have strengthened the idea that femtosecond momentum microscopy is a powerful tool to study the correlated interaction between the exciton's electron and hole in twisted TMD heterostructures, thanks to the photo-emitted electron still carrying information about the precedent bound state with the hole.

In this chapter, we established the theoretical framework for understanding optical excitations in TMD bilayers, focusing on the thermalization process of excitons and

emphasizing the significant impact of hybridization on exciton dynamics. Experimental observations in TMD heterostructures, particularly in the MoSe<sub>2</sub>-WSe<sub>2</sub> system, revealed a remarkable charge transfer process between layers following resonant excitation. This ultrafast charge transfer, occurring on the hundreds femtosecond timescale, holds promise for future terahertz applications. Utilizing the tools developed in Chapter 2, we delved into the details of the thermalization process in TMD heterostructures, specifically exploring the MoSe<sub>2</sub>-WSe<sub>2</sub> heterostructure in the R<sub>h</sub><sup>h</sup> stacking configuration. We employed the hybrid-exciton basis to compute the energy landscape, revealing the crucial role of highly hybridized states in the relaxation cascade. Our analysis demonstrated a two-step charge transfer process: initially, excitons rapidly relax to highly hybridized states, where electrons and holes exist in a superposition across both layers. Subsequently, the process leads to the formation of the most energetically favorable interlayer state, facilitated by phonon-mediated scatterings. The existence of highly hybridized states not only alters the energy landscape but also significantly influences relaxation dynamics by activating scattering channels through which phonons mediate the charge transfers. The study's key findings include the rapid charge transfer process, occurring within hundreds of femtoseconds, and the successful explanation of the experimentally observed ultrafast charge transfer. Moreover, the characteristic charge transfer time,  $\tau$ , was introduced as a measurable quantity, demonstrating its dependence on temperature and stacking configurations.

In the following chapter, we extend our exploration by investigating the ARPES signature of highly hybridized states. The choice of this topic is inspired by the intriguing questions raised from the results presented in this chapter. Specifically, we investigate how highly hybridized states are manifesting in ARPES experiments, providing valuable insights into the specific fingerprint of these states and enhancing our understanding of their properties.

---

## Hybrid exciton signatures

---

In our earlier papers (Paper 2-3), we employed ARPES experiments in a joint experiment-theory collaboration to investigate the interlayer exciton formation process, highlighting the significance of hybridized states. Building upon these results, we investigate the distinguishing signature of highly hybridized signal in ARPES. We predict here the arising of a double peak signal stemming from these hybrid states.

### 4.1 Energy landscape and hybrid exciton dynamics

We utilize the tools developed in Section 2.10 to calculate the ARPES signal of the naturally available homobilayer MoS<sub>2</sub>-MoS<sub>2</sub> in H<sub>h</sub><sup>h</sup> stacking. This choice is motivated by two main reasons. First, the most energetically favorable states are momentum-dark  $\Gamma_{\text{hyb}}$  hybrid excitons, that, due to a lack of lower-lying states and their momentum/layer indirect character, exhibit long lifetimes facilitating their observation in ARPES spectra. Second, the strong interlayer tunneling results in a large splitting of the valance bands at the  $\Gamma$  point. As a result, the hole in  $\Gamma_{\text{hyb}}$  excitons is delocalized over a large spectral range and we expect to find pronounced hybrid hole signatures in ARPES spectra. To begin our analysis, we study the energy landscape available to optical excitation in this specific TMDs structure and use it in combination with equation 2.56 to study the dynamics of the system. We decide to update our notation and use the exciton valley index to name each hybrid state, using as subscript the respective electron/hole layer or hyb in the presence of hybridized electron or hole. Looking at Figure 4.1 a) we can see that an optical excitation at  $\simeq 1.9\text{eV}$ , reflecting an injection of excitons resonant to the intralayer  $\text{K}_1\text{K}_1$  state, leads to an ultrafast population transfer from the initially occupied intralayer state to the highly hybridized  $\Gamma_{\text{hyb}}\text{K}^{(\prime)}$  states. This is followed by a thermalization process in which the charge is redistributed between the two lowest lying almost degenerate states. We note that, from the Figure 4.1 b),  $\Gamma_{\text{hyb}}\Lambda_{\text{hyb}}$  exciton could, in principle, be important for the dynamics considering its low energy. However this can be neglected for two main reasons. (i) the direct scattering would require a simultaneous electron and hole scattering from

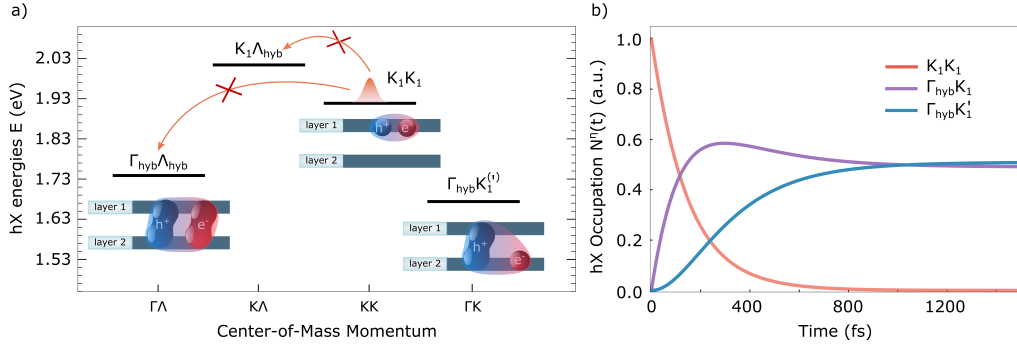


Figure 4.1: a) Hybrid exciton (hX) dispersion illustrating possible relaxation channels (note that  $\Gamma_{hyb}K_1^{(l)}$  states are almost degenerate in energy). b) Hybrid exciton dynamics. After optical excitation of a MoS<sub>2</sub> homobilayer at  $\simeq 1.9\text{eV}$  (resonant to the  $K_1K_1$  exciton), ultrafast exciton relaxation dynamics occurs resulting in the highest occupation  $N^n$  of the energetically most favorable momentum-dark  $\Gamma K^{(l)}$  hybrid exciton (red and purple lines). Picture adapted from Paper 4.

the  $K_1K_1$  state. This two-phonon process is thus of higher-order and has been neglected in our equations of motion derivation; (ii) the indirect scattering involving one-phonon processes,  $K_1K_1 \rightarrow K\Lambda_{hyb} \rightarrow \Gamma_{hyb}\Lambda_{hyb}$  and  $K_1K_1 \rightarrow \Gamma_{hyb}K_1^{(l)} \rightarrow \Gamma_{hyb}\Lambda_{hyb}$  are based on phonon absorption processes, leading to a negligible role in the relaxation dynamics.

## 4.2 Double peak ARPES signal

After having determined the hybrid exciton occupation time evolution, we can now focus on evaluating equation 2.65 to investigate the time- and momentum-resolved ARPES signal in MoS<sub>2</sub> homobilayers. Previous studies [59, 93], have shown that the excitonic ARPES signal in monolayers appears at the momentum corresponding to the electron valley and it is spectrally located one excitonic energy above the valence band (or one exciton binding energy below the conduction band). The shape of the signal is characterized by a negative curvature reflecting the valence band one (reflecting the hole dispersion), if the exciton population is very sharp in momentum. Focusing on the energy-momentum map in Figure 4.2, we follow the time evolution of the ARPES signal. Starting from time 0 fs, we observe an ARPES signal reflecting the nature of the almost purely intralayer  $K_1K_1$  exciton which is characterized by a well pronounced single peak (Fig. 4.2(a)). On a sub-100 fs timescale, we see the appearance of the strongly hybridized  $\Gamma_{hyb}K_1^{(l)}$  excitons. They are characterized by two peaks, one slightly above the  $K_1K_1$  exciton and one red-shifted by more than 600 meV (Fig. 4.2(b)). The last step of the dynamics leads to a thermalization of the hybrid excitons occupation. After 400 fs, the entire population has reached an equilibrium distribution (Fig. 4.2(c)), where only the signatures stemming from  $\Gamma_{hyb}K_1^{(l)}$  excitons have remained. Focusing on the shape of the signal we see that momentum-narrow excitonic distribution, results in a signal with a negative curvature (Fig. 4.2(a)) while thermally distributed populations are smeared out in momentum and energy, where the shape of the

## 4.2. DOUBLE PEAK ARPES SIGNAL

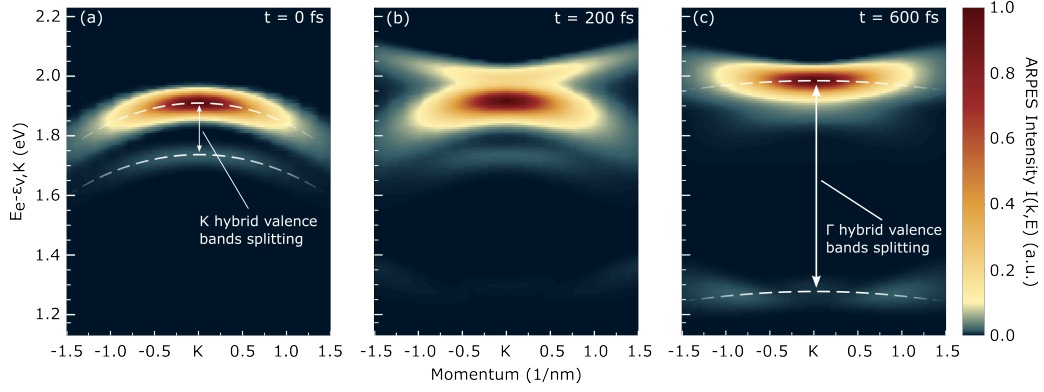


Figure 4.2: Momentum-resolved ARPES map. Hybrid exciton dynamics tracked in a tr-ARPES signal (a) revealing the excitation of the nearly purely intralayer  $K_1K_1$  exciton state (0 fs), (b) the formation of the strongly hybridized  $\Gamma_{hyb}K_1$  state (200 fs) and (c) the thermalized hybrid exciton distribution (600 fs). The dashed lines show the shifted split valence bands of the hybrid hole at the K point (with the splitting  $\Delta E_K^v$ ) and at the  $\Gamma$  point (with the splitting  $\Delta E_\Gamma^v$ ). The energies are shown with respect to the upper hybrid valence band ( $\varepsilon_{v,K}$ ) at the K point. Picture taken from Paper 4.

final ARPES signal is reflecting a mixture of the hybrid valence bands (curved downwards) and the hybrid exciton parabola (curved upwards), cf. Fig.4.2 (c). Our work's main result is predicting a distinctive double-peak ARPES signal, characteristic of hybrid exciton states. In the case of the  $\text{MoS}_2$  homobilayer, the ARPES signal is governed by the energetically lowest  $\Gamma_{hyb}K_1$  hybrid exciton, which ARPES signal exhibits (Figure 4.2(c)) the two peaks that are separated by approximately 0.6 eV. Their position corresponds to the energy of the split hybrid valence bands (illustrated by dashed lines in the picture).

We can justify the presence of the double peak signal by considering the single particle picture of the correlated electron-hole pair. The two valence bands ( $|\pm\rangle$ ) at  $\Gamma$  are completely delocalized across both layers, i.e.  $|\pm\rangle = (|1\rangle \pm |2\rangle)/\sqrt{2}$ , where  $|n\rangle$  indicates the valence band of the pure monolayer  $n$ . In this picture, the hybrid exciton is formed with an electron that is strongly localized in one of the two layers (at the K point), e.g. layer 1. The Coulomb interaction partially drags the hole into the same layer to reduce the energy, favouring a hole wave function that is mostly in layer 1 too, i.e.  $|1\rangle = (|+\rangle + |-\rangle)/\sqrt{2}$ . Consequently, the energetically most favourable two-body state ( $\Gamma_{hyb}K_1$  hybrid exciton) is build by a superposition of the two hybrid valence bands  $|\pm\rangle$ . When the  $K_1$  electron from the  $\Gamma_{hyb}K_1$  hybrid exciton is ejected, a  $\Gamma$  hole is left behind, remaining in the superposition that has previously formed the exciton. The conservation of energy and momentum ensures that by measuring the energy of the ejected electron, we obtain information about the energy of the hole as well. While the hole within the hybrid exciton is in a quantum mixture of two energy levels, the relative energy between electron and hole is fixed by the two-particle exciton energy. This correlation between electron and hole transfers the superposition of hole energies to the electron, whose energy is consequently undefined as well. Measuring the energy of ejected electrons therefore allows us the reconstruct the underlying energy distribution of the holes. The appearing of the double peak can

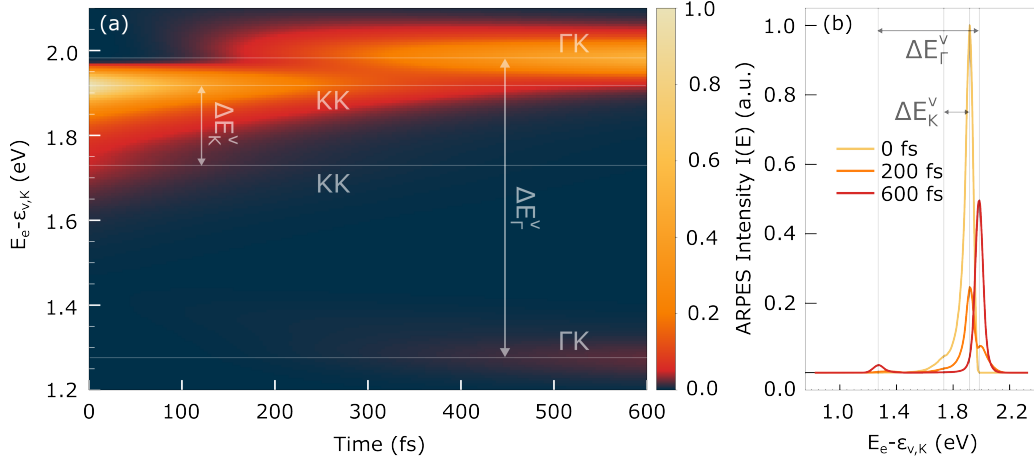


Figure 4.3: Momentum-integrated ARPES map. (a) Energy- and time-resolved ARPES signal, showing the characteristic double-peak structure reflecting the hybrid hole being spread over two valence bands at K point (initial signal) and at the  $\Gamma$  point (final thermalized signal). (b) ARPES signal at fixed times plotted as a function of energy. The energies are shown with respect to the upper hybrid valence band ( $\epsilon_{v,K}$ ) at the K point as reference. Picture taken from Paper 4.

be better observed in the momentum integrated ARPES intensity plotted in Figure 4.3. As last remark, although the choice of MoS<sub>2</sub> homobilayer is favorable for the reasons explained at the beginning, the hybridization of the hole (50% - 50%) is similar to the exciton hybridization giving rise to the predicted relatively small double-peak intensity ratio. Being the percentage of hybridization of both excitons and valence bands the key behind the peak intensity ratio, we expect that heterostructures exhibiting a considerably different degree of hybridization for holes and excitons should give rise to larger intensity ratios that are easier accessible in ARPES experiments. For more details about the peak intensity ratio and more details about the theory we refer to the SI of Paper 4.

In conclusion, we've thoroughly investigated the distinct signals that hybrid exciton states in MoS<sub>2</sub> homobilayers leave in ARPES experiments. The double-peak pattern in the ARPES signal, particularly from the  $\Gamma$ hybK<sub>1</sub> hybrid exciton, offers crucial insights into how electrons and holes interact. As we move into the next chapter, our aim widens to look at the broader picture of exciton thermalization, especially at lower energies. This chapter, focusing on ARPES intricacies, complements our earlier study of high-energy dissipation. In the upcoming discussion, we focus into the final stages of thermalization, aiming to understand the final intravalley equilibration step, that normally leads to a Boltzmann-like equilibrium. However, things get intriguingly complicated when twist angles come into play, reshaping the landscape and significantly impacting thermalization dynamics. Exploring this twist-induced complexity will enhance our overall understanding of exciton dynamics in 2D semiconductor structures.

---

## Moiré exciton thermalization

---

In the previous chapters, we analyzed the thermalization of excitons in heterostructures, without considering any twist angle between the layers. Using the tools presented in Sections 2.7,2.8,2.9, we study the final step of the thermalization process, focusin on energy ranges heavily affected by the the twist angle dependent moiré potential.

### 5.1 Energy landscape and moiré exciton dynamics

Studying the relaxation process in TMD heterostructures in the previous chapters, we have explained the general pathways of hybrid excitons during their thermalization process. The possibility of neglecting the twist angle in the previous description is possible thanks to the energy scales involved in the process. Exciting resonantly to an intralayer excitons in fact, requires hundreds of meV. However, in Section 2.7, we observed that in the presence of a twist angle, excitonic parabolas are deformed, creating a new periodicity. We expect, as in the quantum well case, that the higher the energy, the less impact the moiré potential effect has on the bands. On the other hand, near the parabolic minimum, the effect of the twist angle is much greater, and therefore, we expect the moiré potential to significantly influence the intravalley relaxation.

In the case of heterostructures, the process studied in Papers 1-4 describing intervalley energy relaxation leads to reach the ground state of the system, in which subsequently excitons reach a Boltzmann equilibrium distribution around the minimum. However in the presence of twist angle this final step can be strongly influenced by the deformation induced by the moiré potential (Figure 5.1 (a)). The energy-momentum relaxation description is translated into real space as a change in the spatial exciton distribution, where starting from a delocalized configuration excitons relax into the pockets of moiré potential (Figure 5.1 (b)). Recent experiments have emphasized that, in the presence of a twist angle, the low-energy excitonic relaxation dynamics deviate from a Boltzmann-like relaxation. They show long-lived excited states [27, 43, 94] that, in Photoluminescence experiments, exhibit brighter responses [27], closely related to the increased occupation of these bands. Despite

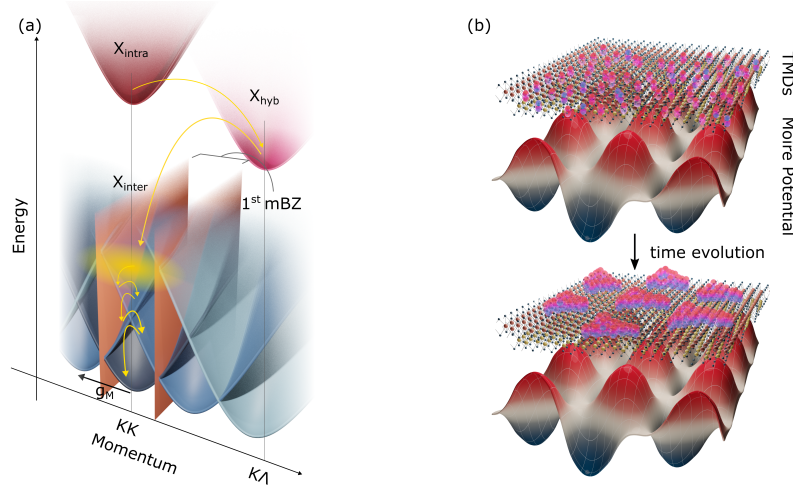


Figure 5.1: Sketch of exciton dynamics in a twisted TMD heterostructure. (a) After optical excitation of intralayer excitons ( $X_{intra}$ ) in one of the layers, exciton population relaxes to the energetically lowest states (interlayer excitons  $X_{inter}$  in the case of  $\text{MoSe}_2\text{-WSe}_2$  investigated here) via momentum-dark hybrid excitons  $X_{hyb}$ . We depict the exemplary case of parabolic bands, in which a new periodicity ( $\mathbf{g}_M$  reciprocal lattice moiré vector) arises, forming the new mini Brillouin Zone (mBZ). In the case of small twist angles, there is, in addition to the new periodicity, a change in the band curvature, resulting in flat bands. (b) Exciton relaxation in momentum space is reflected by the change of exciton localization in real space: the thermalization process brings the exciton population (purple dots) from a delocalized phase to the most favourable configuration of trapped states. Picture taken from Paper 5.

these intriguing and unconventional experimental results, there is no microscopic study in the literature that justifies the observations.

Building upon these results, we delved into the dynamics in the final stages of relaxation, within an energy window highly influenced by the moiré potential.

We focus here on studying the exemplary case of the  $\text{MoSe}_2\text{-WSe}_2$  heterostructure, where, as seen previously, the interlayer KK state is the most energetically favorable. The starting point is to calculate the energy band structure of the system, relying on equation 2.50. Solving the eigenvalue problem, in the small twist angle limit ( $\simeq 1^\circ$ , we can observe that the moiré potential highly modifies the band topology. At these small twist angles, the bands not only acquire a new periodicity, defined by the mini-Brillouin zone (mBZ), but also undergo deformation, becoming flat [95]. From previous works, the emergence of flat bands in the energy structure is related to strongly trapped states, characterized by strongly localized wavefunctions around minima of the moiré potential [55] (flat bound states  $X_{0,1,2,3}$ ), and free states ( $X_{free}$ ) which show a more delocalized wavefunction [55]. Our goal now is to excite the system to a relatively low energy near to the ground state and observe the modifications brought by the presence of flat bands in the exciton thermalization. Therefore, we initialize an exciton population at  $\simeq 40\text{-}50$  meV from the ground state, and numerically solve equation 2.56, using the beyond-second order Born-Markov approach corrections for the dephasing (2.9). Our study focuses on the

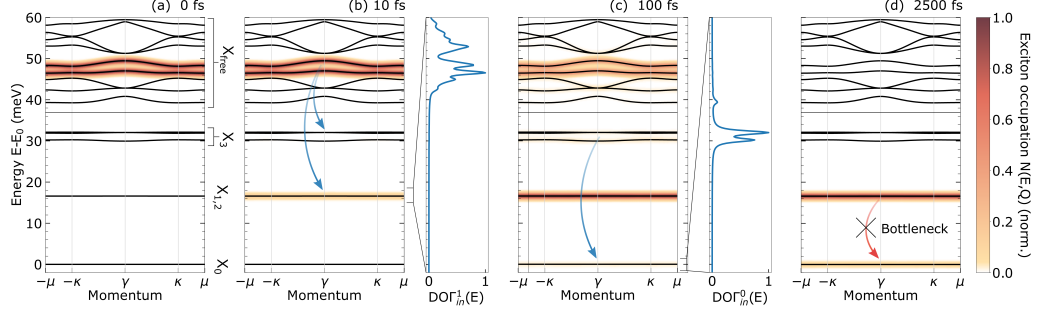


Figure 5.2: Interlayer exciton energy landscape of the MoSe<sub>2</sub>-WSe<sub>2</sub> heterostructure (with a 1° twist angle) consisting of bound states ( $X_{0,1,2}$ ), intermediate states ( $X_3$ ), and free states ( $X_{free}$ ), plotted with respect to the ground state ( $E_0$ ). Superimposed on the bands, the energy- and momentum-resolved exciton occupation (red-orange shaded) at subsequent steps of the dynamics at 40 K: (a) at 0 fs an initial hot distribution of excitons. (b) At an early stage of the dynamics (10 fs), the emission of optical phonon drives the population predominantly to the first degenerate excited states  $X_{1,2}$ . (c)  $X_0$  is occurring at a much slower speed, driven by the filling of intermediate states  $X_3$  due to the scattering with acoustic phonons (100 fs). This different energy dependence, becomes clear by analyzing the density of in-scattering states  $DO\Gamma_{in}^n(E)$  (normalized) for  $X_0$  and  $X_{1,2}$ . (d) In the final stage of the dynamics on the timescale of a few ps, we observe a bottleneck effect. This results in a strong out-of-equilibrium exciton distribution, where excited states show a higher occupation than the ground state. Picture taken from Paper 5.

temporal evolution of excitons for the system in the low temperature regime ( $\simeq 40$  K).

The result of the dynamics is very different from the usual relaxation as can be seen from figure 5.2, where we plot the band structure with the excitonic density  $N(E, \mathbf{Q})$  superimposed as a function of time and energy at different time frames. In panel (a), we highlight the initial excitation condition. The subsequent thermalization of moiré excitons can be described in terms of two competing processes, driven by emission of optical and acoustic phonons, respectively. Scattering with acoustic phonons, characterized by a small transfer of energy and momentum, populates the adjacent energy bands, i.e. the intermediate states  $X_3$ . The scattering with optical phonons makes excitons dissipate faster and relax further down to the first excited states  $X_{1,2}$ , cf. the arrows in Fig. 5.2(b). In order to understand the next step, we utilize the density of in-scattering states 2.57, with which we calculate the states contributing the most to the incoming flux for the ground state and the first excited states, as shown alongside panels (b) and (c). From the analysis of these graphs, we can observe that the excitonic population at intermediate energies  $X_3$  contributes more to filling the ground state, while energies within the range of free states contribute more to filling the first excited states ( $X_{1,2}$ ). Figure 5.2(d) shows that, even for longer times of a few ps, the occupation of the ground state remains clearly lower than the one of the first excited states - in contrast to what we would expect from a thermalized distribution. This indicates the emergence of a pronounced relaxation bottleneck that keeps the exciton occupation out of thermal equilibrium.

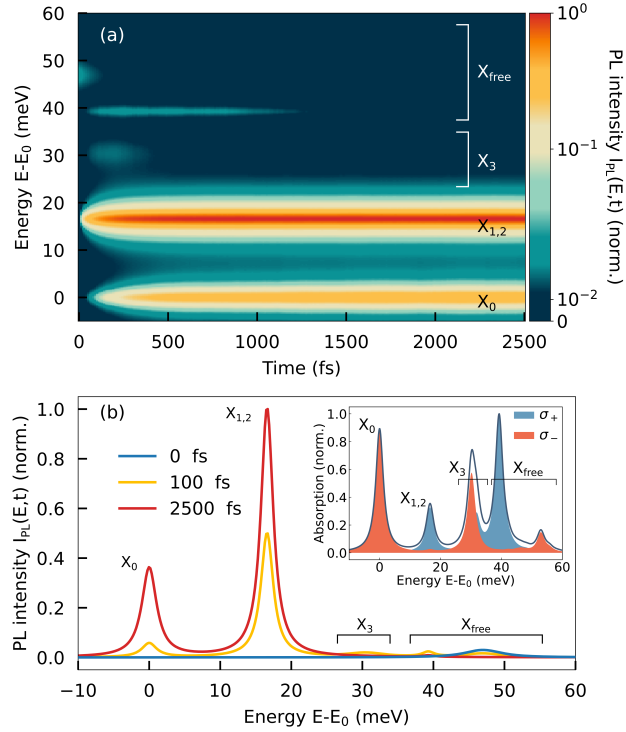


Figure 5.3: (a) Photoluminescence spectrum as a function of energy and time and (b) at different fixed time cuts. We include the absorption spectrum as inset in (b) to highlight the optical selection rules of different states. Here, the solid grey line shows the total absorption, while red and blue lines denote the contribution of the  $\sigma_-$  and  $\sigma_+$  circularly polarized light, respectively. Picture taken from Paper 5.

## 5.2 Time resolved photoluminescence

The much higher occupation of the first excited states is affecting also the optical response of this states. If we compute the photoluminescence spectrum for the process under study (figure 5.3), we can see in the energy-time map of the signal 5.3(a), that after the initial fast relaxation, leading most of the population into  $X_{1,2}$ , the dynamics result in being stacked, with brighter response on first excited states when comparing with the ground state. To contextualize better, the PL intensity depends on the exciton occupation in a certain state weighted by its optical matrix element. The latter describes the oscillator strength of the states and can be directly accessed in a linear absorption spectrum (cf. the inset 5.3(b)). Looking at the selection rules expressed through the absorption spectrum, a higher PL peak of  $X_{1,2}$  means that its occupation has to be significantly larger than the one of  $X_0$ , which is only the case for a highly non-equilibrium exciton distribution emerging as a consequence of a pronounced relaxation bottleneck. This results in clear agreement with the experimental observations of long living excited states and brighter response of excited states.

### 5.3 Characteristic relaxation time

In order to characterize in more details the bottleneck effect, we conduct a temperature dependent study. A suitable quantity to track the emergence of the bottleneck is the relaxation time from the first excited states to the ground state,  $\tau_{1 \rightarrow 0} = 1/\Gamma_{1 \rightarrow 0}$ , where  $\Gamma_{1 \rightarrow 0}$  is the out-scattering from state  $X_1$  to  $X_0$ . As first step, we compare in figure 5.4 (a-b) the momentum-integrated time-dependent exciton occupation at 40 K and 300 K. The two dynamics are of course different, but the key point we can observe is that while at 40 K the occupation is far away from the Boltzmann distribution (the occupation should be almost entirely in the ground state), at 300 K the relaxation reaches a Boltzmann-like equilibrium, showed in the picture by blue and orange solid lines reaching the dashed lines. This hints to the presence of a temperature dependent activation of the bottleneck effect. Plotting  $\tau_{1 \rightarrow 0}$  as a function of temperature shows that our initial guess is correct, with  $\tau_{1 \rightarrow 0}$  varying of several order of magnitude from the low to the high temperature regime, with temperature lower than 100 K slowed down, resulting in an extremely large relaxation time being on a timescale comparable or even longer than the recombination time of interlayer excitons of typically  $\simeq 10^2 - 10^3$  ps [46]. In the inset of figure 5.4(b) we show the out-scattering rate from  $\Gamma_{1 \rightarrow 0}^{out}$  (that is the inverse of  $\tau_{1 \rightarrow 0}$ ), separating the two acoustic and optical phonon contributions. To explain the predominant role of optical phonons we can use an energy and center-of-mass momentum argument. The conservation of energy contained in equation 2.58, reading  $\Delta_{\mathbf{Q}\mathbf{Q}'}^{\eta\xi\pm} = E_{\mathbf{Q}'}^{\xi} - E_{\mathbf{Q}}^{\eta} \pm \Omega_{j\mathbf{Q}'-\mathbf{Q}}$ , in combination with the flatness of the bands, imposes a strong boundary to the available scattering partners for this transition. Given the excitonic flat dispersion for both the initial ( $X_{1,2}$ ) and the final state ( $X_0$ ), the energy conservation plays the key role. The energy difference between  $X_{1,2}$  and  $X_0$  is  $\simeq 16$  meV. Acoustic phonons with their linear dispersion, would require a huge momentum transfer to be able to dissipate this amount of energy. The momentum required is larger than 10 moiré Brillouin zones, where the exciton-phonon matrix element becomes negligibly small, as the overlap of the moiré exciton wavefunctions of the involved states is mostly localized in the first and second mBZ, as seen in Figure 2.7 [55]. In contrast, optical phonons exhibit an energy of  $\simeq 20 - 25$  meV that is closer to the energy condition required for the transition. The activation of this channel is then explained in terms of the temperature-dependent broadening of the phonon-induced dephasing.

### 5.4 Real space equilibrium distribution

The moiré exciton relaxation dynamics discussed so far in the momentum space, can be also tracked in the real space. Focusing in particular on the final equilibrium distribution, we can observe how the greater occupation of first excited states impact the space distribution of excitons. To understand this statement, we have to focus on the moiré excitons wavefunction. The ground state  $X_0$  is characterized by an s-type wave function, whereas the excited states  $X_{1,2}$  are described by p-type wave functions [55]. In the absence of bottleneck, the relaxation dynamics starts with free states, characterized by a spatially delocalized wavefunction, bringing the population to relax into a localized equilibrium distribution in

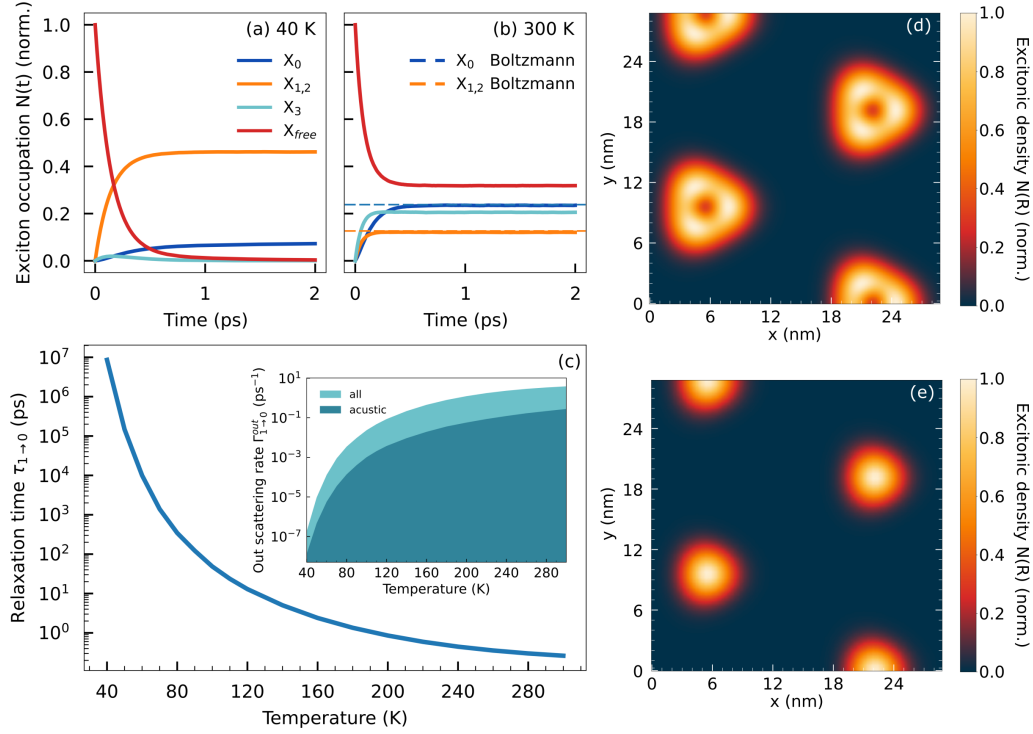


Figure 5.4: Momentum-integrated exciton dynamics at (a) 40 K and (b) 300 K. At low temperatures, we observe a much larger stationary occupation of the first excited states  $X_{1,2}$ , highlighting the importance of the relaxation bottleneck leading to a strong deviation from a thermal distribution. In contrast, at higher temperatures, the exciton occupation clearly relaxes into a Boltzmann distribution (dashed lines). (c) The relaxation time  $\tau_{1 \rightarrow 0}$  from the first excited state to the ground state as function of temperature, showing that the bottleneck effect becomes significantly strong at temperatures smaller than approximately 100 K leading to recombination times in ns or even  $\mu$ s range. In the inset, we plot the out-scattering rate  $\Gamma_{1 \rightarrow 0}^{\text{out}}$  (inverse of  $\tau_{1 \rightarrow 0}$ ), identifying the different contributions of acoustic and optical phonons. (d,e) Equilibrium moiré exciton distribution in real space, highlighting the different situation in the case of (d) highly occupied excited states with a p-type orbital character and (e) highly occupied ground state with an s-type orbital character. Picture taken from Paper 5.

the ground state with a threefold s-type orbital that is maximally centered at each moiré potential minimum (5.4 (d)). In presence of a pronounced bottleneck instead, one has an equilibrium distribution with excitons occupying both the ground state and excited states. Translated in real space, this results in a mixture of s-type and p-type orbitals around the moiré traps (5.4 (e)). As p-type states are characterized by a broader excitonic wavefunction than their s-type counterpart, one finds a larger excitonic wavefunction overlap between different spatial traps, resulting in an increase of the tunneling probability.

## 5.5. INITIAL CONDITIONS

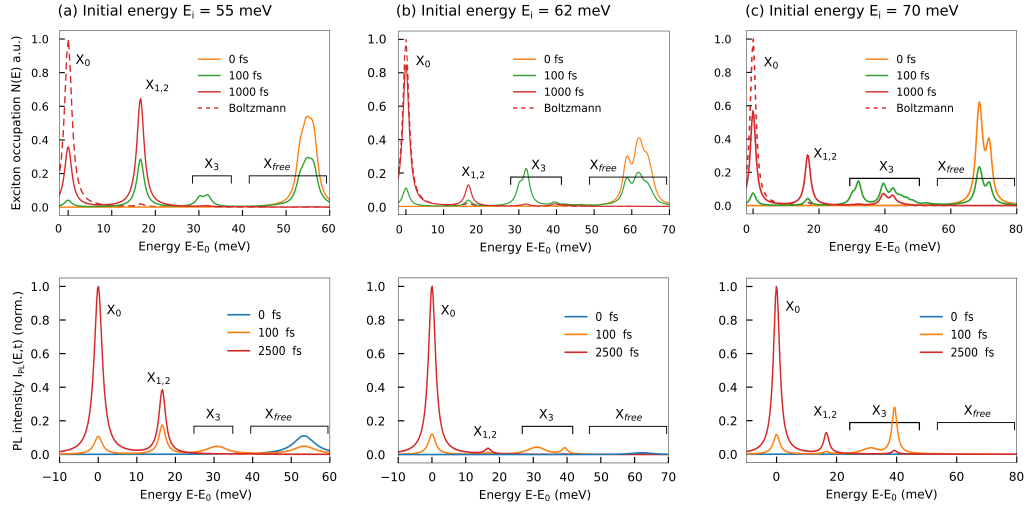


Figure 5.5: Study of the moiré exciton dynamics at 40 K for different initial conditions. We initialize the system with a uniform energy distribution of excitons centered at (a)  $E_i = 55$  meV, (b)  $E_i = 62$  meV and (c)  $E_i = 70$  meV. In the top row we show energy-resolved and momentum-integrated exciton occupation at different time cuts with the red dashed line corresponding to the Boltzmann distribution. In the bottom row, we show photoluminescence spectra as a function of energy at different fixed time cuts. Picture taken from Paper SI 5.

## 5.5 Initial conditions

As final analysis is important to discuss the importance of initial conditions for our simulations. Looking again at DOF, we see that the quantity is not uniform in energy, meaning that different close in energy initial conditions, can lead to very different outcomes. Although this is true for the specific ratio of exciton population in  $X_0$  and  $X_{1,2}$ , the main message of our study remains unchanged, i.e. the equilibrium distribution is deviating from a Boltzmann distribution due to the bottleneck effect. In order to verify this statement, we perform a study varying the energy initial conditions, reporting the results in Figure 5.5. Here we plot on the first row the momentum-integrated energy-resolved exciton occupation, while on the second row the PL spectra. Moving from an initial condition of 55 (a), to 62 (b) to 70 (c) meV, we see that although the relative intensity of the peaks changes there is a common pattern. Focusing on the upper row, comparing the equilibrium distribution (red line) with the Boltzmann distribution (red dashed line), all the initial conditions bring to a deviation from the usual thermal equilibrium described by the Boltzmann distribution. The specific ratio of occupation, influencing the final optical PL response of the system is strongly initial condition dependent, since the amount and the predominant scattering channels are varying across the energy landscape.

## 5.6 Large twist angle limit

To complete our analysis we provide a additional study investigating the opposite limit we investigated, i.e. the large twist angle limit ( $3^\circ$ ). We show the results of this study in Figure 5.6. As can be seen from panel (a) we choose an initial condition comparable to the case of small twist angle. We can see that the energy band structure, still resents of the moiré potential presenting a non trivial band topology. Comparing panel (b) and (c), where we plot the momentum integrate moiré exciton occupation as function of time for 40 and 300 K, we can observe that the presence of the bottleneck effect at 40 K results softened allowing a slow exchange of excitons between the two lowest energy states. This can be much better observed and quantitatively appreciated by comparing the relaxation time  $\tau_{1 \rightarrow 0}$  for  $1^\circ$  and  $3^\circ$  (respectively line blue and red in 5.6 (d)). The largest difference in the relaxation time is found at low temperatures. The slowed-down relaxation process at  $1^\circ$  can be traced back to flat exciton bands and the restricted scattering efficiency due to the energy conservation. This is pronounced, in particular, at low temperatures, where the broadening of states is small and thus a strict energy conservation needs to be fulfilled. The effect is much less pronounced at  $3^\circ$  exhibiting parabolic bands, where the number of possible scattering partners is much higher than in the case of flat bands at  $1^\circ$ . As the temperature increases the relaxation time at both twist angles starts to merge leading to a comparable relaxation time at room temperature. Overall, we can conclude that the key ingredient for the emergence of the relaxation bottleneck is the peculiar flat bandstructure of moiré excitons.

To summarize, in this study, we have investigated the relaxation dynamics of interlayer excitons in a twisted MoSe<sub>2</sub>-WSe<sub>2</sub> heterostructure exhibiting flat moiré bands. Using the microscopic model introduced in Chapter 2, we demonstrate the relaxation cascade of an initial hot distribution of interlayer excitons and identify a pronounced relaxation bottleneck at low temperatures and low twist angles. This results in quasi-stationary exciton occupations far away from the Boltzmann distribution. As a direct consequence the higher occupation of excited exciton states explains their larger emission compared to the ground state, explaining the experimental observations in photoluminescence spectra of twisted TMD heterostructures. Furthermore, we studied the temperature-dependent activation of the relaxation bottleneck, identifying its microscopic origin to a combination of the energy separation and the flatness of the involved moiré exciton sub-bands.

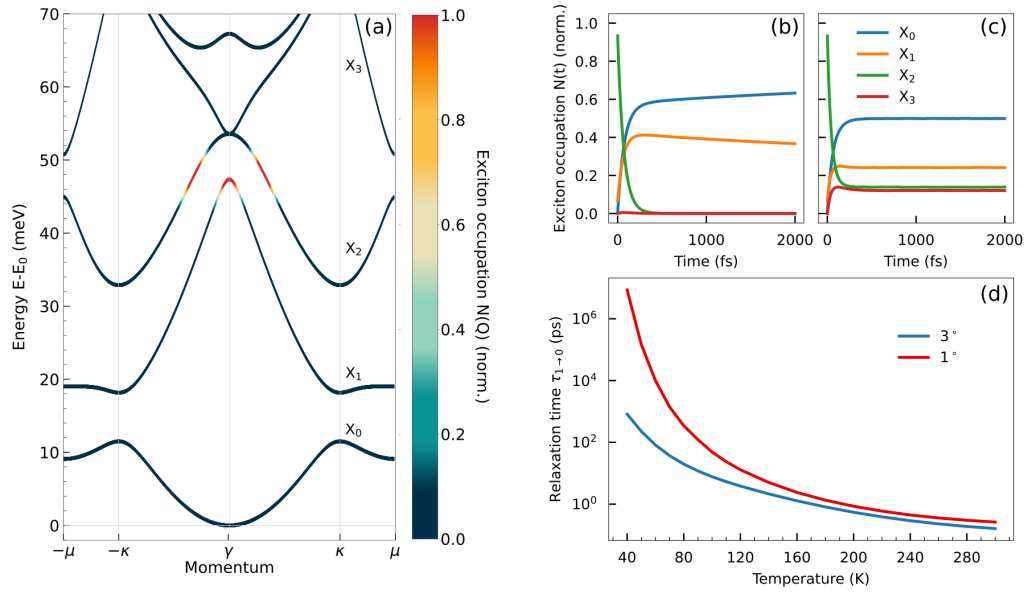


Figure 5.6: Relaxation dynamics at the larger twist angle of  $3^\circ$ . (a) Moiré exciton band structure, where the initial momentum-dependent occupation is highlighted with a color scheme. We plot the momentum-integrated and time-dependent exciton occupation for each band relevant for the relaxation process at (b) 40 K and (c) 300 K. (d) Direct comparison of the temperature-dependent relaxation time at  $1^\circ$  and  $3^\circ$  showing that the  $X_1 \rightarrow X_0$  transition is slow even for  $3^\circ$ , but still several orders of magnitude faster than at  $1^\circ$ , where the flat bands strongly restrict the number of possible scattering states. Picture taken from SI Paper 5.



---

## Conclusions

---

In conclusion, our work represents a significant advancement in the theoretical framework for studying optical excitations in heterostructures consisting of vertically stacked transition metal dichalcogenides (TMDs). We have introduced novel theoretical tools and expanded our microscopic model to account for hybrid exciton states, crucial for investigating charge transfer and exciton thermalization processes in these materials. In joint theory-experiment collaborations with our colleagues from Göttingen, we have shed light on hybrid exciton dynamics and their optical signatures as well as tracked the relaxation path of moire excitons in twisted TMD heterostructures.

We summarize here the key insights of our research:

- We provided a microscopic explanation for the experimentally observed ultrafast charge transfer mechanism. Investigating the  $\text{MoSe}_2\text{-WSe}_2$  and  $\text{MoS}_2\text{-WS}_2$  heterostructures, we characterize the process and predict it in terms of a two-step phonon-mediated process via momentum-dark hybrid states. This process has been further characterized through a temperature- and stacking-dependent study.
- We explored and explained different timescales of electron and hole transfer mechanisms in the  $\text{WSe}_2\text{-MoS}_2$  heterostructure. We uncovered a surprising gain in energy for the photo-emitted electron during a hole transfer process and traced it back to the correlation between the measured ejected electron and the remaining hole.
- We developed equations to describe the ARPES signal for hybrid excitons and applied this tool to a  $\text{MoS}_2\text{-MoS}_2$  homobilayer. Our findings indicate that the characteristic signature of hybrid excitons manifests as a double-peak signal, arising from the strong correlation between the electron and a hole in a superposition of the two layers.
- We investigated the relaxation cascade of hot interlayer excitons in a twisted TMD heterostructure. We identified a pronounced relaxation bottleneck at low tempera-

---

tures and in the small twist angle regime, resulting in highly non-thermal exciton distribution. This explains the experimental observations of long-lived excited states with bright emission in PL spectra.

Our research contributes significantly to a better microscopic understanding of charge transfer, exciton optics, and relaxation dynamics in TMD heterostructures. Future research is needed to spatially track deformations, changes in dielectric constants, and layer distances that can be correlated with exciton dynamics and relaxation timescales. Furthermore, the presence of twist angle dependent lattice reconstructions, the tunability of strained heterostructures, and strongly correlated states, such as generalized Wigner crystals and Mott insulators represent further fascinating aspects to investigate in this fascinating material system. Our work and the presented theoretical framework lay the foundation for further advancements in the field of atomically thin semiconductors.

---

# Acknowledgements

---

During these years of doctoral studies, I have encountered numerous wonderful individuals who welcomed me and made me feel like part of a family. I believe it is time to express my gratitude.

First and foremost, I would like to thank my supervisor, Ermin Malic, firstly for the opportunity he offered me by selecting me as a Ph.D. candidate. I want to express my thanks for his constant support and assistance, which have always motivated and guided me during my research. Your expertise and passion always encouraged me. Thanks for your unwavering support, motivation and always honest feedback.

I would also like to thank my second referee Prof. Dr. Florian Gebhard and examiners Prof. Dr. Stefan Wippermann and Prof. Dr. Stefan Mathias for their patience in reading my thesis and for reviewing my work.

I would also like to extend my gratitude to Samuel Brem and Lea Käbitz. Samuel, thank you for your guidance and colossal support in the professional environment. Thanks for being a reference point in the research journey. I want to thank both Samuel and Lea, who have become dear friends over these years. Thanks for the wonderful evenings and the moments spent together that lightened and made my stay in Marburg unforgettable. I want to thank Willy Knorr, my reliable space adventures companion and office mate. Our days in the office always seemed to fly by, thanks to our conversations about Lord of the Rings, One piece and videogames. Not to mention introducing me to the world of Crossfit! My thanks to Joshua Thompson for his support, friendship, and always-ready humor. I want to express gratitude to all the members of the Ultrafast Quantum Dynamics group in general, for the enjoyable moments together and the support. Countless were the occasions for discussion that pushed me to continually improve and learn (thanks also for the Beyblade tournaments). I want to thank my girlfriend, Silvia De Gobbi. Despite the distance and challenges, you have always made me feel loved, encouraging me to give my best, being there in both the good and bad days. Finally, I want to express my gratitude to my family, who has always been present, motivating me and always caring for me. Without them, I wouldn't have been able to reach this milestone.



---

# Bibliography

---

- [1] Kostya S Novoselov, Andre K Geim, Sergei V Morozov, De-eng Jiang, Yanshui Zhang, Sergey V Dubonos, Irina V Grigorieva, and Alexandr A Firsov. Electric field effect in atomically thin carbon films. *science*, 306(5696):666–669, 2004.
- [2] Kostya S Novoselov, Da Jiang, F Schedin, TJ Booth, VV Khotkevich, SV Morozov, and Andre K Geim. Two-dimensional atomic crystals. *Proceedings of the National Academy of Sciences*, 102(30):10451–10453, 2005.
- [3] Phaedon Avouris. Graphene: electronic and photonic properties and devices. *Nano letters*, 10(11):4285–4294, 2010.
- [4] Francesco Bonaccorso, Zhipei Sun, Tawfique Hasan, and AC Ferrari. Graphene photonics and optoelectronics. *Nature photonics*, 4(9):611–622, 2010.
- [5] Sajedeh Manzeli, Dmitry Ovchinnikov, Diego Pasquier, Oleg V Yazyev, and Andras Kis. 2d transition metal dichalcogenides. *Nature Reviews Materials*, 2(8):1–15, 2017.
- [6] Ruben Mas-Balleste, Cristina Gomez-Navarro, Julio Gomez-Herrero, and Felix Zamora. 2d materials: to graphene and beyond. *Nanoscale*, 3(1):20–30, 2011.
- [7] Sheneve Z Butler, Shawna M Hollen, Linyou Cao, Yi Cui, Jay A Gupta, Humberto R Gutiérrez, Tony F Heinz, Seung Sae Hong, Jiaying Huang, Ariel F Ismach, et al. Progress, challenges, and opportunities in two-dimensional materials beyond graphene. *ACS nano*, 7(4):2898–2926, 2013.
- [8] Andreas Pospischil and Thomas Mueller. Optoelectronic devices based on atomically thin transition metal dichalcogenides. *Applied Sciences*, 6(3):78, 2016.
- [9] Heather M Hill, Albert F Rigosi, Cyrielle Roquelet, Alexey Chernikov, Timothy C Berkelbach, David R Reichman, Mark S Hybertsen, Louis E Brus, and Tony F Heinz. Observation of excitonic rydberg states in monolayer mos2 and ws2 by photoluminescence excitation spectroscopy. *Nano letters*, 15(5):2992–2997, 2015.
- [10] Kin Fai Mak and Jie Shan. Photonics and optoelectronics of 2d semiconductor transition metal dichalcogenides. *Nature Photonics*, 10(4):216–226, 2016.

- [11] Thomas Mueller and Ermin Malic. Exciton physics and device application of two-dimensional transition metal dichalcogenide semiconductors. *npj 2D Materials and Applications*, 2(1):29, 2018.
- [12] Gang Wang, Alexey Chernikov, Mikhail M Glazov, Tony F Heinz, Xavier Marie, Thierry Amand, and Bernhard Urbaszek. Colloquium: Excitons in atomically thin transition metal dichalcogenides. *Reviews of Modern Physics*, 90(2):021001, 2018.
- [13] Keliang He, Nardeep Kumar, Liang Zhao, Zefang Wang, Kin Fai Mak, Hui Zhao, and Jie Shan. Tightly bound excitons in monolayer wse 2. *Physical review letters*, 113(2):026803, 2014.
- [14] Raul Perea-Causin, Daniel Erkensten, Jamie M Fitzgerald, Joshua JP Thompson, Roberto Rosati, Samuel Brem, and Ermin Malic. Exciton optics, dynamics, and transport in atomically thin semiconductors. *APL Materials*, 10(10), 2022.
- [15] Qing Hua Wang, Kourosch Kalantar-Zadeh, Andras Kis, Jonathan N Coleman, and Michael S Strano. Electronics and optoelectronics of two-dimensional transition metal dichalcogenides. *Nature nanotechnology*, 7(11):699–712, 2012.
- [16] Branimir Radisavljevic, Aleksandra Radenovic, Jacopo Brivio, Valentina Giacometti, and Andras Kis. Single-layer mos2 transistors. *Nature nanotechnology*, 6(3):147–150, 2011.
- [17] Oriol Lopez-Sanchez, Dominik Lembke, Metin Kayci, Aleksandra Radenovic, and Andras Kis. Ultrasensitive photodetectors based on monolayer mos2. *Nature nanotechnology*, 8(7):497–501, 2013.
- [18] A Steinhoff, J-H Kim, F Jahnke, M Rosner, D-S Kim, Ch Lee, Gang Hee Han, Mun Seok Jeong, TO Wehling, and C Gies. Efficient excitonic photoluminescence in direct and indirect band gap monolayer mos2. *Nano letters*, 15(10):6841–6847, 2015.
- [19] Swastibrata Bhattacharyya and Abhishek K Singh. Semiconductor-metal transition in semiconducting bilayer sheets of transition-metal dichalcogenides. *Physical Review B*, 86(7):075454, 2012.
- [20] Andre K Geim and Irina V Grigorieva. Van der waals heterostructures. *Nature*, 499(7459):419–425, 2013.
- [21] Ashwin Ramasubramaniam, Doron Naveh, and Elias Towe. Tunable band gaps in bilayer transition-metal dichalcogenides. *Physical Review B*, 84(20):205325, 2011.
- [22] Hannu-Pekka Komsa and Arkady V Krasheninnikov. Electronic structures and optical properties of realistic transition metal dichalcogenide heterostructures from first principles. *Physical Review B*, 88(8):085318, 2013.
- [23] Pasqual Rivera, John R Schaibley, Aaron M Jones, Jason S Ross, Sanfeng Wu, Grant Aivazian, Philip Klement, Kyle Seyler, Genevieve Clark, Nirmal J Ghimire, et al. Observation of long-lived interlayer excitons in monolayer MoSe<sub>2</sub>–WSe<sub>2</sub> heterostructures. *Nature Communications*, 6(1):1–6, 2015.

- [24] Bastian Miller, Alexander Steinhoff, Borja Pano, Julian Klein, Frank Jahnke, Alexander Holleitner, and Ursula Wurstbauer. Long-lived direct and indirect interlayer excitons in van der waals heterostructures. *Nano Letters*, 17(9):5229–5237, 2017.
- [25] Jens Kunstmann, Fabian Mooshammer, Philipp Nagler, Andrey Chaves, Frederick Stein, Nicola Paradiso, Gerd Plechinger, Christoph Strunk, Christian Schüller, Gotthard Seifert, et al. Momentum-space indirect interlayer excitons in transition-metal dichalcogenide van der waals heterostructures. *Nature Physics*, 14(8):801–805, 2018.
- [26] Chenhao Jin, Emma C Regan, Aiming Yan, M Iqbal Bakti Utama, Danqing Wang, Sihan Zhao, Ying Qin, Sijie Yang, Zhiren Zheng, Shenyang Shi, et al. Observation of moiré excitons in  $WSe_2/WS_2$  heterostructure superlattices. *Nature*, 567(7746):76–80, 2019.
- [27] Kha Tran, Galan Moody, Fengcheng Wu, Xiaobo Lu, Junho Choi, Kyoungwan Kim, Amritesh Rai, Daniel A Sanchez, Jiamin Quan, Akshay Singh, et al. Evidence for moiré excitons in van der waals heterostructures. *Nature*, 567(7746):71–75, 2019.
- [28] Kyle L Seyler, Pasqual Rivera, Hongyi Yu, Nathan P Wilson, Essance L Ray, David G Mandrus, Jiaqiang Yan, Wang Yao, and Xiaodong Xu. Signatures of moiré-trapped valley excitons in  $MoSe_2/WSe_2$  heterobilayers. *Nature*, 567(7746):66–70, 2019.
- [29] Evgeny M Alexeev, David A Ruiz-Tijerina, Mark Danovich, Matthew J Hamer, Daniel J Terry, Pramoda K Nayak, Seongjoon Ahn, Sangyeon Pak, Juwon Lee, Jung Inn Sohn, et al. Resonantly hybridized excitons in moiré superlattices in van der waals heterostructures. *Nature*, 567(7746):81–86, 2019.
- [30] David A Ruiz-Tijerina and Vladimir I Fal’ko. Interlayer hybridization and moiré superlattice minibands for electrons and excitons in heterobilayers of transition-metal dichalcogenides. *Physical Review B*, 99(12):125424, 2019.
- [31] Lukas Sigl, Mirco Troue, Manuel Katzer, Malte Selig, Florian Sigger, Jonas Kiemle, Mauro Brotons-Gisbert, Kenji Watanabe, Takashi Taniguchi, Brian D Gerardot, et al. Optical dipole orientation of interlayer excitons in  $MoSe_2/WS_2$  heterostacks. *Physical Review B*, 105(3):035417, 2022.
- [32] Johannes Holler, Malte Selig, Michael Kempf, Jonas Zipfel, Philipp Nagler, Manuel Katzer, Florian Katsch, Mariana V Ballottin, Anatolie A Mitroglu, Alexey Chernikov, et al. Interlayer exciton valley polarization dynamics in large magnetic fields. *Physical Review B*, 105(8):085303, 2022.
- [33] Rafi Bistritzer and Allan H MacDonald. Moiré bands in twisted double-layer graphene. *Proceedings of the National Academy of Sciences*, 108(30):12233–12237, 2011.
- [34] Lei Wang, En-Min Shih, Augusto Ghiotto, Lede Xian, Daniel A Rhodes, Cheng Tan, Martin Claassen, Dante M Kennes, Yusong Bai, Bumho Kim, et al. Correlated electronic phases in twisted bilayer transition metal dichalcogenides. *Nature materials*, 19(8):861–866, 2020.

- [35] Yuan Cao, Valla Fatemi, Shiang Fang, Kenji Watanabe, Takashi Taniguchi, Efthimios Kaxiras, and Pablo Jarillo-Herrero. Unconventional superconductivity in magic-angle graphene superlattices. *Nature*, 556(7699):43–50, 2018.
- [36] Yuxuan Lin, Xi Ling, Lili Yu, Shengxi Huang, Allen L Hsu, Yi-Hsien Lee, Jing Kong, Mildred S Dresselhaus, and Tomás Palacios. Dielectric screening of excitons and trions in single-layer mos2. *Nano letters*, 14(10):5569–5576, 2014.
- [37] Jason S Ross, Sanfeng Wu, Hongyi Yu, Nirmal J Ghimire, Aaron M Jones, Grant Aivazian, Jiaqiang Yan, David G Mandrus, Di Xiao, Wang Yao, et al. Electrical control of neutral and charged excitons in a monolayer semiconductor. *Nature communications*, 4(1):1474, 2013.
- [38] Iris Niehues, Robert Schmidt, Matthias Druppel, Philipp Marauhn, Dominik Christiansen, Malte Selig, Gunnar Berghäuser, Daniel Wigger, Robert Schneider, Lisa Braasch, et al. Strain control of exciton–phonon coupling in atomically thin semiconductors. *Nano letters*, 18(3):1751–1757, 2018.
- [39] M Goryca, Jing Li, Andreas V Stier, Takashi Taniguchi, Kenji Watanabe, Emmanuel Courtade, Shivangi Shree, Cedric Robert, Bernhard Urbaszek, Xavier Marie, et al. Revealing exciton masses and dielectric properties of monolayer semiconductors with high magnetic fields. *Nature communications*, 10(1):4172, 2019.
- [40] Daniel Erkensten, Samuel Brem, Raül Perea-Causín, Joakim Hagel, Fedele Tagarelli, Edoardo Lopriore, Andras Kis, and Ermin Malic. Electrically tunable dipolar interactions between layer-hybridized excitons. *Nanoscale*, 2023.
- [41] Fedele Tagarelli, Edoardo Lopriore, Daniel Erkensten, Raül Perea-Causín, Samuel Brem, Joakim Hagel, Zhe Sun, Gabriele Pasquale, Kenji Watanabe, Takashi Taniguchi, et al. Electrical control of hybrid exciton transport in a van der waals heterostructure. *Nature Photonics*, pages 1–7, 2023.
- [42] Ermin Malic, Raül Perea-Causin, Roberto Rosati, Daniel Erkensten, and Samuel Brem. Exciton transport in atomically thin semiconductors. *nature communications*, 14(1):3430, 2023.
- [43] Junho Choi, Matthias Florian, Alexander Steinhoff, Daniel Erben, Kha Tran, Dong Seob Kim, Liuyang Sun, Jiamin Quan, Robert Claassen, Somak Majumder, et al. Twist angle-dependent interlayer exciton lifetimes in van der waals heterostructures. *Physical Review Letters*, 126(4):047401, 2021.
- [44] Trithep Devakul, Valentin Crépel, Yang Zhang, and Liang Fu. Magic in twisted transition metal dichalcogenide bilayers. *Nature communications*, 12(1):6730, 2021.
- [45] Pramoda K Nayak, Yevhen Horbatenko, Seongjoon Ahn, Gwangwoo Kim, Jae-Ung Lee, Kyung Yeol Ma, A-Rang Jang, Hyunseob Lim, Dogyeong Kim, Sunmin Ryu, et al. Probing evolution of twist-angle-dependent interlayer excitons in mose2/wse2 van der waals heterostructures. *ACS nano*, 11(4):4041–4050, 2017.

- [46] Ying Jiang, Shula Chen, Weihao Zheng, Biyuan Zheng, and Anlian Pan. Interlayer exciton formation, relaxation, and transport in tmd van der waals heterostructures. *Light: Science & Applications*, 10(1):72, 2021.
- [47] Heather M Hill, Albert F Rigosi, Kwang Taeg Rim, George W Flynn, and Tony F Heinz. Band alignment in mos2/ws2 transition metal dichalcogenide heterostructures probed by scanning tunneling microscopy and spectroscopy. *Nano letters*, 16(8):4831–4837, 2016.
- [48] V Ongun Özcelik, Javad G Azadani, Ce Yang, Steven J Koester, and Tony Low. Band alignment of two-dimensional semiconductors for designing heterostructures with momentum space matching. *Physical Review B*, 94(3):035125, 2016.
- [49] Xiaoping Hong, Jonghwan Kim, Su-Fei Shi, Yu Zhang, Chenhao Jin, Yinghui Sun, Sefaattin Tongay, Junqiao Wu, Yanfeng Zhang, and Feng Wang. Ultrafast charge transfer in atomically thin mos2/ws2 heterostructures. *Nature nanotechnology*, 9(9):682–686, 2014.
- [50] Frank Ceballos, Matthew Z Bellus, Hsin-Ying Chiu, and Hui Zhao. Ultrafast charge separation and indirect exciton formation in a mos2–mose2 van der waals heterostructure. *ACS nano*, 8(12):12717–12724, 2014.
- [51] Ziheng Ji, Hao Hong, Jin Zhang, Qi Zhang, Wei Huang, Ting Cao, Ruixi Qiao, Can Liu, Jing Liang, Chuanhong Jin, et al. Robust stacking-independent ultrafast charge transfer in mos2/ws2 bilayers. *ACS nano*, 11(12):12020–12026, 2017.
- [52] Philipp Merkl, Fabian Mooshammer, Philipp Steinleitner, Anna Girnghuber, K-Q Lin, Philipp Nagler, Johannes Holler, Christian Schüller, John M Lupton, Tobias Korn, et al. Ultrafast transition between exciton phases in van der waals heterostructures. *Nature Materials*, 18(7):691–696, 2019.
- [53] David Schmitt, Jan Philipp Bange, Wiebke Bennecke, AbdulAziz AlMutairi, Kenji Watanabe, Takashi Taniguchi, Daniel Steil, D Russell Luke, R Thomas Weitz, Sabine Steil, et al. Formation of moire interlayer excitons in space and time. *arXiv preprint arXiv:2112.05011*, 2021.
- [54] Thorsten Deilmann and Kristian Sommer Thygesen. Interlayer excitons with large optical amplitudes in layered van der waals materials. *Nano Letters*, 18:2984, 2018.
- [55] Samuel Brem, Christopher Linderälv, Paul Erhart, and Ermin Malic. Tunable phases of moiré excitons in van der waals heterostructures. *Nano letters*, 20(12):8534–8540, 2020.
- [56] Di Huang, Junho Choi, Chih-Kang Shih, and Xiaoqin Li. Excitons in semiconductor moiré superlattices. *Nature Nanotechnology*, 17(3):227–238, 2022.
- [57] Neil R Wilson, Paul V Nguyen, Kyle Seyler, Pasqual Rivera, Alexander J Marsden, Zachary PL Laker, Gabriel C Constantinescu, Viktor Kandyba, Alexei Barinov,

- Nicholas DM Hine, et al. Determination of band offsets, hybridization, and exciton binding in 2d semiconductor heterostructures. *Science advances*, 3(2):e1601832, 2017.
- [58] Dominik Christiansen, Malte Selig, Ermin Malic, Ralph Ernstorfer, and Andreas Knorr. Theory of exciton dynamics in time-resolved arpes: Intra-and intervalley scattering in two-dimensional semiconductors. *Physical Review B*, 100(20):205401, 2019.
- [59] Julien Madéo, Michael KL Man, Chakradhar Sahoo, Marshall Campbell, Vivek Pareek, E Laine Wong, Abdullah Al-Mahboob, Nicholas S Chan, Arka Karmakar, Bala Murali Krishna Mariserla, et al. Directly visualizing the momentum-forbidden dark excitons and their dynamics in atomically thin semiconductors. *Science*, 370(6521):1199–1204, 2020.
- [60] David Schmitt, Jan Philipp Bange, Wiebke Bennecke, AbdulAziz AlMutairi, Giuseppe Meneghini, Kenji Watanabe, Takashi Taniguchi, Daniel Steil, D Russell Luke, R Thomas Weitz, et al. Formation of moiré interlayer excitons in space and time. *Nature*, 608(7923):499–503, 2022.
- [61] Gerald D Mahan. *Many-particle physics*. Springer Science & Business Media, 2000.
- [62] Alexander L Fetter and John Dirk Walecka. *Quantum theory of many-particle systems*. Courier Corporation, 2012.
- [63] Ermin Malic and Andreas Knorr. *Graphene and carbon nanotubes: ultrafast optics and relaxation dynamics*. John Wiley & Sons, 2013.
- [64] Hartmut Haug and Stephan W Koch. *Quantum theory of the optical and electronic properties of semiconductors*. World Scientific Publishing Company, 2009.
- [65] Mackillo Kira and Stephan W Koch. *Semiconductor quantum optics*. Cambridge University Press, 2011.
- [66] Fábio Ferreira, SJ Magorrian, VV Enaldiev, DA Ruiz-Tijerina, and VI Fal'ko. Band energy landscapes in twisted homobilayers of transition metal dichalcogenides. *Applied Physics Letters*, 118(24):241602, 2021.
- [67] Paolo Giannozzi, Stefano De Gironcoli, Pasquale Pavone, and Stefano Baroni. Ab initio calculation of phonon dispersions in semiconductors. *Physical Review B*, 43(9):7231, 1991.
- [68] Alejandro Molina-Sanchez and Ludger Wirtz. Phonons in single-layer and few-layer mos 2 and ws 2. *Physical Review B*, 84(15):155413, 2011.
- [69] Jin Z, Li X, Mullen J T, and Kim K W. Intrinsic transport properties of electrons and holes in monolayer transition-metal dichalcogenides. *Phys. Rev. B*, 90:045422, 2014.

- [70] Natalia S Rytova. Screened potential of a point charge in a thin film. *arXiv preprint arXiv:1806.00976*, 2018.
- [71] LV Keldysh. Coulomb interaction in thin semiconductor and semimetal films. In *SELECTED PAPERS OF LEONID V KELDYSH*, pages 155–158. World Scientific, 2024.
- [72] Samuel Brem, Jonas Zipfel, Malte Selig, Archana Raja, Lutz Waldecker, Jonas D Ziegler, Takashi Taniguchi, Kenji Watanabe, Alexey Chernikov, and Ermin Malic. Intrinsic lifetime of higher excitonic states in tungsten diselenide monolayers. *Nanoscale*, 11(25):12381–12387, 2019.
- [73] Marlan O Scully and M Suhail Zubairy. Quantum optics, 1999.
- [74] M Lindberg and Stephan W Koch. Effective bloch equations for semiconductors. *Physical Review B*, 38(5):3342, 1988.
- [75] Mackillo Kira and Stephan W Koch. Many-body correlations and excitonic effects in semiconductor spectroscopy. *Progress in quantum electronics*, 30(5):155–296, 2006.
- [76] Hartmut Haug and Stefan Schmitt-Rink. Electron theory of the optical properties of laser-excited semiconductors. *Progress in Quantum Electronics*, 9(1):3–100, 1984.
- [77] Samuel Brem, Malte Selig, Gunnar Berghäuser, and Ermin Malic. Exciton relaxation cascade in two-dimensional transition metal dichalcogenides. *Scientific reports*, 8(1): 1–8, 2018.
- [78] Malte Selig, Gunnar Berghäuser, Marten Richter, Rudolf Bratschitsch, Andreas Knorr, and Ermin Malic. Dark and bright exciton formation, thermalization, and photoluminescence in monolayer transition metal dichalcogenides. *2D Materials*, 5(3):035017, 2018.
- [79] Joakim Hagel, Samuel Brem, Christopher Linderälv, Paul Erhart, and Ermin Malic. Exciton landscape in van der waals heterostructures. *Physical Review Research*, 3(4): 043217, 2021.
- [80] Samuel Brem, Kai-Qiang Lin, Roland Gillen, Jonas M Bauer, Janina Maultzsch, John M Lupton, and Ermin Malic. Hybridized intervalley moiré excitons and flat bands in twisted wse 2 bilayers. *Nanoscale*, 12(20):11088–11094, 2020.
- [81] Simon Ovesen, Samuel Brem, Christopher Linderälv, Mikael Kuisma, Tobias Korn, Paul Erhart, Malte Selig, and Ermin Malic. Interlayer exciton dynamics in van der waals heterostructures. *Communications Physics*, 2(1):1–8, 2019.
- [82] Alberto Ciarrocchi, Dmitrii Unuchek, Ahmet Avsar, Kenji Watanabe, Takashi Taniguchi, and Andras Kis. Polarization switching and electrical control of interlayer excitons in two-dimensional van der waals heterostructures. *Nature photonics*, 13(2): 131–136, 2019.

- [83] Zhe Sun, Alberto Ciarrocchi, Fedele Tagarelli, Juan Francisco Gonzalez Marin, Kenji Watanabe, Takashi Taniguchi, and Andras Kis. Excitonic transport driven by repulsive dipolar interaction in a van der waals heterostructure. *Nature Photonics*, 16(1):79–85, 2022.
- [84] Joakim Hagel, Samuel Brem, and Ermin Malic. Electrical tuning of moiré excitons in mose<sub>2</sub> bilayers. *arXiv preprint arXiv:2207.01890*, 2022. doi: 10.48550/arXiv.2207.01890.
- [85] Xiaobo Lu, Xiaoqin Li, and Li Yang. Modulated interlayer exciton properties in a two-dimensional moiré crystal. *Physical Review B*, 100(15):155416, 2019.
- [86] E Cappelluti, Rafael Roldán, JA Silva-Guillén, Pablo Ordejón, and F Guinea. Tight-binding model and direct-gap/indirect-gap transition in single-layer and multilayer mos<sub>2</sub>. *Physical Review B*, 88(7):075409, 2013.
- [87] Roland Gillen and Janina Maultzsch. Interlayer excitons in MoSe<sub>2</sub>/WSe<sub>2</sub> heterostructures from first principles. *Physical Review B*, 97(16):165306, 2018.
- [88] A Thränhardt, S Kuckenburger, A Knorr, T Meier, and SW Koch. Quantum theory of phonon-assisted exciton formation and luminescence in semiconductor quantum wells. *Physical Review B*, 62(4):2706, 2000.
- [89] Fausto Rossi and Tilmann Kuhn. Theory of ultrafast phenomena in photoexcited semiconductors. *Reviews of Modern Physics*, 74(3):895, 2002.
- [90] Andrea Damascelli, Zahid Hussain, and Zhi-Xun Shen. Angle-resolved photoemission studies of the cuprate superconductors. *Reviews of modern physics*, 75(2):473, 2003.
- [91] Minjie Wang and Eui-Hyeok Yang. Thz applications of 2d materials: Graphene and beyond. *Nano-Structures & Nano-Objects*, 15:107–113, 2018.
- [92] Fengcheng Wu, Timothy Lovorn, and AH MacDonald. Theory of optical absorption by interlayer excitons in transition metal dichalcogenide heterobilayers. *Physical Review B*, 97(3):035306, 2018.
- [93] Martin Weinelt, Michael Kutschera, Thomas Fauster, and Michael Rohlfing. Dynamics of exciton formation at the si (100) c (4 × 2) surface. *Physical review letters*, 92(12):126801, 2004.
- [94] Zidong Li, Xiaobo Lu, Darwin F Cordovilla Leon, Zhengyang Lyu, Hongchao Xie, Jize Hou, Yanzhao Lu, Xiaoyu Guo, Austin Kaczmarek, Takashi Taniguchi, et al. Interlayer exciton transport in mose<sub>2</sub>/wse<sub>2</sub> heterostructures. *ACS nano*, 15(1):1539–1547, 2021.
- [95] Zhiming Zhang, Yimeng Wang, Kenji Watanabe, Takashi Taniguchi, Keiji Ueno, Emanuel Tutuc, and Brian J LeRoy. Flat bands in twisted bilayer transition metal dichalcogenides. *Nature Physics*, 16(11):1093–1096, 2020.

---

Paper 1

---

## RESEARCH ARTICLE

# Ultrafast phonon-driven charge transfer in van der Waals heterostructures

Giuseppe Meneghini<sup>1</sup>  | Samuel Brem<sup>1</sup>  | Ermin Malic<sup>1,2</sup>

<sup>1</sup>Department of Physics, Philipps University of Marburg, Marburg, Germany

<sup>2</sup>Department of Physics, Chalmers University of Technology, Göteborg, Sweden

## Correspondence

Giuseppe Meneghini, Department of Physics, Philipps University of Marburg, 35037

Marburg, Germany.

Email:

[giuseppe.meneghini@physik.uni-marburg.de](mailto:giuseppe.meneghini@physik.uni-marburg.de)

## Funding information

Graphene Flagship, Grant/Award Number: 881603; Deutsche Forschungsgemeinschaft, Grant/Award Number: SFB 1083 (Project B9)

## Abstract

Van der Waals heterostructures built by vertically stacked transition metal dichalcogenides (TMDs) exhibit a rich energy landscape, including interlayer and intervalley excitons. Recent experiments demonstrated an ultrafast charge transfer in TMD heterostructures. However, the nature of the charge transfer process has remained elusive. Based on a microscopic and material-realistic exciton theory, we reveal that phonon-mediated scattering via strongly hybridized intervalley excitons governs the charge transfer process that occurs on a sub-100fs timescale. We track the time-, momentum-, and energy-resolved relaxation dynamics of optically excited excitons and determine the temperature- and stacking-dependent charge transfer time for different TMD bilayers. The provided insights present a major step in microscopic understanding of the technologically important charge transfer process in van der Waals heterostructures.

## Key Points:

- Microscopic and fully quantum-mechanic model is developed to calculate exciton dynamics in van der Waals heterostructures
- Charge transfer occurs on a femtosecond timescale and is a phonon-mediated two-step process
- Strongly hybridized dark exciton states play a crucial role for the charge transfer

## KEYWORDS

charge transfer dynamics, dark excitons, exciton dynamics, exciton hybridization, van der Waals heterostructures

Transition-metal dichalcogenides (TMDs) have been in the focus of current research due to their enhanced light-matter and Coulomb interaction leading to a rich energy landscape of tightly bound excitons.<sup>1–4</sup> Stacking TMD monolayers into van der Waals heterostructures introduces spatially separated interlayer states adding another exciton species with long lifetimes and an out-of-plane dipole moment.<sup>5–14</sup> Recent experiments demonstrated the ultrafast

charge transfer in optically excited TMD heterobilayers resulting in a formation of interlayer states on a sub-picosecond timescale.<sup>15–20</sup> Typically, TMD heterobilayers exhibit a type-II band alignment<sup>21,22</sup> favoring the tunneling of an electron or hole into the opposite layer. However, the underlying microscopic nature of the charge transfer process has not yet been well understood. In an early previous work, we have suggested a defect-assisted interlayer tunneling directly at

This is an open access article under the terms of the [Creative Commons Attribution](https://creativecommons.org/licenses/by/4.0/) License, which permits use, distribution and reproduction in any medium, provided the original work is properly cited.

© 2022 The Authors. *Natural Sciences* published by Wiley-VCH GmbH.

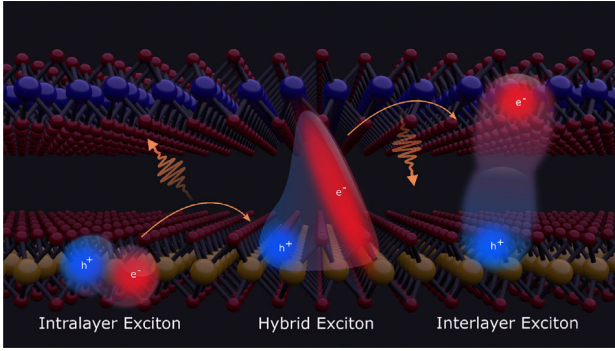


**FIGURE 1** Sketch of the charge transfer process. Starting from an exciton localized in the bottom layer, phonon-mediated scattering to a hybrid exciton state (where, e.g., the electron lives in both layers) allows for the transfer of the charge (here electron) to the upper layer resulting in a spatially separated interlayer exciton state. In analogy, hole transfer can also take place if hybrid excitons with delocalized holes are present

the K point.<sup>18,23</sup> Alternatively, a phonon-mediated charge transfer could occur involving intervalley scattering to the strongly hybridized  $\Lambda$  or  $\Gamma$  valleys.<sup>24–26</sup> A sophisticated microscopic model of such a phonon-assisted formation of interlayer excitons is still missing.

In this work, we address this open question and reveal the crucial many-particle mechanism behind the ultrafast charge transfer in TMD heterostructures. To this end, we combine first-principle calculations<sup>27</sup> with the excitonic density matrix formalism<sup>28,29</sup> to obtain a material-realistic model of the excitonic energy landscape, the internal substructure of different exciton species, and the phonon-mediated scattering into layer-hybridized dark intervalley states.<sup>30,31</sup> We first calculate the exciton energy landscape of the exemplary  $\text{MoS}_2\text{-WS}_2$  and  $\text{MoSe}_2\text{-WSe}_2$  heterostructures by solving the Wannier equation for perfectly layer-polarized intra- and interlayer excitons and subsequently computing hybrid excitons based on first-principle interlayer tunneling parameters.<sup>18,23,28,30,31</sup> Then, we develop and numerically solve equations of motion describing the time- and momentum-resolved evolution of hybrid excitons. This allows us to track the relaxation dynamics of excitons from optically excited intralayer excitons toward charge separated interlayer exciton states. We identify the phonon-mediated intervalley scattering from intralayer  $\text{KK}$  into the strongly hybridized  $\text{K}\Lambda'$  excitons, followed by the relaxation into energetically lower interlayer  $\text{KK}^{(l)}$  states, as the crucial mechanism behind the ultrafast charge transfer in these heterostructures, cf. Figure 1. We further determine the characteristic temperature- and stacking-dependent charge transfer time that can guide future experiments investigating interlayer excitons in van der Waals heterostructures.

#### Microscopic approach

The starting point of this work is the Hamilton operator describing electrons and holes of the heterostructure in the basis of mono-

layer eigenstates (localized in one of both layers). Here, we include a stacking-dependent alignment shift of the two monolayer band structures<sup>32</sup> as well as interlayer tunneling terms resulting from the wave function overlap between the adjacent layers. The necessary material-specific parameters have been extracted from first-principle calculations.<sup>27</sup> Moreover, we include many-particle interaction Hamiltonians, such as electron–light and electron–phonon coupling, as well as the Coulomb interaction between electrons and holes. Here, the scattering between electrons and photons/phonons preferably occurs locally within one of the two layers, whereas we explicitly include the Coulomb interaction between particles residing in different layers. The different intra- and interlayer Coulomb matrix elements are computed with a modified Keldysh-type potential<sup>23,28,30</sup> accounting for the dielectric environment created by the TMD layers and the substrate.<sup>33</sup> To achieve a numerically feasible model, we set the twist-angle between the two monolayers to zero and study the charge transfer in a spatially homogeneous system characterized by a single atomic alignment. Although the twist-angle is known to have a large impact on the hybridization of exciton states,<sup>30</sup> we expect the qualitative charge transfer behavior to remain the same also in twisted heterostructures. Moreover, we do not consider spin-flipping processes and restrict our model to the optically active (A exciton) spin configuration, as the spin-flipping processes are expected to occur on a slower timescale.<sup>34,35</sup>

Now, we derive the dynamics of the system by initially performing a series of basis transformations. First, we solve the Wannier equation for pure intra- or interlayer excitons<sup>23</sup> and use the eigenfunctions  $\psi^\mu(\mathbf{k})$  to introduce a new set of excitonic operators<sup>30</sup>  $X_{\mathbf{Q}}^{\mu\dagger} = \sum_{\mathbf{k}} \psi^\mu(\mathbf{k}) a_{c,\zeta_e,L_e,\mathbf{k}+\alpha\mathbf{Q}}^\dagger a_{v,\zeta_h,L_h,\mathbf{k}-\beta\mathbf{Q}}$  with the compound quantum number  $\mu = (n, \zeta, L)$  labeling the excitonic states. Here,  $n$  is associated with the series of Rydberg-like states determining the relative electron-hole motion,  $\zeta = (\zeta_e, \zeta_h)$  denotes the electron and hole valleys, and the layer compound index  $L = (L_e, L_h)$  contains the electron and hole layer. Furthermore, we have introduced the center-of-mass momentum  $\mathbf{Q}$  and the relative momentum  $\mathbf{k}$  between electrons and holes. The operator  $a_i^{(\dagger)}$  is annihilating (creating) electrons with the set of quantum numbers denoted by  $i$ . We use the new exciton operators to perform a basis transformation to obtain an effective single-particle Hamiltonian for excitons, reading

$$H_X = \sum_{\mu\mathbf{Q}} E_{\mathbf{Q}}^\mu X_{\mathbf{Q}}^{\mu\dagger} X_{\mathbf{Q}}^\mu + \sum_{\mu\nu\mathbf{Q}} \mathcal{T}_{\mu\nu} X_{\mathbf{Q}}^{\mu\dagger} X_{\mathbf{Q}}^\nu \quad (1)$$

with the exciton energy  $E_{\mathbf{Q}}^\mu$  obtained from the Wannier equation and the excitonic tunneling matrix elements  $\mathcal{T}_{\mu\nu}$ , which contain apart from electronic tunneling rates also the overlap of excitonic wave functions.

Next, we diagonalize the exciton Hamiltonian Equation (1) by introducing a new set of operators  $Y_{\mathbf{Q}}^\eta = \sum_{\mu} c_{\mu}^\eta(\mathbf{Q}) X_{\mathbf{Q}}^\mu$  describing hybrid excitons. These are layer-hybridized states consisting of intra- and interlayer excitons with the mixing coefficients  $c_{\mu}^\eta(\mathbf{Q})$  and the new quantum number  $\eta$  defining the hybrid-exciton bands. The diagonalized Hamiltonian reads in this basis  $H_Y = \sum_{\eta} \mathcal{E}_{\mathbf{Q}}^\eta Y_{\mathbf{Q}}^{\eta\dagger} Y_{\mathbf{Q}}^\eta$  with

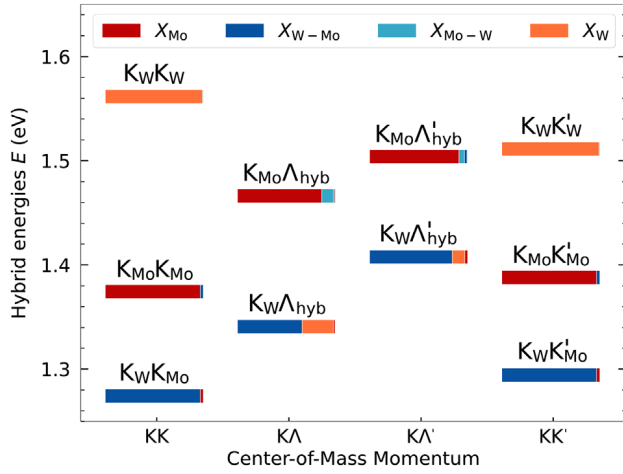


**FIGURE 2** Hybrid-exciton energy landscape for MoSe<sub>2</sub>-WSe<sub>2</sub> (R<sub>h</sub><sup>h</sup> stacking). We use different colors for depicting the four initial intra- and interlayer excitonic states named with X<sub>h-l<sub>e</sub></sub> (using only one index for intralayer excitons). The final hybrid exciton states are denoted with two capital letters (K, Λ) describing the valley and the subscripts (W, Mo) describing the layer, in which the hole (first letter) and electron (second letter) are localized. We highlight for each hybrid exciton the percentage of the involved intra- and interlayer exciton states. Due to the strong tunneling experienced by electrons, the states in the KΛ<sup>(l)</sup> valleys are strongly hybridized. Note that we plot only a selection of low-energy hybrid exciton states contributing directly to the relaxation dynamics.

the corresponding hybrid-exciton energies  $\mathcal{E}_{\mathbf{Q}}^{\eta}$ . With the procedure described above, we have a microscopic access to the full spectrum of strongly or weakly hybridized exciton states, including bright KK as well as momentum-dark intervalley states,<sup>36,37</sup> such as KΛ<sup>(l)</sup> and KK<sup>(l)</sup>, cf. Figure 2 that will be discussed further below.

Finally, we consider the interaction of hybrid exciton states with phonons. As we restrict our study to the low-density regime, exciton-exciton scattering can be neglected.<sup>38</sup> Starting from the electron-hole picture and performing the same change of basis as described above, we obtain the following Hamiltonian for the hybrid-exciton-phonon interaction<sup>30</sup>

$$H_{Y\text{-ph}} = \sum_{\substack{\mathbf{Q}, \mathbf{q} \\ j, \eta, \xi}} D_{j\mathbf{q}\mathbf{Q}}^{\xi\eta} Y_{\mathbf{Q}+\mathbf{q}}^{\xi\dagger} Y_{\mathbf{Q}}^{\eta} b_{j,\mathbf{q}} + h.c. \quad (2)$$

as well as for the hybrid-exciton-light coupling  $H_{Y\text{-l}} = \sum_{\sigma, \mathbf{Q}, \eta} \mathbf{A} \cdot \mathcal{M}_{\sigma\mathbf{Q}}^{\eta} Y_{\mathbf{Q}}^{\eta} + h.c.$  All details on the basis transformation and the resulting hybrid matrix elements can be found in the [Supporting Information](#).

Having determined the Hamilton operator  $H = H_Y + H_{Y\text{-ph}} + H_{Y\text{-l}}$  for hybrid-excitons and their interaction with phonons and light, we can now derive equations of motion describing the exciton dynamics. Here, we exploit the Heisenberg equation of motion for the occupation numbers  $N_{\mathbf{Q}}^{\eta} = \langle Y_{\mathbf{Q}}^{\eta\dagger} Y_{\mathbf{Q}}^{\eta} \rangle$ , truncating the Martin-Schwinger hierarchy arising from the exciton phonon-scattering within the second-order Born-Markov approximation.<sup>36,39-41</sup> Considering separately the coherent polarization  $P_{\mathbf{Q}}^{\eta} = \langle Y_{\mathbf{Q}}^{\eta\dagger} \rangle$  and the purely incoherent population  $\delta N_{\mathbf{Q}}^{\eta} =$

$N_{\mathbf{Q}}^{\eta} - |P_{\mathbf{Q}}^{\eta}|^2$ , we arrive at the semiconductor Bloch-equations in hybrid-exciton basis

$$i\hbar\dot{P}_{\mathbf{Q}}^{\eta} = -(\mathcal{E}_{\mathbf{Q}}^{\eta} + i\Gamma_{\mathbf{Q}}^{\eta})P_{\mathbf{Q}}^{\eta} - \mathcal{M}_{\mathbf{Q}}^{\eta} \cdot \mathbf{A}(t) \quad (3)$$

$$\delta\dot{N}_{\mathbf{Q}}^{\eta} = \sum_{\xi} W_{0\mathbf{Q}}^{\xi\eta} |P_{\mathbf{Q}}^{\eta}|^2 + \sum_{\xi, \mathbf{Q}'} \left( W_{\mathbf{Q}'\mathbf{Q}}^{\xi\eta} \delta N_{\mathbf{Q}'}^{\xi} - W_{\mathbf{Q}\mathbf{Q}'}^{\eta\xi} \delta N_{\mathbf{Q}}^{\eta} \right).$$

The details on the scattering tensor  $W_{\mathbf{Q}\mathbf{Q}'}^{\eta\xi}$  can be found in the [Supporting Information](#). Equation (3) provides full microscopic access to the dynamics of hybrid excitons, including optical excitation as well as phonon-scattering-induced relaxation across intra- and intervalley as well as intra- and interlayer states, effectively giving rise to a multi-step charge transfer process.

## HYBRID EXCITON LANDSCAPE

We focus here on the two most studied heterostructures in literature, MoS<sub>2</sub>-WS<sub>2</sub> and MoSe<sub>2</sub>-WSe<sub>2</sub>. For simplicity, we show the results for the latter in the main text and the former in the [Supporting Information](#). We start by presenting the hybrid exciton landscape that has been calculated by solving the Wannier equation in the hybrid-exciton basis, cf. Figure 2. This energy landscape is the key to understanding the charge transfer process. We use the following notation for the hybrid exciton states: the capital letters describe the valley and the subscript the layer, where the first letter denotes the hole and the second the electron. To give an example, K<sub>W</sub>K'<sub>Mo</sub> means that the hole is located at the K point of the WSe<sub>2</sub> layer, while the electron is localized at the K' valley of the MoSe<sub>2</sub> layer. Furthermore, we use the subscript hyb to underline that the electron/hole in the corresponding valley is strongly hybridized between both layers, for example, in K<sub>W</sub>Λ<sub>hyb</sub>, the electron at the Λ valley lives in both layers.

Figure 2 shows the energy landscape of hybrid-excitons in the MoSe<sub>2</sub>-WSe<sub>2</sub> heterostructure for the case of R<sub>h</sub><sup>h</sup> stacking, that is, the metal atoms of one layer are placed on top of the metal atoms of the other layer. The corresponding landscape for the other two high-symmetry stackings R<sub>h</sub><sup>X</sup> and R<sub>h</sub><sup>M27</sup> (where either the chalcogen atom X or the metal atom M of the upper layer is above the hole/void of the other layer) as well as for the MoS<sub>2</sub>-WS<sub>2</sub> heterostructure can be found in the [Supporting Information](#). We show only the hybrid exciton states that are energetically close to or lower than the intralayer K<sub>W</sub>K<sub>W</sub> exciton in the WSe<sub>2</sub> layer, since we will resonantly excite the material at this exciton energy and phonon-driven relaxation processes will distribute the excitons toward lower energies. We have checked that the contribution of higher exciton states to the relaxation dynamics and the charge transfer process, that is, due to absorption of phonons, is negligible. Note that for this particular heterostructure, ΓK excitons do not play a role for the charge transfer process, while these are crucial for the MoS<sub>2</sub>-WS<sub>2</sub> heterostructure considered in the [Supporting Information](#).

In the exciton basis, the hybridization of electronic states corresponds to a mixing of intra- and interlayer excitons. We quantify the contribution of each state to the new hybrid-exciton states by

evaluating the mixing coefficients. Here,  $|c_{\mu}^{\eta}(\mathbf{Q})|^2$  can be interpreted as the percentage of the exciton state  $\mu$  inside the hybrid state  $\eta$ . In the presence of strong tunneling, the new hybrid states are expected to be heavily influenced by different excitonic species. In contrast, a weak tunneling should result in hybrid states that are almost purely intra- or interlayer excitons. The degree of hybridization of each state is illustrated in Figure 2 by adopting a color scheme, where we highlight for each hybrid state the different exciton contributions. Here, a hybrid state of a pure intralayer or interlayer character is just red or blue, respectively. In contrast, strongly hybridized states consist of different colors. Figure 2 illustrates that hybrid states involving excitons at the  $\Lambda$  valley ( $K_W\Lambda_{\text{hyb}}$ ,  $K_W\Lambda'_{\text{hyb}}$ ) contain large contributions of several species, whereas the states at the K valley are either intra- or interlayer excitons to a very high percentage. The weak hybridization of KK excitons is well known in literature.<sup>42,43</sup> The electronic wave functions at the K valley are mostly composed of d orbitals localized at transition metal atoms, which are sandwiched by the selenium atoms preventing an efficient overlap of wave functions. In contrast, the electronic wave function at the  $\Lambda$  valley has large contributions at the selenium atoms resulting in much more efficient hybridization of  $K_W\Lambda_{\text{hyb}}^{(\eta)}$  states.<sup>30,31,42,43</sup>

The energetically lowest states in the investigated  $\text{MoSe}_2$ - $\text{WSe}_2$  heterostructure are  $K_W K_{\text{Mo}}^{(\eta)}$  excitons that are almost purely of interlayer exciton character (blue). When exciting the material resonantly to the intralayer  $K_W K_W$  state (orange), there are a number of spectrally lower-lying states that will give rise to a phonon-mediated cascade of transitions down to the energetically lowest states. Note that the scattering process between two hybrid states requires that the initial and final states live at least partially in the same layer. Therefore, we expect the strongly hybridized exciton states  $K_W\Lambda_{\text{hyb}}^{(\eta)}$  to play a major role for the relaxation dynamics and the charge transfer process.

## HYBRID EXCITON DYNAMICS

Now, we investigate the time- and momentum-resolved relaxation cascade of hybrid excitons after an optical excitation resonant to the purely intralayer  $K_W K_W$  exciton localized in the  $\text{WSe}_2$  layer, cf. Figure 2. To focus on the charge transfer process and to avoid interplay effects with the exciting laser pulse, we directly initialize the system with a population in the  $K_W K_W$  state. We have also performed calculations, including the laser pulse and the interference of optical excitation and relaxation dynamics, which are presented in the [Supporting Information](#). Note that we focus on the 1s ground state for all exciton species, as higher-energy states in the Rydberg-like series of excitons exhibit a much smaller scattering probability compared to the 1s-1s transitions.<sup>44</sup> This has been verified by numerically evaluating phonon-assisted scattering involving higher-energy states.

Evaluating the semiconductor Bloch equations (cf. Equation 3), we have full microscopic access to the time-, energy-, and momentum-resolved relaxation cascade of nonequilibrium excitons. Figure 3 shows the momentum-integrated exciton dynamics in  $\text{MoSe}_2$ - $\text{WSe}_2$  (in  $R_h^h$  stacking) at 77 K. We see a decrease of the initially populated intralayer

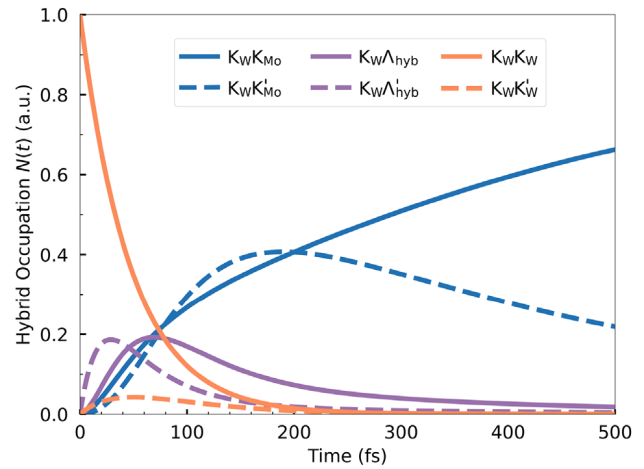


**FIGURE 3** Momentum-integrated hybrid-exciton dynamics at 77 K for  $\text{MoSe}_2$ - $\text{WSe}_2$  in  $R_h^h$  stacking. By solving Equation (3), we have microscopic access to the phonon-mediated relaxation dynamics of hybrid exciton and the resulting charge transfer mechanism. Starting with an initial occupation of intralayer  $K_W K_W$  excitons localized in the  $\text{WSe}_2$  layer (orange line) via phonon-mediated scattering into the strongly hybridized  $K_W \Lambda_{\text{hyb}}^{(\eta)}$  states (purple lines), we end up in the energetically lowest interlayer  $K_W K_{\text{Mo}}^{(\eta)}$  excitons (blue lines), that is, the electron has been transferred to the  $\text{MoSe}_2$  layer

$K_W K_W$  exciton state (solid orange line). At the same time, we find an ultrafast increase in the population of the hybrid  $K_W \Lambda_{\text{hyb}}^{(\eta)}$  excitons on a timescale of sub-100fs (solid and dashed purple lines). The microscopic origin of this efficient scattering lies in the nature of the hybrid-exciton-phonon coupling. Phonons can only couple states that share the same layer quantum number  $L = (L_e, L_h)$  as exciton-phonon scattering is considered to be a local process. For this reason, phonons can couple pure intra- and interlayer states only through scattering via hybrid states. Once the electron/hole has been scattered into a hybridized state, that is, into a superposition between both layers, there is a nonzero probability of further scattering into the opposite layer.

Following the relaxation cascade, we can track the population transfer from the hybridized  $K_W \Lambda_{\text{hyb}}^{(\eta)}$  to the interlayer  $K_W K_{\text{Mo}}^{(\eta)}$  excitons (solid and dashed blue lines in Figure 3). After 100 fs, the initially populated intralayer  $K_W K_W$  exciton states has been almost completely emptied and most occupation is found in the interlayer  $K_W K_{\text{Mo}}^{(\eta)}$  excitons, where electrons and holes are spatially separated. As a result, the transfer of electrons from the initial  $\text{WSe}_2$  layer into the opposite  $\text{MoSe}_2$  layer occurs on sub-100fs timescale.

To further illustrate the main scattering processes governing the relaxation cascade, Figure 4 shows the momentum-resolved exciton dynamics for different times. We find that in the first step, the hybridized  $K_W \Lambda_{\text{hyb}}$  and  $K_W \Lambda'_{\text{hyb}}$  states are not populated (0 fs). The scattering into the latter happens on a faster timescale, as here M phonons are involved, which are known to give rise to a very efficient scattering with excitons.<sup>45</sup> With some delay, there is an efficient phonon-mediated scattering from these hybridized states into the interlayer  $K_W K_{\text{Mo}}$  and  $K_W K'_{\text{Mo}}$  excitons. The population of the latter

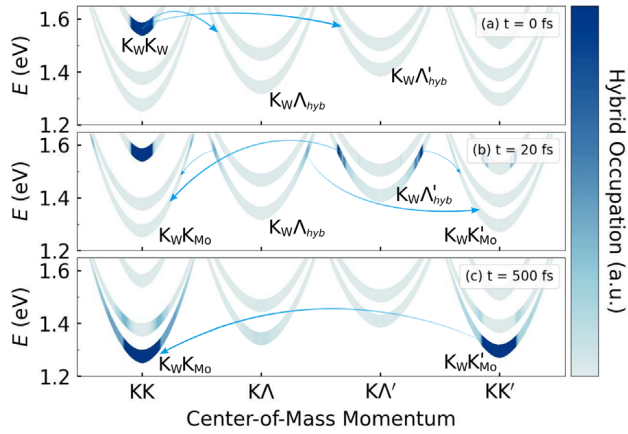


**FIGURE 4** Momentum-resolved hybrid-exciton dynamics at (a) 0 fs, (b) 20 fs, and (c) 500 fs. Starting from a population created in the intralayer  $K_W K_W$  exciton, we highlight the most important phonon-driven scattering processes. Note that the blue-shading in the parabolas corresponds to a microscopically calculated exciton occupation. The charge transfer of electrons occurs in a two-step process with an initial partial transfer into the hybrid  $K_W \Lambda_{\text{hyb}}^{(l)}$  exciton states (with the electron living in both layers) followed by the complete transfer to the energetically lower interlayer  $K_W K_{\text{Mo}}^{(l)}$  states (with the electron localized in the second layer).

occurs faster again due to the involved M phonons. In the final step, this state becomes partially depopulated in favor of the energetically lowest  $K_W K_{\text{Mo}}$  state. After approximately 500 fs, a thermalized exciton distribution is reached with the highest occupation in  $K_W K_{\text{Mo}}$  followed by a certain thermal occupation in  $K_W K_{\text{Mo}}'$ . All other states have only a negligible population.

So far, we have investigated the simplified situation of an initially populated  $K_W K_W$ . In a real experiment, this state will be continuously optically excited throughout a finite time window, and there will be an interplay of excitation and phonon-mediated scattering. Evaluating Equation (3), we can resolve this interplay and find the same general behavior as described above, cf. the [Supporting Information](#). We observe the same main relaxation steps and a very similar timescale for the charge transfer mechanism. However, tracking the dynamics becomes more complicated during the initial phase of the relaxation due to the simultaneous pumping of excitons in the system that immediately start to relax very rapidly. The main difference between the simulation with a pump pulse (Figure S3) and the instantaneous initialization is that at the time when the laser pulse reaches its maximum, a large fraction of excitons has already relaxed to lower energy states, which quantitatively modifies the delay between peak populations of hybrid and interlayer exciton states. This suggests that we can capture the main features of the process using instantaneous excitation, which allows us to gain a much more intuitive picture of the charge transfer without losing generality.

## INTERLAYER CHARGE TRANSFER

Summarizing the exciton dynamics in a nutshell, the initially inserted occupation of the intralayer  $K_W K_W$  excitons is distributed to the

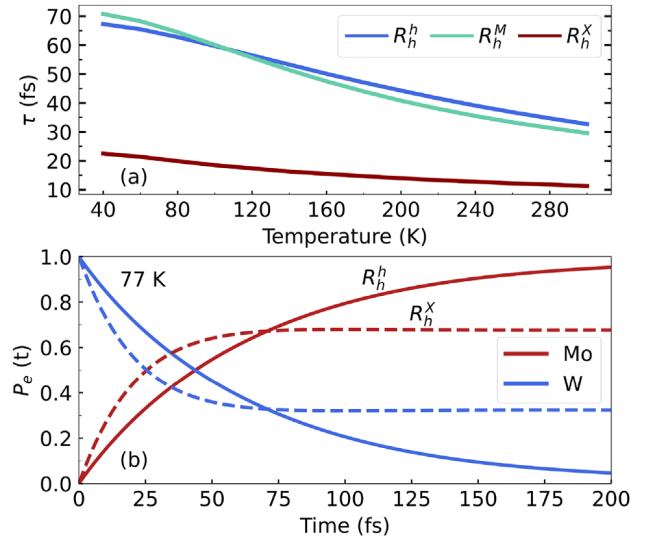


**FIGURE 5** (a) Characteristic electron transfer time as a function of temperature for  $\text{MoSe}_2$ - $\text{WSe}_2$  in different high-symmetry stackings. The time is extracted from an exponential fit of the layer-dependent electron probability  $P_e(t)$  as shown in part (b). We find a considerable decrease in the charge transfer time with temperature reflecting a more efficient exciton-phonon scattering. Interestingly, we predict a much faster transfer time for  $R_h^X$  stacking, as here the hybrid  $\Lambda_{\text{hyb}}^{(l)}$  states are very close to the interlayer  $K_W K_{\text{Mo}}^{(l)}$  states, cf. the [Supporting Information](#). The faster electron transfer speed comes at the cost of a more incomplete transfer process as the stationary occupation of the  $\Lambda_{\text{hyb}}^{(l)}$  excitons is relatively high, where the electrons are delocalized between both layers, cf. the dashed versus solid lines in part b

energetically lowest interlayer  $K_W K_{\text{Mo}}^{(l)}$  states through an intermediate step involving strongly hybridized  $K\Lambda/\Lambda^{(l)}$  states. This means that the charge transfer is a two-step process, where the electron is first transferred into a hybrid state (representing a superposition of both layers) and in a second step, it is transferred to the opposite layer. The characteristic charge transfer time  $\tau$  is illustrated in Figure 5a as a function of temperature for different high-symmetry stackings. We can quantify the charge transfer speed by computing the layer- and stacking-dependent probability  $P_e(t) = \langle a_c^\dagger a_c \rangle$  of one electron being localized in the  $\text{MoSe}_2$  layer after excitation of an intralayer state in the  $\text{WSe}_2$  layer, cf. Figure 5b. By exponentially fitting the temporal evolution of  $P_e(t)$ , we can extract the characteristic electron transfer time  $\tau$ . We find an ultrafast transfer rate of  $\tau = 33$  fs for  $\text{MoSe}_2$ - $\text{WSe}_2$  in  $R_h^h$  stacking at room temperature. The electrons are almost completely transferred from the initially occupied  $\text{WSe}_2$  layer to the  $\text{MoSe}_2$  layer, that is, one finds the electron with a probability of 95% after 200 fs, cf. the solid red and blue lines in Figure 5b.

Since the relaxation cascade is mediated by phonons, we find a pronounced temperature dependence of the transfer time. Concretely, we predict an increase in  $\tau(T)$  by approximately a factor of 2 to  $\tau = 67$  fs at 40 K for  $R_h^h$  stacking. The reason is the reduced scattering efficiency with phonons at lower temperatures. Nevertheless, even at cryogenic temperatures, we find an ultrafast charge transfer as the relaxation cascade occurs toward energetically lower exciton states and is driven by phonon emission.

Interestingly, we find an unexpected acceleration of the charge transfer for  $R_h^X$  stacking (whereas,  $R_h^M$  stacking is rather similar to the  $R_h^h$  stacking investigated so far). This originates from the hybrid-energy landscape for different stackings (cf. the [Supporting Information](#)). The stronger tunneling at the  $K\Lambda$  valley for the  $R_h^X$  stacking<sup>27</sup> and the resulting larger red-shift of exciton energies has as a consequence that the relevant energy levels are closer than in other stackings, cf. Figure S2a. In particular, the strongly hybridized  $K\Lambda_{\text{hyb}}$  states and the interlayer  $K_W K_{\text{Mo}}^{(l)}$  excitons are nearly degenerate. As a result, the second step in the charge transfer process is much more efficient compared to the  $R_h^h$  stacking. Note, however, that while the charge transfer is indeed faster for the  $R_h^X$  stacking, there is only an incomplete transfer. This means that the electron is not transferred to almost 100% as in the case of  $R_h^h$  stacking, but there is still a probability of approximately 40% to find the electron in the initially populated layer, cf. the dashed lines in Figure 5b. The reason behind this is that a large percentage of the hybrid-exciton population remains in the hybrid  $K\Lambda_{\text{hyb}}$  state as it is threefold degenerate and very close in energy with the lowest interlayer  $K_W K_{\text{Mo}}$  state. Hence, the electron remains partially delocalized between the two layers and the charge transfer is incomplete.

So far, we have investigated the  $\text{MoSe}_2$ - $\text{WSe}_2$  heterostructure. The comparison with  $\text{MoS}_2$ - $\text{WS}_2$  (shown in the [Supporting Information](#)) yields the same general behavior for the hybrid-exciton relaxation dynamics. We find a somewhat slower charge transfer with  $\tau = 88$  fs for  $R_h^h$  stacking at room temperature, mainly due to the much larger energy window involved in the relaxation dynamics, cf. the energy landscape in Figure S4. Analyzing the results in more detail, we find the main difference originating from the importance of  $\Gamma_{\text{hyb}}K$  excitons. The strong tunneling occurring in the  $\Gamma$  valley results in a large red-shift of the corresponding exciton states making them energetically lowest in  $\text{MoS}_2$ - $\text{WS}_2$ . Interestingly, we find that in contrast to  $\text{MoSe}_2$ - $\text{WSe}_2$  discussed above, we find here the slowest charge transfer for the  $R_h^X$  stacking. This can be explained by considering  $\Gamma_{\text{hyb}} K_W$  states, which trap excitons. The reason behind this is that despite  $K\Lambda_{\text{hyb}}^{(l)}$  excitons being close in energy and sharing the same composition a scattering into these states requires a simultaneous electron and hole transfer and is thus a negligible higher-order process. A more detailed description of the relaxation dynamics as well as temperature- and stacking-dependent charge transfer times in the  $\text{MoS}_2$ - $\text{WS}_2$  heterostructure can be found in the [Supporting Information](#).

In conclusion, we have developed a microscopic and material-specific theory allowing us to access the relaxation dynamics of hybrid excitons in van der Waals heterostructures. In particular, we identify the extremely efficient phonon-mediated relaxation via strongly hybridized  $K\Lambda_{\text{hyb}}$  excitons as the crucial mechanism behind the ultrafast charge transfer process in the  $\text{MoSe}_2$ - $\text{WSe}_2$  heterostructure. We predict charge transfer times in the range of tens of femtoseconds that are strongly dependent on temperature and stacking of the layers. Our work presents an important step toward a microscopic understanding of the relaxation cascade and ultrafast charge transfer in technologically promising van der Waals heterostructures.

## ACKNOWLEDGMENTS

We acknowledge the support from Deutsche Forschungsgemeinschaft (DFG) via SFB 1083 (Project B9) and the European Unions Horizon 2020 Research and Innovation Program, under Grant Agreement No. 881603 (Graphene Flagship).

## CONFLICT OF INTEREST

The authors declare no conflict of interest.

## AUTHOR CONTRIBUTIONS

Giuseppe Meneghini: formal analysis, investigation, software, writing - review & editing. Samuel Brem: conceptualization, supervision, writing - review & editing. Ermin Malic: conceptualization, funding acquisition, project administration, supervision, writing - review & editing.

## ETHICAL STATEMENT

The authors confirm that they have followed the ethical policies of the journal.

## DATA AVAILABILITY STATEMENT

The data that support the findings of this study are available from the corresponding author upon reasonable request.

## PEER REVIEW

The peer review history for this article is available at <https://publons.com/publon/10.1002/ntls.20220014>

## ORCID

Giuseppe Meneghini  <https://orcid.org/0000-0002-1889-2380>

Samuel Brem  <https://orcid.org/0000-0001-8823-1302>

## REFERENCES

1. He K, Kumar N, Zhao L, et al. Tightly bound excitons in monolayer  $\text{WSe}_2$ . *Phys Rev Lett*. 2014;113:026803.
2. Chernikov A, Berkelbach TC, Hill HM, et al. Exciton binding energy and nonhydrogenic Rydberg series in monolayer  $\text{WS}_2$ . *Phys Rev Lett*. 2014;113:076802.
3. Wang G, Chernikov A, Glazov MM, et al. Colloquium: excitons in atomically thin transition metal dichalcogenides. *Rev Mod Phys*. 2018;90:021001.
4. Mueller T, Malic E. Exciton physics and device application of two-dimensional transition metal dichalcogenide semiconductors. *npj 2D Mater Appl*. 2018;2:1-12.
5. Rivera P, Schaibley JR, Jones AM, et al. Observation of long-lived interlayer excitons in monolayer  $\text{MoSe}_2$ - $\text{WSe}_2$  heterostructures. *Nat Commun*. 2015;6:1-6.
6. Miller B, Steinhoff A, Pano B, et al. Long-lived direct and indirect interlayer excitons in van der Waals heterostructures. *Nano Lett*. 2017;17:5229-5237.
7. Kunstmann J, Mooshammer F, Nagler P, et al. Momentum-space indirect interlayer excitons in transition-metal dichalcogenide van der Waals heterostructures. *Nat Phys*. 2018;14:801-805.
8. Jin C, Regan EC, Yan A, et al. Observation of Moiré excitons in  $\text{WSe}_2/\text{WS}_2$  heterostructure superlattices. *Nature*. 2019;567:76-80.
9. Tran K, Moody G, Wu F, et al. Evidence for Moiré excitons in van der Waals heterostructures. *Nature*. 2019;567:71-75.

10. Seyler KL, Rivera P, Yu H, et al. Signatures of Moiré-trapped valley excitons in MoSe<sub>2</sub>/WSe<sub>2</sub> heterobilayers. *Nature*. 2019;567:66-70.
11. Alexeev EM, Ruiz-Tijerina DA, Danovich M, et al. Resonantly hybridized excitons in Moiré superlattices in van der Waals heterostructures. *Nature*. 2019;567:81-86.
12. Ruiz-Tijerina DA, Fal'ko VI. Interlayer hybridization and Moiré superlattice minibands for electrons and excitons in heterobilayers of transition-metal dichalcogenides. *Phys Rev B*. 2019;99:125424.
13. Sigl L, Troue M, Katzer M, et al. Optical dipole orientation of interlayer excitons in MoSe 2- WSe 2 heterostacks. *Phys Rev B*. 2022;105:035417.
14. Holler J, Selig M, Kempf M, et al. Interlayer exciton valley polarization dynamics in large magnetic fields. *Phys Rev B*. 2022;105:085303.
15. Hong X, Kim J, Shi S-F, et al. Ultrafast charge transfer in atomically thin MoS<sub>2</sub>/WS<sub>2</sub> heterostructures. *Nat Nanotechnol*. 2014;9:682-686.
16. Ceballos F, Bellus MZ, Chiu H-Y, Zhao H. Ultrafast charge separation and indirect exciton formation in a MoS<sub>2</sub>-MoSe<sub>2</sub> van der Waals heterostructure. *ACS Nano*. 2014;8:12717-12724.
17. Ji Z, Hong H, Zhang J, et al. Robust stacking-independent ultrafast charge transfer in MoS<sub>2</sub>/WS<sub>2</sub> bilayers. *ACS Nano*. 2017;11:12020-12026.
18. Merkl P, Mooshammer F, Steinleitner P, et al. Ultrafast transition between exciton phases in van der Waals heterostructures. *Nat Mater*. 2019;18:691-696.
19. Schmitt D, Bange JP, Bennecke W, et al. Formation of Moire interlayer excitons in space and time. *arXiv preprint arXiv:2112.05011*. 2021.
20. Deilmann T, Thygesen KS. Interlayer excitons with large optical amplitudes in layered van der Waals materials. *Nano Lett*. 2018;18:2984.
21. Hill HM, Rigosi AF, Rim KT, Flynn GW, Heinz TF. Band alignment in MoS<sub>2</sub>/WS<sub>2</sub> transition metal dichalcogenide heterostructures probed by scanning tunneling microscopy and spectroscopy. *Nano Lett*. 2016;16:4831-4837.
22. Özcelik VO, Azadani JG, Yang Ce, Koester SJ, Low T. Band alignment of two-dimensional semiconductors for designing heterostructures with momentum space matching. *Phys Rev B*. 2016;94:035125.
23. Ovesen S, Brem S, Linderälv C, et al. Interlayer exciton dynamics in van der Waals heterostructures. *Commun Phys*. 2019;2:1-8.
24. Wang Y, Wang Z, Yao W, Liu G-B, Yu H. Interlayer coupling in commensurate and incommensurate bilayer structures of transition-metal dichalcogenides. *Phys Rev B*. 2017;95:115429.
25. Zheng Q, Saidi WA, Xie Y, et al. Phonon-assisted ultrafast charge transfer at van der Waals heterostructure interface. *Nano Lett*. 2017;17:6435-6442.
26. Liu F, Li Q, Zhu X-Y. Direct determination of momentum-resolved electron transfer in the photoexcited van der Waals heterobilayer W S 2/Mo S 2. *Phys Rev B*. 2020;101:201405.
27. Hagel J, Brem S, Linderälv C, Erhart P, Malic E. Exciton landscape in van der Waals heterostructures. *Phys Rev Res*. 2021;3:043217.
28. Brem S, Linderälv C, Erhart P, Malic E. Tunable phases of Moiré excitons in van der Waals heterostructures. *Nano Lett*. 2020;20:8534-8540.
29. Katsch F, Selig M, Carmele A, Knorr A. Theory of exciton-exciton interactions in monolayer transition metal dichalcogenides. *Phys Status Solidi (b)*. 2018;255:1800185.
30. Brem S, Lin K-Q, Gillen R, et al. Hybridized intervalley Moiré excitons and flat bands in twisted WSe 2 bilayers. *Nanoscale*. 2020;12:11088-11094.
31. Merkl P, Mooshammer F, Brem S, et al. Twist-tailoring Coulomb correlations in van der Waals homobilayers. *Nat Commun*. 2020;11:1-7.
32. Kormányos A, Burkard G, Gmitra M, et al. k-p theory for two-dimensional transition metal dichalcogenide semiconductors. *2D Materials*. 2015;2:022001.
33. Laturia A, Put ML, Vandenberghe WG. Dielectric properties of hexagonal boron nitride and transition metal dichalcogenides: from monolayer to bulk. *npj 2D Mater Appl*. 2018;2:1-7.
34. Song Y, Dery H. Transport theory of monolayer transition-metal dichalcogenides through symmetry. *Phys Rev Lett*. 2013;111:026601.
35. Glazov MM, Amand T, Marie X, Lagarde D, Bouet L, Urbaszek B. Exciton fine structure and spin decoherence in monolayers of transition metal dichalcogenides. *Phys Rev B*. 2014;89:201302.
36. Selig M, Berghäuser G, Richter M, Bratschitsch R, Knorr A, Malic E. Dark and bright exciton formation, thermalization, and photoluminescence in monolayer transition metal dichalcogenides. *2D Materials*. 2018;5:035017.
37. Deilmann T, Thygesen KS. Finite-momentum exciton landscape in mono- and bilayer transition metal dichalcogenides. *2D Materials*. 2019;6:035003.
38. Erkensten D, Brem S, Wagner K, et al. Dark exciton-exciton annihilation in monolayer transition-metal dichalcogenides. *Phys Rev B*. 2021;104:L241406.
39. Haug H, Koch SW. *Quantum Theory of the Optical and Electronic Properties of Semiconductors*. World Scientific Publishing Company; 2009.
40. Thränhardt A, Kuckenburg S, Knorr A, Meier T, Koch SW. Quantum theory of phonon-assisted exciton formation and luminescence in semiconductor quantum wells. *Phys Rev B*. 2000;62:2706.
41. Brem S, Selig M, Berghäuser G, Malic E. Exciton relaxation cascade in two-dimensional transition metal dichalcogenides. *Sci Rep*. 2018;8:1-8.
42. Cappelluti E, Roldán R, Silva-Guillén JA, Ordejón P, Guinea F. Tight-binding model and direct-gap/indirect-gap transition in single-layer and multilayer MoS 2. *Phys Rev B*. 2013;88:075409.
43. Gillen R, Maultzsch J. Interlayer excitons in MoSe<sub>2</sub>/WSe<sub>2</sub> heterostructures from first principles. *Phys Rev B*. 2018;97:165306.
44. Brem S, Zipfel J, Selig M, et al. Intrinsic lifetime of higher excitonic states in tungsten diselenide monolayers. *Nanoscale*. 2019;11:12381-12387.
45. Jin Z, Li X, Mullen TJ, Kim WK. Intrinsic transport properties of electrons and holes in monolayer transition-metal dichalcogenides. *Phys Rev B*. 2014;90:045422.

## SUPPORTING INFORMATION

Additional supporting information can be found online in the Supporting Information section at the end of this article.

**How to cite this article:** Meneghini G, Brem S, Malic E. Ultrafast phonon-driven charge transfer in van der Waals heterostructures. *Nat Sci*. 2022;e20220014. <https://doi.org/10.1002/ntls.20220014>

# Ultrafast phonon-driven charge transfer in van der Waals heterostructures

## Supplementary Information

Giuseppe Meneghini,<sup>1,\*</sup> Samuel Brem,<sup>1</sup> and Ermin Malic<sup>1,2</sup>

<sup>1</sup>*Department of Physics, Philipps University of Marburg, 35037 Marburg, Germany*

<sup>2</sup>*Department of Physics, Chalmers University of Technology, 41258 Göteborg, Sweden*

### THEORETICAL APPROACH

**Keldysh potential:** To describe the TMD bilayer system we need to include the correct dielectric screening originating from the presence of two different TMDs monolayers. Choosing a reference at  $z = 0$  at the interface of the two layers, we can address the position of a charge placed in the middle of one of the two layers (denoted by the index  $L = 0, 1$ ), i.e.  $z = \pm d_L/2$  with the layer width  $d_L$ , addressing the background dielectric constant (with the subscript  $bg$ ). We can write the general dielectric constant as

$$\epsilon^L(\mathbf{r}) = \begin{cases} \epsilon_{bg}^L, & \text{if } z < -d_0 \\ \epsilon_0^L, & \text{if } -d_0 < z < 0 \\ \epsilon_1^L, & \text{if } 0 < z < d_1 \\ \epsilon_{bg}^L, & \text{if } z > d_1 \end{cases} \quad (1)$$

and solve the Poisson equation for the system using as boundary conditions Eq. (1) [1, 2]. This way we obtain an analytical expression for the screened Coulomb matrix element

$$W_{\mathbf{q}}^{LL'} = \frac{e_0^2}{2\epsilon_0 A q \epsilon_{LL'}(q)} \quad (2)$$

$$\epsilon_{LL'}(q) = \begin{cases} \epsilon_{intra}^L(q), & \text{if } L = L' \\ \epsilon_{inter}(q), & \text{if } L \neq L' \end{cases}$$

with  $\epsilon_{inter}(q) = \kappa_{bg} g_q^0 g_q^1 f_q$  and  $\epsilon_{intra}^L(q) = \frac{\kappa_{bg} g_q^{1-L} f_q}{ch(\delta_{1-L} q/2) h_q^L}$ ,  $\kappa = \sqrt{\epsilon^{\parallel} \epsilon^{\perp}}$ ,  $\delta_L = \alpha_L d_L$ ,  $\alpha = \sqrt{\epsilon^{\parallel} / \epsilon^{\perp}}$ . Here, have introduced the following abbreviations:

$$f_q = 1 + \frac{1}{2} \left[ \left( \frac{\kappa_0}{\kappa_{bg}} + \frac{\kappa_{bg}}{\kappa_0} \right) th(\delta_0 q) + \left( \frac{\kappa_1}{\kappa_{bg}} + \frac{\kappa_{bg}}{\kappa_1} \right) th(\delta_1 q) + \left( \frac{\kappa_0}{\kappa_1} + \frac{\kappa_1}{\kappa_0} \right) th(\delta_0 q) th(\delta_1 q) \right]$$

$$h_q^L = 1 + \frac{\kappa_{bg}}{\kappa_L} th(\delta_L q) + \frac{\kappa_{bg}}{\kappa_{1-L}} th(\delta_{1-L} q/2) + \frac{\kappa_L}{\kappa_{1-L}} th(\delta_L q) th(\delta_{1-L} q/2) \quad (3)$$

$$g_q^L = \frac{ch(\delta_L q)}{ch(\delta_{1-L} q/2) \left[ 1 + \frac{\kappa_{bg}}{\kappa_L} th(\delta_L q) \right]}$$

**Tunnelling Hamiltonian:** In this section, we provide details on the transformation of the tunneling Hamiltonian into the exciton basis [3]. Starting from the electron-hole picture we can write the tunnelling Hamiltonian in the following way:

$$T = \sum_{i,j,\mathbf{k},\lambda} T_{ij}^{\lambda}(\mathbf{k}\mathbf{q}) a_{\lambda i\mathbf{k}+\mathbf{q}}^{\dagger} a_{\lambda j\mathbf{k}} \quad (4)$$

with  $T_{ij}^{\lambda}(\mathbf{k}\mathbf{q}) = (1 - \delta_{L_i L_j}) \langle \lambda i\mathbf{k} + \mathbf{q} | V_0 + V_1 | \lambda j\mathbf{k} \rangle$ , where  $\lambda = c, v$  is the band index,  $i/j = (L, \zeta)$  and  $V_L$  (with  $L = 0, 1$ ) the electrostatic potentials generated by the two layers. Assuming tight-binding wave functions, the overlap of electronic wavefunctions is becoming rapidly very small for  $q > 0$ , and thus justifying the restriction

to processes of vanishing momentum transfer  $q$ . In our effective model, where we describe electrons and holes in proximity of high-symmetry points of the Brillouin zone using an effective mass approximation, this allows only intravalley tunneling. We now perform the change of basis into the excitonic picture, as explained in the theory section of the main part yielding:

$$T_X = \sum_{\mu,\nu,\mathbf{Q}} \mathcal{T}_{\mu\nu} X_{\mathbf{Q}}^{\mu\dagger} X_{\mathbf{Q}}^{\nu}. \quad (5)$$

We have introduced the excitonic tunnelling matrix elements

$$\begin{aligned} \mathcal{T}_{\mu\nu} &= \delta_{L_h^\mu L_h^\nu} (1 - \delta_{L_e^\mu L_e^\nu}) \mathcal{T}_{\mu\nu}^c - \delta_{L_e^\mu L_e^\nu} (1 - \delta_{L_h^\mu L_h^\nu}) \mathcal{T}_{\mu\nu}^v \\ \mathcal{T}_{\mu\nu}^c &= \delta_{\zeta^\mu \zeta^\nu} T_{ij}^c \mathcal{F}_{\mu\nu} \quad \text{and} \quad \mathcal{T}_{\mu\nu}^v = \delta_{\zeta^\mu \zeta^\nu} T_{ij}^v \mathcal{F}_{\mu\nu} \end{aligned} \quad (6)$$

with  $\mathcal{F}_{\mu\nu} = \sum_{\mathbf{k}} \psi^{\mu*}(\mathbf{k}) \psi^\nu(\mathbf{k})$  and  $T_{ij}^\lambda$  defined as in Eq. (4) with  $i, j$  describing the electron/hole quantum numbers.

**Hybrid-exciton-phonon and hybrid-exciton-light Hamiltonian:** The contribution of the electron-phonon interaction to the Hamiltonian reads in second quantization

$$\begin{aligned} H_{e-ph} &= \sum_{m,n,\lambda,j} D_{j,\mathbf{k}_m-\mathbf{k}_n}^{\zeta_m^\lambda \zeta_n^\lambda} a_{\lambda,m}^\dagger a_{\lambda,n} \left( b_{j,\mathbf{k}_n-\mathbf{k}_m} + b_{j,\mathbf{k}_m-\mathbf{k}_n}^\dagger \right) \\ \text{with } D_{j,\mathbf{q}}^{\zeta_m^\lambda \zeta_n^\lambda} &\approx \sqrt{\frac{\hbar}{2\rho_{L_j^{ph}} A \Omega_{j\mathbf{q}}}} \tilde{D}_{j,\mathbf{q}}^{\zeta_m^\lambda \zeta_n^\lambda} \\ \text{and } \tilde{D}_{j,\mathbf{q}}^{\zeta_m^\lambda \zeta_n^\lambda} &= \begin{cases} \tilde{D}_{\zeta}^\lambda \mathbf{q} & \text{if } \zeta_m^\lambda = \zeta_n^\lambda = \zeta \quad \text{and } \kappa_j = TA, LA \\ \tilde{D}_{\zeta_m^\lambda \zeta_n^\lambda}^\lambda & \text{else} \end{cases} \\ \text{and } \Omega_{j\mathbf{q}} &= \begin{cases} v_j \mathbf{q} & \text{if } \kappa_j = TA, LA \\ \Omega_j & \text{else} \end{cases} \end{aligned} \quad (7)$$

where  $a_m^{\lambda(\dagger)}$  are electron (creation) annihilation operators with  $\lambda$  as the band index and  $m = (\mathbf{k}_m, \zeta_m, L_m)$  labelling the different electronic quantum states. Here,  $\mathbf{k}_m$  denotes the electron momentum with respect to the main high-symmetry point labeled by  $\zeta_m$ . Furthermore, we have introduced  $b_{j,\mathbf{q}}^{(\dagger)}$  as phonon (creation) annihilation operators with  $j = (\kappa_j, \zeta_j^{ph}, L_j^{ph})$  as compound index including the phonon branch  $\kappa_j$ , the phonon valley index  $\zeta_j^{ph}$  and the phonon layer index  $L_j^{ph}$ . Finally,  $\rho$  denotes the surface mass density of the TMD layer. The strength of the electron-phonon coupling  $\tilde{D}_{\zeta_m^\lambda \zeta_n^\lambda}^\lambda$ , the sound velocities ( $v_\alpha$ ) and energy of optical phonons ( $\Omega_{\zeta_j^{ph}}^\lambda$ ) are taken from DFT calculations [4].

Now, we change into the excitonic basis yielding the exciton-phonon Hamiltonian

$$\begin{aligned} H_{X-ph} &= \sum_{j,\mathbf{Q},\mathbf{q},\mu,\nu} \tilde{D}_{j,\mathbf{q},\mathbf{Q}}^{\nu\mu} X_{\mathbf{Q}+\mathbf{q}}^{\nu\dagger} X_{\mathbf{Q}}^\mu b_{j,\mathbf{q}} + h.c. \\ \text{with } \tilde{D}_{j,\mathbf{q},\mathbf{Q}}^{\nu\mu} &= D_{j,\mathbf{q}}^{\zeta_\mu^e \zeta_\nu^e} \delta_{\zeta_\mu^e \zeta_\nu^e} \delta_{\zeta_\mu^e - \zeta_\nu^e, \zeta_j^{ph}} \delta_{L_\nu^e, L_j^{ph}} \delta_{L_\nu^e, L_\mu^e} \mathcal{F}^{\mu\nu} (\beta_\nu [\mathbf{q} + s_{\mu\nu} \mathbf{Q}]) + \\ &\quad - D_{j,\mathbf{q}}^{\zeta_\mu^h \zeta_\nu^h} \delta_{\zeta_\mu^h \zeta_\nu^h} \delta_{\zeta_\mu^h - \zeta_\nu^h, \zeta_j^{ph}} \delta_{L_\nu^h, L_j^{ph}} \delta_{L_\nu^h, L_\mu^h} \mathcal{F}^{\mu\nu} (-\alpha_\nu [\mathbf{q} + s_{\mu\nu} \mathbf{Q}]) \\ \text{and } \mathcal{F}^{\mu\nu}(\mathbf{q}) &= \sum_{\mathbf{k}} \psi^{\mu*}(\mathbf{k} + \mathbf{q}) \psi^\nu(\mathbf{k}) \end{aligned} \quad (8)$$

with the excitonic eigenfunction  $\psi^\mu(\mathbf{k})$  and with  $s_{\mu\nu} = 1 - M_\nu/M_\mu$ . Since  $s_{\mu\nu} \mathbf{Q}$  is a small vector in comparison to the phonon momentum in the intervalley scattering process, we can neglect the  $\mathbf{Q}$ -dependence in the form

factors  $\mathcal{F}$ . This implies  $\mathcal{D}_{j,\mathbf{q},\mathbf{Q}}^{\nu\mu} \approx \mathcal{D}_{j,\mathbf{q}}^{\nu\mu}$ . Finally, we perform the change into the hybrid-exciton basis [3], as introduced in the main text, and we arrive at the following final hybrid-exciton-phonon Hamiltonian

$$H_{Y-ph} = \sum_{j,\mathbf{Q},\mathbf{q},\eta,\xi} \mathcal{D}_{j,\mathbf{q},\mathbf{Q}}^{\xi\eta} Y_{\mathbf{Q}+\mathbf{q}}^{\xi\dagger} Y_{\mathbf{Q}}^{\eta} b_{j,\mathbf{q}} + h.c. \quad (9)$$

with  $\mathcal{D}_{j,\mathbf{q},\mathbf{Q}}^{\xi\eta} = \sum_{\mu,\nu} c_{\mu}^{\eta*}(\mathbf{Q}) c_{\nu}^{\xi}(\mathbf{Q}+\mathbf{q}) \tilde{\mathcal{D}}_{j,\mathbf{q}}^{\nu\mu}$ .

To include an optical excitation with a laser pulse, we use the interband part of the light-electron interaction Hamiltonian

$$H_{e-l} = \frac{e_0}{m_0} \sum_{m,n,\sigma} \mathbf{A} \cdot \mathbf{M}_{mn,\sigma}^{cv} a_{c,m}^{\dagger} a_{v,n} \quad (10)$$

where  $e_0, m_0$  are the electron charge and mass, respectively. Furthermore,  $\mathbf{M}_{mn,\sigma}^{cv} = -i\hbar \langle n_v | \nabla | m_c \rangle$  is the optical matrix element containing the selection rules for the system with  $\sigma$  describing the polarization and  $\mathbf{A}$  the vector potential of the light pulse. Now, we change to the exciton picture obtaining

$$H_{X-l} = \sum_{\sigma,\mathbf{Q},\mu} \mathbf{A} \cdot \mathcal{M}_{\mathbf{Q}\sigma}^{\mu} X_{\mathbf{Q}}^{\mu} + h.c. \quad (11)$$

with  $\mathcal{M}_{\mathbf{Q}\sigma}^{\mu} = \frac{e_0}{m_0} \delta_{\zeta_e^{\mu} \zeta_h^{\mu}, \mathbf{K}\mathbf{K}} \mathbf{M}_{\mathbf{Q}\sigma}^{cv} \sum_{\mathbf{k}} \psi^{\mu*}(\mathbf{k})$ .

It is important to notice that inside  $\mathbf{M}_{\mathbf{Q}\sigma}^{cv}$  the selection rules imply that the electron and hole have to be localized at the K valley, since photons exhibit only a negligible momentum and can only induce direct transitions. In the hybrid-exciton basis, we obtain

**Hybrid-exciton dynamics:** After truncating the hierarchy problem to include only single-particle and two-particle contributions, we obtain two coupled equations

$$\partial_t N_{\mathbf{Q}}^{\eta} = \frac{2}{\hbar} \sum_{\xi,\mathbf{Q},\pm} \text{Im} \left( \mathcal{D}_{j,\mathbf{q}}^{\xi\eta} \mathcal{C}_{j\mathbf{q}\mathbf{Q}}^{\eta\xi,\pm} \right) \quad (12)$$

$$i\hbar \partial_t \mathcal{C}_{j\mathbf{q}\mathbf{Q}}^{\eta\xi,\pm} = \left( \mathcal{E}_{\mathbf{Q}-\mathbf{q}}^{\xi} - \mathcal{E}_{\mathbf{Q}}^{\eta} \mp \hbar\Omega_{j\mathbf{q}} \right) \mathcal{C}_{j\mathbf{q}\mathbf{Q}}^{\eta\xi,\pm} - \mathcal{D}_{j,\mathbf{q}}^{\xi\eta*} \left( \beta_{\mathbf{q}}^{\mp} N_{\mathbf{Q}-\mathbf{q}}^{\xi} - \beta_{\mathbf{q}}^{\mp} N_{\mathbf{Q}}^{\eta} \right)$$

where we have defined  $\mathcal{C}_{j\mathbf{q}\mathbf{Q}}^{\eta\xi,\pm} = \langle Y_{\mathbf{Q}}^{\eta\dagger} Y_{\mathbf{Q}-\mathbf{q}}^{\xi} b_{j,\mp,\mathbf{q}}^{\dagger/0} \rangle$ , and  $\beta_{\mathbf{q}}^{\pm} = 1/2 \mp 1/2 + \langle b_{\mathbf{q}}^{\dagger} b_{\mathbf{q}} \rangle$ . To obtain the second equation we have neglected non-linear terms in the densities ( $\propto N^2$ ). Now, we apply the Markov approximation [5–8] for solving the equation for  $\mathcal{C}_{j\mathbf{q}\mathbf{Q}}^{\eta\xi,\pm}$  yielding

$$\mathcal{C}_{j\mathbf{q}\mathbf{Q}}^{\eta\xi,\pm} \approx i\pi \mathcal{D}_{j,\mathbf{q}}^{\xi\eta*} \left( \beta_{\mathbf{q}}^{\mp} N_{\mathbf{Q}-\mathbf{q}}^{\xi} - \beta_{\mathbf{q}}^{\pm} N_{\mathbf{Q}}^{\eta} \right) \delta \left( \mathcal{E}_{\mathbf{Q}-\mathbf{q}}^{\xi} - \mathcal{E}_{\mathbf{Q}}^{\eta} \mp \hbar\Omega_{j\mathbf{q}} \right) \quad (13)$$

which inserted in the first equation of Eq. (12) results in the Boltzmann scattering equation

$$\partial_t N_{\mathbf{Q}}^{\eta} = \sum_{\xi,\mathbf{Q}'} \left( W_{\mathbf{Q}'\mathbf{Q}}^{\xi\eta} N_{\mathbf{Q}'}^{\xi} - W_{\mathbf{Q}\mathbf{Q}'}^{\eta\xi} N_{\mathbf{Q}}^{\eta} \right) \quad (14)$$

$$W_{\mathbf{Q}\mathbf{Q}'}^{\eta\xi} = \frac{2\pi}{\hbar} \sum_{j,\pm} \left| \mathcal{D}_{j,\mathbf{Q}'-\mathbf{Q}}^{\eta\xi} \right|^2 \left( \frac{1}{2} \pm \frac{1}{2} + n_{j,\mathbf{Q}'-\mathbf{Q}}^{ph} \right) \delta \left( \mathcal{E}_{\mathbf{Q}'}^{\xi} - \mathcal{E}_{\mathbf{Q}}^{\eta} \mp \hbar\Omega_{j\mathbf{Q}'-\mathbf{Q}} \right)$$

We introduce the coherent hybrid polarization  $P_{\mathbf{Q}}^{\eta} = \langle Y_{\mathbf{Q}}^{\eta\dagger} \rangle$  and the incoherent hybrid exciton population

$$\delta N_{\mathbf{Q}}^{\eta} = \langle Y_{\mathbf{Q}}^{\eta\dagger} Y_{\mathbf{Q}}^{\eta} \rangle - \langle Y_{\mathbf{Q}}^{\eta\dagger} \rangle \langle Y_{\mathbf{Q}}^{\eta} \rangle = N_{\mathbf{Q}}^{\eta} - \left| P_{\mathbf{Q}}^{\eta} \right|^2. \quad (15)$$

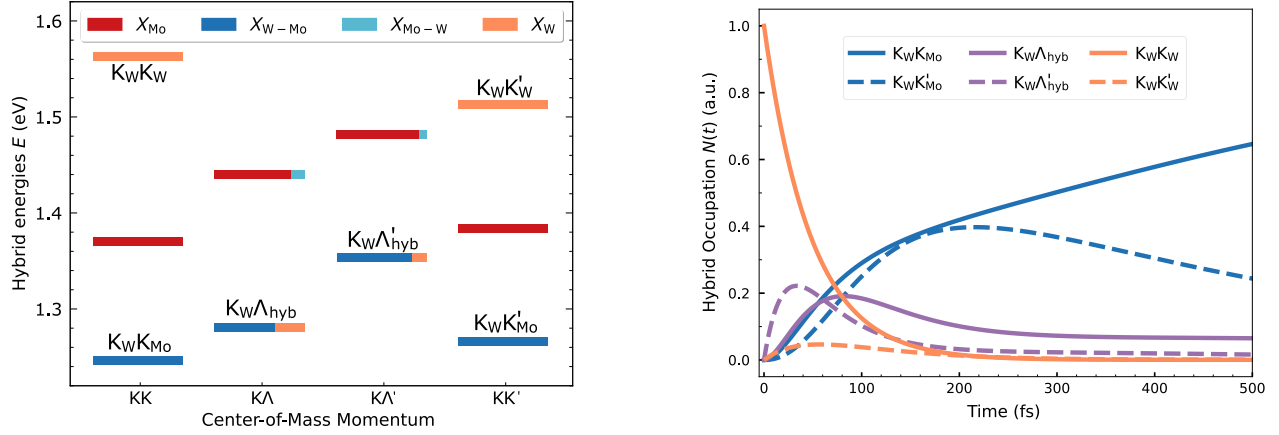


FIG. 1: (a) Hybrid-exciton energy landscape and (b) momentum-integrated dynamics for MoSe<sub>2</sub>-WSe<sub>2</sub> in R<sub>h</sub><sup>M</sup> stacking at 77 K.

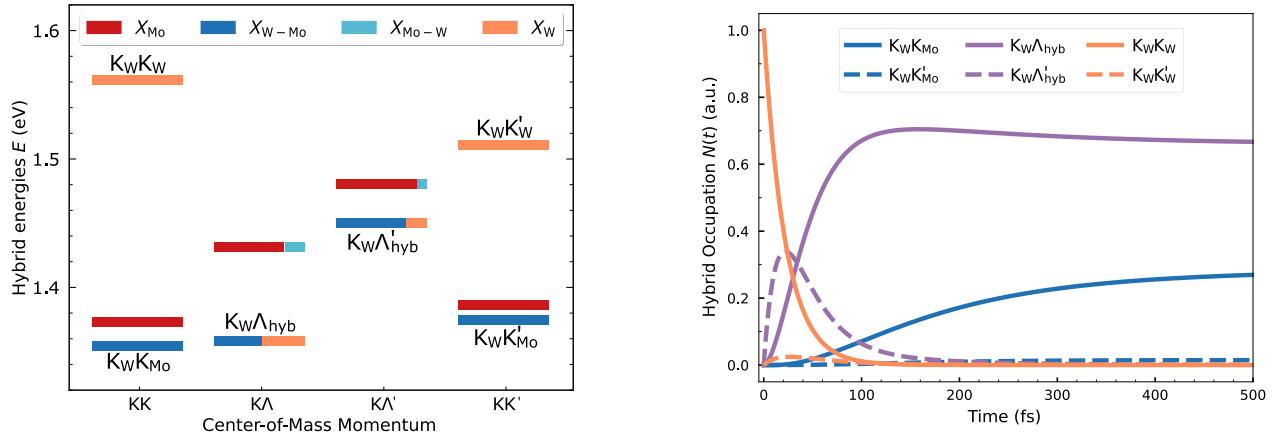


FIG. 2: (a) Hybrid-exciton energy landscape and (b) momentum-integrated dynamics for MoSe<sub>2</sub>-WSe<sub>2</sub> in R<sub>h</sub><sup>X</sup> stacking at 77 K.

As next, we derive the equation of motion for the coherent polarization

$$i\hbar\partial_t P_0^\eta = -(\mathcal{E}_0^\eta + i\Gamma_0^\eta)P_0^\eta - \tilde{\mathcal{M}}_0^\eta \cdot \mathbf{A}(t) \quad (16)$$

where 0 refers to  $\mathbf{Q} = 0$  due to the condition that the laser pulse only creates hybrid excitons around  $\mathbf{Q} = 0$  at the K valley. The incoherent dynamics is given by

$$\delta\dot{N}_\mathbf{Q}^\eta = \partial_t \left( N_\mathbf{Q}^\eta - |P_\mathbf{Q}^\eta|^2 \right) = \dot{N}_\mathbf{Q}^\eta - 2\text{Re} \left\{ \dot{P}_\mathbf{Q}^\eta P_\mathbf{Q}^{\eta*} \right\} \delta_{\mathbf{Q}=0} \quad (17)$$

which yields the equation of motion for incoherent hybrid exciton densities

$$\delta\dot{N}_\mathbf{Q}^\eta = \sum_\xi W_{0\mathbf{Q}}^{\xi\eta} |P_0^\eta|^2 + \sum_{\xi, \mathbf{Q}'} \left( W_{\mathbf{Q}\mathbf{Q}'}^{\xi\eta} \delta N_{\mathbf{Q}'}^\xi - W_{\mathbf{Q}\mathbf{Q}'}^{\eta\xi} \delta N_\mathbf{Q}^\eta \right) \quad (18)$$

We use the last equation to track the dynamics of hybrid excitons in TMD heterostructures including the polarization to population transfer creating incoherent excitons as well as phonon-assisted exciton relaxation into an equilibrium Boltzmann distribution.

## CHARGE TRANSFER IN THE MOSE<sub>2</sub>-WSE<sub>2</sub> HETEROSTRUCTURE

In the main manuscript, we have discussed the hybrid exciton landscape and dynamics in  $R_h^h$  stacking. Here, we show the other two high-symmetry stackings  $R_h^M$  and  $R_h^X$ . The main difference originates from a more pronounced tunneling at the  $\Lambda$  point. This is due to wave function overlap around the  $\Lambda$  point which has a significantly high contribution also from chalcogen atoms in these stackings [9]. This results in larger red-shifts of  $K\Lambda_{\text{hyb}}$  excitons bringing them closer to the energetically lowest interlayer  $K_W K_{M_0}$  excitons, cf. Figs. 1(a) and 2(a). The hybrid-exciton dynamics remains generally the same as for the  $R_h^h$  stacking, i.e. the charge transfer occurs in a two-step process via phonon-mediated scattering into the strongly hybridized  $K\Lambda_{\text{hyb}}$  excitons, cf. Figs. 1(b) and 2(b). The main difference is a larger stationary population of the hybrid  $K\Lambda_{\text{hyb}}$  excitons state as they are closer in energy to the  $K_W K_{M_0}$  excitons (cf. solid purple line in Figs. 1(b) and 2(b)). This means that the charge transfer is more incomplete compared to the  $R_h^h$  stacking. This is in particular the case for the  $R_h^X$  stacking, where  $K\Lambda_{\text{hyb}}$  and  $K_W K_{M_0}$  excitons are nearly degenerate, cf. Figs. 2(a), as further discussed in the main text.

## INTERPLAY OF OPTICAL PUMPING AND DYNAMICS

While in the main text we have considered the situation of an instantaneous initial non-equilibrium population in the intralayer  $K_W K_W$  exciton and the subsequent relaxation cascade, we investigate here the hybrid-exciton dynamics taking explicitly into account the interplay of optical pumping and relaxation dynamics.

We apply a laser pulse with a width of 50 fs and an energy resonant to  $K_W K_W$  excitons and investigate the MoSe<sub>2</sub>-WSe<sub>2</sub> heterostructure in  $R_h^h$  at 77 K, cf. Fig. 3. Comparing the dynamics with the instantaneous initial population in the main text, we observe the same qualitative behaviour in terms of the two-step charge transfer process via phonon-mediated scattering into the strongly hybridized  $K\Lambda_{\text{hyb}}$  excitons. The main difference occurs in the early stage of the dynamics, i.e. as soon as hybrid-excitons are generated they start relaxing to lower energy state. As a result, the maximum occupation of  $K_W K_W$  does not go beyond 0.5.

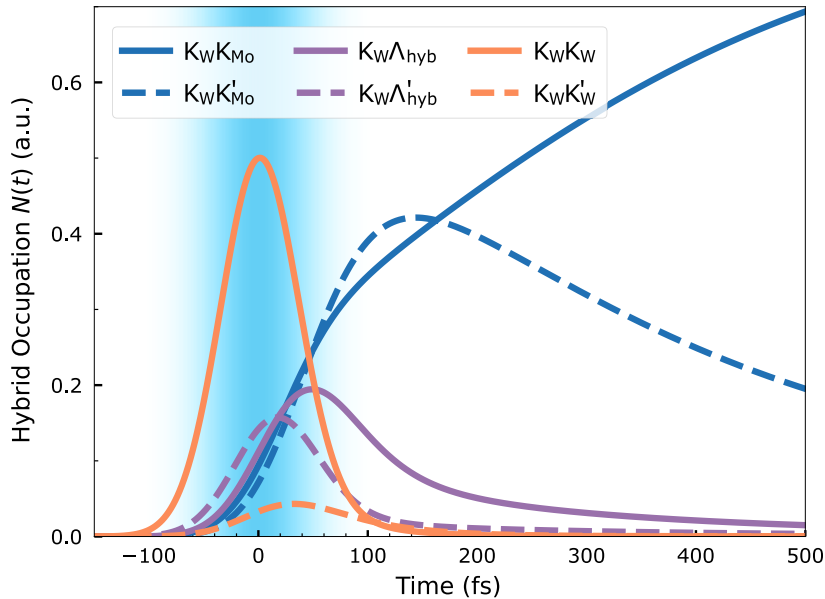


FIG. 3: Momentum-integrated hybrid-exciton dynamics at 77 K for MoSe<sub>2</sub>-WSe<sub>2</sub> in  $R_h^h$  stacking after optical excitation with a laser pulse that is resonant to the  $K_W K_W$  excitons in the WSe<sub>2</sub> layer and has width of 50 fs. During the laser pulse there is an interplay of optical excitation and phonon-mediated hybrid-exciton relaxation and charge transfer processes.

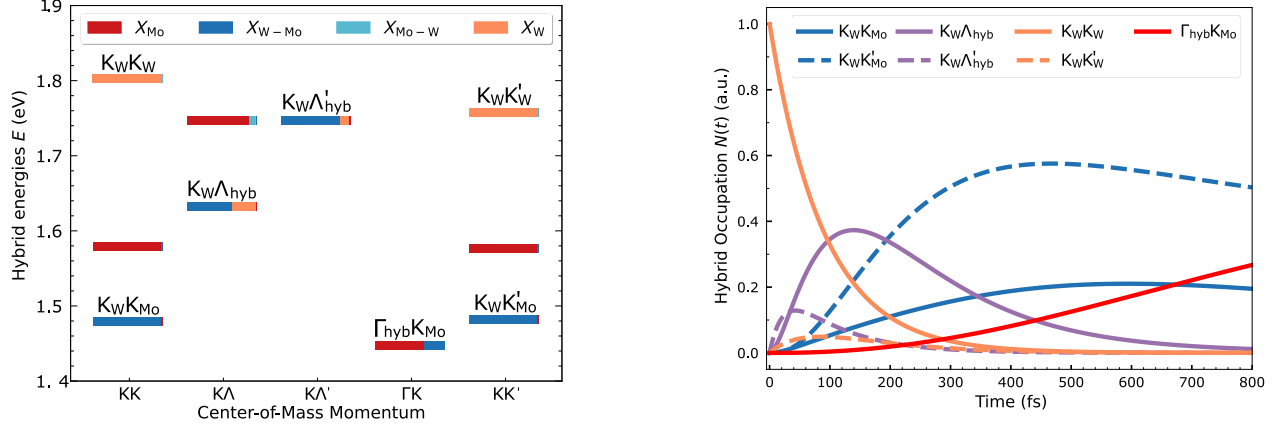


FIG. 4: (a) Hybrid-exciton energy landscape and (b) momentum-integrated dynamics for MoS<sub>2</sub>-WS<sub>2</sub> in R<sub>h</sub><sup>h</sup> stacking at 77 K.

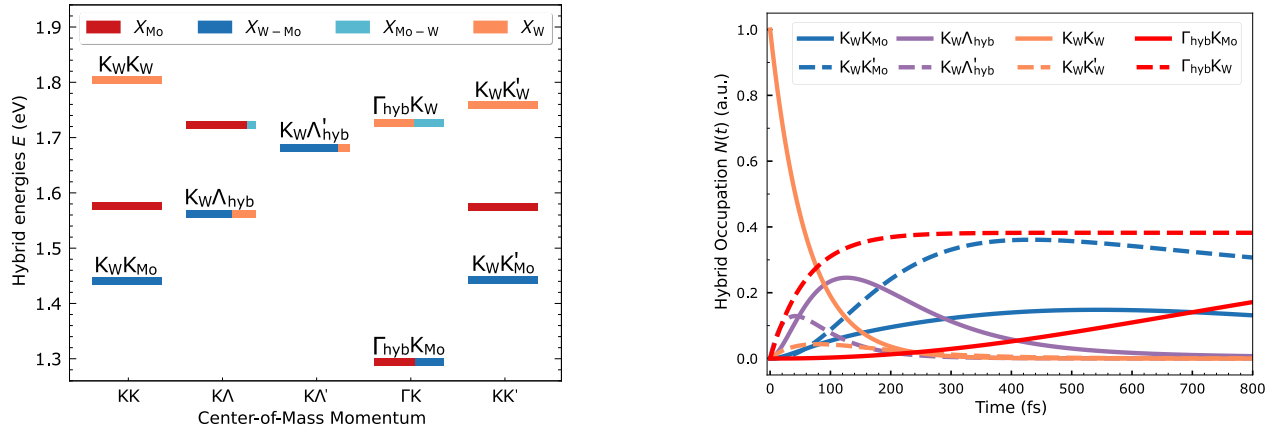


FIG. 5: (a) Hybrid-exciton energy landscape and (b) momentum-integrated dynamics for MoS<sub>2</sub>-WS<sub>2</sub> in R<sub>h</sub><sup>M</sup> stacking at 77 K.

Other than that the hybrid exciton dynamics is almost identical with the one in the main text. However, the interplay of an inward and outward flux of hybrid-excitons from the initial state add an external dependence on the excitation processes, which makes the evaluation of an intrinsic timescale for the charge transfer more complicated. As the dynamics is the same, we have decided to study the charge transfer using the simpler initialization in the main text.

### CHARGE TRANSFER IN THE MoS<sub>2</sub>-WS<sub>2</sub> HETEROSTRUCTURE

Here, we present the results for the MoS<sub>2</sub>-WS<sub>2</sub> heterostructure and discuss in particular the differences compared to the MoSe<sub>2</sub>-WSe<sub>2</sub> heterostructure discussed in the main part. The main difference in the hybrid-exciton energy landscape is the appearance of the Γ<sub>hyb</sub>K<sub>Mo</sub> exciton as the energetically lowest state for all three high-symmetry stackings, cf. Figs. 4, 5, and 6. We find that it is a highly hybridized state consisting of interlayer and intralayer excitons in the Mo layer. This means that for the MoS<sub>2</sub>-WS<sub>2</sub> heterostructure the charge transfer will be a three-step process. There is first a phonon-mediated electron transfer that occurs via scattering to the hybridized K<sub>W</sub>Λ<sub>hyb</sub> excitons to the interlayer K<sub>W</sub>K<sub>Mo</sub> states - similar to the situation in the MoSe<sub>2</sub>-WSe<sub>2</sub> bilayer, discussed in the main part. In contrast to the latter, in MoS<sub>2</sub>-WS<sub>2</sub>, the electron transfer is followed by a consecutive hole transfer to the energetically lowest Γ<sub>hyb</sub>K<sub>Mo</sub> excitons. This occurs on a slower timescale in the range of hundreds of femtoseconds, cf. the red solid lines in Figs. 4(b), 5(b),

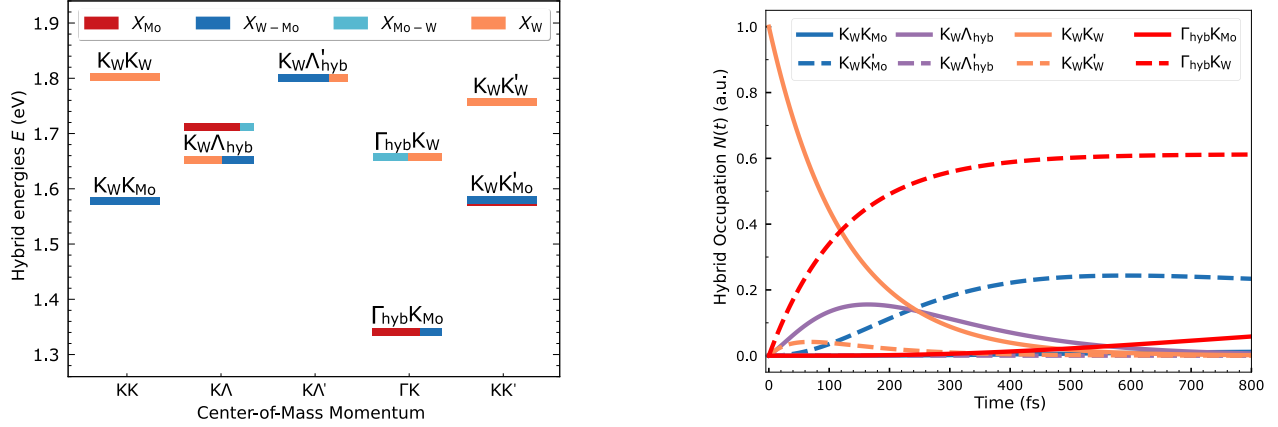


FIG. 6: (a) Hybrid-exciton energy landscape and (b) momentum-integrated dynamics for MoS<sub>2</sub>-WS<sub>2</sub> in  $R_h^X$  stacking at 77 K.

and 6(b).

The much larger energy window and the relative energy difference between the states relevant for the relaxation cascade make the charge transfer processes slower in MoS<sub>2</sub>-WS<sub>2</sub>. We predict a characteristic time for the charge transfer to be  $\tau = 142$  fs for  $R_h^h$  stacking at 77 K (Fig. 7(a)), which is almost double as large as for MoSe<sub>2</sub>-WSe<sub>2</sub>. Furthermore, the stacking dependence is more pronounced, since the strong tunnelling at the  $\Gamma$  point and the corresponding red-shift makes the  $\Gamma_{hyb} K_W$  state accessible through scattering with phonons in the case of  $R_h^M$  and  $R_h^X$  stacking (cf. Figs. 5(a) and 6(a)). This state considerably slows down the

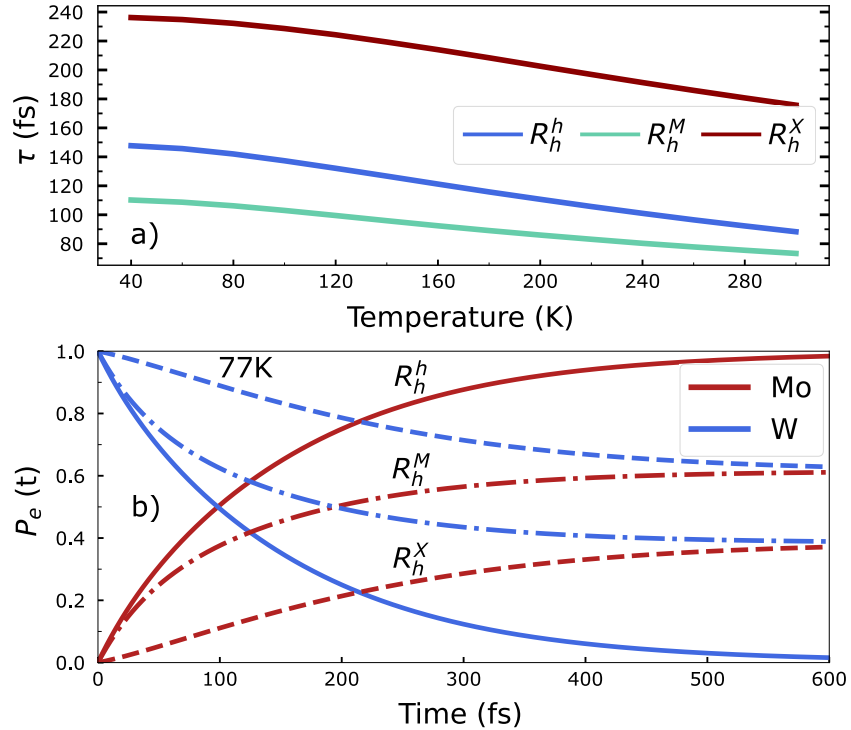


FIG. 7: (a) Characteristic charge transfer time for MoS<sub>2</sub>-WS<sub>2</sub> for all three high-symmetry stackings at 77 K. The time is evaluated through an exponential fit of the electron probability  $P_e$  plotted in part (b). We observe a complete charge transfer for  $R_h^h$  stacking (solid lines), while there is only a partial charge transfer for  $R_h^X$  and  $R_h^M$  stackings (dashed and dashed-dotted lines).

electron transfer, since the population entering the state is trapped and cannot further relax. There is only the  $K_W\Lambda_{\text{hyb}}$  state in the vicinity which has a similar composition and could be a scattering partner. However, the scattering into this state requires a simultaneous electron and hole scatter, which is a weak high-order process. As the  $\Gamma_{\text{hyb}}K_W$  state is relatively low in energy in the  $R_h^X$  stacking, the percentage of population trapped in this state is higher with respect to the  $R_h^M$  stacking ( $P_e = 0.38$  for  $R_h^X$  against  $P_e = 0.61$  for  $R_h^M$ , cf. Fig. 7(b)). This explains the slowest charge transfer found for  $R_h^X$  stacking.

---

\* giuseppe.meneghini@physik.uni-marburg.de

- [1] Simon Ovesen, Samuel Brem, Christopher Linderälv, Mikael Kuisma, Tobias Korn, Paul Erhart, Malte Selig, and Ermin Malic, “Interlayer exciton dynamics in van der waals heterostructures,” *Communications Physics* **2**, 1–8 (2019).
- [2] Samuel Brem, Christopher Linderälv, Paul Erhart, and Ermin Malic, “Tunable phases of moiré excitons in van der waals heterostructures,” *Nano letters* **20**, 8534–8540 (2020).
- [3] Samuel Brem, Kai-Qiang Lin, Roland Gillen, Jonas M Bauer, Janina Maultzsch, John M Lupton, and Ermin Malic, “Hybridized intervalley moiré excitons and flat bands in twisted wse 2 bilayers,” *Nanoscale* **12**, 11088–11094 (2020).
- [4] Jin Z, Li X, Mullen J T, and Kim K W, “Intrinsic transport properties of electrons and holes in monolayer transition-metal dichalcogenides,” *Phys. Rev. B* **90**, 045422 (2014).
- [5] Malte Selig, Gunnar Berghäuser, Marten Richter, Rudolf Bratschitsch, Andreas Knorr, and Ermin Malic, “Dark and bright exciton formation, thermalization, and photoluminescence in monolayer transition metal dichalcogenides,” *2D Materials* **5**, 035017 (2018).
- [6] Hartmut Haug and Stephan W Koch, *Quantum theory of the optical and electronic properties of semiconductors* (World Scientific Publishing Company, 2009).
- [7] A Thränhardt, S Kuckenburger, A Knorr, T Meier, and SW Koch, “Quantum theory of phonon-assisted exciton formation and luminescence in semiconductor quantum wells,” *Physical Review B* **62**, 2706 (2000).
- [8] Samuel Brem, Malte Selig, Gunnar Berghäuser, and Ermin Malic, “Exciton relaxation cascade in two-dimensional transition metal dichalcogenides,” *Scientific reports* **8**, 1–8 (2018).
- [9] Joakim Hagel, Samuel Brem, Christopher Linderälv, Paul Erhart, and Ermin Malic, “Exciton landscape in van der waals heterostructures,” *Physical Review Research* **3**, 043217 (2021).

---

Paper 2

---

# Formation of moiré interlayer excitons in space and time

<https://doi.org/10.1038/s41586-022-04977-7>

Received: 5 November 2021

Accepted: 14 June 2022

Published online: 17 August 2022

 Check for updates

David Schmitt<sup>1</sup>, Jan Philipp Bange<sup>1</sup>, Wiebke Bennecke<sup>1</sup>, AbdulAziz AlMutairi<sup>2</sup>, Giuseppe Meneghini<sup>3</sup>, Kenji Watanabe<sup>4</sup>, Takashi Taniguchi<sup>5</sup>, Daniel Steil<sup>1</sup>, D. Russell Luke<sup>6</sup>, R. Thomas Weitz<sup>1,7</sup>, Sabine Steil<sup>1</sup>, G. S. Matthijs Jansen<sup>1</sup>, Samuel Brem<sup>3</sup>, Ermin Malic<sup>3,8</sup>, Stephan Hofmann<sup>2</sup>, Marcel Reutzell<sup>1,✉</sup> & Stefan Mathias<sup>1,7,✉</sup>

Moiré superlattices in atomically thin van der Waals heterostructures hold great promise for extended control of electronic and valleytronic lifetimes<sup>1–7</sup>, the confinement of excitons in artificial moiré lattices<sup>8–13</sup> and the formation of exotic quantum phases<sup>14–18</sup>. Such moiré-induced emergent phenomena are particularly strong for interlayer excitons, where the hole and the electron are localized in different layers of the heterostructure<sup>19,20</sup>. To exploit the full potential of correlated moiré and exciton physics, a thorough understanding of the ultrafast interlayer exciton formation process and the real-space wavefunction confinement is indispensable. Here we show that femtosecond photoemission momentum microscopy provides quantitative access to these key properties of the moiré interlayer excitons. First, we elucidate that interlayer excitons are dominantly formed through femtosecond exciton–phonon scattering and subsequent charge transfer at the interlayer-hybridized  $\Sigma$  valleys. Second, we show that interlayer excitons exhibit a momentum fingerprint that is a direct hallmark of the superlattice moiré modification. Third, we reconstruct the wavefunction distribution of the electronic part of the exciton and compare the size with the real-space moiré superlattice. Our work provides direct access to interlayer exciton formation dynamics in space and time and reveals opportunities to study correlated moiré and exciton physics for the future realization of exotic quantum phases of matter.

The advent of two-dimensional van der Waals materials<sup>21</sup> has led to remarkable strategies to manipulate correlated material properties. In transition-metal dichalcogenides (TMDs), exceptional light–matter coupling and weak Coulomb screening of photoexcited electron–hole pairs allows the realization of novel spin, valley and excitonic properties of matter<sup>22,23</sup>. Even more intriguing material properties can be accomplished in TMDs by stacking several monolayers into heterostructures<sup>19,20,24</sup>. In type II band-aligned stacks, novel excitonic states can be created, where the electron and the hole contribution to the exciton are separated between the van der Waals-coupled TMDs<sup>13</sup> (Fig. 1e). A key question that remains unanswered is how these interlayer excitons (ILXs) are formed. Furthermore, the lattice mismatch and the twist angle between the TMDs induce a moiré superlattice, which makes it necessary to understand how precisely the interaction of the exciton and the moiré potential determines the material properties (Fig. 1d). Most intriguingly, it has been shown by optical<sup>10–12</sup> and momentum microscopy<sup>13</sup> experiments that ILXs can be confined within the moiré potential minima. However, a substantial open

challenge is the experimental identification of universal hallmarks that indicate signatures of the moiré superlattice imprinted onto the ILX.

Experimental quantitative insight into the ILX formation process and the influence of moiré modulation on the ILX is currently limited. All-optical spectroscopy techniques are sensitive only to transitions within the light cone<sup>25</sup> and thus lack the momentum information that is necessary to gain access to the time-dependent energy–momentum fingerprints of the probed quasiparticles<sup>26–28</sup>. Using multidimensional time- and angle-resolved photoelectron spectroscopy (trARPES) on a tungsten diselenide/molybdenum disulfide ( $WSe_2/MoS_2$ ) heterostructure, we experimentally find that ILXs are dominantly formed through exciton–phonon scattering via intermediate dark excitonic states at the  $\Sigma$  valleys of the hexagonal Brillouin zones. These results are fully supported by a microscopic model including exciton–light and exciton–phonon interaction on a microscopic footing. Furthermore, we observe a complex momentum fingerprint of the ILX, and we show that this fingerprint is a direct hallmark signature of the moiré

<sup>1</sup>Physikalisches Institut, Georg-August-Universität Göttingen, Göttingen, Germany. <sup>2</sup>Department of Engineering, University of Cambridge, Cambridge, UK. <sup>3</sup>Fachbereich Physik, Philipps-Universität, Marburg, Germany. <sup>4</sup>Research Center for Functional Materials, National Institute for Materials Science, Tsukuba, Japan. <sup>5</sup>International Center for Materials Nanoarchitectonics, National Institute for Materials Science, Tsukuba, Japan. <sup>6</sup>Institute for Numerical and Applied Mathematics, Georg-August-Universität Göttingen, Göttingen, Germany. <sup>7</sup>International Center for Advanced Studies of Energy Conversion (ICASEC), University of Göttingen, Göttingen, Germany. <sup>8</sup>Department of Physics, Chalmers University of Technology, Gothenburg, Sweden.

✉e-mail: marcel.reutzell@phys.uni-goettingen.de; smathias@uni-goettingen.de

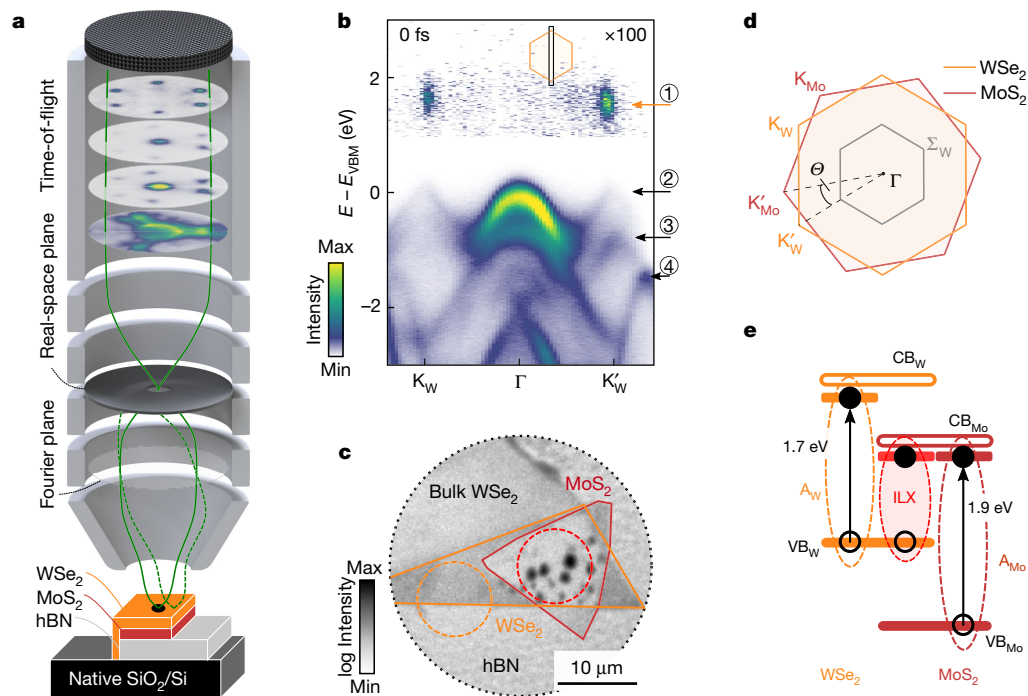


**Fig. 1 | Inter- and intralayer excitons in WSe<sub>2</sub>/MoS<sub>2</sub> probed by femtosecond momentum microscopy.** **a**, Illustration of the experimental set-up and the WSe<sub>2</sub>/MoS<sub>2</sub>/hBN sample. **b**, The valence bands of WSe<sub>2</sub> (2), MoS<sub>2</sub> (3) and hBN (4) are labelled in the energy–momentum cut. At 0 fs, bright A<sub>w</sub> excitons (1) are detected at the K<sub>w</sub> and K'<sub>w</sub> valleys of WSe<sub>2</sub>. **c**, The heterostructure can be identified in the real-space mode of the microscope. The WSe<sub>2</sub>/MoS<sub>2</sub> and WSe<sub>2</sub> regions of interest are indicated by red and orange circles, respectively

(10- $\mu$ m diameter; Methods). **d**, The hexagonal Brillouin zones of WSe<sub>2</sub> (orange) and MoS<sub>2</sub> (dark red) are misaligned by a twist angle  $\theta$ . **e**, Bright A<sub>w</sub> and A<sub>Mo</sub> excitons of WSe<sub>2</sub> (orange) and MoS<sub>2</sub> (dark red) can be resonantly excited with 1.7-eV and 1.9-eV pump photons, respectively (VB<sub>w</sub> and VB<sub>Mo</sub>, valence-band maxima; CB<sub>w</sub> and CB<sub>Mo</sub>, conduction-band minima). The hole and the electron contribution of the ILX resides in the WSe<sub>2</sub> and MoS<sub>2</sub> layers, respectively.

superlattice modification. From this data, we then reconstruct the real-space wavefunction probability density of the electronic part of the exciton’s wavefunction, which we compare with the moiré superlattice size.

### Electronic band structure of WSe<sub>2</sub>/MoS<sub>2</sub>

We focus our study on the model system WSe<sub>2</sub>/MoS<sub>2</sub> with a twist angle of  $9.8 \pm 0.8^\circ$  (Extended Data Figs. 1 and 4)<sup>29</sup> and use our customized trARPES system that combines a momentum microscope<sup>30</sup> with a high-repetition-rate high-harmonic generation beamline (Fig. 1a and Methods)<sup>31,32</sup>. The 100- $\mu$ m<sup>2</sup> heterobilayer region can be identified in the real-space distribution of the measured photoelectron yield (Fig. 1c and Extended Data Fig. 1e,f). By placing an aperture into the real-space image plane of the microscope (red circle in Fig. 1c), we can selectively probe the occupied band structure of WSe<sub>2</sub>/MoS<sub>2</sub>. The sample quality is evidenced by the sharp spectral features of the occupied electronic structure and the signature of interlayer hybridization of the valence bands of WSe<sub>2</sub> and MoS<sub>2</sub> at the  $\Gamma$  valley<sup>33</sup> (Fig. 1b, energy resolution of about 200 meV; Extended Data Figs. 2 and 3).

### Femtosecond ILX formation dynamics

We follow the build-up process of the ILX by resonantly exciting the optically bright A<sub>w</sub> exciton of WSe<sub>2</sub> with 1.7 eV,  $50 \pm 5$  fs pulses and study the subsequent ILX formation via photoemission with 26.5 eV,  $21 \pm 5$  fs extreme ultraviolet (XUV) probe pulses (see Extended Data Fig. 5 for spectral assignment of the valence and conduction bands and the WSe<sub>2</sub> and MoS<sub>2</sub> A excitons). Figure 2a shows the highest spectral weight for the electronic part of the bright A<sub>w</sub> exciton at a delay of around 0 fs and 1.7 eV above the valence-band maximum (orange dashed line; exciton

density  $(5.4 \pm 1.0) \times 10^{12}$  cm<sup>-2</sup>; compare with Extended Data Fig. 8b)<sup>26–28,34</sup>. On the few-hundred-femtosecond timescale, we observe the formation of a second peak at lower photoemission energy (red dashed line). We identify this peak as the photoemitted electronic contribution of the ILX. The long-lived photoemission signature is detected below the A<sub>w</sub> exciton resonance at about 1.1 eV above the valence-band maximum of WSe<sub>2</sub>, in agreement with static photoluminescence experiments on a WSe<sub>2</sub>/MoS<sub>2</sub> heterobilayer<sup>35</sup>. For the unambiguous attribution of the photoemission yield to an interlayer effect, we repeated the same analysis with data obtained from monolayer WSe<sub>2</sub> (Fig. 2b and dashed orange circle in Fig. 1c). Here, no spectral weight is observed in the ILX’s energetic region, which clearly shows that the spectral weight in the heterobilayer measurement results from the charge transfer of the electron contribution of the exciton into the MoS<sub>2</sub> layer. We note that the identification of the ILX is in agreement with a recent trARPES study on 2°-twisted WSe<sub>2</sub>/MoS<sub>2</sub> (ref. 13). Interestingly, in addition to the electron contribution to the ILX, ref. 13 also identified the hole contribution to the ILX in energy–momentum-resolved spectra. Such a signature is not found in our analysis (Fig. 1b), which is most likely related to the different twist angles and related exciton confinement effects.

The exact mechanism of the ILX formation and the corresponding ultrafast charge separation is still a major open question<sup>20</sup>. It has been proposed that the ILX can be formed through interlayer tunnelling of its electron contribution at the K valleys<sup>5,6</sup>, or, alternatively, through the intermediate formation of dark intralayer excitons, where the electron contribution is first scattered to the  $\Sigma$  valley and, subsequently, transferred to the neighbouring layer<sup>4,36,37</sup>. In this context, the strength of the trARPES experiment is that the femtosecond evolution of optically dark  $\Sigma_w$  excitons can be explicitly monitored<sup>26–28</sup>. In Fig. 2c, we therefore investigate the delay-dependent transfer of spectral weight between the electronic parts of the bright WSe<sub>2</sub> A<sub>w</sub> exciton, the dark WSe<sub>2</sub>  $\Sigma_w$

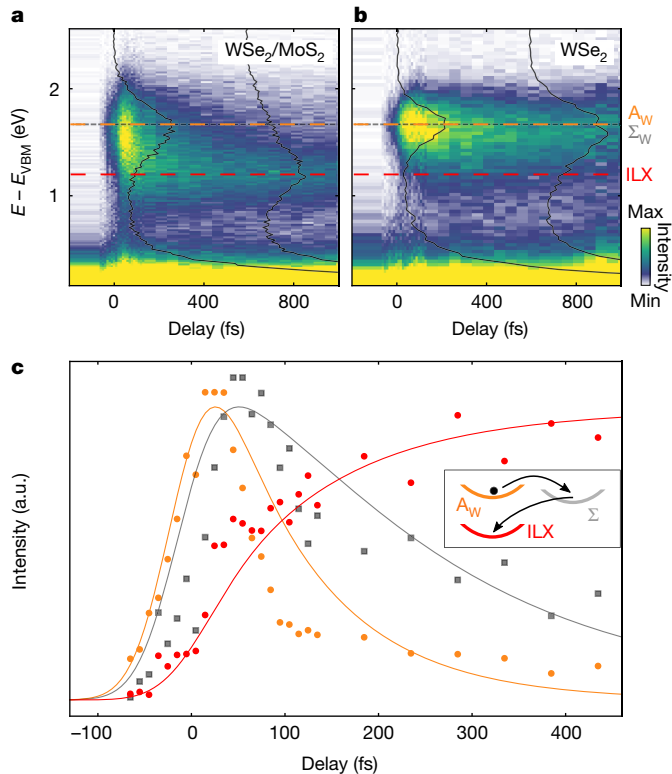


**Fig. 2 | Ultrafast formation dynamics of ILXs. a, b,** Delay-dependent evolution of the momentum-integrated energy-distribution curves for WSe<sub>2</sub>/MoSe<sub>2</sub> (a) and WSe<sub>2</sub> (b). In the monolayer, the signal decays on the picosecond timescale without a notable change in binding energy (dashed orange and grey lines). In the heterobilayer, the ILX formation is evident by the shift of spectral weight to smaller binding energies on the sub-100-fs timescale (dashed red line). The black line profiles are exemplary energy-distribution curves taken at -5 fs and 585 fs. **c,** The ILX formation is extracted through the delay-dependent photoemission yield of the ILX (red), the bright A<sub>W</sub> excitons (orange) and the dark Σ<sub>W</sub> excitons (grey; details on data analysis in Extended Data Figs. 6 and 7). The data points are experimental data and solid lines are calculated within a fully microscopic model. The inset shows the dominant charge-transfer channel. The energy-distribution curves in **a** and **b** are corrected for space-charge- and photovoltage-induced rigid band shifts of maximally 70 meV (Extended Data Fig. 8a).

exciton and the ILX (data handling in Extended Data Figs. 6 and 7; long-term picosecond dynamics in Extended Data Fig. 9). Initially, during the duration of the pump pulse, we find that bright WSe<sub>2</sub> A<sub>W</sub> excitons are efficiently excited (orange data points). Subsequently, the weight of their photoemission signature decreases in intensity, whereas, concomitant, spectral yield is detected for the WSe<sub>2</sub> Σ<sub>W</sub> exciton (grey) and the ILX (red). In particular, we find that for the time evolution after the optical excitation and the initial build-up, the decrease of spectral weight of the electronic contribution of the Σ<sub>W</sub> exciton is synchronous to the increase of spectral weight of the ILX, strongly hinting at an ILX formation process through intermediate scattering through the Σ<sub>W</sub> valley. Here, a quantitative analysis yields delayed onsets with respect to the A<sub>W</sub> exciton signal of 33 ± 6 fs for the Σ<sub>W</sub>-exciton formation and 54 ± 7 fs for the ILX (Extended Data Fig. 9a). To corroborate the proposition of interlayer charge transfer through the Σ<sub>W</sub> valley, we compare the trARPES data with predictions stemming from a fully microscopic model. We combine the density matrix formalism<sup>6,38</sup> with material-specific parameters from first principle calculations to simulate the formation dynamics of interlayer excitons after the optical excitation of intralayer excitons. In the model, we include the full exciton landscape of bright and dark intralayer, interlayer and hybrid excitons

and all phonon-assisted transition channels between these states. We find that the most efficient exciton relaxation pathway is given by the cascade of optically excited exciton states A<sub>W</sub> → Σ<sub>W</sub> → ILX (inset in Fig. 2c; compare with Supplementary Information). The direct comparison of experiment (symbols) and theory (lines) in Fig. 2c confirms an excellent agreement. This shows, from both an experimental and a theoretical point of view, that phonon-assisted scattering through dark-layer mixed states is indeed the dominant pathway for the formation of the ILX in the 9.8 ± 0.8°-twisted WSe<sub>2</sub>/MoSe<sub>2</sub> heterostructure.

### The ILX moiré superlattice hallmark

Although trARPES with XUV pulses is an ideal approach to study the ILX formation process, the combination with multidimensional momentum microscopy allows the identification of momentum-space signatures that are caused by the real-space moiré superlattice. In this manner, Fig. 3a–c shows the momentum structure of the A<sub>W</sub> exciton, the Σ<sub>W</sub> exciton and the ILX, respectively (additional data in Extended Data Fig. 6). Although the momentum fingerprints of the A<sub>W</sub> exciton and the Σ<sub>W</sub> exciton appear as expected<sup>26,27</sup>, the ILX momentum structure is clearly more complex. Without consideration of the moiré superlattice, for the ILX, one would expect to detect photoemission yield at the in-plane momentum of the electron contribution to the quasiparticle, that is, at the K<sub>Mo</sub> (K'<sub>Mo</sub>) valleys of MoSe<sub>2</sub> (corners of the dotted dark red hexagon in Fig. 3c). However, the measured momentum fingerprint shows a strikingly richer structure. We observe a complex momentum structure that is dominated by three peaks that are centred around the K<sub>W</sub> (K'<sub>W</sub>) valleys (orange hexagon in Fig. 3c). Apparently, the ILX momentum fingerprint exhibits additional features that are not observed for any other spectral feature in our data: so far, all other occupied bands and excitonic states were unambiguously assignable to the periodicity of either the WSe<sub>2</sub> top layer or the MoSe<sub>2</sub> bottom layer.

The most interesting question now is whether the observed ILX momentum structure may be identified as a hallmark of the moiré superlattice that is created by the 9.8 ± 0.8°-twisted Brillouin zones of WSe<sub>2</sub> and MoSe<sub>2</sub>. To answer this question, we construct the momentum-space equivalent of the real-space moiré periodicity, which is the mini Brillouin zone (mBZ) that is shown on top of the momentum-resolved photoemission data of the ILX in Fig. 3c (red hexagon). Within the mBZ, we can now unambiguously identify that the three-peak structure is indeed a fingerprint of the moiré superlattice, as the spectral features clearly coincide with the high-symmetry k valleys of the mBZ.

Having identified the correlation between the ILX momentum fingerprint and the moiré superlattice, we aim to model the distinct photoemission intensity distribution of the ILX. For this purpose, we make use of previous studies on interlayer interaction in incommensurate atomic layers<sup>39</sup>. In particular, we follow the notation in ref. <sup>39</sup>, where the interlayer coupling in reciprocal space is expressed in terms of a generalized umklapp process (Fig. 3d; details in Methods). A straightforward geometrical construction following this work yields the intensity distribution shown in Fig. 3d: the highest photoemission yield is expected for momenta marked by circles, which correspond to the k points of the mBZ. Weaker photoemission yield is expected in areas marked by squares, which indeed are partially and faintly visible in the data. Finally, negligible signal is expected in momentum areas marked by triangles, consistent with our experimental data.

However, despite the good agreement of the data with this generalized umklapp process, the interpretation of the momentum structure being a result of interlayer interaction is not obvious, because interlayer coupling at the K valleys was mostly regarded as negligibly small owing to the in-plane orbital character in this valley<sup>4,36</sup>. A regular final-state scattering can be excluded, as only the ILX signal is exhibiting these replicas. The threefold signal should also not be a result of an exciton wavefunction that is confined in a single moiré potential well, as a modification of the

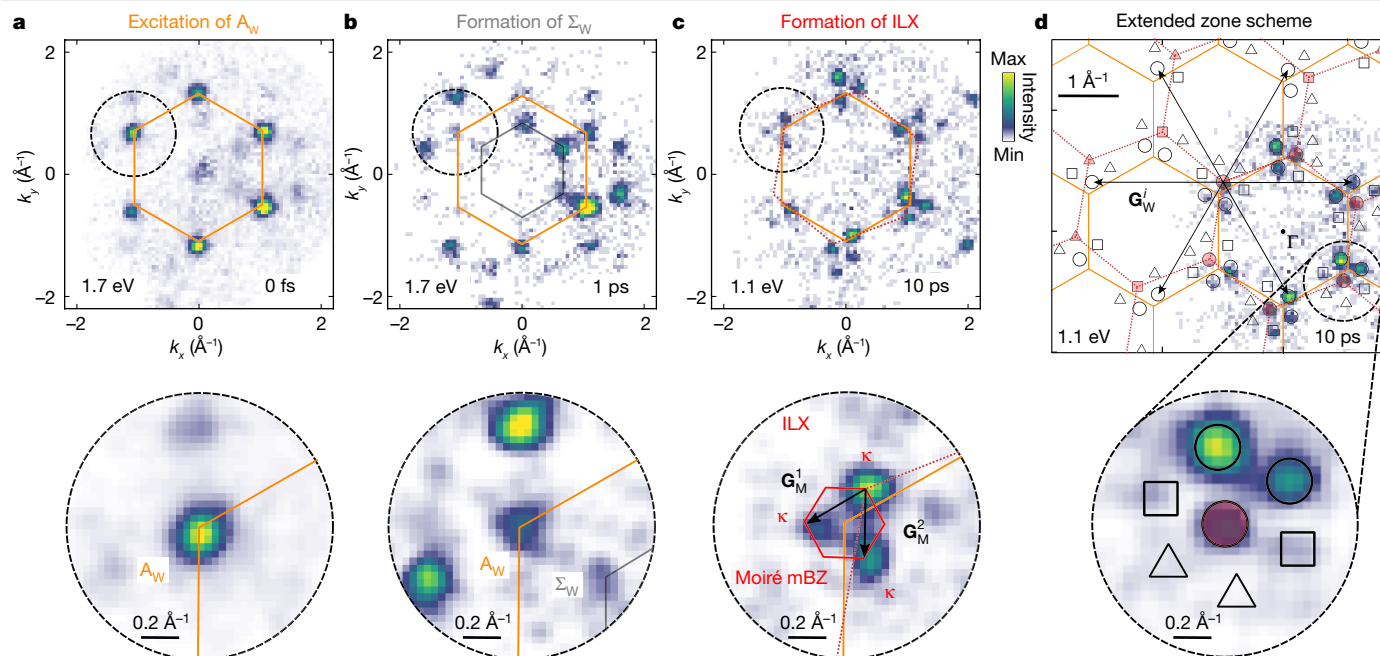


**Fig. 3 | Momentum fingerprints of the moiré interlayer excitons.** **a–c**, Momentum fingerprints of the bright  $A_W$  exciton (**a**), the dark  $\Sigma_W$  exciton (**b**) and the ILX (**c**). Photoemission yield of the  $A_W$  exciton, the  $\Sigma_W$  exciton, and the ILX are detected at the  $K_W$  valleys (orange hexagon), the  $\Sigma_W$  valleys (black hexagon) and the  $\kappa$  valleys of the mBZ (red hexagon), respectively. The bottom row shows zoom-ins from the circled areas in the top row. **d**, The intensity

distribution of the momentum fingerprint of the ILX can be constructed using a generalized umklapp process<sup>39</sup>. The red filled symbols label  $K_{Mo}$  valleys of the first (circles) and higher-order (squares and triangles) Brillouin zones. Open circles, squares and triangles represent a hierarchy of expected spectral weight from high to low, resulting from generalized umklapp processes with  $WSe_2$  reciprocal lattice vectors  $G_W^i$  (black arrows).

relative or centre-of-mass motion of the electron–hole pair becomes important for only large moiré wavelengths, that is, for twist angles less than  $2^\circ$  (refs. 10–12), in agreement with a recent momentum microscopy experiment<sup>13</sup> (Extended Data Fig. 10). Instead, as the photoemitted electron of the ILX has been bound to a hole that remains in the heterostructure, we find here that the umklapp process is transferred through the Coulomb interaction. Thus, to imprint the moiré superlattice onto the excitonic photoemission signal, it is necessary that the electron and the hole components are found in the neighbouring TMD layers such that the quasiparticle experiences the lattice periodicities of both.

In consequence, for intralayer  $A_W$  and  $\Sigma_W$  excitons, where electron and hole reside in  $WSe_2$ , we do not expect and also do not observe the moiré superlattice hallmark in the momentum-resolved photoemission intensity (Fig. 3a,b and Extended Data Fig. 4). To unambiguously assign the microscopic origin of the moiré hallmark in the excitonic momentum fingerprint, however, further theory on photoemission from excitonic quasiparticles is necessary. Nevertheless, our analysis shows that the complex momentum structure of the ILX is a hallmark fingerprint of moiré superlattice modification that has not been observed so far and is clearly unique for the ILXs in a twisted heterostructure.

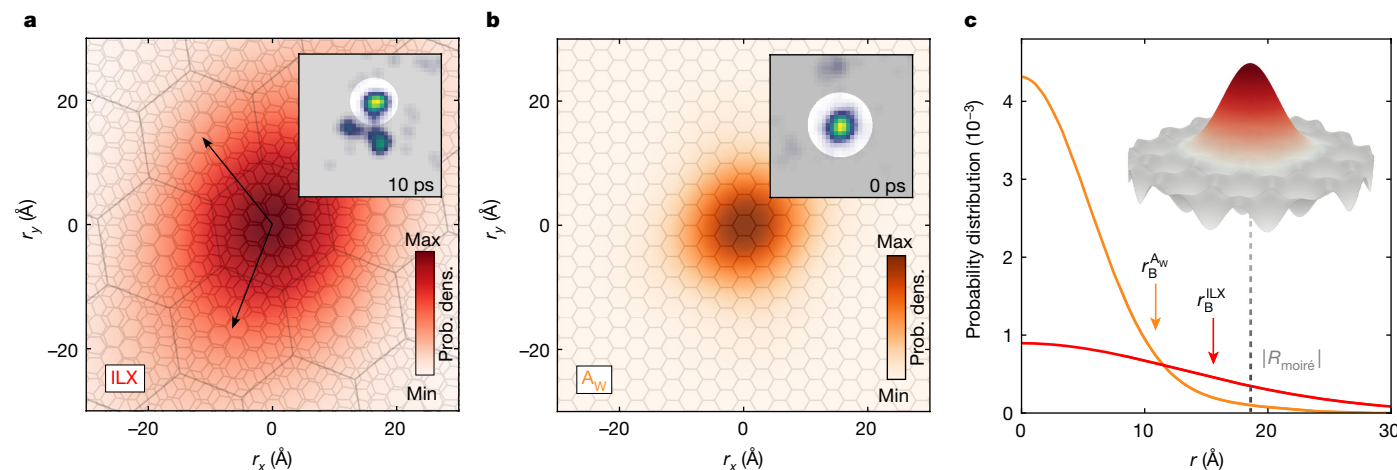


**Fig. 4 | Real-space exciton wavefunction reconstruction and spatial relation to the moiré superlattice.** **a, b**, Real-space reconstructions of the wavefunction of the electron contribution to the ILX (**a**) and the  $WSe_2 A_W$  exciton (**b**). In **a**, the overlay with small (atomic lattices of the twisted  $WSe_2$  and  $MoS_2$  layers) and large (moiré lattice) hexagons illustrates the extension of the electron contribution to the ILX wavefunction over multiple moiré unit cells

(black arrows, moiré lattice vectors). In **b**, only the lattice periodicity of  $WSe_2$  is overlain on the data. The insets show the masks used to select a single valley for the reconstruction. **c**, Line profiles through the probability density. The inset schematically shows how the electronic contribution to the ILX wavefunction (red) is spread over multiple moiré cells (grey).

## ILX real-space wavefunction analysis

Finally, we determine the electron contribution to the real-space wavefunction of intra- and interlayer excitons. We follow the framework of photoemission orbital tomography<sup>40</sup> and recent developments that have been carried out for TMD excitons<sup>13,28,34</sup>. We use the relation  $I(k_x, k_y) \propto |\text{FT}\{\Psi(r_x, r_y)\}|^2$  that connects the real-space wavefunction  $\Psi(r_x, r_y)$  with the momentum-resolved photoemission intensity  $I(k_x, k_y)$  within the plane-wave approximation<sup>28,40</sup> (Methods). The multidimensional data collection scheme now facilitates the direct comparison of the real-space extension  $r_{x,y}$  of the electronic wavefunction contribution of the excitons with the spatial extension of the moiré unit cell (Fig. 4). We extract the respective Bohr radii as  $r_B^{\text{ILX}} = 1.6 \pm 0.2$  nm and  $r_B^{\text{Aw}} = 1.1 \pm 0.1$  nm (root mean square), which is in agreement with a recent analysis<sup>13</sup> (Methods). We can draw two conclusions. The extension of the electronic contribution to the ILX wavefunction is larger than the moiré period of the  $9.8 \pm 0.8^\circ$ -twisted heterostructure ( $|R_{\text{moiré}}| = 1.84 \pm 0.15$  nm), that is, the ILX can propagate laterally through the heterostructure and is not confined to a single moiré potential well. Second, the analysis shows that the ILX extension is significantly broader than that of the  $\text{WSe}_2/\text{Aw}$  exciton. The charge separation across the two TMD layers leads to a weaker attractive interaction between the electron and the hole contribution to the exciton, and the wavefunction exhibits a larger spread in real space.

## Online content

Any methods, additional references, Nature Research reporting summaries, source data, extended data, supplementary information, acknowledgements, peer review information; details of author contributions and competing interests; and statements of data and code availability are available at <https://doi.org/10.1038/s41586-022-04977-7>.

- Hong, X. et al. Ultrafast charge transfer in atomically thin  $\text{MoS}_2/\text{WS}_2$  heterostructures. *Nat. Nanotechnol.* **9**, 682–686 (2014).
- Rivera, P. et al. Observation of long-lived interlayer excitons in monolayer  $\text{MoSe}_2$ - $\text{WSe}_2$  heterostructures. *Nat. Commun.* **6**, 6242 (2015).
- Kim, J. et al. Observation of ultralong valley lifetime in  $\text{WSe}_2/\text{MoS}_2$  heterostructures. *Sci. Adv.* **3**, e1700518 (2017).
- Wang, Y., Wang, Z., Yao, W., Liu, G.-B. & Yu, H. Interlayer coupling in commensurate and incommensurate bilayer structures of transition-metal dichalcogenides. *Phys. Rev. B* **95**, 115429 (2017).
- Merkel, P. et al. Ultrafast transition between exciton phases in van der Waals heterostructures. *Nat. Mater.* **18**, 691–696 (2019).
- Ovesen, S. et al. Interlayer exciton dynamics in van der Waals heterostructures. *Commun. Phys.* **2**, 23 (2019).
- Förg, M. et al. Moiré excitons in  $\text{MoSe}_2$ - $\text{WSe}_2$  heterobilayers and heterotrilayers. *Nat. Commun.* **12**, 1656 (2021).
- Yu, H., Liu, G.-B., Tang, J., Xu, X. & Yao, W. Moiré excitons: from programmable quantum emitter arrays to spin-orbit-coupled artificial lattices. *Sci. Adv.* **3**, e1701696 (2017).
- Wu, F., Lovorn, T. & MacDonald, A. H. Theory of optical absorption by interlayer excitons in transition metal dichalcogenide heterobilayers. *Phys. Rev. B* **97**, 035306 (2018).
- Seyler, K. L. et al. Signatures of moiré-trapped valley excitons in  $\text{MoSe}_2/\text{WSe}_2$  heterobilayers. *Nature* **567**, 66–70 (2019).
- Alexeev, E. M. et al. Resonantly hybridized excitons in moiré superlattices in van der Waals heterostructures. *Nature* **567**, 81–86 (2019).
- Tran, K. et al. Evidence for moiré excitons in van der Waals heterostructures. *Nature* **567**, 71–75 (2019).
- Karni, O. et al. Structure of the moiré exciton captured by imaging its electron and hole. *Nature* **603**, 247–252 (2022).
- Su, J.-J. & MacDonald, A. H. How to make a bilayer exciton condensate flow. *Nat. Phys.* **4**, 799–802 (2008).
- Wu, F., Lovorn, T., Tutuc, E. & MacDonald, A. H. Hubbard model physics in transition metal dichalcogenide moiré bands. *Phys. Rev. Lett.* **121**, 026402 (2018).
- Cao, Y. et al. Unconventional superconductivity in magic-angle graphene superlattices. *Nature* **556**, 43–50 (2018).
- Wang, L. et al. Correlated electronic phases in twisted bilayer transition metal dichalcogenides. *Nat. Mater.* **19**, 861–866 (2020).
- Regan, E. C. et al. Mott and generalized Wigner crystal states in  $\text{WSe}_2/\text{WS}_2$  moiré superlattices. *Nature* **579**, 359–363 (2020).
- Rivera, P. et al. Interlayer valley excitons in heterobilayers of transition metal dichalcogenides. *Nat. Nanotechnol.* **13**, 1004–1015 (2018).
- Jin, C. et al. Ultrafast dynamics in van der Waals heterostructures. *Nat. Nanotechnol.* **13**, 994–1003 (2018).
- Novoselov, K. S. et al. A roadmap for graphene. *Nature* **490**, 192–200 (2012).
- Wang, G. et al. Colloquium: Excitons in atomically thin transition metal dichalcogenides. *Rev. Mod. Phys.* **90**, 021001 (2018).
- Mueller, T. & Malic, E. Exciton physics and device application of two-dimensional transition metal dichalcogenide semiconductors. *npj 2D Mater. Appl.* **2**, 29 (2018).
- Geim, A. K. & Grigorieva, I. V. Van der Waals heterostructures. *Nature* **499**, 419–425 (2013).
- Yu, H., Wang, Y., Tong, Q., Xu, X. & Yao, W. Anomalous light cones and valley optical selection rules of interlayer excitons in twisted heterobilayers. *Phys. Rev. Lett.* **115**, 187002 (2015).
- Madéo, J. et al. Directly visualizing the momentum-forbidden dark excitons and their dynamics in atomically thin semiconductors. *Science* **370**, 1199–1204 (2020).
- Wallauer, R. et al. Momentum-resolved observation of exciton formation dynamics in monolayer  $\text{WS}_2$ . *Nano Lett.* **21**, 5867–5873 (2021).
- Dong, S. et al. Direct measurement of key exciton properties: energy, dynamics, and spatial distribution of the wave function. *Nat. Sci.* **1**, e10010 (2021).
- Taniguchi, T. & Watanabe, K. Synthesis of high-purity boron nitride single crystals under high pressure by using Ba-BN solvent. *J. Cryst. Growth* **303**, 525–529 (2007).
- Medjanik, K. et al. Direct 3D mapping of the Fermi surface and Fermi velocity. *Nat. Mater.* **16**, 615–621 (2017).
- Keunecke, M. et al. Time-resolved momentum microscopy with a 1 MHz high-harmonic extreme ultraviolet beamline. *Rev. Sci. Instrum.* **91**, 063905 (2020).
- Keunecke, M. et al. Electromagnetic dressing of the electron energy spectrum of Au(111) at high momenta. *Phys. Rev. B* **102**, 161403 (2020).
- Wilson, N. R. et al. Determination of band offsets, hybridization, and exciton binding in 2D semiconductor heterostructures. *Sci. Adv.* **3**, e1601832 (2017).
- Man, M. K. L. et al. Experimental measurement of the intrinsic excitonic wave function. *Sci. Adv.* **7**, eabg0192 (2021).
- Karni, O. et al. Infrared interlayer exciton emission in  $\text{MoS}_2/\text{WSe}_2$  heterostructures. *Phys. Rev. Lett.* **123**, 247402 (2019).
- Kunstmann, J. et al. Momentum-space indirect interlayer excitons in transition-metal dichalcogenide van der Waals heterostructures. *Nat. Phys.* **14**, 801–805 (2018).
- Wallauer, R. et al. Momentum-resolved observation of ultrafast interlayer charge transfer between the topmost layers of  $\text{MoS}_2$ . *Phys. Rev. B* **102**, 125417 (2020).
- Brem, S., Linderälv, C., Erhart, P. & Malic, E. Tunable phases of moiré excitons in van der Waals heterostructures. *Nano Lett.* **20**, 8534–8540 (2020).
- Koshino, M. Interlayer interaction in general incommensurate atomic layers. *New J. Phys.* **17**, 015014 (2015).
- Puschnig, P. et al. Reconstruction of molecular orbital densities from photoemission data. *Science* **326**, 702–706 (2009).

**Publisher's note** Springer Nature remains neutral with regard to jurisdictional claims in published maps and institutional affiliations.

Springer Nature or its licensor holds exclusive rights to this article under a publishing agreement with the author(s) or other rightsholder(s); author self-archiving of the accepted manuscript version of this article is solely governed by the terms of such publishing agreement and applicable law.

© The Author(s), under exclusive licence to Springer Nature Limited 2022

### Heterostructure fabrication

The  $\text{WSe}_2/\text{MoS}_2$ /hexagonal boron nitride (hBN) heterostructures were assembled using mechanical exfoliation and dry transfer, as summarized in Extended Data Fig. 1a–d. First, a  $p^+$ -silicon (Si) substrate (1–10  $\Omega\text{cm}$ ) with polished native oxide was plasma cleaned with oxygen gas (100 W, 10 standard cubic centimetres per minute, 10 min). hBN was immediately mechanically exfoliated on the substrate using standard office tape. Using optical contrast, a hBN flake with thickness between 20 nm and 30 nm was identified. In parallel,  $\text{MoS}_2$  and  $\text{WSe}_2$  (HQ graphene) were mechanically exfoliated using blue tape (Ultron Systems 1008R-6.0) on a polydimethylsiloxane (PDMS) sheet (Gel-Pak PF-20/17-X4). Similar to hBN exfoliation, optical contrast was used to identify monolayer  $\text{MoS}_2$  and  $\text{WSe}_2$ . Unlike the standard dry-transfer assembly, the assembly of the heterostructure was started by assembling the  $\text{WSe}_2/\text{MoS}_2$  heterostructure on PDMS first. The two flakes were aligned visually and the  $\text{MoS}_2$  flake was dry transferred on top of the  $\text{WSe}_2$  flake on PDMS. Then the  $\text{WSe}_2/\text{MoS}_2$  heterostructure was dry transferred on top of the hBN. During the last transfer, the multilayer part of the  $\text{WSe}_2$  flake was intentionally placed in direct contact with the Si substrate to reduce sample charging (compare with Extended Data Fig. 1e,f). It is worth noting that although the exfoliation part was done in ambient conditions, the heterostructure assembly was done in a controlled argon environment in a glovebox with oxygen and water  $<0.1$  ppm. An optical microscope image of the van der Waals stack is shown in Extended Data Fig. 1e.

### Sample preparation for photoemission spectroscopy

The Si wafer with the heterostructure is clamped onto a sample holder under ambient conditions and transferred into ultrahigh vacuum. In an ultrahigh-vacuum preparation chamber (background pressure  $<5 \times 10^{-9}$  mbar), the sample is annealed for 2 h at a temperature of approximately 670 K; such sample treatment has shown successful ARPES results on similar sample systems, for example, ref. <sup>41</sup>. Subsequently, the sample is transferred into the momentum microscope. All experiments have been performed at room temperature at a background pressure of approximately  $1 \times 10^{-10}$  mbar.

### Femtosecond momentum microscopy

The experimental set-up is detailed and benchmarked in ref. <sup>31</sup>. It consists of two major parts, namely, a time-of-flight momentum microscope<sup>30</sup> (ToF Momentum Microscope, Surface Concept), shown schematically in Fig. 1a, and a high-power femtosecond laser system (Active Fiber Systems). In the following, we briefly describe the experimental set-up.

The strength of the time-of-flight momentum microscope is the simultaneous measurement of the two-dimensional in-plane momenta and the kinetic energy of the photoelectrons within the full photoemission horizon<sup>30</sup>. To study high-quality TMD heterostructures with a diameter of approximately 10  $\mu\text{m}$ , the key advantage of the set-up lies in the microscopy-type photoelectron detection scheme. In the electrostatic lens system, a real- and a reciprocal-space image of the photoelectrons is formed and either image can be projected onto the photoelectron detector (Fig. 1a). The real-space mode of the microscope is used to map the spatial structure of the sample system (Fig. 1c and Extended Data Fig. 1f). In direct comparison with an optical microscope image (Extended Data Fig. 1e), the monolayer  $\text{WSe}_2$  and  $\text{MoS}_2$  regions as well as the  $\text{WSe}_2/\text{MoS}_2$  heterobilayer region can be identified through the differing photoemission contrast. By placing an aperture into the real-space plane of the microscope, either photoelectrons originating from the  $\text{WSe}_2$  monolayer or the  $\text{WSe}_2/\text{MoS}_2$  heterobilayer can be selected and projected onto the detector (Extended Data Fig. 2). By exploiting this capability of the time-of-flight momentum microscope, we collect in-plane momentum- and energy-resolved photoelectron

distributions for the regions of interest highlighted by circles in Fig. 1c. The energy resolution of the momentum microscope combined with the spectral width of the 26.5-eV XUV light pulses lead to an overall Gaussian broadening of the measured photoelectron signal with a full-width at half-maximum of  $200 \pm 30$  meV (ref. <sup>31</sup>). The achievable momentum resolution of the instrument is  $<0.01 \text{ \AA}^{-1}$  (ref. <sup>42</sup>). From a fit of the cut-off of the photoemission horizon, we can verify that the momentum resolution for the given experimental settings in the paper is better than  $0.04 \pm 0.01 \text{ \AA}^{-1}$ . The time resolution is  $54 \pm 7$  fs for infrared pump pulses of  $50 \pm 5$  fs and XUV probe pulses of  $21 \pm 5$  fs as used in this experiment<sup>31</sup>. This value is confirmed with a fit to the replica signal caused by the laser-assisted photoelectric effect (LAPE)<sup>31,43</sup> (see, for example, Fig. 3a or Extended Data Fig. 6c at 0-fs delay), which yields an infrared-pump–XUV-probe cross-correlation of  $49 \pm 1$  fs.

The laser set-up is based on a 300-W fibre laser system (Active Fiber Systems) that operates at a repetition rate of 500 kHz and drives a high-harmonic generation beamline and a high-power optical parametric amplifier (OPA, Orpheus-F/HP from Light Conversion). To first induce and subsequently probe excitonic dynamics occurring in the TMD heterostructure (Fig. 2), we use a pump–probe scheme. First, bright  $\text{WSe}_2 A_W$  excitons are excited with light pulses generated with the OPA (1.7 eV,  $50 \pm 5$  fs measured per autocorrelation). Subsequently, the femto- to picosecond evolution of the intra- and interlayer excitonic dynamics is probed with an XUV light pulse (26.5 eV,  $p$ -polarized,  $21 \pm 5$  fs (ref. <sup>31</sup>)), which photoemits the electron contribution of the quasiparticle into the detector. Additional experiments are performed with 1.9-eV and 2.4-eV pump light, which is generated through the OPA and frequency doubling of the compressed laser output, respectively. The data in Figs. 1b and 2, and Extended Data Figs. 4c,d, 5, 7, 8a,b and 9 are obtained with an  $s$ -polarized pump light. The data in Figs. 3 and 4, and Extended Data Figs. 4a,b and 6 are obtained with a  $p$ -polarized pump light. For the  $p$ -polarized pump, one creates band replicas owing to the LAPE, which then can be used to determine pump–probe overlap (time zero) and the time resolution<sup>32,43</sup>. For the  $s$ -polarized pump, the time-resolved signal is free of such LAPE replicas, which is helpful for the analysis of spectral features and exciton dynamics.

### Real-space imaging and static band mapping of $\text{WSe}_2/\text{MoS}_2$ /hBN

After preparation of the van der Waals stack for the momentum microscopy experiment, we first perform real-space imaging of the sample with an ultraviolet diode delivering 4.96-eV photons. In Extended Data Fig. 1e,f, the photoemission real-space map is compared with an optical microscope image. In both images, the  $\text{WSe}_2/\text{MoS}_2$ /hBN heterostructure, the doped Si substrate, the bulk hBN, the  $\text{WSe}_2$  and  $\text{MoS}_2$  monolayers, and the bulk  $\text{WSe}_2$  can be distinguished.

Having identified the regions of interest, we place an aperture into the real-space image of the microscope to selectively probe the energy- and momentum-resolved photoelectron distribution of the  $\text{WSe}_2$  monolayer and the  $\text{WSe}_2/\text{MoS}_2$  heterobilayer (compare with Fig. 1a). Using an aperture with a diameter of 100  $\mu\text{m}$  and a lens setting with a magnification of 10, we are sensitive to photoelectrons originating from an effective area with diameter of 10  $\mu\text{m}$  on the heterostructure (circles in Fig. 1c).

Static band mapping of the occupied electronic band structure is shown in Extended Data Fig. 2. The high quality of the van der Waals stack is evident from the well resolved features in the band structure and, in particular, by the visible spin-splitting of the  $\text{WSe}_2$  valence bands at the  $K_W$  and  $K'_W$  valleys<sup>44</sup> (marked with 1 and 2 in Extended Data Fig. 2). In addition, only in the heterobilayer region, we resolve clear signatures of the valence-band maximum of  $\text{MoS}_2$  at  $-1.1$  eV with respect to the valence-band maximum ( $E_{\text{VBM}}$ ) of  $\text{WSe}_2$  (marked with 3 in Extended Data Fig. 2b). Owing to interlayer interaction between the  $\text{WSe}_2$  and  $\text{MoS}_2$  layers, we resolve the expected hybridized valence bands at the  $\Gamma_{\text{W,Mo}}$  valley (marked with 4 and 5 in Extended Data Fig. 2b)<sup>33</sup>. The observation of these hybridized bands is a clear signature that the blisters found in

the real-space image in Extended Data Fig. 1e,f do not dominate the photoemission yield from the heterobilayer. In contrast, in the monolayer WSe<sub>2</sub> region, the valence band at the  $\Gamma_W$  valley is a single band (Extended Data Fig. 2a). Furthermore, the valence-band maximum is localized at the  $K'_W$  ( $K'_W$ ) valley, as expected for the monolayer limit of WSe<sub>2</sub>, where it becomes a direct bandgap semiconductor<sup>33</sup>. In addition, we observe a clear signature of the valence band of hBN that we label with 6 in Extended Data Fig. 2a. Within our energy and momentum resolution, we do not resolve moiré induced mini-band replicas of the valence bands, such as discussed in refs.<sup>41,45</sup>.

### Inhomogeneous broadening from sample

In our experiment, the energy resolution is mainly limited by the bandwidth of the short-pulse XUV light source. Convolved with the instrument resolution, we achieve a total energy resolution on the order of  $200 \pm 30$  meV (ref.<sup>31</sup>). For reference, Extended Data Fig. 3 shows an exemplary energy-distribution curve obtained in a momentum region of  $\pm 0.10 \text{ \AA}^{-1}$  centred at the  $K'_W$  valley. As in the case of ref.<sup>26</sup>, we extract a full-width at half-maximum of  $280 \pm 10$  meV. However, our spectrum is broadened by 200 meV by the light source and the instrument, so that the full-width at half-maximum peak width of the valence-band maximum is on the order of 200 meV. This broadening is attributed to, for example, inhomogeneity of the sample and local field effects.

### Twist-angle determination of the WSe<sub>2</sub>/MoS<sub>2</sub> heterostack

In trARPES experiments, it is known that the electron contribution of the A excitons are identified through spectral weight at the corresponding K valleys of the TMD structure<sup>26-28</sup>. Consequently, the photoemission signature of the  $A_W$  and  $A_{Mo}$  excitons can directly be used to determine the twist angle of a heterostructure. Here, for the unambiguous identification of the  $A_W$  and  $A_{Mo}$  excitons in the  $K_W$  and  $K_{Mo}$  valleys, we carry out resonant excitation using 1.7-eV and 1.9-eV pump light, respectively.

In Extended Data Fig. 4, we show momentum maps of the resonantly pumped WSe<sub>2</sub>  $A_W$  exciton (Extended Data Fig. 4a), the resonantly pumped MoS<sub>2</sub>  $A_{Mo}$  exciton (Extended Data Fig. 4c), and the corresponding signature of the ILX after a delay of 1 ps (Extended Data Fig. 4b,d). From the misalignment of the  $\Gamma$ - $K_W$  and  $\Gamma$ - $K_{Mo}$  directions (orange and dark red dashed lines), we calculate the momentum mismatch between the  $K_W$  and the  $K_{Mo}$  valleys, and, accordingly, determine the twist angle to  $\theta = 9.8 \pm 0.8^\circ$ . The direct comparison with the 1-ps data in Extended Data Fig. 4b,d then facilitates the correlation of the ILX momentum signature to the in-plane momenta of the  $K_W$  and the  $K_{Mo}$  valleys.

### Spectral assignments of conduction and valence bands and the $A_{W,Mo}$ excitons

We study the ultrafast exciton dynamics of the heterobilayer after resonant excitation of the  $A_W$  exciton of WSe<sub>2</sub> with 1.7-eV pump pulses. To unambiguously identify the photoemission signatures shown in Figs. 2 and 3 as excitons, Extended Data Fig. 5a,b shows energy-momentum cuts when using above-bandgap excitation conditions with 2.4-eV pump pulses to the monolayer WSe<sub>2</sub> region indicated by the orange circle in Fig. 1c. In temporal overlap of the pump and probe laser pulses (0 fs), above-bandgap excitation allows for the transient occupation of the conduction band and we correspondingly observe parabolic bands with positive dispersion centred at  $E - E_{VBM} = 1.8$  eV at the  $K_W$  valley. As the delay is increased to 300 fs, the spectral yield at the  $K_W$  valley shifts to smaller energies and the parabolic signature transfers to a more spherical shape. We attribute the photoemission yield from the parabolic dispersion at 0 fs to photoelectrons originating from both higher-quantum-number excitons and charge carriers from the conduction band of WSe<sub>2</sub>, as has been described previously and is in full agreement with ref.<sup>26</sup>. Subsequently, the delay-dependent shift of the spectral weight to smaller energies can be understood by the formation

of excitons (compare with the energy-distribution curves in Extended Data Fig. 5b). In Extended Data Fig. 5c, we compare the above-bandgap excitation results with energy-distribution curves obtained from the 1.7-eV pump-light experiment. Under these resonant excitation conditions, already at 0-fs pump-probe delay the exciton signal is observed at  $E - E_{VBM} = 1.7$  eV. Importantly, the signal does not decrease in energy with proceeding delay and does not show a positive parabolic dispersion (compare with Fig. 1b and Extended Data Fig. 6).

By repeating the same analysis as described above for a monolayer MoS<sub>2</sub> sample, we can discriminate the  $A_{Mo}$  exciton from charge carriers in the conduction-band minimum (Extended Data Fig. 5d-f). It is noted that we do not resolve the pump-probe delay-dependent energy shift for the case of MoS<sub>2</sub>, but the parabolic momentum dispersion at 0 fs can again be distinguished from the more spherical shape at 250 fs.

### Additional time-resolved momentum microscopy data of the twisted WSe<sub>2</sub>/MoS<sub>2</sub> heterostructure

Extended Data Fig. 6 summarizes, in addition to Fig. 3,  $E(k)$  and  $k_x$ - $k_y$  momentum maps of the formation dynamics of the ILX.

### Filtering excitonic photoemission signatures in energy and momentum space

The time-of-flight momentum microscope collects in-plane momentum and energy-resolved data cubes for each pump-probe delay<sup>31</sup>. To monitor the pump-probe delay-dependent exciton dynamics, the excitonic photoemission signatures need to be filtered on these coordinates to avoid mixing of different photoemission signals. Therefore, in Extended Data Fig. 7a,b, we show two momentum maps that are integrated for all measured pump-probe delays in an energy window between  $E - E_{VBM} = 1.5$ -2.4 eV and  $E - E_{VBM} = 0.8$ -1.3 eV, respectively. First, we recognize that the signal of the  $\Sigma_W$  exciton (black circle) can be easily separated from the  $A_W$  exciton (orange) and the ILX (red) in momentum space. Still, we choose the lower bound of the integration window for the  $\Sigma_W$ -exciton signal well above the energy of the ILX on the energy axis to determine the pump-probe-delay-dependent spectral weight plotted in Fig. 2c (integration window  $E - E_{VBM} = 1.5$ -2.4 eV). The separation of the spectral weight of the  $A_W$  exciton and the ILX needs to be further analysed and filtered on the energy axis as, in momentum space, the regions of interest are close to each other. From the evolution of the energy-distribution curves of the  $A_W$ -exciton-momentum-filtered areas in Extended Data Fig. 7c (upper panel), it is obvious that the  $A_W$  photoemission signal strongly dominates over the ILX signal for  $E - E_{VBM} > 1.5$  eV. Consequently, in Fig. 2c, we plot the  $A_W$ -exciton signal as obtained within the momentum region indicated by the orange circles in Extended Data Fig. 7a and for  $E - E_{VBM} = 1.5$ -2.4 eV (orange boxed energy region in Extended Data Fig. 7c, upper panel). For the ILX signal, the correct identification of the energy-integration window is more complex and therefore further analysed based on the evolution of the energy-distribution curves of the ILX-momentum-filtered areas in Extended Data Fig. 7c (middle panel). To separate the signal of the ILX, which is centred at  $E - E_{VBM} \approx 1.1$  eV, from the photoemission yield at higher energies, we systematically vary the energy window that is used to integrate the ILX signal (blueish boxes in Extended Data Fig. 7c, middle panel). The resulting spectral weight versus pump-probe delay plots are shown in the lower panel of Extended Data Fig. 7c. For small-energy-integration boxes (dark blue and blue), we find an identical evolution of the spectral weight that we attribute to the ILXs. However, as the box becomes too large (light blue), at about 50 fs, spurious signal from higher energies leads to deviations. Consequently, we use the appearance of this additional photoemission signal at about 50 fs to determine the upper bound of the maximum energy-integration window for the ILXs to  $E - E_{VBM} < 1.3$  eV. This sets the boundaries for the energy-integration box of the ILXs to  $E - E_{VBM} = 0.8$ -1.3 eV, which is plotted in Fig. 2c.

## Correction of space-charge and photovoltage effects

In trARPES experiments, even in the sub-1 mJ cm<sup>-2</sup> fluence regime, one often observes space-charge and/or photovoltage effects. These effects are induced by Coulomb interaction of the photoelectrons or the remaining holes, which were excited by the pump and the probe laser pulses<sup>46–48</sup>. These effects are well known in the trARPES community and, in a moderate regime, cause only a rigid spectral shift of all probe photoelectrons, that is, a shift of the entire photoelectron spectrum. In this regime, one automatically monitors space-charge- and photovoltage-induced shifts when collecting the trARPES data and one correspondingly corrects for these ‘rigid’ shifts before analysing the data. For all data presented in our paper, we observe such rigid shifts of the full ARPES spectrum, which is on the order of several millielectronvolts up to a maximum of about 70 meV (Extended Data Fig. 8a). The pump–probe-delay-dependent energy difference  $\Delta E$  is calculated by fitting a selected peak in the full momentum-integrated energy-distribution curves and subtracting its energy position from the reference measurement data shown in the inset. Although this energy difference  $\Delta E$  is small compared with our energy resolution and barely influences the analysis procedure, we routinely correct our data for these effects before carrying out the data analysis. This means that all data shown in this paper are corrected for this rigid energy offset. It is noted that for the analysis of the ILX momentum fingerprint, the energy shift is irrelevant, because the data are analysed on the picosecond timescale.

## Determination of the exciton density

It has been shown in TMDs that for optical pumping with sufficiently high fluence, a Mott transition from excitonic states to free carriers can be induced when the excited exciton density is in the range of 10<sup>12</sup>–10<sup>14</sup> cm<sup>-2</sup> (refs. 49–53). This transition leads to giant bandgap renormalizations of up to 500 meV (ref. 49) and thus might influence our interpretation of A<sub>w</sub>-exciton generation and the subsequent dynamics. In the following, we describe the calculation of the exciton density in our experiment, and subsequently show pump–probe-delay-dependent energy-distribution curves of the valence-band maxima of WSe<sub>2</sub> to directly exclude the contribution of band renormalizations to our experimental analysis.

Using the real-space mode of the microscope, we can extract the 1/e<sup>2</sup> radius of the pump beam on the sample to 151 ± 1 μm. For the data shown in Fig. 2c, the heterostructure was irradiated with s-polarized 1.7-eV photons with a peak fluence of 280 ± 20 μJ cm<sup>-2</sup>. By following the analysis of ref. 50, we calculate the absorbed fluence to be 1.5 ± 0.2 μJ cm<sup>-2</sup>, which results in an exciton density of (5.4 ± 1.0) × 10<sup>12</sup> cm<sup>-2</sup>. As this exciton density is in the 10<sup>12</sup>–10<sup>14</sup> cm<sup>-2</sup> threshold regime<sup>49–53</sup>, it is important to provide experimental evidence that our experiment probes excitons and not quasi-free carriers in the conduction bands.

We therefore analyse our data for the possible generation of quasi-free carriers and the corresponding renormalization of the band structure. In Extended Data Fig. 8b, we monitor the position of the WSe<sub>2</sub> valence-band maximum at the K<sub>w</sub> valley compared with the position at -2 ps as a function of delay, which, in the case of generation of quasi-free carriers, is expected to strongly upshift in energy (compare with ref. 49). In ref. 53, using trARPES, for example, the energetic position of the valence-band maximum shifts up by 360 meV and then relaxes back to its unperturbed value on the picosecond timescale. Importantly, within the scattering of our data (about ±50 meV in Extended Data Fig. 8b), the photoemission energy of the valence-band edge at the K<sub>w</sub> valley does not change with pump–probe delay. In particular, it does not upshift in energy, as would be expected for an exciton density above the Mott threshold. This directly implies that the dominant excitation in our experiment is governed by A<sub>w</sub> excitons in WSe<sub>2</sub>, from which the subsequent exciton dynamics is induced, whereas the role of quasi-free carriers is negligible. It is noted that the

error bars around 0 fs are enlarged because of a typical broadening of the occupied bands in temporal overlap (compare with Extended Data Fig. 6a,b).

## Quantitative analysis of charge-transfer times to the Σ<sub>w</sub> excitons and the ILX

The intermediate steps of the exciton dynamics occurring in the WSe<sub>2</sub>/MoS<sub>2</sub> heterostructure are summarized in the excitation diagram shown in the inset of Fig. 2c. A<sub>w</sub> excitons are resonantly excited with 1.7-eV pump photons, exciton–phonon scattering leads to the formation of Σ<sub>w</sub> excitons and, subsequently, ILXs are formed through interlayer charge transfer at the Σ valleys. Typically, one would use a rate-equation model to quantify the respective charge-transfer times. However, this approach is not feasible here, as it does not accurately describe the coherent polarization induced when the pump pulse is present on the sample<sup>27</sup>. In addition, because of photoemission cross-section effects, we cannot unambiguously correlate the measured photoemission signal to the exciton occupation density, as would be necessary to extract meaningful transfer rates from a rate-equation model. Therefore, we assume the most simple model for a quantitative analysis. The states are filled by a Gaussian excitation or transfer rate. This rise in spectral weight follows an error function. In Extended Data Fig. 9a, we fit the pump–probe-delay-dependent spectral weight with error functions  $I/I_{\max} = 0.5 \times (\text{erf}((t - t_i)/w) + 1)$ , which give us access to the delayed onset  $t_{\Sigma w}$  and  $t_{\text{ILX}}$  of the photoemission yield from the Σ<sub>w</sub> exciton and the ILX, respectively, compared with the build-up of the A<sub>w</sub> exciton ( $t_{\text{AW}}$ ). We calculate delayed onset times of  $t_{\Sigma w} - t_{\text{AW}} = 33 \pm 6$  fs and  $t_{\text{ILX}} - t_{\text{AW}} = 54 \pm 7$  fs. These delayed onsets are in overall agreement with earlier reports on charge transfer on the WSe<sub>2</sub>/MoS<sub>2</sub> system<sup>54,55</sup>; however, the momentum-resolved data collection scheme now facilitates the separate extraction of this dynamics for the intermediate Σ<sub>w</sub> excitons.

## Long-term picosecond relaxation dynamics of the observed excitons

Extended Data Fig. 9b shows the picosecond exciton relaxation dynamics of the WSe<sub>2</sub>/MoS<sub>2</sub> heterostructure. In accordance with the snapshots in Extended Data Fig. 6, at 10-ps pump–probe delay, photoemission yield from the A<sub>w</sub> exciton and the Σ<sub>w</sub> exciton is at the detection limit of the experiment. In contrast, for the ILX, notable photoemission yield is still present at this time delay and remains beyond delays of 50 ps, which is the largest delay measured in our experiment. In Extended Data Fig. 9b, we quantify this observation and fit the relaxation dynamics of the excitons with single-exponential decays, for which we extract lifetimes of 3.1 ± 0.3 ps, 3.0 ± 0.4 ps and 33.2 ± 4.7 ps for the A<sub>w</sub> exciton, the Σ<sub>w</sub> exciton and the ILX, respectively. We find that the ILX lifetime is an order of magnitude larger than the lifetimes of the intralayer excitons, in agreement with earlier reports<sup>55</sup>. In addition, we note that the lifetimes of the intralayer excitons in the heterostructure are considerably quenched compared with the lifetime of the intralayer excitons in the WSe<sub>2</sub> monolayer (Fig. 2a,b), which is caused by the additional decay channel into the ILX.

## Construction of the ILX momentum fingerprint in the extended zone scheme

We follow the interlayer interaction model in ref. 39 to describe the intensity distribution of the ILX fingerprint in momentum space. In Fig. 3d, we plot the measured ILX momentum distribution at 10-ps pump–probe delay together with the twisted extended zone schemes of WSe<sub>2</sub> (orange hexagons) and MoS<sub>2</sub> (dotted dark red hexagons). The K<sub>mo</sub> valleys, at which the electron contribution to the ILX is expected without contribution of the moiré superlattice, are labelled with red filled symbols. The increasing momentum distance of the K<sub>mo</sub> valleys in higher-order Brillouin zones with respect to the Γ valley of the centre Brillouin zone is indicated by the changing red symbols, that is, the

transition from circles to squares and to triangles. By umklapp scattering with the reciprocal lattice vector  $\mathbf{G}_w^i$  of  $\text{WSe}_2$  (black arrows), that is, the periodicity of the layer where the hole contribution to the ILX is localized, the momenta indicated with open symbols can be reached. As detailed in refs.<sup>39,56</sup>, the efficiency of umklapp scattering decreases with increasing distance from the  $\Gamma$  valley of the centre Brillouin zone. Consequently, we observe a strong hierarchy of photoemission signal from the ILX. The strongest photoemission signal is found and expected at the momenta labelled with circles. The weaker and negligible signal is found at the momenta labelled with squares and triangles, respectively.

For heterostructures with different twist angles, the ILX momentum structure is modified accordingly. This is exemplarily illustrated in Extended Data Fig. 10 for twist angles of  $9^\circ$  and  $2^\circ$ . Here, the  $2^\circ$  illustration corresponds to the sample structure in a recent study<sup>13</sup>, and shows that for finite momentum resolution and small twist angles, the ILX momentum structure that we found in our work cannot be resolved.

### Real-space reconstruction

Following the plane-wave model for photoemission, the measured ARPES intensity  $I(\mathbf{k})$  can be expressed as

$$I(\mathbf{k}) = |\mathbf{A} \cdot \mathbf{k}|^2 |\text{FT}\{\psi(\mathbf{r})\}|^2 \delta(E_b + E_{\text{kin}} + \phi - \hbar\omega),$$

which includes the Fourier transform of the real-space electronic wavefunction  $\psi(\mathbf{r})$ , a polarization factor  $|\mathbf{A} \cdot \mathbf{k}|^2$  that depends on the vector potential  $\mathbf{A}$  of the incident radiation and electron momentum  $\mathbf{k}$ , and a Dirac delta function that ensures conservation of energy ( $E_b$ : binding energy,  $E_{\text{kin}}$ : kinetic energy of electrons,  $\phi$ : work function,  $\hbar\omega$ : photon energy). As the electronic contribution to the interlayer excitonic quasiparticle is confined to a single  $\text{MoS}_2$  monolayer, we can treat it similar to how it is done for orbital tomography of molecular orbitals in planar aromatic molecules<sup>40,57</sup>, in agreement with the approach that has been recently carried out for excitons in TMDs<sup>13,28,34</sup>. Here, the wavefunction is assumed to be thin in the vertical dimension and photoemission is therefore assumed to be independent of the out-of-plane momentum  $k_z$ .

We start our analysis based on the momentum maps of the  $A_w$  exciton and the ILX. As highlighted in the main text based on the insets in Fig. 4a,b, we perform separate two-dimensional Fourier transforms to each excitonic photoemission feature to reconstruct the real-space extension of the electronic contribution to the exciton wavefunction, as plotted in Fig. 4a,b for the ILX and the  $A_w$  exciton, respectively. In this analysis, we have eliminated broadening effects owing to the finite momentum resolution of the momentum microscope ( $0.04 \text{ \AA}^{-1}$ ) using Wiener–Hunt deconvolution and subtracted a weak background determined from the full dataset. Finally, we assumed a flat phase profile over the full accessible momentum range, following the approach detailed in ref.<sup>28</sup>. To determine the Bohr radii, we calculate the root-mean-square radii of the real-space probability density distribution. The Bohr radii for the electron contribution to the ILX and the  $A_w$  exciton are  $r_B^{\text{ILX}} = 1.6 \pm 0.2 \text{ nm}$  and  $r_B^{A_w} = 1.1 \pm 0.1 \text{ nm}$ , respectively, and were acquired by taking the weighted average of the Bohr radii determined for individual  $\kappa$  and  $K_w$  valleys. For the ILX, only the features with a signal-to-noise ratio better than 10 were taken into account.

It is noted that on the heterostructure with a twist angle of more than  $5^\circ$ , we can safely assume in our analysis that the centre-of-mass momentum is narrowly distributed around zero<sup>11,38</sup>, and the momentum width of the photoemission signatures at the  $\kappa$  and  $K_w$  valleys relates to the relative coordinate of the excitons<sup>13</sup>. In a recent report on a  $2^\circ$ -twisted  $\text{WSe}_2/\text{MoS}_2$  heterostructure, ref.<sup>13</sup> reported the root-mean-square radius of the relative coordinate to the ILX wavefunction to  $2.6 \pm 0.4 \text{ nm}$ . This corresponds to a root-mean-square radius of the

probability density of  $1.8 \pm 0.3 \text{ nm}$ , which is in agreement with our analysis of a Bohr radius of  $r_B^{\text{ILX}} = 1.6 \pm 0.2 \text{ nm}$ . Similarly, our reconstructed Bohr radius of the  $A_w$  exciton of  $r_B^{A_w} = 1.1 \pm 0.1 \text{ nm}$  is in agreement with the root-mean-square radius of the probability density of  $\text{WSe}_2$  of ref.<sup>34</sup> (about  $1.0 \text{ nm}$ ).

### Data availability

The data that support the findings of this study are available from the corresponding authors upon reasonable request.

- Stansbury, C. H. et al. Visualizing electron localization of  $\text{WS}_2/\text{WSe}_2$  moiré superlattices in momentum space. *Sci. Adv.* **7**, eabf4387 (2021).
- Tusche, C., Krasnyuk, A. & Kirschner, J. Spin resolved bandstructure imaging with a high resolution momentum microscope. *Ultramicroscopy* **159**, 520–529 (2015).
- Miaja-Avila, L. et al. Laser-assisted photoelectric effect from surfaces. *Phys. Rev. Lett.* **97**, 113604 (2006).
- Ulstrup, S. et al. Imaging microscopic electronic contrasts at the interface of single-layer  $\text{WS}_2$  with oxide and boron nitride substrates. *Appl. Phys. Lett.* **114**, 151601 (2019).
- Jones, A. J. H. et al. Visualizing band structure hybridization and superlattice effects in twisted  $\text{MoS}_2/\text{WS}_2$  heterobilayers. *2D Mater.* **9**, 015032 (2021).
- Schönhense, G. et al. Suppression of the vacuum space-charge effect in fs-photoemission by a retarding electrostatic front lens. *Rev. Sci. Instrum.* **92**, 053703 (2021).
- Hellmann, S., Rossnagel, K., Marczyński-Bühlow, M. & Kipp, L. Vacuum space-charge effects in solid-state photoemission. *Phys. Rev. B* **79**, 035402 (2009).
- Passlack, S. et al. Space charge effects in photoemission with a low repetition, high intensity femtosecond laser source. *J. Appl. Phys.* **100**, 024912 (2006).
- Chernikov, A., Ruppert, C., Hill, H. M., Rigosi, A. F. & Heinz, T. F. Population inversion and giant bandgap renormalization in atomically thin  $\text{WS}_2$  layers. *Nat. Photon.* **9**, 466–470 (2015).
- Dendzik, M. et al. Observation of an excitonic mott transition through ultrafast core-cum-conduction photoemission spectroscopy. *Phys. Rev. Lett.* **125**, 096401 (2020).
- Steinleitner, P. et al. Direct observation of ultrafast exciton formation in a monolayer of  $\text{WSe}_2$ . *Nano Lett.* **17**, 1455–1460 (2017).
- Steinhoff, A. et al. Exciton fission in monolayer transition metal dichalcogenide semiconductors. *Nat. Commun.* **8**, 1166 (2017).
- Liu, F., Ziffer, M. E., Hansen, K. R., Wang, J. & Zhu, X. Direct determination of band-gap renormalization in the photoexcited monolayer  $\text{MoS}_2$ . *Phys. Rev. Lett.* **122**, 246803 (2019).
- Zimmermann, J. E. et al. Ultrafast charge-transfer dynamics in twisted  $\text{MoS}_2/\text{WSe}_2$  heterostructures. *ACS Nano* **15**, 14725–14731 (2021).
- Zhu, H. et al. Interfacial charge transfer circumventing momentum mismatch at two-dimensional van der Waals heterojunctions. *Nano Lett.* **17**, 3591–3598 (2017).
- Ahn, S. J. et al. Dirac electrons in a dodecagonal graphene quasicrystal. *Science* **361**, 782–786 (2018).
- Jansen, G. S. M. et al. Efficient orbital imaging based on ultrafast momentum microscopy and sparsity-driven phase retrieval. *New J. Phys.* **22**, 063012 (2020).

**Acknowledgements** This work was funded by the Deutsche Forschungsgemeinschaft (DFG, German Research Foundation) - 432680300/SFB 1456, project B01, 217133147/SFB 1073, projects B07 and B10, and 223848855/SFB 1083, project B9. G.S.M.J. acknowledges financial support by the Alexander von Humboldt Foundation. A.A. and S.H. acknowledge funding from EPSRC (EP/T001038/1, EP/P005152/1). A.A. acknowledges financial support by the Saudi Arabian Ministry of Higher Education. K.W. and T.T. acknowledge support from the Elemental Strategy Initiative conducted by the MEXT, Japan (Grant Number JPMXP0112101001) and JSPS KAKENHI (grant numbers 19H05790, 20H00354 and 21H05233). E.M. acknowledges support from the European Union Horizon 2020 research and innovation programme under grant agreement number 881603 (Graphene Flagship) as well as Vinnova via the competence centre ‘2D-TECH’ and the Knut and Alice Wallenberg Foundation via the Grant KAW 2019.0140.

**Author contributions** D. Steil, R.T.W., S.S., G.S.M.J., S.H., M.R. and S.M. conceived the research. D. Schmitt, J.P.B. and W.B. carried out the time-resolved momentum microscopy experiments and analysed the data. W.B., D.R.L. and G.S.M.J. carried out the real-space reconstruction of the momentum fingerprints. A.A. fabricated the samples. G.M., S.B. and E.M. developed the microscopic model and analysed the results. All authors discussed the results. M.R. and S.M. were responsible for the overall project direction and wrote the manuscript with contributions from all co-authors. K.W. and T.T. synthesized the hBN crystals.

**Competing interests** The authors declare no competing interests.

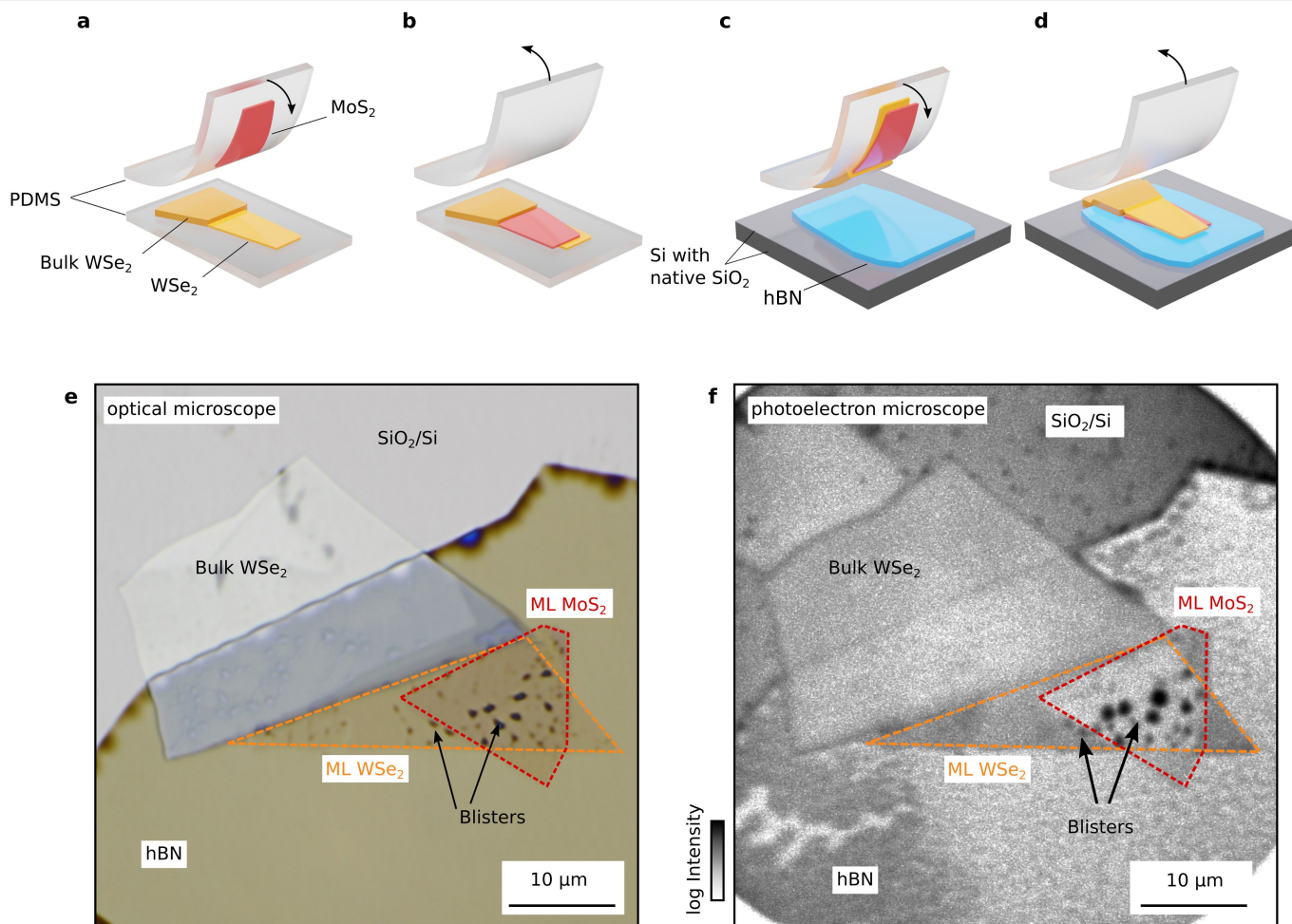
### Additional information

**Supplementary information** The online version contains supplementary material available at <https://doi.org/10.1038/s41586-022-04977-7>.

**Correspondence and requests for materials** should be addressed to Marcel Reutzel or Stefan Mathias.

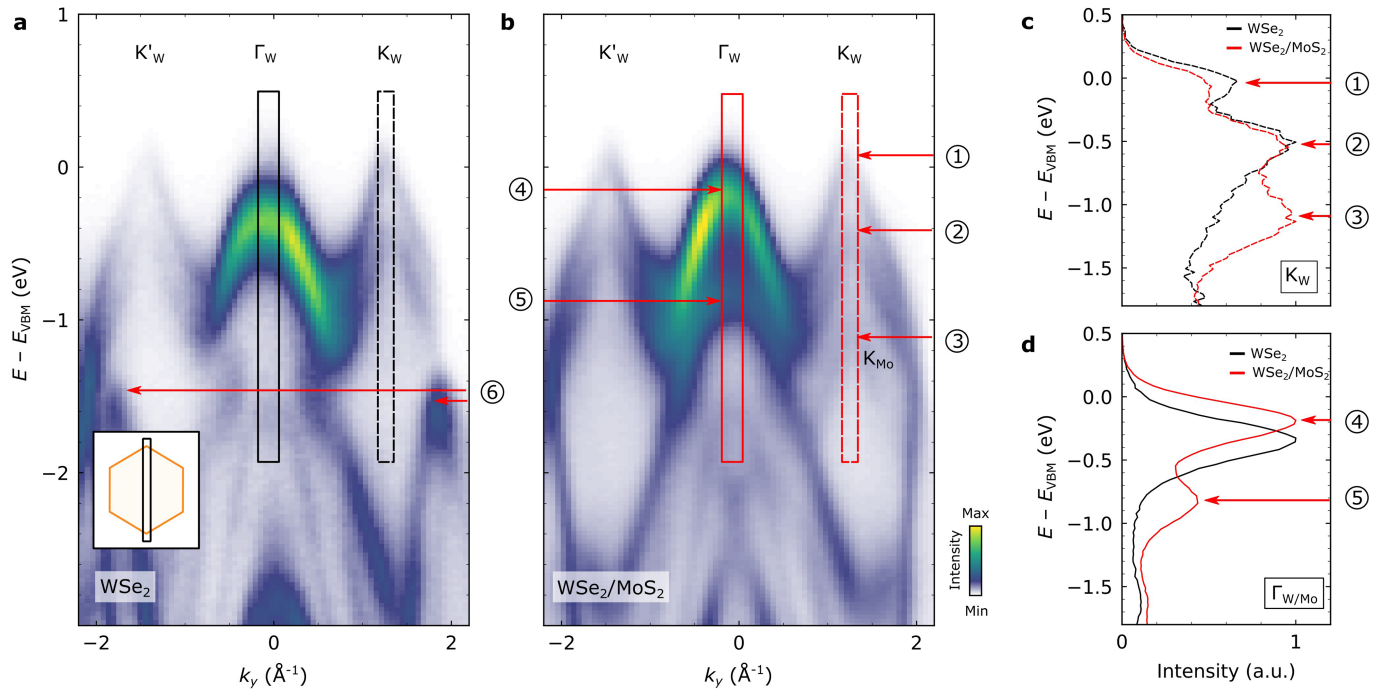
**Peer review information** Nature thanks Alessandra Lanzara, Simone Latini and Soren Ulstrup for their contribution to the peer review of this work.

**Reprints and permissions information** is available at <http://www.nature.com/reprints>.



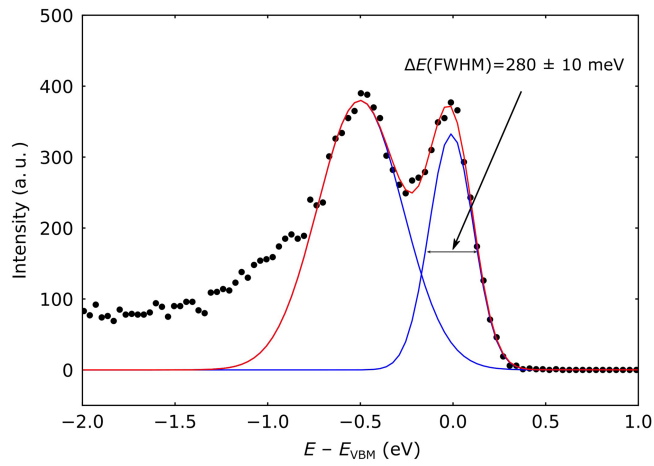
**Extended Data Fig. 1 | Fabrication and real-space imaging of the of the WSe<sub>2</sub>/MoS<sub>2</sub>/hBN heterostructure.** **a–d** Schematic of the WSe<sub>2</sub>/MoS<sub>2</sub>/hBN heterostructure assembly on a Si substrate with a native oxide layer. **a** A PDMS stamp with monolayer MoS<sub>2</sub> flake (red) is aligned with another PDMS stamp holding a monolayer WSe<sub>2</sub> (yellow), then the top PDMS stamp is brought in contact with bottom PDMS. **b** The top PDMS stamp is then withdrawn, leaving the MoS<sub>2</sub> on top of the WSe<sub>2</sub>. **c** The PDMS stamp holding the WSe<sub>2</sub>/MoS<sub>2</sub> is then brought into contact with SiO<sub>2</sub>/Si substrate with hBN (blue). **d** the PDMS is then

withdrawn, leaving behind the final WSe<sub>2</sub>/MoS<sub>2</sub>/hBN heterostructure. **e/f** The WSe<sub>2</sub>/MoS<sub>2</sub>/hBN heterostructure, the uncovered SiO<sub>2</sub>/Si substrate, bulk hBN, the WSe<sub>2</sub> and MoS<sub>2</sub> monolayers, and bulk WSe<sub>2</sub> are labelled in the **e** optical microscope and the **f** photoemission real-space image ( $\hbar\omega = 4.96$  eV). Point-like structures (blisters) in the heterostructure region can be attributed to residual gas trapped either at the MoS<sub>2</sub>/hBN or the WSe<sub>2</sub>/MoS<sub>2</sub> interface. The blisters in the monolayer WSe<sub>2</sub> region are most likely trapped at the WSe<sub>2</sub>/hBN interface.

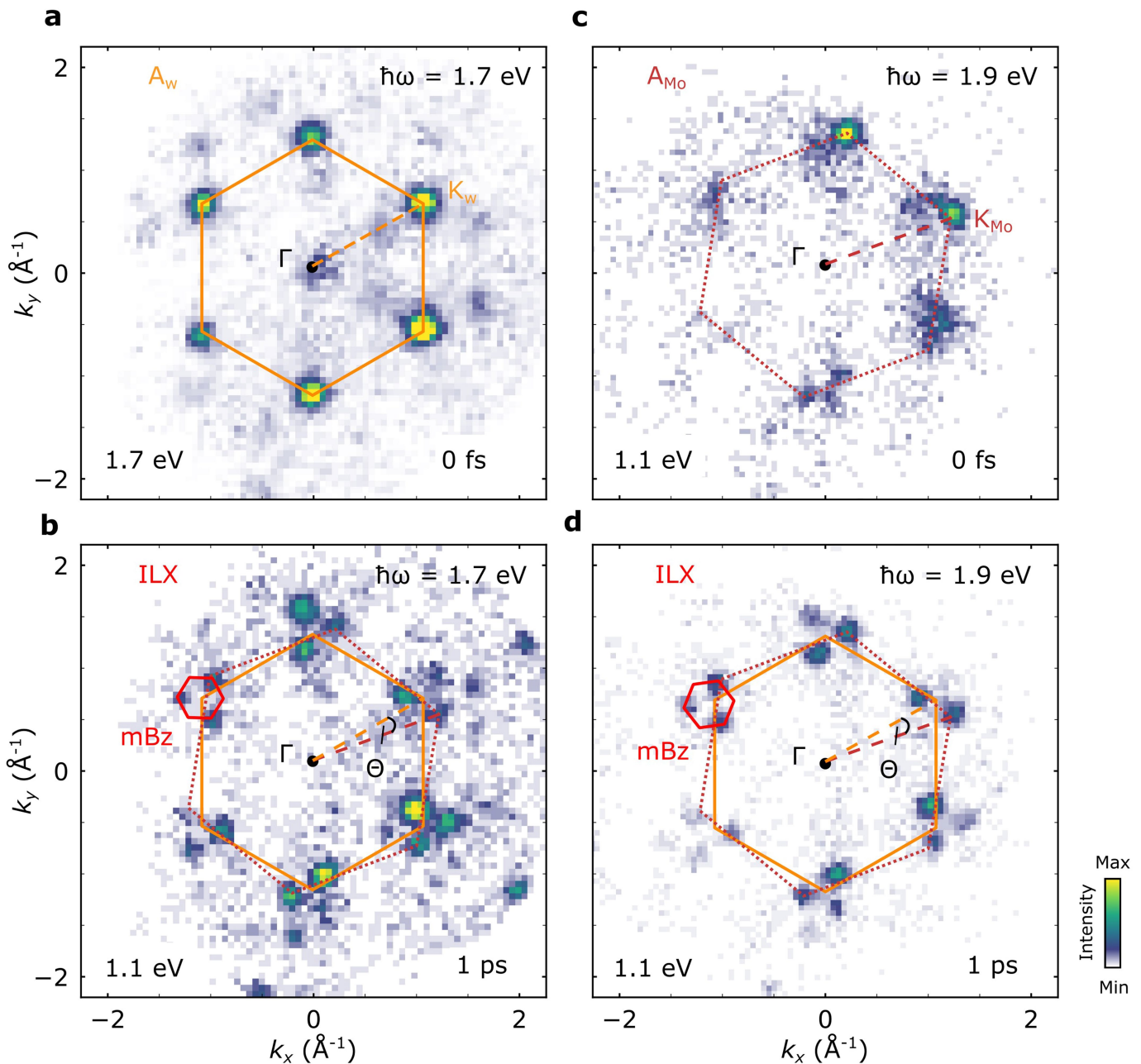


**Extended Data Fig. 2 | Static band mapping of the monolayer WSe<sub>2</sub> and the heterobilayer WSe<sub>2</sub>/MoS<sub>2</sub>.** **a, b** Energy-momentum representation of the static photoemission intensity obtained in the momentum microscopy experiment along the  $K'_W$ - $\Gamma$ - $K_W$  direction (see inset). The important

spectroscopic features are labelled in the figure: (1, 2) spin-split valence bands of WSe<sub>2</sub>; (3) valence band of MoS<sub>2</sub>; (4, 5) valence bands at the  $\Gamma_{W, \text{Mo}}$  valley; (6) valence band of hBN. **c, d** Energy-distribution curves taken around the  $K_W$  and  $\Gamma_{W, \text{Mo}}$  ( $\Gamma_W$ ) valley indicated by the coloured boxes in **a** and **b**.

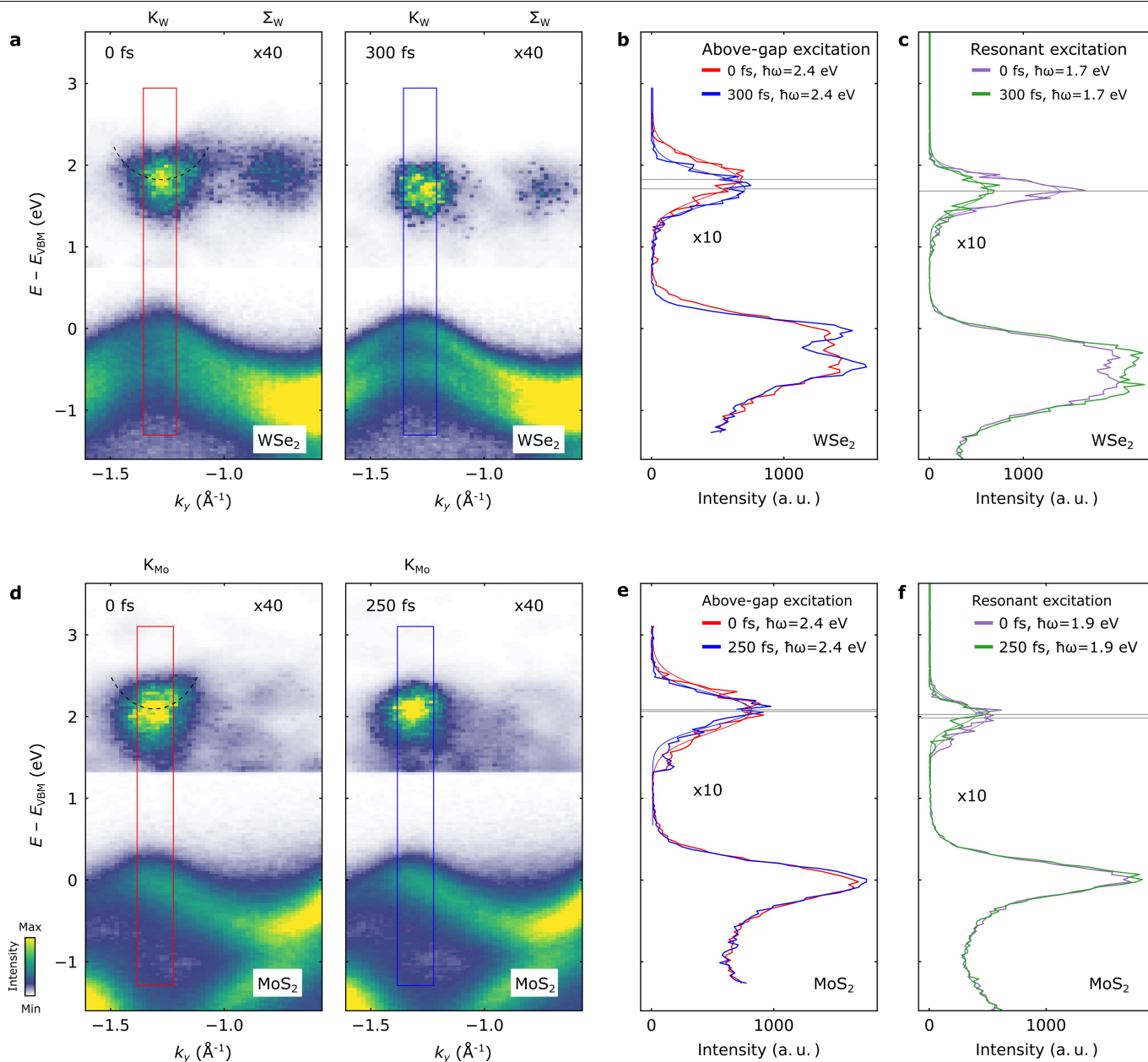


**Extended Data Fig. 3 | Inhomogeneous broadening of the photoemission spectra.** The energy-distribution-curve is obtained in a  $\pm 0.10 \text{ \AA}^{-1}$  region-of-interest centred at the  $K'_w$  valley of  $\text{WSe}_2$ . Gaussian fitting of the valence band maximum centred at  $E - E_{\text{VBM}} = 0$  eV yields a full-width at half-maximum of  $280 \pm 10$  meV.



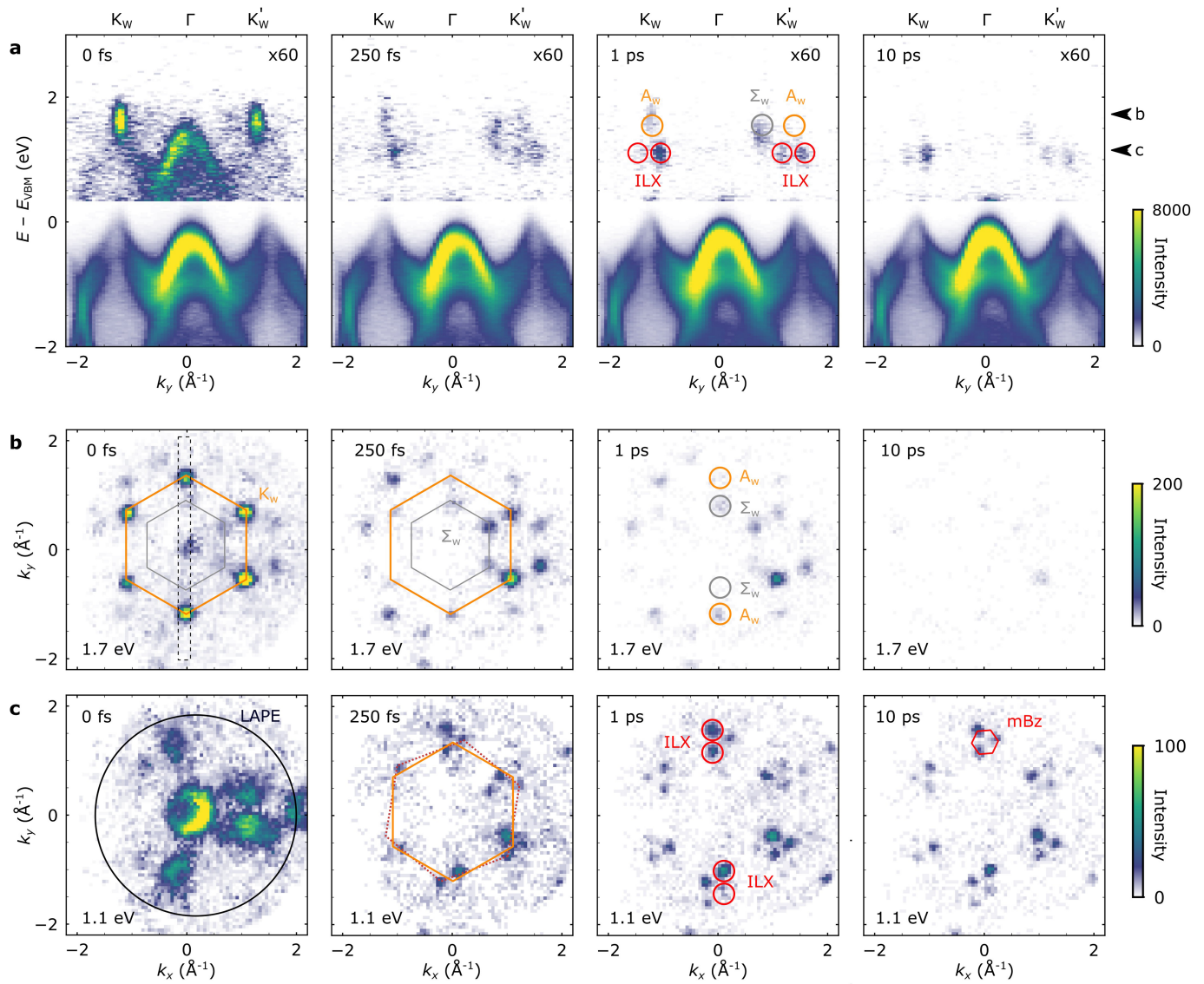
**Extended Data Fig. 4 | Determination of the twist angle  $\theta$  of the  $\text{WSe}_2/\text{MoS}_2$  heterostructure.** The momentum maps in **a** and **c** show the photoemission fingerprint of the  $A_W$ - and  $A_{\text{Mo}}$ -excitons when excited resonantly with 1.7 eV and 1.9 eV photons, respectively, at 0 fs pump-probe delay. Since the  $\text{MoS}_2$   $A_{\text{Mo}}$ -exciton and the ILX are, within our energy resolution, spectrally degenerate, faint signatures of the ILX are already visible **c** at 0 fs delay. The dashed lines indicate the  $\Gamma$ - $K_W$  (orange) and  $\Gamma$ - $K_{\text{Mo}}$  (dark red) direction. From their misalignment, the twist angle is extracted to  $\theta = 9.8 \pm 0.8^\circ$ . **b, d** At 1-ps

pump-probe delay, the ILX momentum fingerprint can be identified, as described by the mBZ (red). The dashed lines indicate the relation of the ILX momentum fingerprint and the  $\Gamma$ - $K_W$  and  $\Gamma$ - $K_{\text{Mo}}$  directions. Note the distinctly different intensity distribution of the combined spectral weight of the  $A_{\text{Mo}}$ -exciton and the faint ILX in **c** vs. the pure signature of the ILX at 1-ps delay in **d**. For each momentum-map, the photoelectron energy with respect to the valence band maximum of  $\text{WSe}_2$  and the pump-probe delay are noted in the lower left and right corner, respectively.



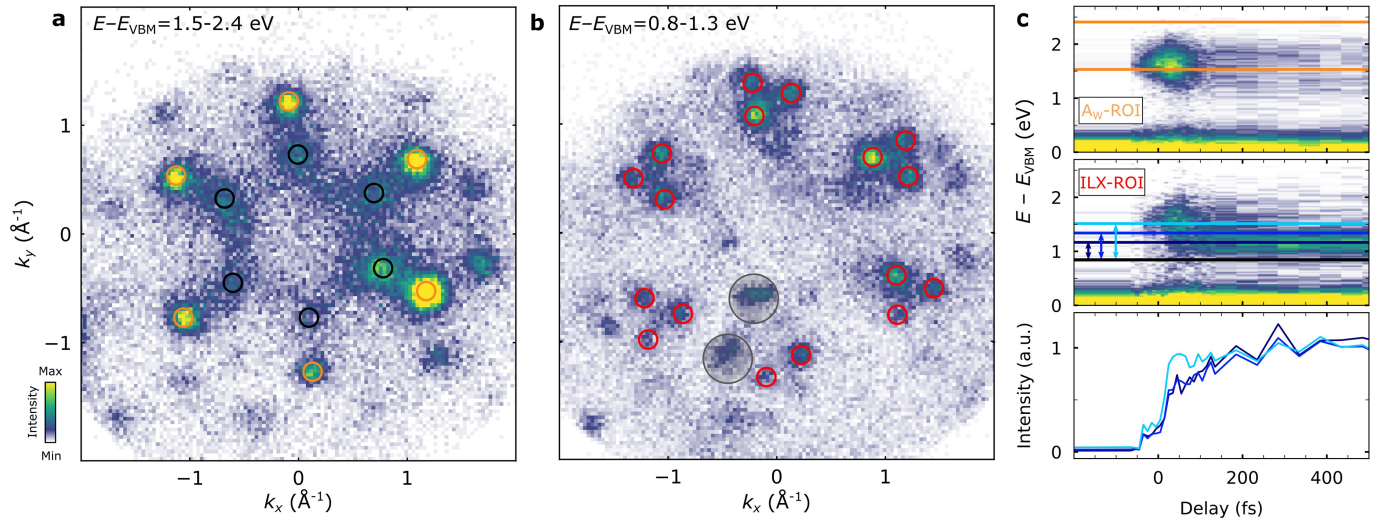
**Extended Data Fig. 5 | Above-band-gap excitation of monolayer WSe<sub>2</sub> and monolayer MoS<sub>2</sub>.** Photoemission yield from bright intralayer excitons and charge carriers in the conduction can be discriminated based on above-band-gap excitation data collected on **a–c** monolayer WSe<sub>2</sub> (orange circle in Fig. 1c) and **d–f** monolayer MoS<sub>2</sub> (real-space image not shown). **a** and **d** show energy–momentum cuts along the  $K$ – $\Sigma$  direction measured on WSe<sub>2</sub> and MoS<sub>2</sub>, respectively, at 0 fs and 300 fs (respectively 250 fs) pump–probe delay. At 0 fs,

a parabolic signature with positive dispersion is detected at the  $K$  valley (noted by the black dashed parabolic line). At 300 fs (250 fs), the signature becomes more spherical. **b** and **e** show energy-distribution curves at the  $K$  valleys (momentum-integration region based on the boxes in **a**, **d**). The peak maxima is indicated by grey horizontal lines. **c** and **f** show the corresponding energy-distribution curves when excited on resonance with the  $A_W$ - and  $A_{Mo}$ -exciton, respectively.



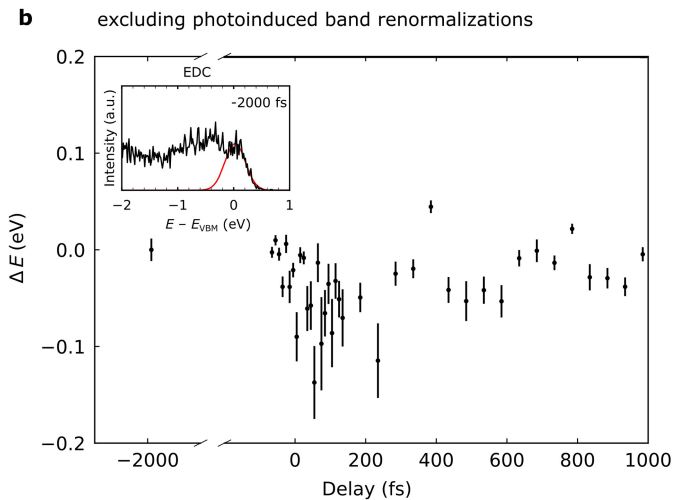
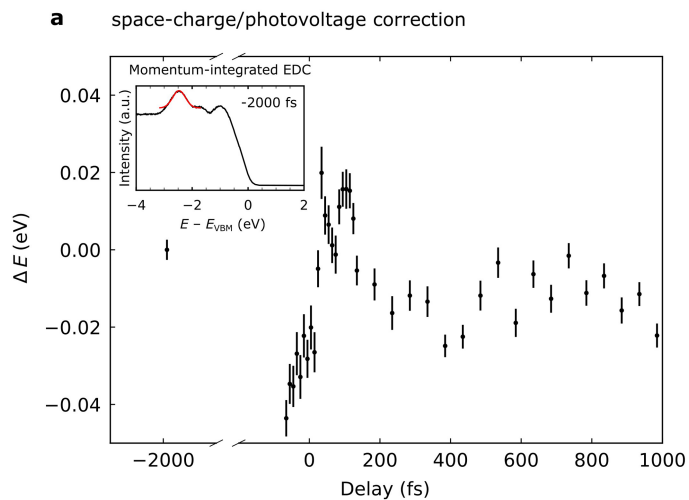
**Extended Data Fig. 6 | Additional trARPES data of the ILX formation.** **a**  $E(k)$  cut along the  $K_W$ - $\Gamma$ - $K'_W$  direction integrated in the  $k$ -region shown by the black dashed box in **b**, 0 fs. The arrowheads on the right side of the figure indicate the photoelectron energies where the momentum maps in **b** and **c** are centred. **b** Within the energy window of the  $k$ -map ( $E - E_{VBM} = 1.7$  eV) and increasing pump-probe delay, spectral weight from the bright  $A_W$ -excitons (orange hexagon) is transferred via exciton-phonon scattering to form dark  $\Sigma_W$ -excitons (grey hexagon). **c** Interlayer charge transfer via the  $\Sigma$ -valleys forms the ILX,

which is observed at  $E - E_{VBM} = 1.1$  eV. The Brillouin zone of  $\text{MoS}_2$  is indicated with a dotted dark red hexagon and the mBZ with a red hexagon. Spectroscopic signatures of the  $A_W$ -exciton, the  $\Sigma_W$ -exciton, and the ILX are indicated by orange, grey, and red circles, respectively, in the 1 ps data. The pump-probe delay and the binding energy of the  $k$ -maps are noted in the top and bottom left corner, respectively. Note that at 0 fs, the strong signal in **c** is mainly caused by LAPE. In addition, in **b** (0 fs), LAPE leads to photoemission yield at the  $\Gamma$  point.



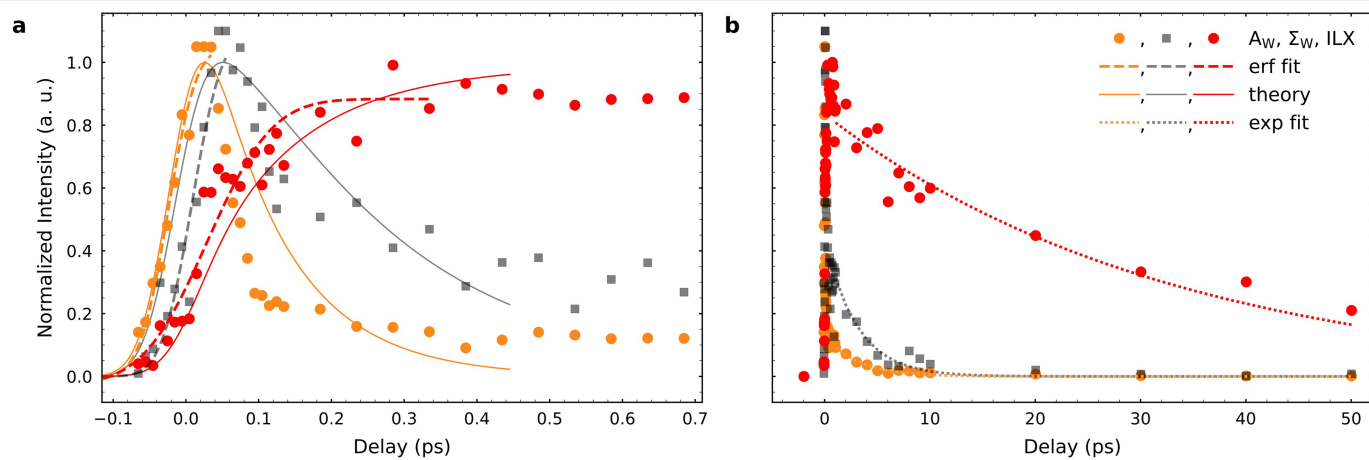
**Extended Data Fig. 7 | Selected regions of interest for the analysis of the  $A_{\text{W}}$ ,  $\Sigma_{\text{W}}$ , and ILX formation dynamics shown in Fig. 2c. a and b show momentum maps integrated over all measured pump-probe delays in the energy intervals of  $E - E_{\text{VBM}} = 1.5 - 2.4$  eV and  $0.8 - 1.3$  eV, respectively. The regions-of-interest that are used for filtering the excitonic photoemission signatures in momentum space are indicated by orange, black, and red circles for the  $A_{\text{W}}$ -exciton, the**

$\Sigma_{\text{W}}$ -exciton, and the ILX, respectively. The grey shaded areas indicate artefacts of the detector. c (top and middle panel) Pump-probe delay evolution of the energy-distribution curves filtered for the orange and red regions of interest. c (bottom panel) Intensity vs. pump-probe delay plots for the energy boxes indicated by the bluish arrows in the middle panel.



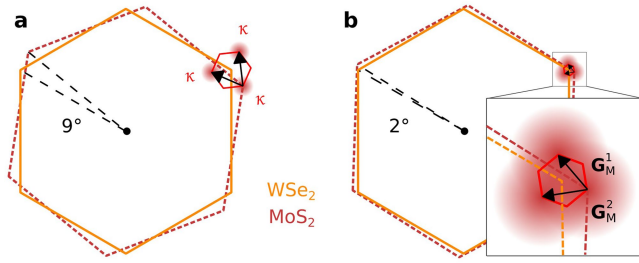
**Extended Data Fig. 8 | Correction of space-charge/photovoltage-induced shifts and exclusion of photoinduced band renormalizations.** **a** The rigid band shift  $\Delta E$  of maximal 70 meV is corrected for each pump-probe delay.  $\Delta E$  is obtained by fitting (red) momentum-integrated energy-distribution curves (black) for each delay, as exemplary shown for the -2000 fs measurement in the inset. The error bars are standard deviations obtained in each fit. **b** We fit the

pump-probe delay-dependent energetic peak position of the valence band maximum of WSe<sub>2</sub> at the  $K_w$  valley with Gaussian distributions (red, inset) and calculate the energy difference  $\Delta E$  with respect to the -2000 fs measurement that is plotted in the inset. Within the scattering of the data,  $\Delta E$  does not upshift with pump-probe delay, excluding a dominant contribution of photoinduced band renormalization such as discussed in refs. <sup>49,53</sup>.



**Extended Data Fig. 9 | Charge-transfer and charge recombination times of the  $A_w$  exciton (orange), the  $\Sigma_w$  exciton (grey), and the ILX (red).** **a** The short-time dynamics (symbols) is fitted with error functions (dashed lines), from which the delayed onset times  $t_i$  are extracted, as detailed in the text.

The solid lines reproduce the model calculations initially shown in Fig. 2c of the main text. **b** The charge recombination time is extracted by performing single-exponential fits to the data for pump-probe delays larger than 1 ps.



**Extended Data Fig. 10 | Sketch of the moiré mBz for small and large twist angles.** The twist angle  $\Theta$  defines the size of the moiré mBz (red hexagon) and the related moiré reciprocal lattice vectors  $\mathbf{G}_M^{1,2}$  (black arrows). **a** For twist angles larger than a few degree,  $\mathbf{G}_M^{1,2}$  is larger than the momentum width of a single  $\kappa$  valley (dark reddish filled circles). All three  $\kappa$  valleys (and higher-order umklapp processes) are detected in the momentum microscopy experiment (Fig. 3c, d). The electronic contribution to the ILX wavefunction is spread across several moiré potential wells (Fig. 4). **b** For sufficiently small twist angles,  $\mathbf{G}_M^{1,2}$  can become smaller than the width of a single  $\kappa$  valley, and the ILX wavefunction can be confined in a single moiré potential well. If the momentum microscopy experiment is performed with a finite momentum resolution, the photoelectron signal from the ILX can appear as a single peak, as reported in Ref. <sup>13</sup> for a  $2^\circ$  twisted  $\text{WSe}_2/\text{MoS}_2$  heterostructure.

**Supplementary information**

---

**Formation of moiré interlayer excitons in space and time**

---

In the format provided by the authors and unedited

# **Formation of moiré interlayer excitons in space and time**

## SUPPLEMENTAL INFORMATION

**Microscopic Model - Overview.** For the microscopic model of the interlayer charge transfer dynamics we have derived effective Boltzmann equations for the exciton-phonon scattering involving hybridized electronic states that are delocalized across the bilayer system. The energies of the involved conduction and valence bands are extracted from the experiment or derived from ab initio calculations. The Coulomb potential is treated on an Hartree-Fock level using a generalized Rytova–Keldysh potential for 2D films. Starting from a many-particle Hamilton operator for electrons and holes, we derive the energies and effective interaction matrix elements for layer-hybridized excitonic states within a low density limit. Finally, we derive the dynamics of the excitonic density matrix after an optical excitation using the Heisenberg equation of motion. The latter is truncated within a second-order Born-Markov approximation and solved numerically with a Runge-Kutta algorithm. Details about the theoretical model are presented in the following section.

As presented in the main text, the direct comparison of experiment and theory in Fig. 2c (main text) confirms an excellent agreement and shows that phonon-assisted scattering via dark layer-mixed states is indeed the dominant pathway for the formation of ILX in the  $9.8 \pm 0.8^\circ$  twisted WSe<sub>2</sub>/MoS<sub>2</sub> heterostructure.

However, we note that a critical comparison of the experimental data and the microscopic model also shows minor deviations for the quantitative formation time of the  $\Sigma_W$ -exciton and the ILX, and for the decay times of the  $A_W$ - and  $\Sigma_W$ -excitons. Possible explanations for this discrepancy might be additional scattering channels such as direct interlayer tunneling at the  $K_W$  and  $K_{M_0}$  valleys<sup>S1–S3</sup> or Auger-type recombination processes<sup>S4,S5</sup>, which are neglected in the microscopic model. However, femtosecond momentum microscopy, which is explicitly sensitive to bright as well as dark intra- and interlayer excitons, clearly provides the capability to retrieve the necessary transfer rates from future twist-angle-dependent studies, and thereby to elucidate such additional processes. Therefore, future experiments performed at higher exciton densities can elucidate how Auger-type recombination processes or electron-hole plasmas contribute to the formation dynamics of ILX.

**Microscopic Model - Detailed description.** In this section, we introduce the main concepts for the theoretical approach applied to calculate the charge transfer dynamics in TMD bilayers. First, we introduce the many-particle Hamilton operator for the non-twisted TMD bilayer in the electronic picture, and, using consecutive basis transformations, we show how the internal quantum structure of hybrid excitons is obtained. Finally, we describe how we compute the phonon-driven dynamics of hybrid excitons.

We start with the Hamiltonian for conduction- ( $c^{(\dagger)}$ ) and valence band electrons ( $v^{(\dagger)}$ ) in a decoupled bilayer system interacting via the Coulomb potential,

$$H_0 = \sum_{i,\mathbf{p}} \left( \varepsilon_{i\mathbf{p}}^c c_{i\mathbf{p}}^\dagger c_{i\mathbf{p}} + \varepsilon_{i\mathbf{p}}^v v_{i\mathbf{p}}^\dagger v_{i\mathbf{p}} \right) + \sum_{i,j} W_{L_i L_j \mathbf{q}} c_{i\mathbf{p}'+\mathbf{q}}^\dagger v_{j\mathbf{p}-\mathbf{q}}^\dagger v_{j\mathbf{p}} c_{i\mathbf{p}'}, \quad (1)$$

with the total electron momentum  $\mathbf{p}_t = \zeta + \mathbf{p}$ , where  $\zeta$  encodes a high-symmetry point (valley) within the first Brillouin zone. The valley is treated as a discrete quantum number that is contained in the compound index  $i = (\zeta_i, L_i)$  additionally containing the layer index ( $L = 0, 1$ ). The energy dispersion  $\varepsilon_{i,\mathbf{p}}^\lambda = \varepsilon_{i,0}^\lambda + \hbar^2 p^2 / (2m_i^\lambda)$  is obtained from a valley-local effective mass approximation, where the band gap and band offset at the K valley are extracted from experiments in the main paper and all the other required parameters (effective masses, spin-orbit splitting and energetic separations of valleys) are taken from ab initio calculations<sup>S6</sup>. The Coulomb matrix element  $W_{L_i L_j \mathbf{q}}$  takes into account the dielectric background screening due to the presence of the two different TMD layers<sup>S2,S7</sup>. We account for the formation of strongly correlated electron-hole pairs, by transforming the Hamiltonian into an excitonic basis<sup>S8-S10</sup>,

$$H_X^0 = \sum_{\mu, \mathbf{Q}} E_{\mathbf{Q}}^\mu X_{\mathbf{Q}}^{\mu\dagger} X_{\mathbf{Q}}^\mu$$

with  $X_{\mathbf{Q}}^{\mu\dagger} = \sum_{\mathbf{k}} \psi^\mu(\mathbf{k}) c_{\mu, \mathbf{k} + \alpha_\mu \mathbf{Q}}^\dagger v_{\mu, \mathbf{k} - \beta_\mu \mathbf{Q}}$  (2)

and  $E_{\mathbf{Q}}^\mu = E_{\zeta^\mu L_e^\mu}^c - E_{\zeta^\mu L_h^\mu}^v + E_{bind}^\mu + E_{\mathbf{Q}, kin}^\mu$ ,

where  $\mu = (n^\mu, \zeta_e^\mu, \zeta_h^\mu, L_e^\mu, L_h^\mu)$ . Here,  $n_\mu$  is the quantum number associated with the new set of excitonic eigenstates. Moreover, the electron-hole mass ratios enter via  $\alpha(\beta) = m_{e(h)} / (m_e + m_h)$ . The exciton eigenfunctions and eigenenergies  $\psi^\mu$  and  $E_{bind}^\mu$  are obtained after solving a bilayer Wannier equation<sup>S10,S11</sup>. Finally,  $E_{\zeta^\mu L_e^\mu}^{c/v}$  are the conduction and va-

lence band energy and  $E_{\mathbf{Q},kin}^\mu = \hbar^2 \mathbf{Q}^2 / (2M^\mu)$  is the kinetic energy of the exciton, which is created/annihilated by the operator  $X^{(\dagger)}$ .

So far, all excitations are decomposed into pure intra- ( $L_e = L_h$ ) or interlayer excitons ( $L_e \neq L_h$ ). Next, we take into account the hybridization of electronic states via the interlayer tunneling Hamiltonian,

$$H_T = \sum_{i,j,\mathbf{p}} T_{ij}^c c_{i\mathbf{p}}^\dagger c_{j\mathbf{p}} + T_{ij}^v v_{i\mathbf{p}}^\dagger v_{j\mathbf{p}} \quad (3)$$

where  $T_{ij}^\lambda = \langle \lambda i\mathbf{p} | H | \lambda j\mathbf{p} \rangle (1 - \delta_{L_i L_j}) \delta_{\zeta_i \zeta_j}$ . After transformation into excitonic basis we obtain

$$H = H_0 + H_T = \sum_{\mu,\mathbf{Q}} E_{\mathbf{Q}}^\mu X_{\mathbf{Q}}^{\mu\dagger} X_{\mathbf{Q}}^\mu + \sum_{\mu,v,\mathbf{Q}} \mathcal{T}_{\mu v} X_{\mathbf{Q}}^{\mu\dagger} X_{\mathbf{Q}}^v \quad (4)$$

with excitonic tunnelling matrix elements

$$\mathcal{T}_{\mu v} = (\delta_{L_h^\mu L_h^v} (1 - \delta_{L_e^\mu L_e^v}) \delta_{\zeta^\mu \zeta^v} T_{\mu_e, v_e}^c - \delta_{L_e^\mu L_e^v} (1 - \delta_{L_h^\mu L_h^v}) \delta_{\zeta^\mu \zeta^v} T_{\mu_h, v_h}^v) \sum_{\mathbf{k}} \psi^{\mu*}(\mathbf{k}) \psi^v(\mathbf{k}) \quad (5)$$

, where  $T^{c/v}$  are obtained by averaging DFT values of MoSe<sub>2</sub>-WSe<sub>2</sub> and MoS<sub>2</sub>-WS<sub>2</sub> heterostructures in<sup>S12</sup>. Finally, we diagonalize the above Hamiltonian to obtain intralayer-interlayer-hybrid excitons by solving the eigenvalue problem,

$$E_{\mathbf{Q}}^\mu c_\mu^\eta(\mathbf{Q}) + \sum_v \mathcal{T}_{\mu v} c_v^\eta(\mathbf{Q}) = \mathcal{E}_{\mathbf{Q}}^\eta c_\mu^\eta(\mathbf{Q}) \quad (6)$$

defining the new hybrid excitons<sup>S10,S12</sup>,

$$H = \sum_\eta \mathcal{E}_{\mathbf{Q}}^\eta Y_{\mathbf{Q}}^{\eta\dagger} Y_{\mathbf{Q}}^\eta \quad \text{and} \quad Y_{\mathbf{Q}}^\eta = \sum_\mu c_\mu^\eta(\mathbf{Q}) X_{\mathbf{Q}}^\mu. \quad (7)$$

As the leading contribution to the exciton relaxation process we take into account the electron-phonon scattering, where the phonon coupling and energies are taken from DFPT calculations<sup>S13</sup>. We perform the change into hybrid exciton basis, which is in detail described in Ref.<sup>S10</sup>, yielding

$$H_{Y-ph} = \sum_{j,\mathbf{Q},\mathbf{q},\eta,\xi} \tilde{\mathcal{D}}_{j,\mathbf{q},\mathbf{Q}}^{\xi\eta} Y_{\mathbf{Q}+\mathbf{q}}^{\xi\dagger} Y_{\mathbf{Q}}^\eta b_{j,\mathbf{q}} + h.c. \quad (8)$$

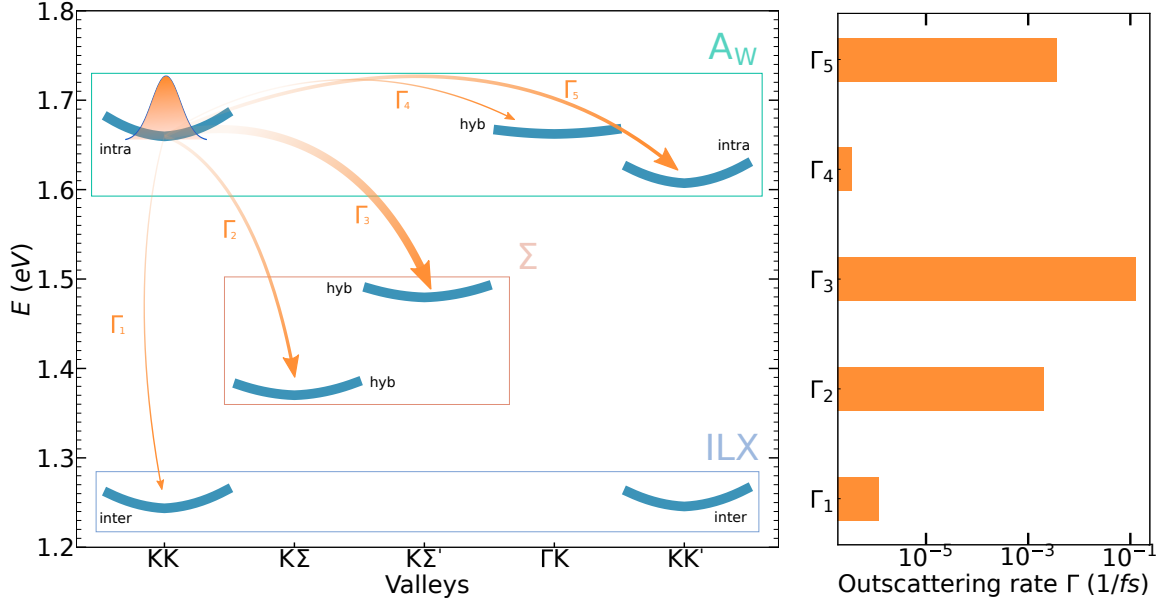
The excitation of the system through a laser pulse is described semi-classically via the minimal-coupling Hamiltonian. After transforming into hybrid basis<sup>S10</sup> we obtain

$$H_{Y-l} = \sum_{\sigma,\mathbf{Q},\eta} \mathbf{A} \cdot \tilde{\mathcal{M}}_{\sigma\mathbf{Q}}^\eta Y_{\mathbf{Q}}^\eta + h.c. \quad (9)$$

Details on the transformation and the definition of the hybrid interaction matrix elements are given in the Supplementary Information of Ref.<sup>S10,S12</sup>. Finally, we compute the dynamics of excitons exploiting the Heisenberg equation of motion for the hybrid occupation  $N^\eta = \langle Y^{\eta\dagger} Y^\eta \rangle$ , including  $H = H_Y + H_{Y-ph} + H_{Y-l}$ . We truncate the Martin-Schwinger hierarchy using a second order Born-Markov approximation<sup>S14-S16</sup>. Moreover, we separate coherent  $P_Q^\eta = \langle Y_Q^{\eta\dagger} \rangle$  and incoherent hybrid populations  $\delta N_Q^\eta = \langle Y_Q^{\eta\dagger} Y_Q^\eta \rangle - \langle Y_Q^{\eta\dagger} \rangle \langle Y_Q^\eta \rangle = N_Q^\eta - |P_Q^\eta|^2$  yielding the coupled equations,

$$\begin{aligned}
i\hbar\partial_t P_0^\eta &= -(\mathcal{E}_0^\eta + i\Gamma_0^\eta)P_0^\eta - \tilde{\mathcal{M}}_0^\eta \cdot \mathbf{A}(t) \\
\delta\dot{N}_Q^\eta &= \sum_\xi W_{0Q}^{\xi\eta} |P_0^\eta|^2 + \sum_{\xi, Q'} \left( W_{QQ'}^{\xi\eta} \delta N_{Q'}^\xi - W_{QQ'}^{\eta\xi} \delta N_Q^\eta \right) \\
\text{with } W_{QQ'}^{\eta\xi} &= \frac{2\pi}{\hbar} \sum_{j, \pm} \left| \mathcal{D}_{j, Q'-Q}^{\eta\xi} \right|^2 \left( \frac{1}{2} \pm \frac{1}{2} + n_{j, Q'-Q}^{ph} \right) \delta \left( \mathcal{E}_{Q'}^\xi - \mathcal{E}_Q^\eta \mp \hbar\Omega_{j, Q'-Q} \right)
\end{aligned} \tag{10}$$

The large twist angle in the experiment gives rise to very short periods of the moire pattern with a length scale comparable with the exciton Bohr radius. Therefore, a strong modification of the excitons center-of-mass motion, i.e. a moire-trapping of excitons is not expected<sup>S9</sup> and experimentally confirmed in Fig. 4. Therefore, we introduce the twist angle as a simple rotation of the two layers' Brillouin zones. The presence of this rotation has the consequence that hybrid bands  $\mathcal{E}_Q^\eta$  and the respective exciton mixing coefficients  $c_\mu^\eta(\mathbf{Q})$  are not isotropic in momentum. We assume that any anisotropy in the valley local population is quickly equilibrated e.g. by elastic scattering with disorder. Hence, we perform an average over the valley local angle of the exciton momentum assuming that the population stays almost isotropic at all times. We define angle-averaged quantities  $\delta N_Q^\eta \approx \delta \tilde{N}_Q^\eta$  with the 1D density  $\tilde{N}_Q^\eta$  depending only on the radial component of the CoM momentum. We then integrate eq.10 over the momentum to obtain averaged scattering rates  $\tilde{W}_{QQ'}^{\eta\xi} = \sum_{\theta, \theta'} W_{QQ'}^{\eta\xi}$ .



Supplemental Fig. 1. **Hybrid exciton dispersion and scattering rates.** Hybrid exciton bandstructure including all possible s-type exciton states with energies below or close to the optically excited intralayer KK state (left). The orange arrows indicate possible relaxation channels, with the corresponding scattering rates displayed on the right.

**Microscopic Model - Analysis.** In our numerical evaluation of the microscopic model described above, we consider all extrema of the valence (K, K' and  $\Gamma$ ) and conduction band (K, K',  $\Sigma$ , and  $\Sigma'$ )<sup>S6</sup> and all possible layer/valley configurations for electron-hole pairs. Furthermore, the exciton-phonon scattering tensor  $W_{\mathbf{Q}\mathbf{Q}'}^{\eta\xi}$  is computed for all possible initial and final exciton states, summing over all available phonon modes (LA, TA, LO, TO, A1) in both layers<sup>S17</sup>. In supplemental Fig. 1a we illustrate the corresponding hybrid exciton bandstructure including all possible s-type exciton states with energies below or close to the optically excited state intralayer KK exciton. The colored boxes indicate which group of exciton states gives rise to the energetically broad photoemission signal in the main text denoted with  $A_W$  (electron at K or K' point of WSe<sub>2</sub>),  $\Sigma$  (electron at  $\Sigma$  or  $\Sigma'$  point) and ILX (electron at K or K' point of MoS<sub>2</sub>, but at lower energies). The orange arrows denoted with  $\Gamma_1$ - $\Gamma_5$  indicate possible relaxation channels for the optically excited intralayer KK exciton. The scattering rates for these channels  $\Gamma_{\eta \rightarrow \xi} = \sum_{\mathbf{Q}\mathbf{Q}'} W_{\mathbf{Q}\mathbf{Q}'}^{\eta\xi} |_{\mathbf{Q}=0}$  are shown in the right panel of supplemental Fig. 1.

We find that  $\Gamma_3 \approx 0.1 \text{ fs}^{-1}$  is by orders of magnitude the fastest relaxation channel. Here the electron of the KK exciton is scattered from the K to the  $\Sigma'$  valley by emitting a zone-edge M phonon, which exhibits the most efficient electron-phonon coupling in TMDs<sup>S17</sup>. In contrast, the direct transition from the KK intralayer to the KK interlayer exciton ( $\Gamma_1$ ) is strongly suppressed. To understand this we consider the coefficients  $c_v^\eta(\mathbf{Q})$  from Eq. (6), determining how strong the interlayer tunneling is mixing pure intra- and interlayer excitons into hybrids.

TABLE I. Energies of the lowest two s-type exciton states for each valley configuration. Columns 4-7 show the contribution of all possible intra- and interlayer excitons (W-W=intralayer , W-Mo=interlayer, hole first). The last column indicates nomenclature used in Tab. II.

Valley	State #	Energy (eV)	Mixing Coefficients				Name
			W-W	Mo-W	W-Mo	Mo-Mo	
KK	1	1.24	0	0	1	0	ILX
	2	1.66	1	0	0	0	$A_W$
K $\Sigma$	1	1.37	0.30	0	0.70	0	$\Sigma_W$
	2	1.74	0.70	0	0.30	0	-
K $\Sigma'$	1	1.48	0.18	0	0.82	0	$\Sigma'_W$
	2	1.91	0.82	0	0.18	0	-
$\Gamma$ K	1	1.66	0	0	0.88	0.12	-
	2	2.07	0.93	0.07	0	0	-
KK'	1	1.25	0	0	1	0	ILX'
	2	1.61	1	0	0	0	$A'_W$

Table I shows the energies of the lowest two s-type exciton states for each valley configuration along with the fractional contribution of all possible intra- and interlayer excitons contributing to this hybrid state. Here "W-W" is denoting the intralayer exciton in the tungsten layer, whereas "W-Mo" corresponds to the fraction of interlayer excitons with the hole in the tungsten and the electron in the molybdenum layer. We find that the KK exciton states are strongly layer-polarized, either being pure intra- or interlayer excitons. Since the electron of the  $A_W$  exciton and the ILX are located in different layers, their wavefunction overlap is

small, drastically quenching the phonon-transition amplitude for this direct charge transfer process. In contrast, the  $K\Sigma$  exciton is strongly hybridized, i.e. by 30% an intra- and by 70% an interlayer exciton. In the electron-hole picture this means that the  $\Sigma$  electron is delocalized across both layers, enabling efficient transitions to (from) final (initial) states in both layers. As a result, the charge transfer occurs in a two-step process via phonon-mediated transition into the strongly hybridised  $K\Sigma$  excitons.

Finally, in Table II we show the out-scattering rates  $\Gamma_{\eta \rightarrow \xi}$  at  $\mathbf{Q} = 0$  for all initial exciton states resolved into all possible final states. By evaluating the most efficient relaxation channels for each state, starting from the optically excited  $A_W$ , we determine the predominant formation channel for ILX. We find that the multistep cascade  $A_W \rightarrow \Sigma'_W \rightarrow \Sigma_W \rightarrow ILX' \rightarrow ILX$  is giving rise to the ultrafast formation of the ILX photoemission signal discussed in the main text (ILX+ILX'), involving the transient occupation of momentum dark states ( $\Sigma_W + \Sigma'_W$ ).

TABLE II. Phonon-driven out-scattering rates at  $\mathbf{Q} = 0$  for all initial exciton states resolved into all possible final states (in  $\text{ps}^{-1}$ ). Channels with "0" are decoupled due to energy conservation for the considered one-phonon processes.

from \ to	$A_W$	$A'_W$	$\Sigma_W$	$\Sigma'_W$	ILX	ILX'
$A_W$	-	3.7	2.0	127.1	$10^{-3}$	$10^{-4}$
$A'_W$	0	-	92.8	5.8	$10^{-4}$	$10^{-3}$
$\Sigma_W$	0	0	-	0	1.0	8.7
$\Sigma'_W$	0	0	121.8	-	3.2	$10^{-4}$
ILX	0	0	0	0	-	$10^{-4}$
ILX'	0	0	0	0	$10^{-4}$	-

## REFERENCES

- [S1] P. Merkl, F. Mooshammer, P. Steinleitner, A. Girnghuber, K. Q. Lin, P. Nagler, J. Holler, C. Schüller, J. M. Lupton, T. Korn, S. Ovesen, S. Brem, E. Malic, and R. Huber, “Ultrafast transition between exciton phases in van der Waals heterostructures,” *Nature Materials* **18**, 691–696 (2019).
- [S2] Simon Ovesen, Samuel Brem, Christopher Linderälv, Mikael Kuisma, Tobias Korn, Paul Erhart, Malte Selig, and Ermin Malic, “Interlayer exciton dynamics in van der Waals heterostructures,” *Communications Physics* **2**, 23 (2019).
- [S3] Jonas E. Zimmermann, Marleen Axt, Fabian Mooshammer, Philipp Nagler, Christian Schüller, Tobias Korn, Ulrich Höfer, and Gerson Mette, “Ultrafast Charge-Transfer Dynamics in Twisted MoS<sub>2</sub>/WSe<sub>2</sub> Heterostructures,” *ACS Nano* **15**, 14725–14731 (2021).
- [S4] Dezheng Sun, Yi Rao, Georg A. Reider, Gugang Chen, Yumeng You, Louis Brézin, Avetik R. Harutyunyan, and Tony F. Heinz, “Observation of rapid exciton–exciton annihilation in monolayer molybdenum disulfide,” *Nano Letters* **14**, 5625–5629 (2014).
- [S5] Daniel Erkensten, Samuel Brem, Koloman Wagner, Roland Gillen, Raúl Perea-Causín, Jonas D. Ziegler, Takashi Taniguchi, Kenji Watanabe, Janina Maultzsch, Alexey Chernikov, and Ermin Malic, “Dark exciton–exciton annihilation in monolayer WSe<sub>2</sub>,” *Physical Review B* **104**, 1–7 (2021), 2106.05035.
- [S6] Andor Kormányos, Guido Burkard, Martin Gmitra, Jaroslav Fabian, Viktor Zólyomi, Neil D Drummond, and Vladimir Fal’ko, “ $k \cdot p$  theory for two-dimensional transition metal dichalcogenide semiconductors,” *2D Materials* **2**, 022001 (2015).
- [S7] Akash Laturia, Maarten L Van de Put, and William G Vandenberghe, “Dielectric properties of hexagonal boron nitride and transition metal dichalcogenides: from monolayer to bulk,” *npj 2D Materials and Applications* **2**, 1–7 (2018).
- [S8] Florian Katsch, Malte Selig, Alexander Carmele, and Andreas Knorr, “Theory of exciton–exciton interactions in monolayer transition metal dichalcogenides,” *physica status solidi (b)* **255**, 1800185 (2018).
- [S9] Samuel Brem, Christopher Linderälv, Paul Erhart, and Ermin Malic, “Tunable Phases of Moiré

- Excitons in van der Waals Heterostructures,” *Nano Letters* **20**, 8534–8540 (2020).
- [S10] Samuel Brem, Kai-Qiang Lin, Roland Gillen, Jonas M Bauer, Janina Maultzsch, John M Lupton, and Ermin Malic, “Hybridized intervalley moiré excitons and flat bands in twisted wse2 bilayers,” *Nanoscale* **12**, 11088–11094 (2020).
- [S11] Simon Ovesen, Samuel Brem, Christopher Linderälv, Mikael Kuisma, Tobias Korn, Paul Erhart, Malte Selig, and Ermin Malic, “Interlayer exciton dynamics in van der waals heterostructures,” *Communications Physics* **2**, 1–8 (2019).
- [S12] Joakim Hagel, Samuel Brem, Christopher Linderälv, Paul Erhart, and Ermin Malic, “Exciton landscape in van der waals heterostructures,” *Physical Review Research* **3**, 043217 (2021).
- [S13] Zhenghe Jin, Xiaodong Li, Jeffrey T Mullen, and Ki Wook Kim, “Intrinsic transport properties of electrons and holes in monolayer transition-metal dichalcogenides,” *Physical Review B* **90**, 045422 (2014).
- [S14] Mackillo Kira and Stephan W Koch, “Many-body correlations and excitonic effects in semiconductor spectroscopy,” *Progress in quantum electronics* **30**, 155–296 (2006).
- [S15] Hartmut Haug and Stephan W Koch, *Quantum theory of the optical and electronic properties of semiconductors* (World Scientific Publishing Company, 2009).
- [S16] Ermin Malic and Andreas Knorr, *Graphene and carbon nanotubes: ultrafast optics and relaxation dynamics* (John Wiley & Sons, 2013).
- [S17] Jin Z, Li X, Mullen J T, and Kim K W, “Intrinsic transport properties of electrons and holes in monolayer transition-metal dichalcogenides,” *Phys. Rev. B* **90**, 045422 (2014).



---

Paper 3

---



## OPTICS

# Probing electron-hole Coulomb correlations in the exciton landscape of a twisted semiconductor heterostructure

Jan Philipp Bange<sup>1</sup>, David Schmitt<sup>1</sup>, Wiebke Bennecke<sup>1</sup>, Giuseppe Meneghini<sup>2</sup>, AbdulAziz AlMutairi<sup>3</sup>, Kenji Watanabe<sup>4</sup>, Takashi Taniguchi<sup>5</sup>, Daniel Steil<sup>1</sup>, Sabine Steil<sup>1</sup>, R. Thomas Weitz<sup>1,6</sup>, G. S. Matthijs Jansen<sup>1</sup>, Stephan Hofmann<sup>3</sup>, Samuel Brem<sup>2</sup>, Ermin Malic<sup>2,7</sup>, Marcel Reutzler<sup>1\*</sup>, Stefan Mathias<sup>1,6\*</sup>

Copyright © 2024 the Authors, some rights reserved; exclusive licensee American Association for the Advancement of Science. No claim to original U.S. Government Works. Distributed under a Creative Commons Attribution License 4.0 (CC BY).

In two-dimensional semiconductors, cooperative and correlated interactions determine the material's excitonic properties and can even lead to the creation of correlated states of matter. Here, we study the fundamental two-particle correlated exciton state formed by the Coulomb interaction between single-particle holes and electrons. We find that the ultrafast transfer of an exciton's hole across a type II band-aligned semiconductor heterostructure leads to an unexpected sub-200-femtosecond upshift of the single-particle energy of the electron being photoemitted from the two-particle exciton state. While energy relaxation usually leads to an energetic downshift of the spectroscopic signature, we show that this upshift is a clear fingerprint of the correlated interaction of the electron and hole parts of the exciton. In this way, time-resolved photoelectron spectroscopy is straightforwardly established as a powerful method to access electron-hole correlations and cooperative behavior in quantum materials. Our work highlights this capability and motivates the future study of optically inaccessible correlated excitonic and electronic states of matter.

## INTRODUCTION

An exciton is a prime example of a quasiparticle that is built up by electrons and holes bound together via Coulomb interaction. As in the case of a hydrogen atom, the exciton's properties are described by its quantum number, its binding energy, and its Bohr radius (1). For low-dimensional materials, these key parameters can be substantially altered by cooperative interactions with surrounding quasiparticles (2, 3). To study such cooperative and emergent behavior, artificial stacks of two-dimensional transition metal dichalcogenides (TMDs) have been shown to provide an exceptional playground for manipulating exciton properties. Examples include the ultrafast formation of interlayer excitons whose electron and hole components are charge-separated across the neighboring TMD layers (4–8), the confinement of excitons in a moiré potential well (9–12), the creation of correlated interlayer exciton insulators (13, 14) and exciton crystals (15, 16), and even the stabilization of Bose-Einstein condensates (17).

It is therefore of fundamental importance to obtain insight into the energy landscape and the ultrafast dynamics of the two-particle correlated exciton state (18, 19). In TMD semiconductors, momentum-indirect and spin-forbidden excitons play a substantial role but are mostly inaccessible (7, 20) using all-optical experimental techniques (21, 22). Recently, time- and angle-resolved photoelectron spectroscopy (trARPES) experiments have been shown to be a powerful technique to fill this gap and to simultaneously probe the

energy landscape and dynamics of optically bright and dark excitons in monolayer (23–25) and twisted bilayer (8, 12, 26, 27) TMDs. When using photoelectron spectroscopy, there is a fundamental aspect that needs to be considered (Fig. 1A): In the photoemission process, the Coulomb correlation between the electron and hole components of the exciton is broken. This is because a single-particle photoelectron is collected with the detector and a single-particle hole remains in the material (28–31). In consequence, photoelectrons originating from excitons are detected at the exciton binding energy below the conduction band minimum (8, 23–25, 32) and show a hole-like energy-momentum dispersion (32, 33). In this way, trARPES provides natural access to the electron contribution of the exciton and can be used to quantify the charge transfer of the exciton's electron across a type II band-aligned heterostructure (Fig. 1B) (8, 27). However, to this day, only very limited energy- and momentum-resolved spectroscopic information on the exciton's hole component is reported (12). Specifically, in contrast to all-optical spectroscopies (4–6, 18, 34–37), it has not been shown that trARPES can be applied to monitor the charge-transfer dynamics of the exciton's hole across the TMD interface (Fig. 1C).

Here, we demonstrate how the Coulomb interaction between the electron- and the hole components of the intra- and interlayer excitons facilitates the study of the ultrafast hole-transfer mechanism in a twisted WSe<sub>2</sub>/MoS<sub>2</sub> heterostructure. We experimentally observe an increase in the exciton's photoelectron energy upon the hole-transfer process across the interface. This is unexpected at first because the electron remains rigid in the conduction band minimum during this hole-transfer process (Fig. 1C) and because any relaxation mechanism is typically expected to cause an overall decrease in the measured electronic quasiparticle energies. However, when taking the correlated nature of the electron-hole pair into account, despite an overall decrease in the quasiparticle energies, we show that such an increase due to hole transfer must be expected for the corresponding exciton's photoelectron. Our work provides microscopic insights into the ultrafast hole-transfer mechanism and, more

<sup>1</sup>Physikalisches Institut, Georg-August-Universität Göttingen, Friedrich-Hund-Platz 1, 37077 Göttingen, Germany. <sup>2</sup>Fachbereich Physik, Philipps-Universität Marburg, 35032 Marburg, Germany. <sup>3</sup>Department of Engineering, University of Cambridge, Cambridge CB3 0FA, UK. <sup>4</sup>Research Center for Functional Materials, National Institute for Materials Science, 1-1 Namiki, Tsukuba 305-0044, Japan. <sup>5</sup>International Center for Materials Nanoarchitectonics, National Institute for Materials Science, 1-1 Namiki, Tsukuba 305-0044, Japan. <sup>6</sup>International Center for Advanced Studies of Energy Conversion (ICASEC), University of Göttingen, Göttingen, Germany. <sup>7</sup>Department of Physics, Chalmers University of Technology, Gothenburg, Sweden. \*Corresponding author. Email: marcel.reutzler@phys.uni-goettingen.de (M.R.); smathias@uni-goettingen.de (S.M.)

generally, highlights the potential of time-resolved momentum microscopy to probe optically inaccessible correlated excitonic and electronic states of matter.

## RESULTS

### Energy landscape and photoemission fingerprints of bright and dark excitons

We start the analysis of the hole-transfer dynamics by first calculating the full energy landscape and formation dynamics of bright and

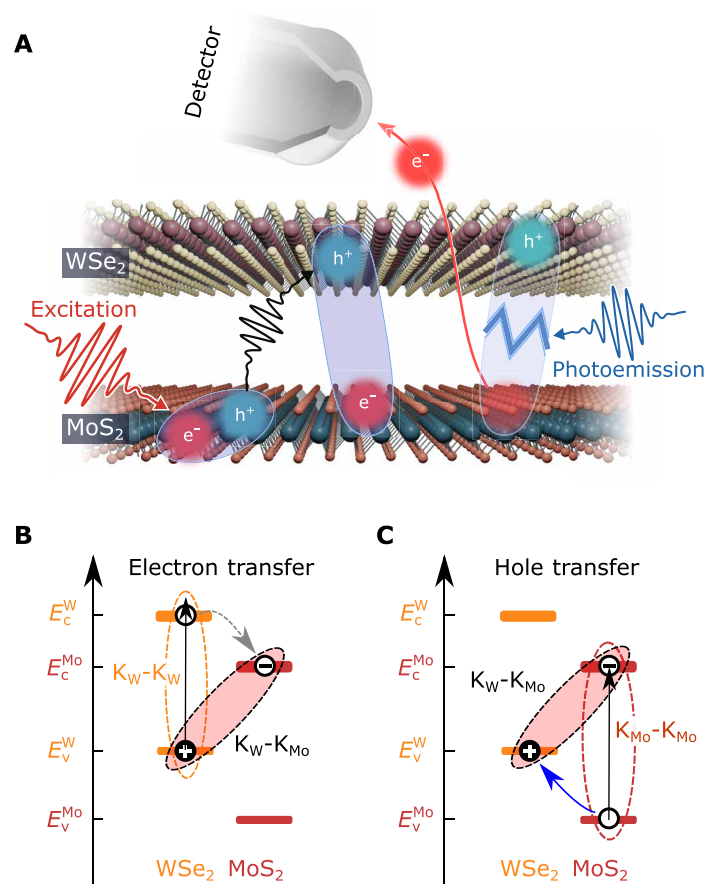


**Fig. 1. Probing Coulomb-correlated electron-hole pairs and their femtosecond dynamics using momentum microscopy.** (A) Schematic illustration of the photoemission process from excitons. Visible femtosecond light pulses (red) are used to optically excite bright excitons that fully reside in the MoS<sub>2</sub> monolayer. The transfer of the hole component into the WSe<sub>2</sub> monolayer leads to the formation of charge-separated interlayer excitons (black arrow). A time-delayed extreme ultraviolet laser pulse (blue) breaks the exciton; single-particle electrons are detected in the photoemission analyzer and single-particle holes remain in the WSe<sub>2</sub> monolayer. (B and C) Single-particle energy-level alignment of the valence and conduction bands (v and c) of MoS<sub>2</sub> and WSe<sub>2</sub>. K<sub>W</sub>-K<sub>Mo</sub> excitons are formed due to interlayer charge transfer of the exciton's hole or electron, respectively, from intralayer K<sub>Mo</sub>-K<sub>Mo</sub> or K<sub>W</sub>-K<sub>W</sub> excitons. Note that in (C), the electron contribution to the exciton remains rigid in the conduction band minimum of MoS<sub>2</sub> during the hole-transfer process. In the abbreviation of the excitons, the capital letters and the subscripts denote the valley (K,  $\Sigma$ , and  $\Gamma$ ) and the layer (W and Mo) where the exciton's hole (first letter) and electron (second letter) are localized. It is not differentiated between momentum-direct and momentum-indirect excitons (e.g., K<sub>W/Mo</sub> and K'<sub>W/Mo</sub> or  $\Sigma$  and  $\Sigma'$ ) because those cannot be differentiated in the photoemission experiment (see fig. S7).

dark excitons in the twisted WSe<sub>2</sub>/MoS<sub>2</sub> heterostructure on a microscopic footing (details in Supplementary Text). The optically excited A1s excitons in the WSe<sub>2</sub> and the MoS<sub>2</sub> layer and their cascaded relaxation via layer-hybridized excitons to the lowest energy interlayer excitons are illustrated in Fig. 2A. If the heterostructure is excited resonantly to the A1s-exciton of WSe<sub>2</sub> with 1.7 eV pulses, then only intralayer K<sub>W</sub>-K<sub>W</sub> A1s excitons are optically excited and decay in a cascaded transition via layer hybridized K<sub>W</sub>- $\Sigma$  excitons to interlayer K<sub>W</sub>-K<sub>Mo</sub> excitons, as we have discussed in detail in our earlier work (8, 27) (i.e., K<sub>W</sub>-K<sub>W</sub>  $\rightarrow$  K<sub>W</sub>- $\Sigma$   $\rightarrow$  K<sub>W</sub>-K<sub>Mo</sub>; Fig. 2A, left-hand side). In the single-particle picture, this cascaded transition can be associated with the transfer of the exciton's electron across the TMD interface (Fig. 1B).

Complementary, if the hole-transfer process across the WSe<sub>2</sub>/MoS<sub>2</sub> interface is considered (Fig. 1C), then the dynamics must be initiated by an excitation of MoS<sub>2</sub> A1s excitons with 1.9 eV light pulses (K<sub>Mo</sub>-K<sub>Mo</sub> excitons in Fig. 2A, right-hand side). Exploiting the density matrix formalism, we calculate the excitonic energy landscape (details below), and track the exciton dynamics, finding that the most efficient mechanism to form interlayer K<sub>W</sub>-K<sub>Mo</sub> excitons occurs via layer hybridized  $\Gamma$ -K<sub>Mo</sub> excitons, where the exciton's electron resides in the K<sub>Mo</sub> valley of MoS<sub>2</sub> and the exciton's hole can be found in the layer-hybridized valence bands at the  $\Gamma$  valley (38). Hence, the hole-transfer dominantly occurs via the K<sub>Mo</sub>-K<sub>Mo</sub>  $\rightarrow$   $\Gamma$ -K<sub>Mo</sub>  $\rightarrow$  K<sub>W</sub>-K<sub>Mo</sub> exciton cascade.

To differentiate the spectral contributions of different excitons in the experiment, we apply our setup for femtosecond momentum microscopy (39, 40) that provides direct access to the photoemission energy-momentum fingerprint of excitons (Fig. 2, B to E). In Fig. 2E, the momentum map of the intralayer K<sub>Mo</sub>-K<sub>Mo</sub> exciton is shown after resonant optical excitation with 1.9-eV pump pulses. Photoelectrons are detected at the in-plane momenta of the K<sub>Mo</sub> and K'<sub>Mo</sub> valleys (0 ps). For better visibility, the Brillouin zone of MoS<sub>2</sub> is overlaid in dark red. Because 1.9-eV pump photons also non-resonantly excite K<sub>W</sub>-K<sub>W</sub> excitons in WSe<sub>2</sub>, the momentum map in Fig. 2C shows photoemission yield at the K<sub>W</sub> and K'<sub>W</sub> valleys of WSe<sub>2</sub> (orange hexagon, 0 ps). Note that the Brillouin zone of WSe<sub>2</sub> is rotated by  $9.8^\circ \pm 0.8^\circ$  with respect to MoS<sub>2</sub>. Moreover, weak photoemission yield from hybrid K<sub>W</sub>- $\Sigma$  excitons is detected at the  $\Sigma$  and  $\Sigma'$  valleys (grey hexagon). At a pump-probe delay of 10 ps (Fig. 2D), the major part of the intralayer excitons has decayed either via the electron- or the hole-transfer process, and spectral yield is dominated by the energetically most stable excitation, i.e., the interlayer K<sub>W</sub>-K<sub>Mo</sub> excitons (fig. S4). For these interlayer excitons, the electron and the hole contributions are now separated between both monolayers of the heterostructure, and the exciton photoemission momentum fingerprint has to be described within the moiré mini-Brillouin zones built up by the  $\kappa$  valleys whose in-plane momentum can be constructed by the reciprocal lattice vectors of WSe<sub>2</sub> and MoS<sub>2</sub> (Fig. 2D, black hexagon) (8, 26).

### Hole- and electron-transfer dynamics

Having identified the exciton fingerprints in the photoemission experiment, we can now proceed with the analysis of the hole-transfer dynamics. For this, fig. S4 provides an overview of the pump-probe delay-dependent evolution of photoemission intensity from intralayer K<sub>Mo</sub>-K<sub>Mo</sub> and K<sub>W</sub>-K<sub>W</sub> excitons, the hybrid K<sub>W</sub>- $\Sigma$  exciton, and the interlayer K<sub>W</sub>-K<sub>Mo</sub> exciton after optical excitation with 1.9 eV (fluence: 140  $\mu\text{J}/\text{cm}^2$ ; optically excited exciton densities of  $7 \times 10^{11}$

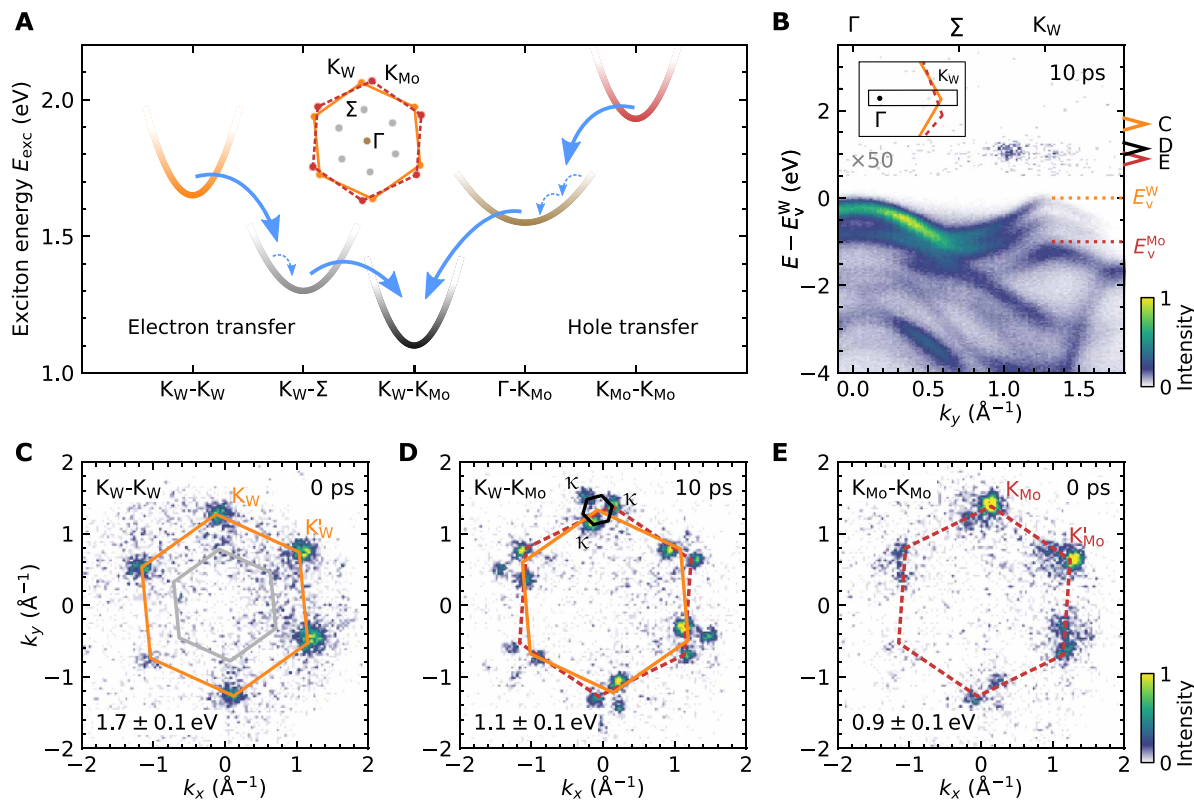


**Fig. 2. Energy landscape and energy-momentum fingerprints of excitons in WSe<sub>2</sub>/MoS<sub>2</sub>.** (A) Calculated low-energy exciton landscape of intralayer, hybrid, and interlayer excitons. The electron- and hole-transfer processes can be initiated via excitation with 1.7- and 1.9-eV light pulses, respectively, and proceed via the  $K_W-K_W \rightarrow K_W-\Sigma \rightarrow K_W-K_{Mo}$  and  $K_{Mo}-K_{Mo} \rightarrow \Gamma-K_{Mo} \rightarrow K_W-K_{Mo}$  cascades. The solid and dashed arrows, respectively, indicate exciton-phonon scattering events leading to inter- and intravalley thermalization of the exciton occupation. The effective mass of the exciton dispersion is extracted from many-body calculations. The inset schematically shows the alignment of the WSe<sub>2</sub> and MoS<sub>2</sub> Brillouin zones and indicates the high-symmetry points in the first Brillouin zone. (B) Energy- and momentum-resolved photoemission spectrum along the  $\Gamma$ - $\Sigma$ - $K_W$  direction (inset) measured on the WSe<sub>2</sub>/MoS<sub>2</sub> heterostructure after photoexcitation with 1.9-eV light pulses at a delay of 10 ps. The WSe<sub>2</sub> and MoS<sub>2</sub> valence band maxima are labeled with  $E_V^W$  and  $E_V^{Mo}$ , respectively. (C to E) Photoemission momentum fingerprints of the (C) intralayer  $K_W-K_W$  exciton (0 ps), the (D) interlayer  $K_W-K_{Mo}$  exciton (10 ps), and the (E) intralayer  $K_{Mo}-K_{Mo}$  exciton (0 ps) after photoexcitation with 1.9-eV light pulses. The photoelectron energies of the momentum maps are given in the figure with respect to the energy of the WSe<sub>2</sub> valence band maximum and are indicated by colored arrowheads in (B). The energetic width of the arrowheads indicates the energy range used for generating the momentum maps (C, D, and E). The Brillouin zones of WSe<sub>2</sub>, MoS<sub>2</sub>, and the moiré superlattice are overlaid on the data by orange, dark red (dashed), and black hexagons, respectively.

and  $3.5 \times 10^{12} \text{ cm}^{-2}$  in WSe<sub>2</sub> and MoS<sub>2</sub> (41), respectively). The formation and thermalization dynamics of all accessible excitons indicate that electron- and hole-transfer processes contribute to the formation of interlayer  $K_W-K_{Mo}$  excitons, which, in consequence, we have to distinguish. To do so, we directly compare the interlayer  $K_W-K_{Mo}$  exciton rise time for 1.7- and 1.9-eV pumping. In Fig. 3A, the black data points show the pump-probe delay-dependent buildup of interlayer  $K_W-K_{Mo}$  exciton photoemission intensity that is formed by electron- and hole-transfer processes (1.9-eV pump photons). For comparison, the green data points show the pump-probe delay-dependent buildup of the interlayer  $K_W-K_{Mo}$  exciton intensity that is formed only via the electron transfer process (1.7-eV pump photons, fluence:  $280 \mu\text{J}/\text{cm}^2$ , exciton density:  $5.4 \times 10^{12} \text{ cm}^{-2}$ ). It is directly obvious that there is a strong hierarchy of timescales for the electron- and hole-transfer processes: When considering the electron-only transfer process (green symbols), the interlayer exciton signal increases rapidly with pump-probe delay and saturates on the sub-200-fs timescale. A quantitative evaluation with rate equation modeling yields a formation time of  $t_{e-\text{transfer}} = 40 \pm 10$  fs (see Supplementary Text). In contrast, the joint buildup of interlayer

$K_W-K_{Mo}$  excitons via electron- and hole-transfer processes after 1.9-eV excitation saturates on the 1-ps timescale (black symbols). For further analyzing this dataset, we assume that the 1.9-eV pump pulses excite A1s excitons in WSe<sub>2</sub> and MoS<sub>2</sub> in a 1:5 ratio, as estimated from the optical absorption coefficient of both monolayers (41), and take the already deduced electron-transfer time  $t_{e-\text{transfer}} = 40 \pm 10$  fs into account. From this fit, we extract  $t_{h-\text{transfer}} = 2.2 \pm 1$  ps, which is more than an order of magnitude larger than the electron-transfer time  $t_{e-\text{transfer}}$  (see rate equation analysis based on fig. S3).

Hence, our experimental data imply that the interlayer hole-transfer mechanism across the WSe<sub>2</sub>/MoS<sub>2</sub> heterointerface is substantially slower compared to the electron-transfer mechanism. To understand our findings on a microscopic footing, we exploit the density matrix formalism to derive excitonic equations of motion within the energy landscape of excitons shown in Fig. 2A and fig. S7 (see details in Supplementary Text) (38, 42). Here, we incorporate exciton-light and exciton-phonon interaction and assume again that the 1.9-eV pump pulses excite A1s excitons in WSe<sub>2</sub> and MoS<sub>2</sub> in a 1:5 ratio (41). We find an excellent qualitative agreement of the microscopic model calculations (Fig. 3B) with the experimentally

quantified rise time (Fig. 3A) of interlayer  $K_W$ - $K_{M_0}$  excitons: The electron-only transfer process saturates for delays  $<200$  fs (green), while the combined electron- and hole-transfer dynamics lead to an increasing interlayer  $K_W$ - $K_{M_0}$  exciton occupation for substantially longer delays (black). Hence, in experiment and theory, we find that the electron-transfer dynamics is roughly one order of magnitude faster than the hole-transfer dynamics.

To understand this drastic difference in the rise time of interlayer  $K_W$ - $K_{M_0}$  exciton formation via the electron- versus the hole-transfer process, we evaluate the calculated exciton dynamics in more detail and make two major observations: First, it is important to realize that the exciton energy difference between the optically excited intralayer exciton and the interlayer exciton is roughly 200 meV larger in the case of 1.9-eV excitation, which initiates the hole-transfer process (see exciton energies in Fig. 2A and fig. S7). The dissipation

of this extra amount of energy via exciton-phonon scattering events with typical phonon frequencies of 0.03 eV (43) leads to overall slower hole-transfer dynamics (arrows in Fig. 2A) (42, 44). In addition, the first step of the exciton cascade leading to the formation of either  $K_W$ - $\Sigma$  or  $\Gamma$ - $K_{M_0}$  excitons in the electron- and hole-transfer process, respectively, is markedly different. In the first Brillouin zone, the  $\Sigma$  and  $\Sigma'$  valleys are each threefold degenerate, while there is only one  $\Gamma$  valley (Fig. 2A, inset). Therefore, the density of final states for the  $K_W$ - $K_W \rightarrow K_W$ - $\Sigma$  versus the  $K_{M_0}$ - $K_{M_0} \rightarrow \Gamma$ - $K_{M_0}$  transition is notably different (42, 43, 45–47). In consequence, hybrid  $K_W$ - $\Sigma$  excitons are more efficiently formed than hybrid  $\Gamma$ - $K_{M_0}$  excitons, favoring faster interlayer exciton formation dynamics for the electron-transfer channel compared to the hole-transfer channel.

Last, we want to point out two important deviations in the exciton dynamics between experiment and theory. First, on the few picosecond timescale, we find that the calculated occupation of interlayer  $K_W$ - $K_{M_0}$  excitons increases up to  $\approx 4$  ps and is composed of a 1:5 ratio of interlayer excitons that are formed from A1s excitons initially excited in the  $WSe_2$  and  $MoS_2$  layers (fig. S8). In contrast, in the experiment, the respective photoemission intensity saturates at roughly 1 ps and the 1:5 ratio cannot be identified (1.9-eV excitation; Fig. 3). This deviation between experiment and theory can be understood by the fact that radiative and defect-assisted decay processes of intralayer, hybrid, and interlayer excitons with lifetimes ranging from 1 ps to tenths of picoseconds (8, 27, 34, 35) are not included in the model calculations. Hence, the model calculations overestimate the exciton occupation at large pump-probe delays.

Second, we find that the experimental data for 1.7- and 1.9-eV excitation rises faster than estimated from the model calculations (sub-200-fs timescale in Fig. 3). This deviation could be related to the fact that the model calculations do not consider exciton-exciton scattering events, which might already contribute to the dynamics in the experiment (25, 48, 49). Although an in-depth pump fluence-dependent analysis of these dynamics appears to be highly interesting, it is beyond the scope of this manuscript, and, in the following, we focus on the identification of a spectroscopic fingerprint of the hole-transfer process.

### The spectroscopic signature of a correlated hole-transfer process

On the basis of this hierarchy of timescales between the electron- and the hole-transfer process, it is possible to separate the interlayer exciton formation dynamics: For delays  $>200$  fs, the change in the exciton photoemission yield from the interlayer  $K_W$ - $K_{M_0}$  exciton is mainly caused by hole-transfer processes. Hence, the final ambition of our work is the unambiguous discrimination of the photoemission spectral signature of intralayer  $K_{M_0}$ - $K_{M_0}$  and interlayer  $K_W$ - $K_{M_0}$  excitons, where, in both cases, the electron contribution to the exciton is situated in the conduction band minimum of the  $MoS_2$  layer (compare Fig. 1C).

In the most naive picture of photoemission, it might be expected that trARPES only yields information on the exciton's electron. Hence, the experiment would not distinguish between photoelectrons being emitted from the conduction band minimum of  $MoS_2$ , irrespective of whether they result from the breakup of intralayer  $K_{M_0}$ - $K_{M_0}$  or interlayer  $K_W$ - $K_{M_0}$  excitons (Fig. 1C). However, it is known that the spectral function in photoemission contains information about many-body interactions (50), and this is also the case for the correlated electron-hole pair. This leads to a very nonintuitive and

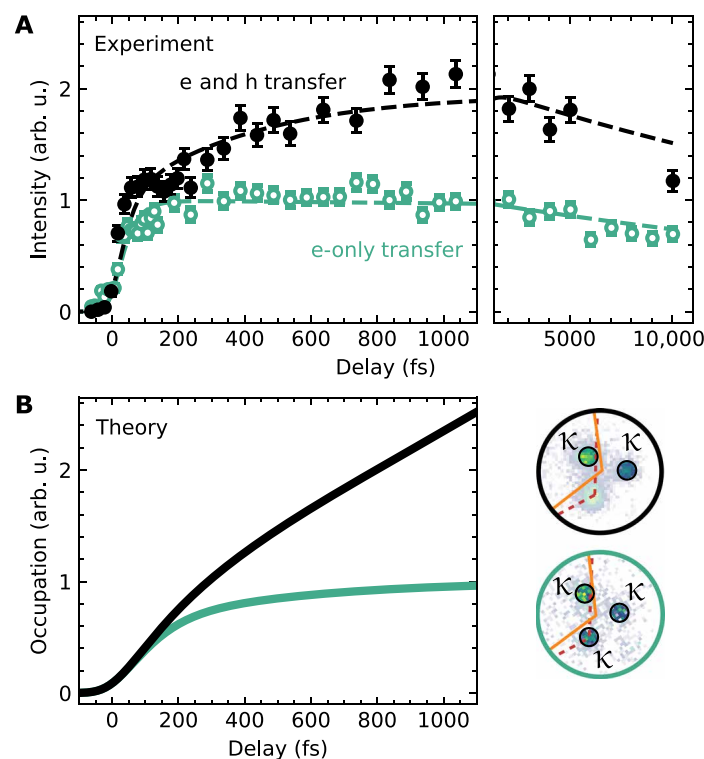


**Fig. 3. Femtosecond-to-picosecond evolution of the hole- and electron-transfer dynamics.** (A) Direct comparison of the interlayer  $K_W$ - $K_{M_0}$  exciton formation dynamics if the heterostructure is excited resonantly to the intralayer  $K_W$ - $K_W$  exciton energy of  $WSe_2$  (1.7 eV, green circles) or the intralayer  $K_{M_0}$ - $K_{M_0}$  exciton of  $MoS_2$  (1.9 eV, black circles). While the electron-only transfer process (1.7 eV) leads to a saturation of photoemission yield from interlayer  $K_W$ - $K_{M_0}$  excitons on the  $<200$ -fs timescale, the combined electron- and hole-transfer dynamics (1.9 eV) leads to an increasing photoemission yield up to 1 ps. The momentum-filtered regions of interest (black circles) used in the 1.7-eV (green contour) and 1.9-eV (black contour) measurements are shown in the bottom panel. The  $\kappa$  valley that overlaps with the original  $K_{M_0}$  valley is excluded in the analysis of the 1.9-eV measurement. (B) Microscopic model calculations of the interlayer  $K_W$ - $K_{M_0}$  exciton formation dynamics. The green curve describes the temporal evolution of the occupation of interlayer  $K_W$ - $K_{M_0}$  excitons after photoexcitation of intralayer  $K_W$ - $K_W$  excitons. For the black curve, the interlayer  $K_W$ - $K_{M_0}$  exciton formation dynamics is induced by the initial excitation of intralayer  $K_W$ - $K_W$  and  $K_{M_0}$ - $K_{M_0}$  excitons. Note that the model calculations do not include additional decay processes.

intriguing experimental observation. Figure 4A shows the pump-probe delay evolution of energy distribution curves (EDCs) filtered for photoelectron yield at the  $\kappa$  valley, whose momentum coincides with the  $K_{Mo}$  valley, i.e., the momentum region where photoelectron yield from intralayer  $K_{Mo}$ - $K_{Mo}$  and interlayer  $K_W$ - $K_{Mo}$  excitons is expected (Fig. 4A, inset). Astonishingly, we find that the energy of the photoelectrons shifts up as a function of pump-probe delay from  $E - E_V^W = 0.93 \pm 0.03$  eV at 15 fs to  $E - E_V^W = 1.10 \pm 0.03$  eV at 1 ps, i.e., a shift of  $\Delta E_{PES}^{h-transfer} = 0.17 \pm 0.04$  eV (Fig. 4B). At first glance, this is an unexpected observation: In temporal overlap of the pump and the probe laser pulses, the optical excitation deposits energy into the system, and the system subsequently relaxes from its excited state to energetically more favorable states via scattering processes. In consequence, energy-resolved pump-probe photoemission spectroscopies of single-particle charge carriers typically show that the mean kinetic energy of the photoelectrons decreases with pump-probe delay (51). An increasing mean kinetic energy might indicate higher-order scattering processes such as Auger recombination (49, 52). For Auger recombination, however, we would expect to observe a decreasing mean kinetic energy on the few-picosecond timescale as the overall exciton density and thus the efficiency for Auger recombination decreases. However, the long-time evaluation of the mean photoelectron energy clearly excludes this scenario (Fig. 4A). In addition, by evaluating the pump-probe delay evolution of the energy position of the  $MoS_2$  valence band maxima, we can exclude a photo-induced renormalization of the band energies (53, 54) (fig. S5). We thus search for the origin of the apparent increase of the mean kinetic energy beyond the single-particle picture, i.e., in the photoemission from excitons whose occupation is dynamically transferring from intralayer  $K_{Mo}$ - $K_{Mo}$  to interlayer  $K_W$ - $K_{Mo}$  excitons.

So far, we have referenced the energies of all emitted single-particle photoelectrons to the valence band maximum of  $WSe_2$  (left energy axis in Fig. 4B). However, especially for the intralayer  $K_{Mo}$ - $K_{Mo}$  exciton that fully resides in the  $MoS_2$  layer, this is clearly not the intrinsically relevant energy axis. We overcome this shortcoming by using an energy scale that is more direct to photoemission from excitons by relating the total energy before ( $E = E_0 + E_{exc} + \hbar\omega$ ) and after ( $E = E_0 - E_{hole} + E_{elec}$ ) the breakup of the correlated electron-hole pair (55). Here,  $E_{exc}$  is the energy necessary to resonantly excite an exciton with a two-particle binding energy  $E_{bin}$  (compare exciton energy landscape in Fig. 2A);  $E_{hole}$  and  $E_{elec}$  denote the energy of the single-particle hole and electron state after the breakup of the exciton, respectively;  $E_0$  is the ground state energy and  $\hbar\omega$  is the photon energy. As energy needs to be conserved when the exciton is broken, the energy of the detected single-particle electron can be expressed as

$$E_{elec} = E_{hole} + E_{exc} + \hbar\omega \quad (1)$$

Therefore, Eq. 1 fixes the energy of the single-particle hole  $E_{hole}$  remaining in the sample as the natural reference point of the photoelectron energy axis for each probed exciton (at a given probe photon energy  $\hbar\omega$ ). For the intralayer  $K_{Mo}$ - $K_{Mo}$  excitons and the interlayer  $K_W$ - $K_{Mo}$  excitons, respectively, the valence band maxima of  $MoS_2$  ( $E_V^{Mo}$ ) and  $WSe_2$  ( $E_V^W$ ) set the energy scale [see Fig. 1 (B and C) and band energies labeled in Fig. 2B)]. Following Eq. 1, we can directly quantify the exciton energies of intralayer  $K_{Mo}$ - $K_{Mo}$  and interlayer  $K_W$ - $K_{Mo}$  excitons from the photoemission data to  $E_{exc}^{MoMo} = 1.93 \pm 0.08$  eV and  $E_{exc}^{WMo} = 1.10 \pm 0.03$  eV, respectively, which are in excellent agreement with earlier results obtained with photoluminescence spectroscopy [ $E_{exc,PL}^{MoMo} = 1.9$  eV and  $E_{exc,PL}^{WMo} = 1.1$  eV; horizontal lines in Fig. 4B)]

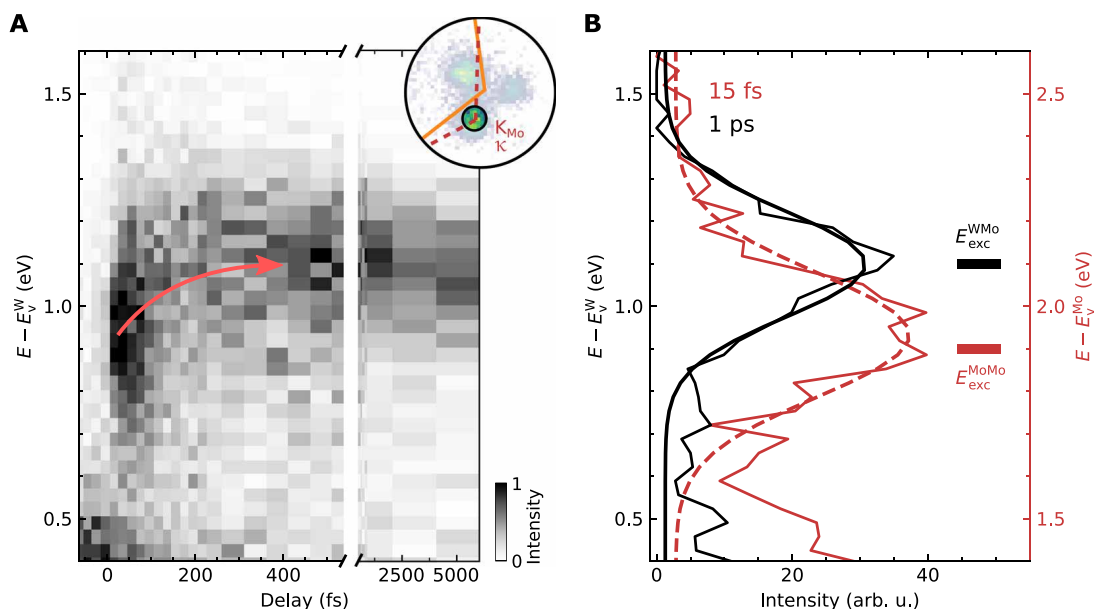


**Fig. 4. Coulomb correlation-induced excitonic energy fingerprints.** (A) Pump-probe delay evolution of the energy distribution curves (EDCs) filtered at the momentum region of the  $K_{Mo}$  valley of  $MoS_2$  (region of interest indicated in the inset, 1.9-eV excitation). At this high-symmetry point, photoemission yield from intralayer  $K_{Mo}$ - $K_{Mo}$  and interlayer  $K_W$ - $K_{Mo}$  excitons is expected (see Fig. 1C). As intralayer  $K_{Mo}$ - $K_{Mo}$  excitons decay and form interlayer  $K_W$ - $K_{Mo}$  excitons, the peak maxima of the photoelectron energy shows an upshift by  $\Delta E_{PES}^{h-transfer} = 0.17 \pm 0.04$  eV (curved arrow). (B) Selected EDCs for pump-probe delays of 15 fs (dark red) and 1 ps (black) illustrating an energetic upshift of the exciton photoemission signal. The horizontal bars indicate expected photoelectron energies for the intralayer  $K_{Mo}$ - $K_{Mo}$  (dark red) and interlayer  $K_W$ - $K_{Mo}$  (black) excitons calculated with Eq. 1 and data from photoluminescence measurements (56, 57). The left and right energy axes in black and dark red show the corresponding energy scales with respect to the valence band maximum of  $WSe_2$  and  $MoS_2$ .

(56, 57). In consequence, we can explain the experimentally observed upshift of the photoelectron energy by  $\Delta E_{\text{PES}}^{\text{h-transfer}} = 0.17 \pm 0.04$  eV with the energy difference between the single-particle electron final states  $E_{\text{elec}}$  of the interlayer  $\text{K}_W\text{-K}_{\text{Mo}}$  and the intralayer  $\text{K}_{\text{Mo}}\text{-K}_{\text{Mo}}$  excitons, i.e., with  $(E_{\text{v}}^{\text{W}} + E_{\text{exc}}^{\text{W}_{\text{Mo}}} + \hbar\omega) - (E_{\text{v}}^{\text{Mo}} + E_{\text{exc}}^{\text{Mo}_{\text{Mo}}} + \hbar\omega) \approx 0.17$  eV (with  $E_{\text{v}}^{\text{W}} - E_{\text{v}}^{\text{Mo}} = 1.00 \pm 0.07$  eV, see Fig. 2B). Hence, the energetic upshift is a direct consequence of the breakup of the correlated electron-hole pair during the photoemission process.

Although the photoelectron energy increases during the hole-transfer process, we strongly emphasize that the overall energy of the system relaxes by  $\Delta E_{\text{exc}}^{\text{h-transfer}} = E_{\text{exc}}^{\text{W}_{\text{Mo}}} - E_{\text{exc}}^{\text{Mo}_{\text{Mo}}} = -0.83 \pm 0.09$  eV (see Fig. 2A). Consistently, if the same analysis is performed for the electron-only transfer process after photoexcitation with 1.7 eV pump pulses, then we find a reduction of the overall exciton energy by  $\Delta E_{\text{exc}}^{\text{e-transfer}} = E_{\text{exc}}^{\text{W}_{\text{Mo}}} - E_{\text{exc}}^{\text{W}_{\text{W}}} = -0.46 \pm 0.07$  eV (fig. S6). In this case, where the exciton's hole remains in the  $\text{WSe}_2$  VBM (Fig. 1B), the reduction of the exciton energy directly translates to a reduction of the single-particle photoelectron energy ( $\Delta E_{\text{PES}}^{\text{e-transfer}} = -0.46 \pm 0.07$  eV). Therefore, as expected, interlayer charge transfer always leads to a reduction of the exciton energy  $E_{\text{exc}}$ , which might, however, result in an up- or a downshift of the photoelectron energy in the photoemission spectrum.

## DISCUSSION

We have shown that femtosecond momentum microscopy is a powerful tool to study the correlated interaction between the exciton's electron and hole in twisted semiconductor heterostructures. Exemplarily, we show that the photoelectron of the correlated two-particle exciton contains direct information about the hole state. We use this correlation in combination with microscopic and material-specific theory to directly follow an ultrafast interlayer hole-transfer process that would otherwise be elusive. Our work opens up means for the future study of correlated states of matter in two-dimensional quantum materials.

## MATERIALS AND METHODS

The time- and angle-resolved photoemission data are measured with a time-of-flight momentum microscope (Surface Concept) (58, 59) that is connected to a table-top high harmonic generation beamline driven by a 300-W fiber laser system (AFS Jena) (40, 60). The overall experimental setup and its application to exfoliated two-dimensional materials are described in (39) and (8), respectively.

In all experiments, the exciton dynamics are induced by resonant optical excitation of the A1s-excitons of  $\text{WSe}_2$  or  $\text{MoS}_2$ . Therefore, 1.7- and 1.9-eV pump pulses with a duration of 50 fs are used (*s*-polarized), respectively. After a variable pump-probe delay, photoemission is induced by 26.5-eV light pulses (20 fs, *p*-polarized).

For the characterization of the temporal resolution and the determination of absolute time zero of the experiment, we have measured the pump-probe delay-dependent photoemission yield of sidebands of the valence bands formed due to the laser-assisted photoelectric effect (40, 61). In fig. S1, a cross-correlation of the pump and probe laser pulse is shown, where both laser pulses are *p*-polarized (1.9-eV pump pulses). The gray line is a Gaussian fit to the data yielding a full width at half maximum of  $60 \pm 5$  fs.

The  $9.8^\circ \pm 0.8^\circ$  twisted  $\text{WSe}_2/\text{MoS}_2$  heterostructure is stamped onto a 20- to 30-nm-thick hBN (62) spacer layer and a  $p^+$ -doped

native oxide silicon wafer. Before the momentum microscopy experiments, the sample is annealed for 1 hour to 670 K. Details on the sample fabrication and characterization (e.g., twist angle) are described in (8).

## Supplementary Materials

This PDF file includes:

Supplementary Text

Figs. S1 to S8

Table S1

References

## REFERENCES AND NOTES

1. G. Wang, A. Chernikov, M. M. Glazov, T. F. Heinz, X. Marie, T. Amand, B. Urbaszek, Colloquium: Excitons in atomically thin transition metal dichalcogenides. *Rev. Mod. Phys.* **90**, 021001 (2018).
2. A. Chernikov, T. C. Berkelbach, H. M. Hill, A. Rigosi, Y. Li, O. B. Aslan, D. R. Reichman, M. S. Hybertsen, T. F. Heinz, Exciton binding energy and nonhydrogenic rydberg series in monolayer  $\text{WS}_2$ . *Phys. Rev. Lett.* **113**, 076802 (2014).
3. K. He, N. Kumar, L. Zhao, Z. Wang, K. F. Mak, H. Zhao, J. Shan, Tightly bound excitons in monolayer  $\text{WSe}_2$ . *Phys. Rev. Lett.* **113**, 026803 (2014).
4. C.-H. Lee, G.-H. Lee, A. M. van der Zande, W. Chen, Y. Li, M. Han, X. Cui, G. Arefe, C. Nuckolls, T. F. Heinz, J. Guo, J. Hone, P. Kim, Atomically thin p-n junctions with van der Waals heterointerfaces. *Nat. Nanotechnol.* **9**, 676–681 (2014).
5. X. Hong, J. Kim, S.-F. Shi, Y. Zhang, C. Jin, Y. Sun, S. Tongay, J. Wu, Y. Zhang, F. Wang, Ultrafast charge transfer in atomically thin  $\text{MoS}_2/\text{WS}_2$  heterostructures. *Nat. Nanotechnol.* **9**, 682–686 (2014).
6. F. Ceballos, M. Z. Bellus, H.-Y. Chiu, H. Zhao, Ultrafast charge separation and indirect exciton formation in a  $\text{MoS}_2\text{-MoSe}_2$  van der waals heterostructure. *ACS Nano* **8**, 12717–12724 (2014).
7. P. Merkli, F. Mooshammer, P. Steinleitner, A. Girnguber, K. Q. Lin, P. Nagler, J. Holler, C. Schüller, J. M. Lupton, T. Korn, S. Ovesen, S. Brem, E. Malic, R. Huber, Ultrafast transition between exciton phases in van der Waals heterostructures. *Nat. Mater.* **18**, 691–696 (2019).
8. D. Schmitt, J. P. Bange, W. Bennecke, A. AlMutairi, G. Meneghini, K. Watanabe, T. Taniguchi, D. Steil, D. R. Luke, R. T. Weitz, S. Steil, G. S. M. Jansen, S. Brem, E. Malic, S. Hofmann, M. Reutzel, S. Mathias, Formation of moiré interlayer excitons in space and time. *Nature* **608**, 499–503 (2022).
9. K. L. Seyler, P. Rivera, H. Yu, N. P. Wilson, E. L. Ray, D. G. Mandrus, J. Yan, W. Yao, X. Xu, Signatures of moiré-trapped valley excitons in  $\text{MoSe}_2/\text{WSe}_2$  heterobilayers. *Nature* **567**, 66–70 (2019).
10. E. M. Alexeev, D. A. Ruiz-Tijerina, M. Danovich, M. J. Hamer, D. J. Terry, P. K. Nayak, S. Ahn, S. Pak, J. Lee, J. I. Sohn, M. R. Molas, M. Koperski, K. Watanabe, T. Taniguchi, K. S. Novoselov, R. V. Gorbachev, H. S. Shin, V. I. Fal'ko, A. I. Tartakovskii, Resonantly hybridized excitons in moiré superlattices in van der Waals heterostructures. *Nature* **567**, 81–86 (2019).
11. K. Tran, G. Moody, F. Wu, X. Lu, J. Choi, K. Kim, A. Rai, D. A. Sanchez, J. Quan, A. Singh, J. Embley, A. Zepeda, M. Campbell, T. Autry, T. Taniguchi, K. Watanabe, N. Lu, S. K. Banerjee, K. L. Silverman, S. Kim, E. Tutuc, L. Yang, A. H. MacDonald, X. Li, Evidence for moiré excitons in van der Waals heterostructures. *Nature* **567**, 71–75 (2019).
12. O. Karni, E. Barré, V. Pareek, J. D. Georganas, M. K. L. Man, C. Sahoo, D. R. Bacon, X. Zhu, H. B. Ribeiro, A. L. O'Beirne, J. Hu, A. Al-Mahboob, M. M. M. Abdelrasoul, N. S. Chan, A. Karmakar, A. J. Winchester, B. Kim, K. Watanabe, T. Taniguchi, K. Barmak, J. Madéo, F. H. da Jornada, T. F. Heinz, K. M. Dani, Structure of the moiré exciton captured by imaging its electron and hole. *Nature* **603**, 247–252 (2022).
13. L. Ma, P. X. Nguyen, Z. Wang, Y. Zeng, K. Watanabe, T. Taniguchi, A. H. MacDonald, K. F. Mak, J. Shan, Strongly correlated excitonic insulator in atomic double layers. *Nature* **598**, 585–589 (2021).
14. Z. Zhang, E. C. Regan, D. Wang, W. Zhao, S. Wang, M. Sayyad, K. Yumigeta, K. Watanabe, T. Taniguchi, S. Tongay, M. Crommie, A. Zettl, M. P. Zaletel, F. Wang, Correlated interlayer exciton insulator in heterostructures of monolayer  $\text{WSe}_2$  and moiré  $\text{WS}_2/\text{WSe}_2$ . *Nat. Phys.* **18**, 1214–1220 (2022).
15. Y. Slobodkin, Y. Mazur-Harpaz, S. Refaely-Abramson, S. Gazit, H. Steinberg, R. Rapoport, Quantum phase transitions of trilayer excitons in atomically thin heterostructures. *Phys. Rev. Lett.* **125**, 255301 (2020).
16. L. Sigl, F. Sigger, F. Kronowetter, J. Kiemle, J. Klein, K. Watanabe, T. Taniguchi, J. J. Finley, U. Wurstbauer, A. W. Holleitner, Signatures of a degenerate many-body state of interlayer excitons in a van der waals heterostack. *Phys. Rev. Res.* **2**, 042044 (2020).

17. Z. Wang, D. A. Rhodes, K. Watanabe, T. Taniguchi, J. C. Hone, J. Shan, K. F. Mak, Evidence of high-temperature exciton condensation in two-dimensional atomic double layers. *Nature* **574**, 76–80 (2019).
18. C. Jin, E. Y. Ma, O. Karni, E. C. Regan, F. Wang, T. F. Heinz, Ultrafast dynamics in van der Waals heterostructures. *Nat. Nanotechnol.* **13**, 994–1003 (2018).
19. R. Perea-Causin, D. Erckensten, J. M. Fitzgerald, J. J. P. Thompson, R. Rosati, S. Brem, E. Malic, Exciton optics, dynamics, and transport in atomically thin semiconductors. *APL Mater.* **10**, 100701 (2022).
20. C. Poellmann, P. Steinleitner, U. Leierseder, P. Nagler, G. Plechinger, M. Porer, R. Bratschitsch, C. Schüller, T. Korn, R. Huber, Resonant internal quantum transitions and femtosecond radiative decay of excitons in monolayer WSe<sub>2</sub>. *Nat. Mater.* **14**, 889–893 (2015).
21. E. Malic, M. Selig, M. Feierabend, S. Brem, D. Christiansen, F. Wendler, A. Knorr, G. Berghäuser, Dark excitons in transition metal dichalcogenides. *Phys. Rev. Mater.* **2**, 014002 (2018).
22. T. Mueller, E. Malic, Exciton physics and device application of two-dimensional transition metal dichalcogenide semiconductors. *NPJ 2D Mater. Appl.* **2**, 29 (2018).
23. J. Madéo, M. K. L. Man, C. Sahoo, M. Campbell, V. Pareek, E. L. Wong, A. Al-Mahboob, N. S. Chan, A. Karmakar, B. M. K. Mariserla, X. Li, T. F. Heinz, T. Cao, K. M. Dani, Directly visualizing the momentum-forbidden dark excitons and their dynamics in atomically thin semiconductors. *Science* **370**, 1199–1204 (2020).
24. R. Wallauer, R. Perea-Causin, L. Münster, S. Zajusch, S. Brem, J. Güdde, K. Tanimura, K.-Q. Lin, R. Huber, E. Malic, U. Höfer, Momentum-resolved observation of exciton formation dynamics in monolayer WS<sub>2</sub>. *Nano Lett.* **21**, 5867–5873 (2021).
25. A. Kunin, S. Chernov, J. Bakalis, Z. Li, S. Cheng, Z. H. Withers, M. G. White, G. Schönhense, X. Du, R. K. Kawakami, T. K. Allison, Momentum-resolved exciton coupling and valley polarization dynamics in monolayer WS<sub>2</sub>. *Phys. Rev. Lett.* **130**, 046202 (2023).
26. D. Schmitt, J. P. Bange, W. Bennecke, G. Meneghini, A. AlMutairi, M. Merboldt, J. Pöhls, K. Watanabe, T. Taniguchi, S. Steil, D. Steil, R. T. Weitz, S. Hofmann, S. Brem, G. S. Matthijs Jansen, E. Malic, S. Mathias, M. Reutzel, Ultrafast nano-imaging of dark excitons. arXiv:2305.18908 (2023).
27. J. P. Bange, P. Werner, D. Schmitt, W. Bennecke, G. Meneghini, A. AlMutairi, M. Merboldt, K. Watanabe, T. Taniguchi, S. Steil, D. Steil, R. T. Weitz, S. Hofmann, G. S. M. Jansen, S. Brem, E. Malic, M. Reutzel, S. Mathias, Ultrafast dynamics of bright and dark excitons in monolayer WSe<sub>2</sub> and heterobilayer WSe<sub>2</sub>/MoS<sub>2</sub>. *2D Mater.* **10**, 035039 (2023).
28. E. Peretto, D. Sangalli, A. Marini, G. Stefanucci, First-principles approach to excitons in time-resolved and angle-resolved photoemission spectra. *Phys. Rev. B* **94**, 245303 (2016).
29. A. Rustagi, A. F. Kemper, Photoemission signature of excitons. *Phys. Rev. B* **97**, 235310 (2018).
30. A. Steinhoff, M. Florian, M. Rösner, G. Schönhoff, T. O. Wehling, F. Jahnke, Exciton fission in monolayer transition metal dichalcogenide semiconductors. *Nat. Commun.* **8**, 1166 (2017).
31. D. Christiansen, M. Selig, E. Malic, R. Ernstorfer, A. Knorr, Theory of exciton dynamics in time-resolved ARPES: Intra- and intervalley scattering in two-dimensional semiconductors. *Phys. Rev. B* **100**, 205401 (2019).
32. S. Dong, M. Puppini, T. Pincelli, S. Beaulieu, D. Christiansen, H. Hübener, C. W. Nicholson, R. P. Xian, M. Dendzik, Y. Deng, Y. W. Windsor, M. Selig, E. Malic, A. Rubio, A. Knorr, M. Wolf, L. Rettig, R. Ernstorfer, Direct measurement of key exciton properties: Energy, dynamics, and spatial distribution of the wave function. *Nat. Sci.* **1**, e10010 (2021).
33. M. K. L. Man, J. Madéo, C. Sahoo, K. Xie, M. Campbell, V. Pareek, A. Karmakar, E. L. Wong, A. Al-Mahboob, N. S. Chan, D. R. Bacon, X. Zhu, M. M. M. Abdelrasoul, X. Li, T. F. Heinz, F. H. da Jornada, T. Cao, K. M. Dani, Experimental measurement of the intrinsic excitonic wave function. *Sci. Adv.* **7**, eabg0192 (2021).
34. H. Zhu, J. Wang, Z. Gong, Y. D. Kim, J. Hone, X. Y. Zhu, Interfacial charge transfer circumventing momentum mismatch at two-dimensional van der Waals heterojunctions. *Nano Lett.* **17**, 3591–3598 (2017).
35. J. E. Zimmermann, M. Axt, F. Mooshammer, P. Nagler, C. Schüller, T. Korn, U. Höfer, G. Mette, Ultrafast charge-transfer dynamics in twisted MoS<sub>2</sub>/WSe<sub>2</sub> heterostructures. *ACS Nano* **15**, 14725–14731 (2021).
36. V. R. Policht, M. Russo, F. Liu, C. Trovatiello, M. Maiuri, Y. Bai, X. Zhu, S. Dal Conte, G. Cerullo, Dissecting interlayer hole and electron transfer in transition metal dichalcogenide heterostructures via two-dimensional electronic spectroscopy. *Nano Lett.* **21**, 4738–4743 (2021).
37. Z. Wang, P. Altmann, C. Gadermaier, Y. Yang, W. Li, L. Ghirardini, C. Trovatiello, M. Finazzi, L. Duò, M. Celebrano, R. Long, D. Akinwande, O. V. Prezhdo, G. Cerullo, S. D. Conte, Phonon-mediated interlayer charge separation and recombination in a MoSe<sub>2</sub>/WSe<sub>2</sub> heterostructure. *Nano Lett.* **21**, 2165–2173 (2021).
38. G. Meneghini, M. Reutzel, S. Mathias, S. Brem, E. Malic, Hybrid exciton signatures in ARPES spectra of van der Waals materials. *ACS Photonics* **10**, 3570–3575 (2023).
39. M. Keunecke, C. Möller, D. Schmitt, H. Nolte, G. S. M. Jansen, M. Reutzel, M. Gutberlet, G. Halasi, D. Steil, S. Steil, S. Mathias, Time-resolved momentum microscopy with a 1 MHz high-harmonic extreme ultraviolet beamline. *Rev. Sci. Instrum.* **91**, 063905 (2020).
40. M. Keunecke, M. Reutzel, D. Schmitt, A. Osterkorn, T. A. Mishra, C. Möller, W. Bennecke, G. S. M. Jansen, D. Steil, S. R. Manmana, S. Steil, S. Kehrein, S. Mathias, Electromagnetic dressing of the electron energy spectrum of Au(111) at high momenta. *Phys. Rev. B* **102**, 161403 (2020).
41. Y. Li, A. Chernikov, X. Zhang, A. Rigosi, H. M. Hill, A. M. van der Zande, D. A. Chenet, E.-M. Shih, J. Hone, T. F. Heinz, Measurement of the optical dielectric function of monolayer transition-metal dichalcogenides: MoS<sub>2</sub>, MoSe<sub>2</sub>, WS<sub>2</sub>, and WSe<sub>2</sub>. *Phys. Rev. B* **90**, 205422 (2014).
42. G. Meneghini, S. Brem, E. Malic, Ultrafast phonon-driven charge transfer in van der Waals heterostructures. *Nat. Sci.* **2**, e20220014 (2022).
43. Z. Jin, X. Li, J. T. Mullen, K. W. Kim, Intrinsic transport properties of electrons and holes in monolayer transition-metal dichalcogenides. *Phys. Rev. B* **90**, 045422 (2014).
44. S. Ovesen, S. Brem, C. Linderälv, M. Kuisma, T. Korn, P. Erhart, M. Selig, E. Malic, Interlayer exciton dynamics in van der Waals heterostructures. *Commun. Phys.* **2**, 23 (2019).
45. M. Selig, G. Berghäuser, M. Richter, R. Bratschitsch, A. Knorr, E. Malic, Dark and bright exciton formation, thermalization, and photoluminescence in monolayer transition metal dichalcogenides. *2D Mater.* **5**, 035017 (2018).
46. A. Raja, M. Selig, G. Berghäuser, J. Yu, H. M. Hill, A. F. Rigosi, L. E. Brus, A. Knorr, T. F. Heinz, E. Malic, A. Chernikov, Enhancement of exciton-phonon scattering from monolayer to bilayer WS<sub>2</sub>. *Nano Lett.* **18**, 6135–6143 (2018).
47. J. Lindlau, M. Selig, A. Neumann, L. Colombier, J. Förste, V. Funk, M. Förg, J. Kim, G. Berghäuser, T. Taniguchi, K. Watanabe, F. Wang, E. Malic, A. Högele, The role of momentum-dark excitons in the elementary optical response of bilayer WSe<sub>2</sub>. *Nat. Commun.* **9**, 2586 (2018).
48. D. Sun, Y. Rao, G. A. Reider, G. Chen, Y. You, L. Brézin, A. R. Harutyunyan, T. F. Heinz, Observation of rapid exciton-exciton annihilation in monolayer molybdenum disulfide. *Nano Lett.* **14**, 5625–5629 (2014).
49. D. Erckensten, S. Brem, K. Wagner, R. Gillen, R. Perea-Causin, J. D. Ziegler, T. Taniguchi, K. Watanabe, J. Maultzsch, A. Chernikov, E. Malic, Dark exciton-exciton annihilation in monolayer WSe<sub>2</sub>. *Phys. Rev. B* **104**, L241406 (2021).
50. A. Damaselli, Z. Hussain, Z.-X. Shen, Angle-resolved photoemission studies of the cuprate superconductors. *Rev. Mod. Phys.* **75**, 473–541 (2003).
51. M. Bauer, A. Marienfeld, M. Aeschlimann, Hot electron lifetimes in metals probed by time-resolved two-photon photoemission. *Prog. Surf. Sci.* **90**, 319–376 (2015).
52. S. Mathias, S. Eich, J. Urbancic, S. Michael, A. V. Carr, S. Emmerich, A. Stange, T. Popmintchev, T. Rohwer, M. Wiesenmayer, A. Ruffing, S. Jakobs, S. Hellmann, P. Matyba, C. Chen, L. Kipp, M. Bauer, H. C. Kapteyn, H. C. Schneider, K. Rossnagel, M. M. Murnane, M. Aeschlimann, Self-amplified photo-induced gap quenching in a correlated electron material. *Nat. Commun.* **7**, 12902 (2016).
53. A. Chernikov, C. Ruppert, H. M. Hill, A. F. Rigosi, T. F. Heinz, Population inversion and giant bandgap renormalization in atomically thin WS<sub>2</sub> layers. *Nat. Photonics* **9**, 466–470 (2015).
54. F. Liu, M. E. Ziffer, K. R. Hansen, J. Wang, X. Zhu, Direct determination of band-gap renormalization in the photoexcited monolayer MoS<sub>2</sub>. *Phys. Rev. Lett.* **122**, 246803 (2019).
55. M. Weinelt, M. Kutschera, T. Fauster, M. Rohlffing, Dynamics of excitation at the Si(100) c(4 × 2) surface. *Phys. Rev. Lett.* **92**, 126801 (2004).
56. O. Karni, E. Barré, S. C. Lau, R. Gillen, E. Y. Ma, B. Kim, K. Watanabe, T. Taniguchi, J. Maultzsch, K. Barmak, R. H. Page, T. F. Heinz, Infrared interlayer exciton emission in MoS<sub>2</sub>-WSe<sub>2</sub> heterostructures. *Phys. Rev. Lett.* **123**, 247402 (2019).
57. J. Kunstmann, C. Mooshammer, P. Nagler, A. Chaves, F. Stein, N. Paradiso, G. Plechinger, C. Strunk, C. Schüller, G. Seifert, D. R. Reichman, T. Korn, Momentum-space indirect interlayer excitons in transition-metal dichalcogenide van der Waals heterostructures. *Nat. Phys.* **14**, 801–805 (2018).
58. K. Medjanik, O. Fedchenko, S. Chernov, D. Kutnyakhov, M. Ellguth, A. Oelsner, B. Schönhense, T. R. F. Peixoto, P. Lutz, C.-H. Min, F. Reinert, S. Däster, Y. Acremann, J. Viehhaus, W. Wurth, H. J. Elmers, G. Schönhense, Direct 3D mapping of the Fermi surface and Fermi velocity. *Nat. Mater.* **16**, 615–621 (2017).
59. B. Krömker, M. Escher, D. Funnemann, D. Hartung, H. Engelhard, J. Kirschner, Development of a momentum microscope for time resolved band structure imaging. *Rev. Sci. Instrum.* **79**, 053702–053707 (2008).
60. M. Düvel, M. Merboldt, J. P. Bange, H. Strauch, M. Stellbrink, K. Pierz, H. W. Schumacher, D. Momeni, D. Steil, G. S. M. Jansen, S. Steil, D. Novko, S. Mathias, M. Reutzel, Far-from-equilibrium electron-phonon interactions in optically excited graphene. *Nano Lett.* **22**, 4897–4904 (2022).
61. G. Saathoff, L. Miaja-Avila, M. Aeschlimann, M. M. Murnane, H. C. Kapteyn, Laser-assisted photoemission from surfaces. *Phys. Rev. A* **77**, 022903 (2008).
62. T. Taniguchi, K. Watanabe, Synthesis of high-purity boron nitride single crystals under high pressure by using Ba-BN solvent. *J. Cryst. Growth* **303**, 525–529 (2007).

63. G. Schönhense, D. Kutnyakhov, F. Pressacco, M. Heber, N. Wind, S. Y. Agustsson, S. Babenkov, D. Vasilyev, O. Fedchenko, S. Chernov, L. Rettig, B. Schönhense, L. Wenthaus, G. Brenner, S. Dziarzhyski, S. Palutke, S. K. Mahatha, N. Schirmel, H. Redlin, B. Manschwetus, I. Hartl, Y. Matveyev, A. Gloskovskii, C. Schlueter, V. Shokeen, H. Duerr, T. K. Allison, M. Beye, K. Rossnagel, H. J. Elmers, K. Medjanik, Suppression of the vacuum space-charge effect in fs-photoemission by a retarding electrostatic front lens. *Rev. Sci. Instrum.* **92**, 053703 (2021).
64. S. Brem, K.-Q. Lin, R. Gillen, J. M. Bauer, J. Maultzsch, J. M. Lupton, E. Malic, Hybridized intervalley moiré excitons and flat bands in twisted WSe<sub>2</sub> bilayers. *Nanoscale* **12**, 11088–11094 (2020).
65. J. Hagel, S. Brem, C. Linderäl, P. Erhart, E. Malic, Exciton landscape in van der Waals heterostructures. *Phys. Rev. Res.* **3**, 043217 (2021).
66. S. Brem, M. Selig, G. Berghaeuser, E. Malic, Exciton relaxation cascade in two-dimensional transition metal dichalcogenides. *Sci. Rep.* **8**, 8238 (2018).
67. M. Kira, S. W. Koch, Many-body correlations and excitonic effects in semiconductor spectroscopy. *Prog. Quantum Electron.* **30**, 155–296 (2006).
68. H. Haug, S. W. Koch, *Quantum Theory of the Optical and Electronic Properties of Semiconductors* (World Scientific Publishing Company, 2009).
69. E. Malic, A. Knorr, *Graphene and Carbon Nanotubes: Ultrafast Optics and Relaxation Dynamics* (John Wiley & Sons, 2013).
70. S. Brem, C. Linderäl, P. Erhart, E. Malic, Tunable phases of moiré excitons in van der Waals heterostructures. *Nano Lett.* **20**, 8534–8540 (2020).

#### Acknowledgments

**Funding:** This work was funded by the Deutsche Forschungsgemeinschaft (DFG; German Research Foundation) (432680300/SFB 1456, project B01; 217133147/SFB 1073, projects B07 and B10; and 223848855/SFB 1083, project B9). A.A. and S.H. acknowledge funding from EPSRC (EP/T001038/1 and EP/P005152/1). A.A. acknowledges financial support from the Saudi Arabian Ministry of Higher Education. E.M. acknowledges support from the European Union's Horizon 2020 research and innovation program under grant agreement no. 881603 (Graphene Flagship). K.W. and T.T. acknowledge support from JSPS KAKENHI (grant numbers 19H05790, 20H00354, and 21H05233). **Author contributions:** D.St., S.S., R.T.W., G.S.M.J., S.H., S.B., E.M., M.R., and S.M. conceived the research. D.Sc., J.P.B., and W.B. carried out the time-resolved momentum microscopy experiments. J.P.B. and D.Sc. analyzed the data. G.M. performed the microscopic model calculations. A.A. fabricated the heterostructure sample. All authors discussed the results. M.R. and S.M. were responsible for the overall project direction and wrote the manuscript with contributions from all coauthors. K.W. and T.T. synthesized the hBN crystals. **Competing interests:** The authors declare that they have no competing interests. **Data and materials availability:** All data needed to evaluate the conclusions of the paper are present in the paper and/or the Supplementary Materials.

Submitted 5 April 2023

Accepted 10 January 2024

Published 7 February 2024

10.1126/sciadv.adi1323

Supplementary Materials for  
**Probing electron-hole Coulomb correlations in the exciton landscape of a  
twisted semiconductor heterostructure**

Jan Philipp Bange *et al.*

Corresponding author: Marcel Reutzel, [marcel.reutzel@phys.uni-goettingen.de](mailto:marcel.reutzel@phys.uni-goettingen.de);  
Stefan Mathias, [smathias@uni-goettingen.de](mailto:smathias@uni-goettingen.de)

*Sci. Adv.* **10**, eadi1323 (2024)  
DOI: 10.1126/sciadv.adi1323

**This PDF file includes:**

Supplementary Text  
Figs. S1 to S8  
Table S1  
References

# Supplementary Text

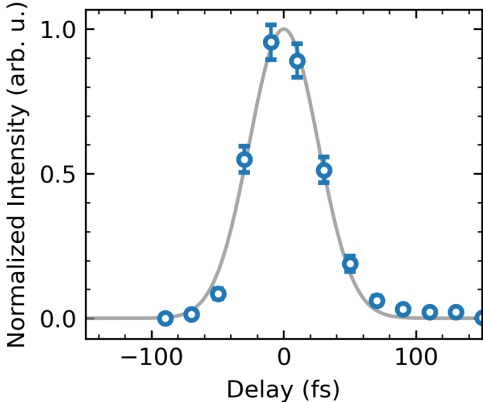


Figure S1: Cross-correlation measurement of the pump and probe laser pulses as obtained in the photoemission experiment due to the measurement of photoemission sidebands formed due to the laser-assisted photoelectric effect.

## Correction of rigid band shifts

As a result of pump- and probe-induced space-charge and surface photovoltage effects, we observe transient energy shifts of the momentum-integrated photoemission spectrum by  $\pm 80$  meV (Fig. S2) (63). This energy offset is extracted from the data by fitting the spectral weight maxima at  $\approx -2.4$  eV (Fig. S2B) for each pump-probe delay. The blue and the black data points show the pump-probe dependence of this peak before and after correction, respectively. The correction is done prior to the data analysis discussed in the main text.

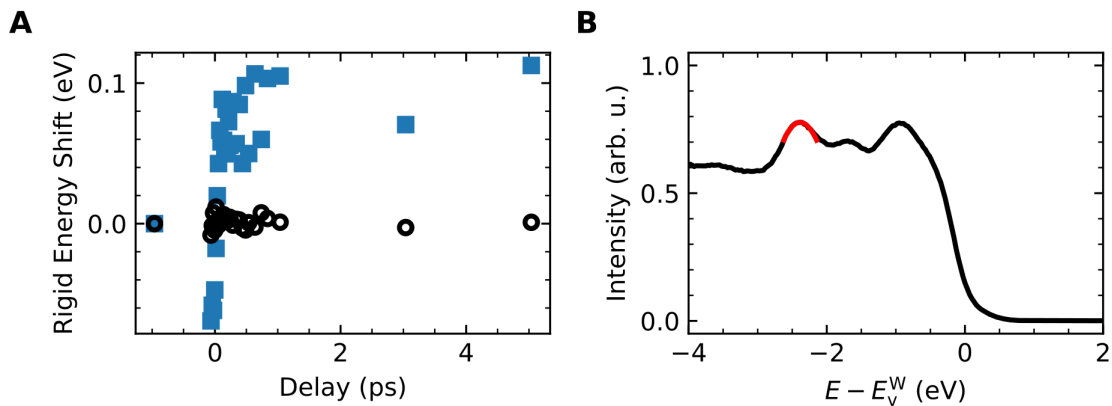


Figure S2: **Correction of rigid energy shifts.** (A) At each pump-probe delay, the momentum-integrated energy spectrum has a distinct rigid energy shift (blue squares) that is evaluated by fitting the red marked peak close to  $E - E_v^W = -2.4$  eV in (B). After the correction of this rigid energy shift, all energy-distribution-curves are aligned (black circle data points in (A)).

## Quantitative analysis of the exciton dynamics - Rate equation modelling

Fig. 3A in the main text and Fig. S3C show the pump-probe delay-dependent photoemission intensity from interlayer  $K_W$ - $K_{Mo}$  excitons in the case that electron- and hole-transfer processes (black circles, 1.9 eV) or that electron-only-transfer processes (green circles, 1.7 eV) contribute. In order to quantitatively analyze the characteristic formation dynamics, we apply a rate equation model to fit the experimental data. The model is schematically shown in Fig. S3A and S3B and the rate equations are listed in the following

$$\frac{dN_W}{dt} = g_W(t) - \frac{N_W}{t_{e\text{-transfer}}}, \quad (S1)$$

$$\frac{dN_{K_W-K_{Mo}}^{e\text{-only}}}{dt} = \frac{N_W}{t_{e\text{-transfer}}} - \frac{N_{K_W-K_{Mo}}^{e\text{-only}}}{\tau_{\text{decay}}}, \quad (S2)$$

$$\frac{dN_{Mo}}{dt} = g_{Mo}(t) - \frac{N_{Mo}}{t_{h\text{-transfer}}} - \frac{N_{Mo}}{\tau_{\text{intra}}}, \quad (S3)$$

$$\frac{dN_{K_W-K_{Mo}}^{e\&h}}{dt} = \frac{N_{Mo}}{t_{h\text{-transfer}}} + \frac{N_W}{t_{e\text{-transfer}}} - \frac{N_{K_W-K_{Mo}}^{e\&h}}{\tau_{\text{decay}}}. \quad (S4)$$

$N_W$  and  $N_{Mo}$  are the intralayer exciton occupation in the  $WSe_2$  and  $MoS_2$  layer, respectively, that are populated with Gaussian shaped excitation  $g_W(t)$  and  $g_{Mo}(t)$  (FWHM = 50 fs). As the probe laser pulse duration is sufficiently short (20 fs), it is neglected in the rate equation fit.  $t_{e\text{-transfer}}$  and  $t_{h\text{-transfer}}$ , respectively, describe the electron- and hole-transfer times from the initial  $N_W$  and  $N_{Mo}$  states into the final  $N_{K_W-K_{Mo}}^{e\&h}$  and  $N_{K_W-K_{Mo}}^{e\text{-only}}$  states. Based on the absorption coefficients of  $MoS_2$  and  $WSe_2$  at excitation with 1.9 eV laser pulses (41), we expect to excite the respective intralayer A1s excitons in a 1:5 ratio, i.e.,  $g_{Mo}(t) = 5 \cdot g_W(t)$ . It is important to note that because of photoemission matrix element effects (25), the direct correlation of the photoemission intensity from excitons to the excitonic occupation is not possible. Hence, the excitation ratio cannot experimentally be extracted from the pump-probe delay-dependent analysis of the photoemission intensity from intralayer  $K_W$ - $K_W$  and  $K_{Mo}$ - $K_{Mo}$  excitons (Fig. S4).

At first glance, it might be expected the the electron-transfer and hole-transfer processes also contribute to the interlayer exciton occupation with a ratio of 1:5. However, this assumption neglects additional decay processes that must be taken into account. In particular, we observe that the hole-mediated interlayer  $K_W$ - $K_{Mo}$  exciton photoemission yield increases on an time-scale of up to 1 ps (Fig. 3A). On this comparably long time-scale, radiative and defect-assisted decay processes of intralayer and hybrid excitons with lifetimes in the regime of a few picoseconds clearly become relevant (8, 27, 34, 35). Hence, not all initially excited intralayer excitons are converted to interlayer excitons. In order to capture these processes in our fit routine, we add the decay constant  $\tau_{intra}$  as a free fit parameter to equation (S3). Moreover, the interlayer exciton state depopulates with a fixed decay time of  $\tau_{decay} = 33$  ps, which was estimated from an exponential decay fit to the long-term dynamics (8).

In our analysis, we first fit the 1.7 eV pumped data set. In the fit routine, equations (S1) and (S2) are solved numerically yielding the delay-dependent evolution of the state  $N_{K_W-K_{Mo}}^{e-only}$ . This is then compared to the data. Fit parameters are amplitude of the excitation and electron transfer time  $t_{e-transfer}$ . Optimization for best fit parameters yields  $t_{e-transfer} = 40 \pm 10$  fs.

In a second step, we fit the 1.9 eV data. Equations (S1), (S3) and (S4) are solved by incorporating the fixed electron-only transfer time  $t_{e-transfer} = 40 \pm 10$  fs from the previous fit and  $g_{Mo}(t) = 5 \cdot g_W(t)$  (see above). The remaining fit parameters are the amplitude of the excitation, the hole-transfer time  $t_{h-transfer}$  and the decay time  $\tau_{intra}$  of the initial  $N_{Mo}$  state. The optimization for the best fit parameters yields a hole-transfer time of  $t_{h-transfer} = 2.2 \pm 1$  ps. Moreover, the fitted decay time  $\tau_{intra} = 600 \pm 200$  fs is in a reasonable order in comparison to earlier work on radiative and defect decay processes of intralayer and hybrid excitons (8, 27, 34, 35).

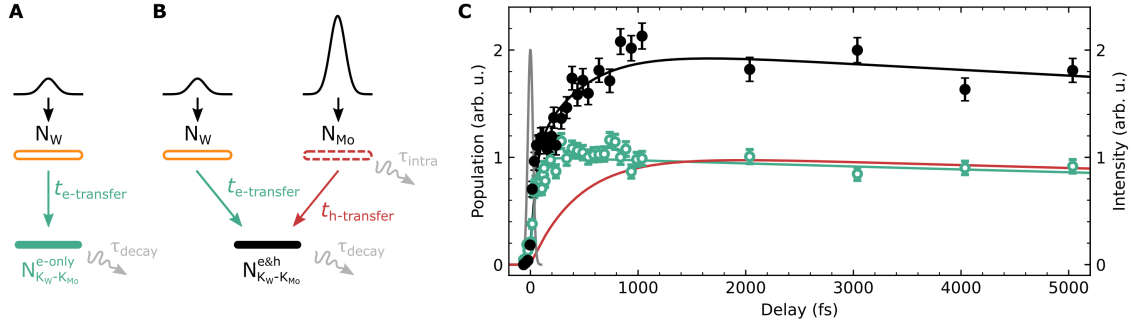


**Figure S3: Quantitative analysis of the interlayer  $K_W$ - $K_{Mo}$  exciton formation dynamics.** (A) Schematic overview of the rate equation model: Exciton population in the  $WSe_2$  layer  $N_W$  is excited by a Gaussian pump pulse. Electron charge-transfer leads to the formation of interlayer  $K_W$ - $K_{Mo}$  excitons ( $N_{K_W-K_{Mo}}^{e-only}$ ) with the scattering time  $t_{e-transfer}$ . (B) Exciton population in the  $MoS_2$  ( $WSe_2$ ) layer  $N_{Mo}$  ( $N_W$ ) is excited by a Gaussian pump pulse. Hole (electron) charge-transfer leads to the formation of interlayer  $K_W$ - $K_{Mo}$  excitons ( $N_{K_W-K_{Mo}}^{e\&h}$ ) with the scattering time  $t_{h-transfer}$  ( $t_{e-transfer}$ ). (C) The pump-probe delay-dependent build-up of photoemission intensity of interlayer  $K_W$ - $K_{Mo}$  excitons is shown after resonant excitation of  $K_{Mo}$ - $K_{Mo}$  excitons in  $MoS_2$  (1.9 eV, black circles) and after resonant excitation of  $K_W$ - $K_W$  excitons in  $WSe_2$  (1.7 eV, green circles), respectively. Note that resonant excitation of  $K_{Mo}$ - $K_{Mo}$  excitons also leads to off-resonant excitation of  $K_W$ - $K_W$  excitons, so that the interlayer exciton occupation is build-up both by hole and electron transfer. Solid lines depict best fit results of the rate equation model. Green and dark red solid lines describe the proportion of the interlayer exciton population that is created due to the electron-only ( $N_{K_W-K_{Mo}}^{e-only}$ ) and hole-only charge transfer, respectively. The black line corresponds to the sum of electron- and hole-transfer processes  $N_{K_W-K_{Mo}}^{e\&h}$ .

## Femtosecond dynamics of intra- and interlayer excitons

Figure S4 shows an overview of the pump-probe delay-dependent evolution of photoemission intensity for all measured excitons after excitation with 1.9 eV light pulses. The first two rows show the optical excitation of intralayer  $K_W$ - $K_W$  excitons (orange) and the subsequent formation of hybrid  $K_W$ - $\Sigma$  excitons (grey). The bottom two panels show the photoemission intensity of selected  $\kappa$  valleys of the moiré mBz. In the case that the  $\kappa$  valley overlaps with the  $K_{Mo}$  valley (dark red), photoemission intensity is composed of signal from intralayer  $K_{Mo}$ - $K_{Mo}$  and interlayer  $K_{Mo}$ - $K_W$  excitons. This  $\kappa$  valley is evaluated in Fig. 4 of the main text. Complementary, if the two  $\kappa$  valleys are evaluated (black) that do not overlap with the  $K_{Mo}$  valley, only photoemission signal from interlayer  $K_{Mo}$ - $K_W$  excitons is detected. These data are shown in Fig. 3A of the main text. Error bars of the data depicted in Fig 3A of the main text and Figure S1, S3B and S4 show the  $1\sigma$  interval of the Poisson distributed count statistics.

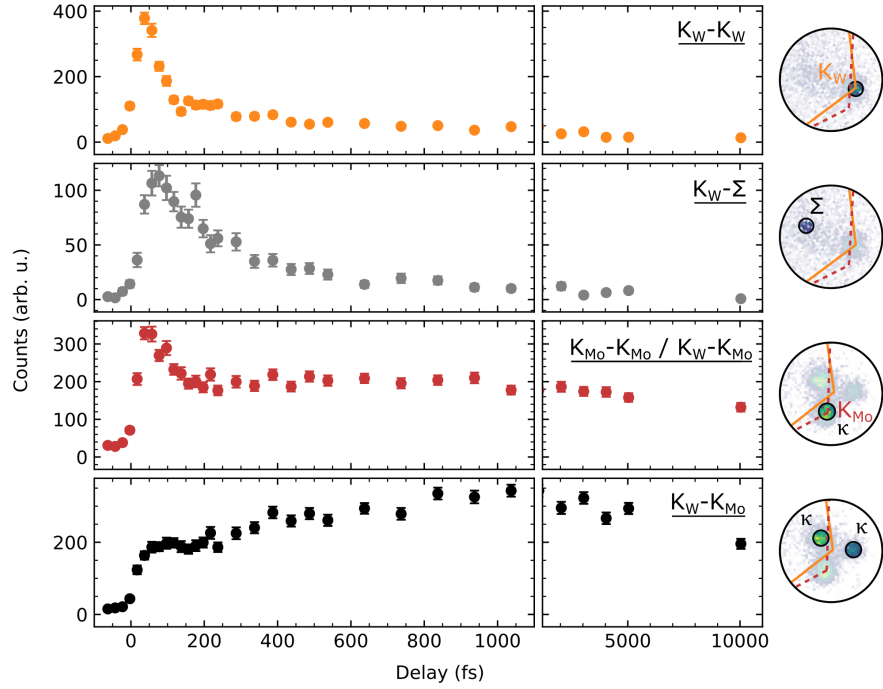


Figure S4: **Femtosecond intra- to interlayer exciton transfer dynamics.** The dynamics for the different exciton signals are depicted:  $K_W-K_W$  (orange),  $K_W-\Sigma$  (grey),  $K_{M_0}-K_{M_0}$  and  $K_W-K_{M_0}$  (dark red) and  $K_W-K_{M_0}$  (black). The round insets show the position of the momentum apertures used for filtering the exciton photoemission signatures. If the  $\kappa$  valley coincides with the  $K_{M_0}$  valley (dark red), photoemission yield is composed of contributions from intralayer  $K_{M_0}-K_{M_0}$  and interlayer  $K_W-K_W$  excitons (see Fig 4 of the main text). In the case that those high-symmetry points do not overlap (black), only photoemission signal from interlayer  $K_W-K_{M_0}$  excitons is detected (see Fig. 3 of the main text). Momentum filters have a diameter of  $0.17 \text{ \AA}^{-1}$  and the signal is summed over all 6 corners of the first Brillouin zone. Energy binning is 2.3-1.3 eV for  $K_W-K_W$  and  $K_W-\Sigma$  and 1.42-0.75 eV for  $K_W-K_{M_0}$  and  $K_{M_0}-K_{M_0}$ .

## Excluding photoinduced band renormalizations

The major spectroscopic signature of interest in our manuscript is a pump-probe delay-dependent upshift of the energy of photoelectrons being emitted from excitons (Fig. 4). We attribute this energy upshift to the formation of interlayer  $K_{Mo}$ - $K_W$  excitons from intralayer  $K_{Mo}$ - $K_{Mo}$  excitons. However, it is well-known that photo-induced band renormalizations (53) can lead to a similar shift of photoemission signatures (54), which, hence, must be excluded.

In addition to photoemission signals from excitons, the multidimensional data acquisition scheme allows to monitor the energetic position of the occupied valence band of  $MoS_2$ . If the electronic bands would renormalize in response to the optical excitation, we would expect to observe an energetic shift of this occupied valence band (54). In Fig. S5, we directly compare the energy position of the  $MoS_2$  valence band and the excitonic photoemission signal. We observe that after the excitation with the pump pulse the excitonic peak position at the  $K_{Mo}$  point exhibits an upshift, while the valence band maximum of the  $MoS_2$  layer remains comparably constant. Hence, we can exclude photo-induced band renormalizations as the origin for the energetic upshift of the main photoemission signal in Fig. 4.

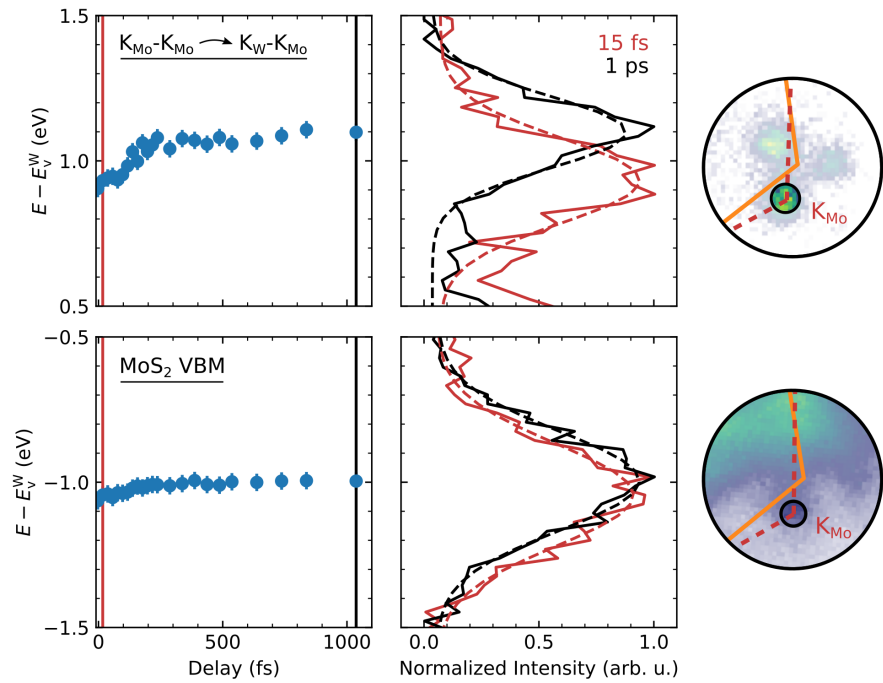


Figure S5: **Excluding photo-induced band renormalizations.** The top and the bottom rows show the peak position of the exciton photoemission signal and the MoS<sub>2</sub> valence band maximum, respectively. In the middle panels, selected EDCs taken at the  $K_{\text{Mo}}$  valley are shown for 15 fs (dark red) and 1 ps (black). In the left panels, the fitted peak maxima of such EDCs are plotted as a function of pump-probe delay. The right panels show the filtered momentum regions (black circles), whereas the momentum-momentum maps are taken at the respective energies of the excitonic photoemission signal and the MoS<sub>2</sub> valence band maximum.

## Exciton energy relaxation during electron- and hole-transfer process

In Fig. 4 of the main text we show an upshift of the photoelectron energy of the exciton signal caused by the hole charge-transfer process. Figure S6 depicts this photoemission signature when pumping with 1.9 eV (Fig. S6A) in comparison to the photoemission signature upon 1.7 eV pumping (Fig. S6B). For the latter case that initiates the electron charge-transfer process, we observe a reduction in the photoelectron energy in agreement with our earlier report (8). We note that in both cases the exciton relaxes towards the energetically lowest lying state in the overall exciton energy landscape, i.e. to the interlayer exciton, as shown by the analysis in the main text.

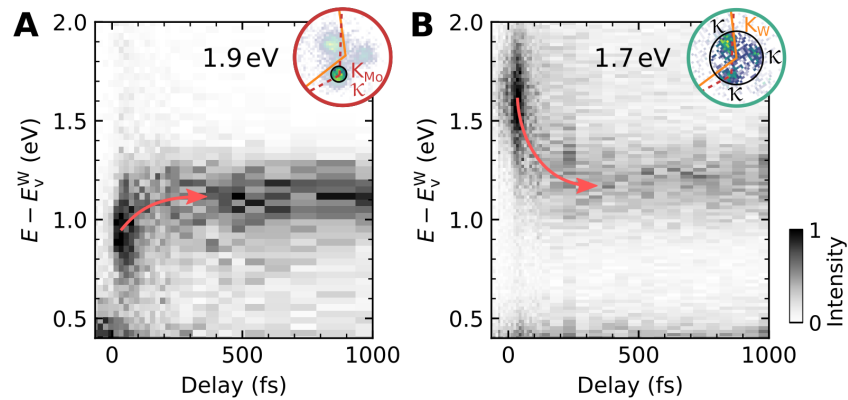


Figure S6: **Pump-probe delay evolution of the exciton energy fingerprints for the case of the hole- and the electron-transfer process.** (A) Pump-probe delay evolution of the momentum filtered energy-distribution curves (EDC) with a pump energy of 1.9 eV resonant to intralayer  $K_{Mo}$ - $K_{Mo}$  excitons. The momentum filter is placed at the  $K_{Mo}$  high-symmetry point (inset). The mean photoelectron energy shows an apparent upshift on the  $< 200$  fs scale as the excitonic energy relaxes. (B) Pump-probe delay evolution of EDCs including the  $K_W$  point and all three  $\kappa$  points. When applying a pump energy of 1.7 eV resonant to intralayer  $K_W$ - $K_W$  excitons the mean photoelectron energy reduces as the exciton energy relaxes.

## Microscopic modelling

In this section, we introduce the main concepts of the theoretical approach applied to calculate the dynamics in TMD bilayers. We start with the excitonic Hamiltonian operator

$$H = H_0 + H_T = \sum_{\mu, \mathbf{Q}} E_{\mathbf{Q}}^{\mu} X_{\mathbf{Q}}^{\mu\dagger} X_{\mathbf{Q}}^{\mu} + \sum_{\mu, \nu, \mathbf{Q}} \mathcal{T}_{\mu\nu} X_{\mathbf{Q}}^{\mu\dagger} X_{\mathbf{Q}}^{\nu} \quad (\text{S5})$$

where we used the superindex  $\mu = (n^{\mu}, \zeta_e^{\mu}, \zeta_h^{\mu}, L_e^{\mu}, L_h^{\mu})$  to describe the exciton states,  $E_{\mathbf{Q}}^{\mu} = E_{\zeta^{\mu} L_e^{\mu}}^c - E_{\zeta^{\mu} L_h^{\mu}}^v + E_{bind}^{\mu} + E_{\mathbf{Q}, kin}^{\mu}$  are the excitonic energies, where  $E_{bind}^{\mu}$  are obtained after solving a bilayer Wannier equation (44, 64),  $E_{\zeta^{\mu} L_e^{\mu}}^{c/v}$  are the conduction and valence band energy and  $E_{\mathbf{Q}, kin}^{\mu} = \hbar^2 \mathbf{Q}^2 / (2M^{\mu})$  is the kinetic energy of the exciton with mass  $M^{\mu} = (m_e^{\mu} + m_h^{\mu})$ . Moreover we introduced the excitonic tunneling between the TMD monolayers with the tunnelling matrix elements

$$\mathcal{T}_{\mu\nu} = (\delta_{L_h^{\mu} L_h^{\nu}} (1 - \delta_{L_e^{\mu} L_e^{\nu}}) \delta_{\zeta^{\mu} \zeta^{\nu}} T_{\mu_e, \nu_e}^c - \delta_{L_e^{\mu} L_e^{\nu}} (1 - \delta_{L_h^{\mu} L_h^{\nu}}) \delta_{\zeta^{\mu} \zeta^{\nu}} T_{\mu_h, \nu_h}^v) \sum_{\mathbf{k}} \psi^{\mu*}(\mathbf{k}) \psi^{\nu}(\mathbf{k}), \quad (\text{S6})$$

where  $\psi^{\mu}$  is the excitonic wave function of the state  $\mu$  defined over the relative momentum between electron and hole,  $T_{ij}^{\lambda} = \langle \lambda i \mathbf{p} | H | \lambda j \mathbf{p} \rangle (1 - \delta_{L_i L_j}) \delta_{\zeta_i \zeta_j}$  are the electronic tunneling elements obtained by averaging DFT values of MoSe<sub>2</sub>-WSe<sub>2</sub> and MoS<sub>2</sub>-WS<sub>2</sub> heterostructures in (65). Diagonalizing Eq. S5 leads to a new set of hybrid excitonic energies  $\mathcal{E}_{\mathbf{Q}}^{\eta}$  that are obtained by solving the hybrid eigenvalue equation (64, 65),

$$E_{\mathbf{Q}}^{\mu} c_{\mu}^{\eta}(\mathbf{Q}) + \sum_{\nu} \mathcal{T}_{\mu\nu} c_{\nu}^{\eta}(\mathbf{Q}) = \mathcal{E}_{\mathbf{Q}}^{\eta} c_{\mu}^{\eta}(\mathbf{Q}). \quad (\text{S7})$$

Now, we can define a diagonal hybrid exciton Hamiltonian (8, 42)

$$H = \sum_{\eta} \mathcal{E}_{\mathbf{Q}}^{\eta} Y_{\mathbf{Q}}^{\eta\dagger} Y_{\mathbf{Q}}^{\eta} \quad (\text{S8})$$

with the hybrid exciton annihilation/creation operators  $Y_{\mathbf{Q}}^{\eta(\dagger)} = \sum_{\mu} c_{\mu}^{\eta}(\mathbf{Q}) X_{\mathbf{Q}}^{\mu(\dagger)}$ . Evaluating the above eigenvalue equation, we predict the hybrid exciton energy landscape for the investigated WSe<sub>2</sub>-MoS<sub>2</sub> heterostructure, see Fig. S7.

The hybrid exciton-phonon scattering plays a crucial role at the low excitation regime (42, 66). The corresponding Hamiltonian can be written as (64)

$$H_{Y-ph} = \sum_{j, \mathbf{Q}, \mathbf{q}, \eta, \xi} \tilde{\mathcal{D}}_{j, \mathbf{q}, \mathbf{Q}}^{\xi \eta} Y_{\mathbf{Q}+\mathbf{q}}^{\xi \dagger} Y_{\mathbf{Q}}^{\eta} b_{j, \mathbf{q}} + h.c. \quad (\text{S9})$$

with the hybrid exciton-phonon coupling  $\tilde{\mathcal{D}}_{j, \mathbf{q}, \mathbf{Q}}^{\xi \eta}$ . The electron-phonon coupling matrix elements, single-particle energies and effective masses are taken from DFPT calculations (43). The excitation of the system through a laser pulse is described semi-classically via the minimal-coupling Hamiltonian that can be written as (64)

$$H_{Y-l} = \sum_{\sigma, \mathbf{Q}, \eta} \mathbf{A} \cdot \tilde{\mathcal{M}}_{\sigma \mathbf{Q}}^{\eta} Y_{\mathbf{Q} \parallel}^{\eta} + h.c. \quad (\text{S10})$$

with hybrid exciton-light coupling  $\tilde{\mathcal{M}}_{\sigma \mathbf{Q}}^{\eta}$ . Details on the transformation and the definition of the hybrid interaction matrix elements and couplings are given in Ref. (64, 65).

Exploiting the Heisenberg equation of motion for the hybrid occupation  $N^{\eta} = \langle Y^{\eta \dagger} Y^{\eta} \rangle$ , including  $H = H_Y + H_{Y-ph} + H_{Y-l}$ , and truncating the Martin-Schwinger hierarchy using a second order Born-Markov approximation (67–69), separating coherent  $P_{\mathbf{Q}}^{\eta} = \langle Y_{\mathbf{Q}}^{\eta \dagger} \rangle$  and incoherent hybrid populations  $\delta N_{\mathbf{Q}}^{\eta} = \langle Y_{\mathbf{Q}}^{\eta \dagger} Y_{\mathbf{Q}}^{\eta} \rangle - \langle Y_{\mathbf{Q}}^{\eta \dagger} \rangle \langle Y_{\mathbf{Q}}^{\eta} \rangle = N_{\mathbf{Q}}^{\eta} - |P_{\mathbf{Q}}^{\eta}|^2$ , leads to the coupled semiconductor Bloch equations

$$i\hbar \partial_t P_0^{\eta} = -(\mathcal{E}_0^{\eta} + i\Gamma_0^{\eta}) P_0^{\eta} - \tilde{\mathcal{M}}_0^{\eta} \cdot \mathbf{A}(t) \quad (\text{S11})$$

$$\delta \dot{N}_{\mathbf{Q}}^{\eta} = \sum_{\xi} W_{0\mathbf{Q}}^{\xi \eta} |P_0^{\eta}|^2 + \sum_{\xi, \mathbf{Q}'} \left( W_{\mathbf{Q}'\mathbf{Q}}^{\xi \eta} \delta N_{\mathbf{Q}'}^{\xi} - W_{\mathbf{Q}\mathbf{Q}'}^{\eta \xi} \delta N_{\mathbf{Q}}^{\eta} \right)$$

with  $W_{\mathbf{Q}\mathbf{Q}'}^{\eta \xi} = \frac{2\pi}{\hbar} \sum_{j, \pm} |\mathcal{D}_{j, \mathbf{Q}'-\mathbf{Q}}^{\eta \xi}|^2 \left( \frac{1}{2} \pm \frac{1}{2} + n_{j, \mathbf{Q}'-\mathbf{Q}}^{ph} \right) \delta \left( \mathcal{E}_{\mathbf{Q}'}^{\xi} - \mathcal{E}_{\mathbf{Q}}^{\eta} \mp \hbar \Omega_{j, \mathbf{Q}'-\mathbf{Q}} \right)$  as the phonon mediated scattering tensor.

The large twist angle in the experiment gives rise to very short moire periods with a length scale comparable with the exciton Bohr radius. Therefore, a strong modification of the exciton center-of-mass motion, i.e. a moire-trapping of excitons is not expected (70) therefore, we neglect the twist angle dependence.

Resonant excitation of the  $K_{Mo}$ - $K_{Mo}$  exciton leads also to a non-resonant excitation of the  $K_W$ - $K_W$  state. The ratio in the exciton occupation of  $N_{Mo}/N_W \simeq 5$  can be extracted from optical absorption coefficients (41). To model this effect in our simulations, we include one main pulse exciting the  $K_{Mo}$ - $K_{Mo}$  state, and a secondary less intense pulse exciting the  $K_W$ - $K_W$  state, imposing the same ratio of the coherent population as in the experiment.

The resulting evolution of exciton population for all contributing states is shown in Figure S8. Note that states with a valley degree of freedom cannot be distinguished in experiment. Therefore these states are summed up, e.g.  $K_{Mo}$ - $K_{Mo}$  and  $K_{Mo}$ - $K'_{Mo}$ .

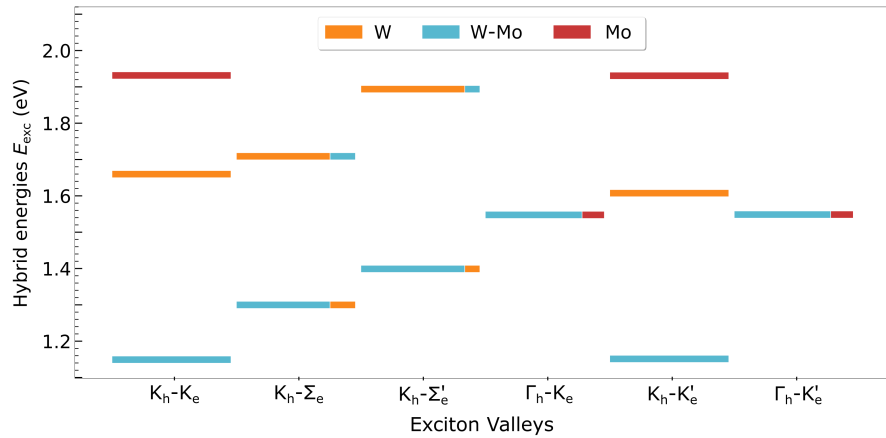


Figure S7: Hybrid-exciton energy landscape for the  $WSe_2/MoS_2$  heterostructure. We use different colors for depicting the percentage of intralayer tungsten (W, orange), intralayer molybdenum (Mo, red) or interlayer (blue) exciton character of the corresponding states. Due to the strong tunneling experienced by electrons or holes,  $K_h$ - $\Sigma_e^{(\prime)}$  and  $\Gamma_h$ - $K_e^{(\prime)}$  states are strongly hybridized. Note that we plot only a selection of low-energy hybrid exciton states contributing directly to the relaxation dynamics.

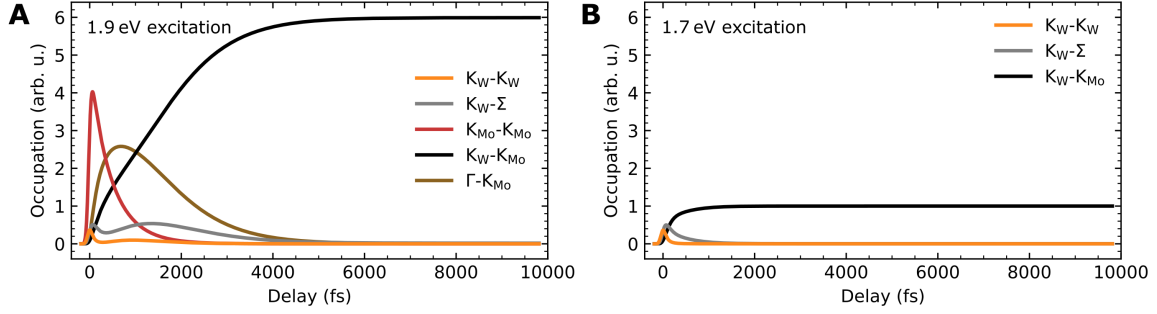


Figure S8: **Exciton occupation dynamics calculated for the electron- and the hole-transfer process.** Note that states with a valley degree of freedom cannot be distinguished in experiment. Therefore these states are summed up, e.g.  $K_{M_0}-K_{M_0}$  and  $K_{M_0}-K'_{M_0}$  excitons are termed  $K_{M_0}-K_{M_0}$  in the legend.

from \ to	$K_W-K_W$	$K_W-K'_W$	$K_W-\Sigma$	$K_W-\Sigma'$	$K_W-K_{M_0}$	$K_W-K'_{M_0}$	$\Gamma-K_{M_0}$	$\Gamma-K'_{M_0}$	$K_{M_0}-K_{M_0}$	$K_{M_0}-K'_{M_0}$
$K_W-K_W$	-	5.07	0.43	22.55	7E-04	1E-04	1E-04	0	0	0
$K_W-K'_W$	4E-09	-	18.95	1.04	8E-05	2E-03	0	3E-05	0	0
$K_W-\Sigma$	0	0	-	0	1.59	13.33	0	0	0	0
$K_W-\Sigma'$	0	0	142.77	-	5.43	0.83	0	0	0	0
$K_W-K_{M_0}$	0	0	0	0	-	0.47	0	0	0	0
$K_W-K'_{M_0}$	0	0	0	0	0	-	0	0	0	0
$\Gamma-K_{M_0}$	0	0	0	0	1.13	0	-	0	0	0
$\Gamma-K'_{M_0}$	0	0	0	0	0	1.00	0	-	0	0
$K_{M_0}-K_{M_0}$	3E-06	2E-07	5E-04	7E-03	2E-03	1E-04	1.62	0	-	0
$K_{M_0}-K'_{M_0}$	3E-07	2E-06	7E-03	6E-04	1E-04	2E-03	0	1.61	0.80	-

Table S1: Exciton-phonon scattering induced out-scattering rates for all initial exciton states resolved into all possible final states ( $\text{ps}^{-1}$ , for  $Q = 0$ ). Out-scattering rates that are given with "0" are fully suppressed due to energy conservation in the one phonon processes.

## REFERENCES AND NOTES

1. G. Wang, A. Chernikov, M. M. Glazov, T. F. Heinz, X. Marie, T. Amand, B. Urbaszek, Colloquium: Excitons in atomically thin transition metal dichalcogenides. *Rev. Mod. Phys.* **90**, 021001 (2018).
2. A. Chernikov, T. C. Berkelbach, H. M. Hill, A. Rigosi, Y. Li, O. B. Aslan, D. R. Reichman, M. S. Hybertsen, T. F. Heinz, Exciton binding energy and nonhydrogenic rydberg series in monolayer WS<sub>2</sub>. *Phys. Rev. Lett.* **113**, 076802 (2014).
3. K. He, N. Kumar, L. Zhao, Z. Wang, K. F. Mak, H. Zhao, J. Shan, Tightly bound excitons in monolayer WSe<sub>2</sub>. *Phys. Rev. Lett.* **113**, 026803 (2014).
4. C.-H. Lee, G.-H. Lee, A. M. van der Zande, W. Chen, Y. Li, M. Han, X. Cui, G. Arefe, C. Nuckolls, T. F. Heinz, J. Guo, J. Hone, P. Kim, Atomically thin p-n junctions with van der Waals heterointerfaces. *Nat. Nanotechnol.* **9**, 676–681 (2014).
5. X. Hong, J. Kim, S.-F. Shi, Y. Zhang, C. Jin, Y. Sun, S. Tongay, J. Wu, Y. Zhang, F. Wang, Ultrafast charge transfer in atomically thin MoS<sub>2</sub>/WS<sub>2</sub> heterostructures. *Nat. Nanotechnol.* **9**, 682–686 (2014).
6. F. Ceballos, M. Z. Bellus, H.-Y. Chiu, H. Zhao, Ultrafast charge separation and indirect exciton formation in a MoS<sub>2</sub>-MoSe<sub>2</sub> van der waals heterostructure. *ACS Nano* **8**, 12717–12724 (2014).
7. P. Merkl, F. Mooshammer, P. Steinleitner, A. Girnghuber, K. Q. Lin, P. Nagler, J. Holler, C. Schüller, J. M. Lupton, T. Korn, S. Ovesen, S. Brem, E. Malic, R. Huber, Ultrafast transition between exciton phases in van der Waals heterostructures. *Nat. Mater.* **18**, 691–696 (2019).
8. D. Schmitt, J. P. Bange, W. Bennecke, A. AlMutairi, G. Meneghini, K. Watanabe, T. Taniguchi, D. Steil, D. R. Luke, R. T. Weitz, S. Steil, G. S. M. Jansen, S. Brem, E. Malic, S. Hofmann, M. Reutzler, S. Mathias, Formation of moiré interlayer excitons in space and time. *Nature* **608**, 499–503 (2022).

9. K. L. Seyler, P. Rivera, H. Yu, N. P. Wilson, E. L. Ray, D. G. Mandrus, J. Yan, W. Yao, X. Xu, Signatures of moiré-trapped valley excitons in MoSe<sub>2</sub>/WSe<sub>2</sub> heterobilayers. *Nature* **567**, 66–70 (2019).
10. E. M. Alexeev, D. A. Ruiz-Tijerina, M. Danovich, M. J. Hamer, D. J. Terry, P. K. Nayak, S. Ahn, S. Pak, J. Lee, J. I. Sohn, M. R. Molas, M. Koperski, K. Watanabe, T. Taniguchi, K. S. Novoselov, R. V. Gorbachev, H. S. Shin, V. I. Fal’ko, A. I. Tartakovskii, Resonantly hybridized excitons in moiré superlattices in van der Waals heterostructures. *Nature* **567**, 81–86 (2019).
11. K. Tran, G. Moody, F. Wu, X. Lu, J. Choi, K. Kim, A. Rai, D. A. Sanchez, J. Quan, A. Singh, J. Embley, A. Zepeda, M. Campbell, T. Autry, T. Taniguchi, K. Watanabe, N. Lu, S. K. Banerjee, K. L. Silverman, S. Kim, E. Tutuc, L. Yang, A. H. MacDonald, X. Li, Evidence for moiré excitons in van der Waals heterostructures. *Nature* **567**, 71–75 (2019).
12. O. Karni, E. Barré, V. Pareek, J. D. Georganas, M. K. L. Man, C. Sahoo, D. R. Bacon, X. Zhu, H. B. Ribeiro, A. L. O’Beirne, J. Hu, A. Al-Mahboob, M. M. M. Abdelrasoul, N. S. Chan, A. Karmakar, A. J. Winchester, B. Kim, K. Watanabe, T. Taniguchi, K. Barmak, J. Madéo, F. H. da Jornada, T. F. Heinz, K. M. Dani, Structure of the moiré exciton captured by imaging its electron and hole. *Nature* **603**, 247–252 (2022).
13. L. Ma, P. X. Nguyen, Z. Wang, Y. Zeng, K. Watanabe, T. Taniguchi, A. H. MacDonald, K. F. Mak, J. Shan, Strongly correlated excitonic insulator in atomic double layers. *Nature* **598**, 585–589 (2021).
14. Z. Zhang, E. C. Regan, D. Wang, W. Zhao, S. Wang, M. Sayyad, K. Yumigeta, K. Watanabe, T. Taniguchi, S. Tongay, M. Crommie, A. Zettl, M. P. Zaletel, F. Wang, Correlated interlayer exciton insulator in heterostructures of monolayer WSe<sub>2</sub> and moiré WS<sub>2</sub>/WSe<sub>2</sub>. *Nat. Phys.* **18**, 1214–1220 (2022).
15. Y. Slobodkin, Y. Mazuz-Harpaz, S. Refaely-Abramson, S. Gazit, H. Steinberg, R. Rapaport, Quantum phase transitions of trilayer excitons in atomically thin heterostructures. *Phys. Rev. Lett.* **125**, 255301 (2020).

16. L. Sigl, F. Sigger, F. Kronowetter, J. Kiemle, J. Klein, K. Watanabe, T. Taniguchi, J. J. Finley, U. Wurstbauer, A. W. Holleitner, Signatures of a degenerate many-body state of interlayer excitons in a van der waals heterostack. *Phys. Rev. Res.* **2**, 042044 (2020).
17. Z. Wang, D. A. Rhodes, K. Watanabe, T. Taniguchi, J. C. Hone, J. Shan, K. F. Mak, Evidence of high-temperature exciton condensation in two-dimensional atomic double layers. *Nature* **574**, 76–80 (2019).
18. C. Jin, E. Y. Ma, O. Karni, E. C. Regan, F. Wang, T. F. Heinz, Ultrafast dynamics in van der Waals heterostructures. *Nat. Nanotechnol.* **13**, 994–1003 (2018).
19. R. Perea-Causin, D. Erkensten, J. M. Fitzgerald, J. J. P. Thompson, R. Rosati, S. Brem, E. Malic, Exciton optics, dynamics, and transport in atomically thin semiconductors. *APL Mater.* **10**, 100701 (2022).
20. C. Poellmann, P. Steinleitner, U. Leierseder, P. Nagler, G. Plechinger, M. Porer, R. Bratschitsch, C. Schüller, T. Korn, R. Huber, Resonant internal quantum transitions and femtosecond radiative decay of excitons in monolayer WSe<sub>2</sub>. *Nat. Mater.* **14**, 889–893 (2015).
21. E. Malic, M. Selig, M. Feierabend, S. Brem, D. Christiansen, F. Wendler, A. Knorr, G. Berghäuser, Dark excitons in transition metal dichalcogenides. *Phys. Rev. Mater.* **2**, 014002 (2018).
22. T. Mueller, E. Malic, Exciton physics and device application of two-dimensional transition metal dichalcogenide semiconductors. *NPJ 2D Mater. Appl.* **2**, 29 (2018).
23. J. Madéo, M. K. L. Man, C. Sahoo, M. Campbell, V. Pareek, E. L. Wong, A. Al-Mahboob, N. S. Chan, A. Karmakar, B. M. K. Mariserla, X. Li, T. F. Heinz, T. Cao, K. M. Dani, Directly visualizing the momentum-forbidden dark excitons and their dynamics in atomically thin semiconductors. *Science* **370**, 1199–1204 (2020).
24. R. Wallauer, R. Perea-Causin, L. Münster, S. Zajusch, S. Brem, J. Güdde, K. Tanimura, K.-Q. Lin, R. Huber, E. Malic, U. Höfer, Momentum-resolved observation of exciton formation dynamics in monolayer WS<sub>2</sub>. *Nano Lett.* **21**, 5867–5873 (2021).

25. A. Kulin, S. Chernov, J. Bakalis, Z. Li, S. Cheng, Z. H. Withers, M. G. White, G. Schönhense, X. Du, R. K. Kawakami, T. K. Allison, Momentum-resolved exciton coupling and valley polarization dynamics in monolayer WS<sub>2</sub>. *Phys. Rev. Lett.* **130**, 046202 (2023).
26. D. Schmitt, J. P. Bange, W. Bennecke, G. Meneghini, A. AlMutairi, M. Merboldt, J. Pöhls, K. Watanabe, T. Taniguchi, S. Steil, D. Steil, R. T. Weitz, S. Hofmann, S. Brem, G. S. Matthijs Jansen, E. Malic, S. Mathias, M. Reutzler, Ultrafast nano-imaging of dark excitons. arXiv:2305.18908 (2023).
27. J. P. Bange, P. Werner, D. Schmitt, W. Bennecke, G. Meneghini, A. AlMutairi, M. Merboldt, K. Watanabe, T. Taniguchi, S. Steil, D. Steil, R. T. Weitz, S. Hofmann, G. S. M. Jansen, S. Brem, E. Malic, M. Reutzler, S. Mathias, Ultrafast dynamics of bright and dark excitons in monolayer WSe<sub>2</sub> and heterobilayer WSe<sub>2</sub>/MoS<sub>2</sub>. *2D Mater.* **10**, 035039 (2023).
28. E. Perfetto, D. Sangalli, A. Marini, G. Stefanucci, First-principles approach to excitons in time-resolved and angle-resolved photoemission spectra. *Phys. Rev. B* **94**, 245303 (2016).
29. A. Rustagi, A. F. Kemper, Photoemission signature of excitons. *Phys. Rev. B* **97**, 235310 (2018).
30. A. Steinhoff, M. Florian, M. Rösner, G. Schönhoff, T. O. Wehling, F. Jahnke, Exciton fission in monolayer transition metal dichalcogenide semiconductors. *Nat. Commun.* **8**, 1166 (2017).
31. D. Christiansen, M. Selig, E. Malic, R. Ernstorfer, A. Knorr, Theory of exciton dynamics in time-resolved ARPES: Intra- and intervalley scattering in two-dimensional semiconductors. *Phys. Rev. B* **100**, 205401 (2019).
32. S. Dong, M. Puppini, T. Pincelli, S. Beaulieu, D. Christiansen, H. Hübener, C. W. Nicholson, R. P. Xian, M. Dendzik, Y. Deng, Y. W. Windsor, M. Selig, E. Malic, A. Rubio, A. Knorr, M. Wolf, L. Rettig, R. Ernstorfer, Direct measurement of key exciton properties: Energy, dynamics, and spatial distribution of the wave function. *Nat. Sci.* **1**, e10010 (2021).
33. M. K. L. Man, J. Madéo, C. Sahoo, K. Xie, M. Campbell, V. Pareek, A. Karmakar, E. L. Wong, A. Al-Mahboob, N. S. Chan, D. R. Bacon, X. Zhu, M. M. M. Abdelrasoul, X. Li, T. F. Heinz, F. H.

- Jornada, T. Cao, K. M. Dani, Experimental measurement of the intrinsic excitonic wave function. *Sci. Adv.* **7**, eabg0192 (2021).
34. H. Zhu, J. Wang, Z. Gong, Y. D. Kim, J. Hone, X. Y. Zhu, Interfacial charge transfer circumventing momentum mismatch at two-dimensional van der Waals heterojunctions. *Nano Lett.* **17**, 3591–3598 (2017).
35. J. E. Zimmermann, M. Axt, F. Mooshammer, P. Nagler, C. Schüller, T. Korn, U. Höfer, G. Mette, Ultrafast charge-transfer dynamics in twisted MoS<sub>2</sub>/WSe<sub>2</sub> heterostructures. *ACS Nano* **15**, 14725–14731 (2021).
36. V. R. Policht, M. Russo, F. Liu, C. Trovatiello, M. Maiuri, Y. Bai, X. Zhu, S. Dal Conte, G. Cerullo, Dissecting interlayer hole and electron transfer in transition metal dichalcogenide heterostructures via two-dimensional electronic spectroscopy. *Nano Lett.* **21**, 4738–4743 (2021).
37. Z. Wang, P. Altmann, C. Gadermaier, Y. Yang, W. Li, L. Ghirardini, C. Trovatiello, M. Finazzi, L. Duò, M. Celebrano, R. Long, D. Akinwande, O. V. Prezhdo, G. Cerullo, S. Dal Conte, Phonon-mediated interlayer charge separation and recombination in a MoSe<sub>2</sub>/WSe<sub>2</sub> heterostructure. *Nano Lett.* **21**, 2165–2173 (2021).
38. G. Meneghini, M. Reutzel, S. Mathias, S. Brem, E. Malic, Hybrid exciton signatures in ARPES spectra of van der waals materials. *ACS Photonics* **10**, 3570–3575 (2023).
39. M. Keunecke, C. Möller, D. Schmitt, H. Nolte, G. S. M. Jansen, M. Reutzel, M. Gutberlet, G. Halasi, D. Steil, S. Steil, S. Mathias, Time-resolved momentum microscopy with a 1 MHz high-harmonic extreme ultraviolet beamline. *Rev. Sci. Instrum.* **91**, 063905 (2020).
40. M. Keunecke, M. Reutzel, D. Schmitt, A. Osterkorn, T. A. Mishra, C. Möller, W. Bennecke, G. S. M. Jansen, D. Steil, S. R. Manmana, S. Steil, S. Kehrein, S. Mathias, Electromagnetic dressing of the electron energy spectrum of Au(111) at high momenta. *Phys. Rev. B* **102**, 161403 (2020).

41. Y. Li, A. Chernikov, X. Zhang, A. Rigosi, H. M. Hill, A. M. van der Zande, D. A. Chenet, E.-M. Shih, J. Hone, T. F. Heinz, Measurement of the optical dielectric function of monolayer transition-metal dichalcogenides: MoS<sub>2</sub>, MoSe<sub>2</sub>, WS<sub>2</sub>, and WSe<sub>2</sub>. *Phys. Rev. B* **90**, 205422 (2014).
42. G. Meneghini, S. Brem, E. Malic, Ultrafast phonon-driven charge transfer in van der Waals heterostructures. *Nat. Sci.* **2**, e20220014 (2022).
43. Z. Jin, X. Li, J. T. Mullen, K. W. Kim, Intrinsic transport properties of electrons and holes in monolayer transition-metal dichalcogenides. *Phys. Rev. B* **90**, 045422 (2014).
44. S. Ovesen, S. Brem, C. Linderälv, M. Kuisma, T. Korn, P. Erhart, M. Selig, E. Malic, Interlayer exciton dynamics in van der Waals heterostructures. *Commun. Phys.* **2**, 23 (2019).
45. M. Selig, G. Berghäuser, M. Richter, R. Bratschitsch, A. Knorr, E. Malic, Dark and bright exciton formation, thermalization, and photoluminescence in monolayer transition metal dichalcogenides. *2D Mater.* **5**, 035017 (2018).
46. A. Raja, M. Selig, G. Berghäuser, J. Yu, H. M. Hill, A. F. Rigosi, L. E. Brus, A. Knorr, T. F. Heinz, E. Malic, A. Chernikov, Enhancement of exciton-phonon scattering from monolayer to bilayer WS<sub>2</sub>. *Nano Lett.* **18**, 6135–6143 (2018).
47. J. Lindlau, M. Selig, A. Neumann, L. Colombier, J. Förste, V. Funk, M. Förg, J. Kim, G. Berghäuser, T. Taniguchi, K. Watanabe, F. Wang, E. Malic, A. Högele, The role of momentum-dark excitons in the elementary optical response of bilayer WSe<sub>2</sub>. *Nat. Commun.* **9**, 2586 (2018).
48. D. Sun, Y. Rao, G. A. Reider, G. Chen, Y. You, L. Brézin, A. R. Harutyunyan, T. F. Heinz, Observation of rapid exciton-exciton annihilation in monolayer molybdenum disulfide. *Nano Lett.* **14**, 5625–5629 (2014).
49. D. Erkensten, S. Brem, K. Wagner, R. Gillen, R. Perea-Causín, J. D. Ziegler, T. Taniguchi, K. Watanabe, J. Maultzsch, A. Chernikov, E. Malic, Dark exciton-exciton annihilation in monolayer WSe<sub>2</sub>. *Phys. Rev. B* **104**, L241406 (2021).

50. A. Damascelli, Z. Hussain, Z.-X. Shen, Angle-resolved photoemission studies of the cuprate superconductors. *Rev. Mod. Phys.* **75**, 473–541 (2003).
51. M. Bauer, A. Marienfeld, M. Aeschlimann, Hot electron lifetimes in metals probed by time-resolved two-photon photoemission, *Prog. Surf. Sci.* **90**, 319–376 (2015).
52. S. Mathias, S. Eich, J. Urbancic, S. Michael, A. V. Carr, S. Emmerich, A. Stange, T. Popmintchev, T. Rohwer, M. Wiesenmayer, A. Ruffing, S. Jakobs, S. Hellmann, P. Matyba, C. Chen, L. Kipp, M. Bauer, H. C. Kapteyn, H. C. Schneider, K. Rossnagel, M. M. Murnane, M. Aeschlimann, Self-amplified photo-induced gap quenching in a correlated electron material. *Nat. Commun.* **7**, 12902 (2016).
53. A. Chernikov, C. Ruppert, H. M. Hill, A. F. Rigosi, T. F. Heinz, Population inversion and giant bandgap renormalization in atomically thin WS<sub>2</sub> layers. *Nat. Photonics* **9**, 466–470 (2015).
54. F. Liu, M. E. Ziffer, K. R. Hansen, J. Wang, X. Zhu, Direct determination of band-gap renormalization in the photoexcited monolayer MoS<sub>2</sub>. *Phys. Rev. Lett.* **122**, 246803 (2019).
55. M. Weinelt, M. Kutschera, T. Fauster, M. Rohlffing, Dynamics of exciton formation at the Si(100) c(4 x 2) surface. *Phys. Rev. Lett.* **92**, 126801 (2004).
56. O. Karni, E. Barré, S. C. Lau, R. Gillen, E. Y. Ma, B. Kim, K. Watanabe, T. Taniguchi, J. Maultzsch, K. Barmak, R. H. Page, T. F. Heinz, Infrared interlayer exciton emission in MoS–2/WSe<sub>2</sub> heterostructures. *Phys. Rev. Lett.* **123**, 247402 (2019).
57. J. Kunstmann, F. Mooshammer, P. Nagler, A. Chaves, F. Stein, N. Paradiso, G. Plechinger, C. Strunk, C. Schüller, G. Seifert, D. R. Reichman, T. Korn, Momentum-space indirect interlayer excitons in transition-metal dichalcogenide van der Waals heterostructures. *Nat. Phys.* **14**, 801–805 (2018).
58. K. Medjanik, O. Fedchenko, S. Chernov, D. Kutnyakhov, M. Ellguth, A. Oelsner, B. Schönhense, T. R. F. Peixoto, P. Lutz, C.-H. Min, F. Reinert, S. Däster, Y. Acremann, J. Viefhaus, W. Wurth, H.

- J. Elmers, G. Schönhense, Direct 3D mapping of the Fermi surface and Fermi velocity. *Nat. Mater.* **16**, 615–621 (2017).
59. B. Krömker, M. Escher, D. Funnemann, D. Hartung, H. Engelhard, J. Kirschner, Development of a momentum microscope for time resolved band structure imaging. *Rev. Sci. Instrum.* **79**, 053702–7 (2008).
60. M. Düvel, M. Merboldt, J. P. Bange, H. Strauch, M. Stellbrink, K. Pierz, H. W. Schumacher, D. Momeni, D. Steil, G. S. M. Jansen, S. Steil, D. Novko, S. Mathias, M. Reutzel, Far-from-equilibrium electron-phonon interactions in optically excited graphene. *Nano Lett.* **22**, 4897–4904 (2022).
61. G. Saathoff, L. Miaja-Avila, M. Aeschlimann, M. M. Murnane, H. C. Kapteyn, Laser-assisted photoemission from surfaces, *Phys. Rev. A* **77**, 022903 (2008).
62. T. Taniguchi, K. Watanabe, Synthesis of high-purity boron nitride single crystals under high pressure by using Ba-BN solvent. *J. Cryst. Growth* **303**, 525–529 (2007).
63. G. Schönhense, D. Kutnyakhov, F. Pressacco, M. Heber, N. Wind, S. Y. Agustsson, S. Babenkov, D. Vasilyev, O. Fedchenko, S. Chernov, L. Rettig, B. Schönhense, L. Wenthaus, G. Brenner, S. Dziarzhyski, S. Palutke, S. K. Mahatha, N. Schirmel, H. Redlin, B. Manschwetus, I. Hartl, Y. Matveyev, A. Gloskovskii, C. Schlueter, V. Shokeen, H. Duerr, T. K. Allison, M. Beye, K. Rosnagel, H. J. Elmers, K. Medjanik, Suppression of the vacuum space-charge effect in fs-photoemission by a retarding electrostatic front lens. *Rev. Sci. Instrum.* **92**, 053703 (2021).
64. S. Brem, K.-Q. Lin, R. Gillen, J. M. Bauer, J. Maultzsch, J. M. Lupton, E. Malic, Hybridized intervalley moiré excitons and flat bands in twisted WSe<sub>2</sub> bilayers. *Nanoscale* **12**, 11088–11094 (2020).
65. J. Hagel, S. Brem, C. Linderälv, P. Erhart, E. Malic, Exciton landscape in van der Waals heterostructures. *Phys. Rev. Res.* **3**, 043217 (2021).
66. S. Brem, M. Selig, G. Berghaeuser, E. Malic, Exciton relaxation cascade in two-dimensional transition metal dichalcogenides. *Sci. Rep.* **8**, 8238 (2018).

67. M. Kira, S. W. Koch, Many-body correlations and excitonic effects in semiconductor spectroscopy. *Prog. Quantum Electron.* **30**, 155–296 (2006).
68. H. Haug, S. W. Koch, *Quantum Theory of the Optical and Electronic Properties of Semiconductors* (World Scientific Publishing Company, 2009).
69. E. Malic, A. Knorr, *Graphene and Carbon Nanotubes: Ultrafast Optics and Relaxation Dynamics* (John Wiley & Sons, 2013).
70. S. Brem, C. Linderälv, P. Erhart, E. Malic, Tunable phases of moiré excitons in van der Waals heterostructures. *Nano Lett.* **20**, 8534–8540 (2020).



---

Paper 4

---

# Hybrid Exciton Signatures in ARPES Spectra of van der Waals Materials

Giuseppe Meneghini,\* Marcel Reutzler, Stefan Mathias, Samuel Brem, and Ermin Malic

Cite This: *ACS Photonics* 2023, 10, 3570–3575

Read Online

ACCESS |



Metrics &amp; More



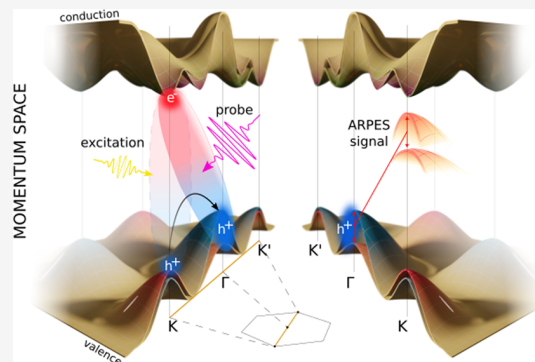
Article Recommendations



Supporting Information

**ABSTRACT:** Van der Waals heterostructures show fascinating physics including trapped moire exciton states, anomalous moire exciton transport, generalized Wigner crystals, etc. Bilayers of transition metal dichalcogenides (TMDs) are characterized by long-lived, spatially separated interlayer excitons. Provided strong interlayer tunneling, hybrid exciton states consisting of interlayer and intralayer excitons can be formed. Here, electrons and holes are in a superposition of both layers. Although crucial for optics, dynamics, and transport, hybrid excitons are usually optically inactive and have therefore not yet been directly observed yet. Based on microscopic and material-specific theory, we show that time- and angle-resolved photoemission spectroscopy (tr-ARPES) is a direct technique to visualize these hybrid excitons. Concretely, we predict a characteristic double-peak ARPES signal arising from the hybridized hole in the MoS<sub>2</sub> homobilayer. The relative intensity is proportional to the quantum mixture of the two hybrid valence bands at the  $\Gamma$  point. Due to the strong hybridization, a peak separation of more than 0.5 eV can be resolved in ARPES experiments. Our study provides a concrete recipe for how to directly visualize hybrid excitons and how to distinguish them from the usually observed regular excitonic signatures.

**KEYWORDS:** hybrid excitons, exciton dynamics, ARPES, TMD heterostructures



## INTRODUCTION

The research on atomically thin nanomaterials has become one of the most active fields in condensed matter physics, showing fascinating phenomena ranging from moire exciton effects to exotic strongly correlated states. Here, the material class of transition metal dichalcogenides (TMDs) has been the focus of many investigations due to their unprecedented properties. TMD monolayers are characterized by tightly bound excitons that govern optics, dynamics, and transport phenomena at room temperature.<sup>1–4</sup> Artificially stacked TMD bilayers exhibit long-lived spatially separated interlayer excitons, where the Coulomb-bound electrons and holes are located in different layers. Furthermore, due to a large tunneling probability (in particular in TMD homobilayers), hybrid excitons (hX) appear, in which Coulomb-bound electrons and/or holes are strongly delocalized over the two layers; cf. Figure 1a. These new quasi-particles can be considered as a quantum superposition of the involved electron and hole states in both layers.

The importance of interlayer excitonic states has been demonstrated in a series of experiments.<sup>5–14</sup> They exhibit a long lifetime and a large dipole moment and thus offer a possibility of controlling exciton optics and transport by external electric fields.<sup>15–18</sup> In contrast, hybrid excitons have been less intensively studied, although they combine a high oscillator strength (intralayer excitons) with a sensitivity to

electric fields (interlayer excitons) enabling tunability of their properties. It is meanwhile well-known that hX are important in particular in TMD homobilayers,<sup>19,20</sup> however, they have not been directly observed, yet. Recently, time- and angle-resolved photoemission spectroscopy (tr-ARPES) has been demonstrated as a powerful technique to directly visualize momentum-dark exciton states in TMD monolayers as well as interlayer exciton dynamics in TMD heterostructures.<sup>21–25</sup> Here, we show that this technique can be further exploited to even map out the wave function of hybrid exciton states. Based on a fully microscopic and material-specific approach, we model the tr-ARPES signal in TMD bilayers. We focus on the exemplary material system of a MoS<sub>2</sub> homobilayer in H<sub>h</sub> stacking exhibiting a large hybridization of excitons.<sup>20</sup> We predict the emergence of a characteristic double-peak ARPES signal reflecting the strongly hybridized hole at the  $\Gamma$  point that is left behind after the ejection of the electron. Here, the relative intensity of the peaks sensitively depends on the degree

Received: May 5, 2023

Published: September 21, 2023



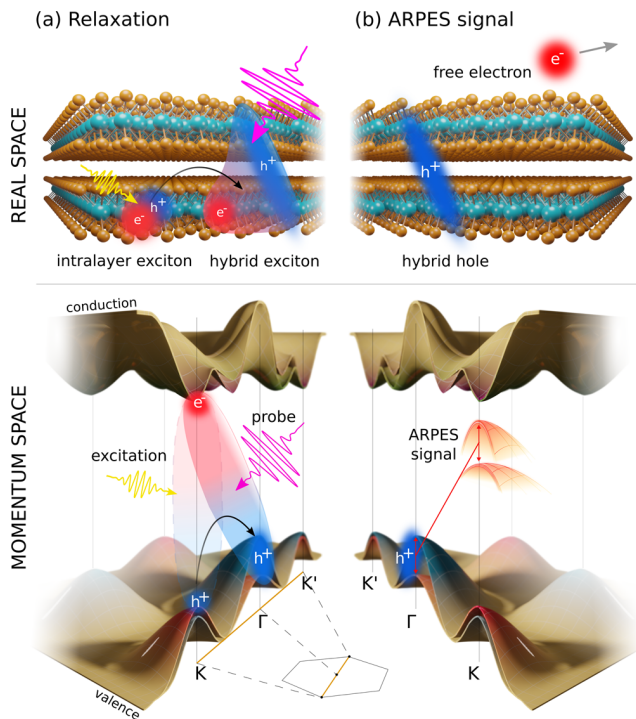


**Figure 1.** ARPES signature of the hybrid excitons. The figure represents the system in real and momentum space (a) during the relaxation and (b) after photon-induced electron ejection via a probe pulse from an excited MoS<sub>2</sub> homobilayer. On the left, after exciting the intralayer bright A exciton in one layer with a first light pulse (yellow arrow), the phonon-induced relaxation (black arrow) brings the population of excitons to the most energetically favorable state, a momentum-dark  $\Gamma$ K hybrid exciton with the hole being strongly delocalized between the layers. The hybrid exciton, via a high energetic probe pulse (in the extreme ultraviolet range, purple arrow), breaks down into an ejected free electron and a superposition of hybrid holes. This gives rise to a characteristic double-peak ARPES signal reflecting the hole superposition between the two hybrid valence bands at the  $\Gamma$  point. The signal appears at the K point and exhibits the negative curvature of the  $\Gamma$  valence bands.

of hole hybridization. This is in strong contrast to the single excitonic signal observed so far in the ARPES experiments. The developed method has been applied to the exemplary TMD homobilayer, but it is of general nature and thus can be applied to a wide range of exciton-dominated material systems.

## RESULTS

**ARPES Signal of Excitons.** To microscopically model the hX dynamics, we first start by defining the electronic Hamiltonian operator for a TMD bilayer, including tunneling between the two layers. The required material-specific input parameters are obtained from first-principle calculations.<sup>26,27</sup> Then, we transform the Hamiltonian first into an exciton and then into a hybrid exciton basis. This allows us to determine the hybrid exciton band structure and calculate the optical selection rules by solving the Wannier equation for a bilayer system.<sup>19,20,28,29</sup> Furthermore, we obtain microscopic access to the hybrid exciton relaxation dynamics via exciton–phonon scattering, where we describe the thermalization process after optical excitation via the Boltzmann scattering equation.<sup>30</sup> These are the key ingredients for a material-specific model for the ARPES experiments. Here, it is crucial to define the initial and final states, as illustrated in Figure 1. First, the TMD bilayer is

optically excited by using a laser pulse. The subsequent relaxation into the energetically most favorable state creates a population of hybrid excitons (Figure 1a). In the second step, the system is illuminated with a second laser pulse that breaks the Coulomb-bound electron–hole pairs into ejected electrons and remaining holes (Figure 1b). The single particle nature of the final state can be effectively portrayed in an electron–hole picture, where the hybridization of the electronic bands causes a huge splitting of the valence band in correspondence to the  $\Gamma$  valley (Figure 1). In an ARPES measurement, the ejected electron is collected in a detector, leaving behind the hole in the material. The latter, in the case of hybrid excitons, will remain in a superposition of the two valence band states that were involved in the photodissociated exciton (cf. the split valence bands at the  $\Gamma$  point in Figure 1b). The ARPES signal allows to reconstruct the exciton energy from the electron information measured, since the Coulomb-bound electrons and holes present a strongly correlated system.

The photoemission probability can be described using a time-dependent perturbation theory yielding Fermi's golden rule<sup>31</sup> for the ARPES signal

$$I(\mathbf{k}, h\nu; t) \propto \sum_{if} |\langle f, \mathbf{k} | H_{\text{int}} | i \rangle|^2 N_i(t) \delta(\Delta E_{f,i,\mathbf{k}}) \quad (1)$$

where  $\Delta E_{f,i,\mathbf{k}} = \hbar^2 k^2 / (2m_0) + E_f - E_i - h\nu$  with the free-electron momentum  $\mathbf{k}$  and the photon energy  $h\nu$ . Furthermore,  $|i\rangle, |f\rangle$  are the initial/final states of the system with eigenenergies  $E_{i/f}$  and the initial state occupation  $N_i(t)$ . The interaction Hamiltonian  $H_{\text{int}} = \sum_{\alpha\beta} \mathcal{M}_{\alpha\beta} a_{i\alpha}^\dagger a_{c\beta}$  describes the excitation of an electron from the conduction band to the free state, with  $a^{(\dagger)}$  denoting the electronic creation/annihilation operator. Note that we use the suffix  $f$  for a free state and  $c/v$  for a conduction–valence band state. The optical selection rules are contained in the optical-matrix element  $\mathcal{M}_{\alpha\beta}$ .

Since the interaction Hamiltonian is defined in terms of single-particle operators, it is important to also determine the initial and final states,  $|i\rangle, |f\rangle$ , entering this equation on a single-particle basis. To reach this, we perform a series of transformations to express the hybrid exciton states with electron operators, as detailed in the Supporting Information (SI). The final state is described by an uncorrelated product of a free electron state and a hybrid hole state, which we derive by solving the eigenvalue problem for the electronic Hamiltonian of a bilayer system, obtaining hybridized valence and conduction bands  $E_{\mathbf{k}\gamma}^{\pm}$ , with  $\gamma = (\pm, \xi_\lambda)$  being the compound index consisting of the quantum number for the split layer-hybridized bands ( $\pm$ ), the valley index  $\xi = \Gamma, \Lambda^{(\prime)}, K^{(\prime)}$ , and the band index  $\lambda = c, v$ . We denote the splitting of the hybrid conduction or valence bands with  $\Delta E_{\mathbf{k}}^{\pm} = E_{\mathbf{k}+}^{\pm} - E_{\mathbf{k}-}^{\pm}$ , i.e., in particular, the hybrid valence band splitting at the K and  $\Gamma$  point relevant for this work read  $\Delta E_{\mathbf{k}}^v$  and  $\Delta E_{\mathbf{k}}^c$ , respectively.

Inserting the initial and final state discussed above (and explicitly shown in the SI) in eq 1, we obtain the final equation for the ARPES signal of hybrid excitonic states

$$I(\mathbf{k}, h\nu; t) \propto \sum_{\eta\mathbf{Q}} |\mathcal{G}_{\mathbf{pk}}^{\eta\mathbf{Q}}|^2 N_{\mathbf{k}-\mathbf{p}}^{\eta} (t) \delta(\Delta E_{\gamma,\mathbf{p},\mathbf{k}}^{\eta}) \quad (2)$$

where  $\Delta E_{\gamma,\mathbf{p},\mathbf{k}}^{\eta} = E_{\mathbf{k}}^{\eta} - E_{\mathbf{p}}^{\eta} - E_{\mathbf{k}-\mathbf{p}}^{\eta} - h\nu$ . The ARPES signal is significantly influenced by the hybrid exciton occupation  $N_{\mathbf{Q}}^{\eta}(t)$  in the hX state  $\eta$  at center-of-mass momentum  $\mathbf{Q}$ . The dynamic occupation is determined microscopically by solving a semiconductor Bloch equation in the second-order Born–

Markov approximation and explicitly including all phonon-mediated scattering channels within the hybrid exciton landscape,<sup>30</sup> cf. SI for more details. Moreover, the energy conservation during the photoemission is of key importance, with  $E_k^c$  denoting the free-electron energy,  $E_{pv}^v$  the hybrid valence band energy, and  $E_{k-p}^{Xp}$  the hybrid exciton energy. The new optical-matrix element  $\mathcal{G}_{pk}^{Xp}$  depends on the excitonic wave function and on the overlap between the layer-mixed hybrid hole and hybrid exciton. A detailed derivation is shown in the SI.

**Hybrid Exciton Dynamics.** We exploit the theoretical framework described above to study the exemplary MoS<sub>2</sub> homobilayer, h-BN encapsulated and at room temperature, in naturally available H<sub>h</sub> stacking. This material is ideal for our study for two reasons: (i) The most energetically favorable states are momentum-dark  $\Gamma_{\text{hyb}}K_1^{(\prime)}$  hybrid excitons. Due to a lack of lower-lying states and their momentum/layer indirect character, they exhibit long lifetimes facilitating their observation in ARPES spectra. (ii) The strong interlayer tunneling results in a large splitting of the valence bands at the  $\Gamma$  point. As a result, the hole in  $\Gamma_{\text{hyb}}K$  excitons is delocalized over a large spectral range and we expect to find pronounced hybrid hole signatures in ARPES spectra.

We start with discussing the relaxation dynamics of hybrid excitons, as the temporal evolution of the exciton occupation is of crucial importance for ARPES spectra, cf. eq 2. Solving the Wannier equation for a bilayer system allowed us to resolve the hybrid exciton landscape. We show the relevant states contributing in the relaxation process in the inset of Figure 2. For studying the dynamics, we start with an initial exciton

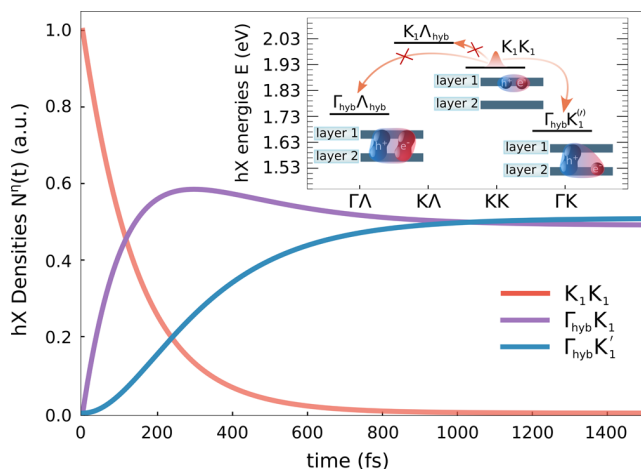


**Figure 2.** Hybrid exciton dynamics. After optical excitation of a MoS<sub>2</sub> homobilayer at  $\approx 1.9$  eV (resonant to the  $K_1K_1$  exciton), ultrafast exciton relaxation dynamics occurs resulting in the highest occupation  $N^h$  of the energetically most favorable momentum-dark  $\Gamma K^{(\prime)}$  hybrid exciton (red and purple lines). The inset shows the hybrid exciton dispersion illustrating possible relaxation channels (note that  $\Gamma_{\text{hyb}}K_1^{(\prime)}$  states are almost degenerate in energy).

population in layer 1 centered around the energy of  $\approx 1.9$  eV, modeling a typical experimental optical excitation resonant to the intralayer  $K_1K_1$  exciton. We solve the equation of motion for the hybrid exciton occupation, including all phonon-mediated scattering channels in the low-density regime. This allows us to track the method of initially excited hybrid excitons in momentum and time. Figure 2 illustrates the

relaxation dynamics of momentum-integrated hybrid exciton densities  $N^h(t)$ . We observe an ultrafast population transfer from the initially occupied  $K_1K_1$  exciton (red line), that is almost completely intralayer-like, to the most energetically favorable momentum-dark hybrid exciton states  $\Gamma_{\text{hyb}}K_1^{(\prime)}$  (purple and blue lines). This is followed by a thermalization process, in which the charge is redistributed between the two almost degenerate  $\Gamma_{\text{hyb}}K_1^{(\prime)}$  states. The different dynamics of the almost degenerate  $\Gamma_{\text{hyb}}K_1^{(\prime)}$  is explained by considering that the bright  $K_1K_1$  population relaxes via phonon emission to the  $\Gamma_{\text{hyb}}K$  state. Note that to observe a phonon-mediated transition from  $K_1K_1$  to  $\Gamma_{\text{hyb}}K_1^{(\prime)}$ , simultaneous scattering of electron and hole must occur, which is a higher-order process and thus very inefficient. For this reason, only after the  $\Gamma K$  state is populated, the thermalization with  $\Gamma K'$  state can take place.

The  $K\Lambda_{\text{hyb}}$  states are not involved in the relaxation process, since they are located above the excitation energy, cf. the inset of Figure 2. Furthermore, the  $\Gamma_{\text{hyb}}\Lambda_{\text{hyb}}$  exciton could, in principle, be important for the dynamics considering its low energy, however, this can be neglected for two main reasons. (i) The direct scattering would require a simultaneous scattering of both electron and hole from the  $K_1K_1$  state. This two-phonon process is thus of higher-order and can be neglected. (ii) The indirect scattering involving one-phonon processes,  $K_1K_1 \rightarrow K\Lambda_{\text{hyb}} \rightarrow \Gamma_{\text{hyb}}\Lambda_{\text{hyb}}$  and  $K_1K_1 \rightarrow \Gamma_{\text{hyb}}K_1^{(\prime)} \rightarrow \Gamma_{\text{hyb}}\Lambda_{\text{hyb}}$  involve phonon absorption processes and will therefore have a negligible role in the relaxation dynamics.

**Hybrid Exciton Signatures in ARPES.** Having determined the hybrid exciton occupation, we can now evaluate eq 2 to investigate the time- and momentum-resolved ARPES signals in MoS<sub>2</sub> homobilayers. In recent studies it has been shown that the excitonic ARPES signal appears at the momentum corresponding to the electron valley, and it is spectrally located one excitonic energy above the valence band (or one exciton binding energy below the conduction band).<sup>21,24,32</sup> The shape of the signal is expected to be characterized by the negative curvature of the valence band (where the hole left behind is located), if the exciton population is very sharp in momentum.<sup>23,33</sup> Note, however, that for a thermally distributed exciton occupation the ARPES signal will be smeared out in energy and momentum. Figure 3 shows the momentum-resolved ARPES map for different time snapshots, where we have fixed the highest valence hybrid band at the K point ( $E_k^v$ ) as a reference energy determining the position of ARPES signals, cf. also Figure S2 in the SI. At the center of the optical excitation pulse (0 fs), we observe an ARPES signal reflecting the nature of the almost purely intralayer  $K_1K_1$  exciton which is characterized by a well pronounced single peak (Figure 3a). We find that the sub-100 fs formation of strongly hybridized  $\Gamma_{\text{hyb}}K_1^{(\prime)}$  excitons corresponds to a delayed appearance of the ARPES signal arising from these states. This can be traced back to the ARPES intensity being dependent not only on the exciton occupation, but also on the exciton wave function and hole hybridization coefficients. They are characterized by two peaks, one slightly above the  $K_1K_1$  exciton and one red-shifted by more than 600 meV (Figure 3b). The last step of the dynamics leads to thermalization of the hX occupation. After 400 fs, the entire population has reached an equilibrium distribution (Figure 3c), where only the signatures stemming from  $\Gamma_{\text{hyb}}K_1^{(\prime)}$  excitons have remained.

Regarding the shape of the ARPES signals, we find that a narrow distribution in momentum leads to a negative

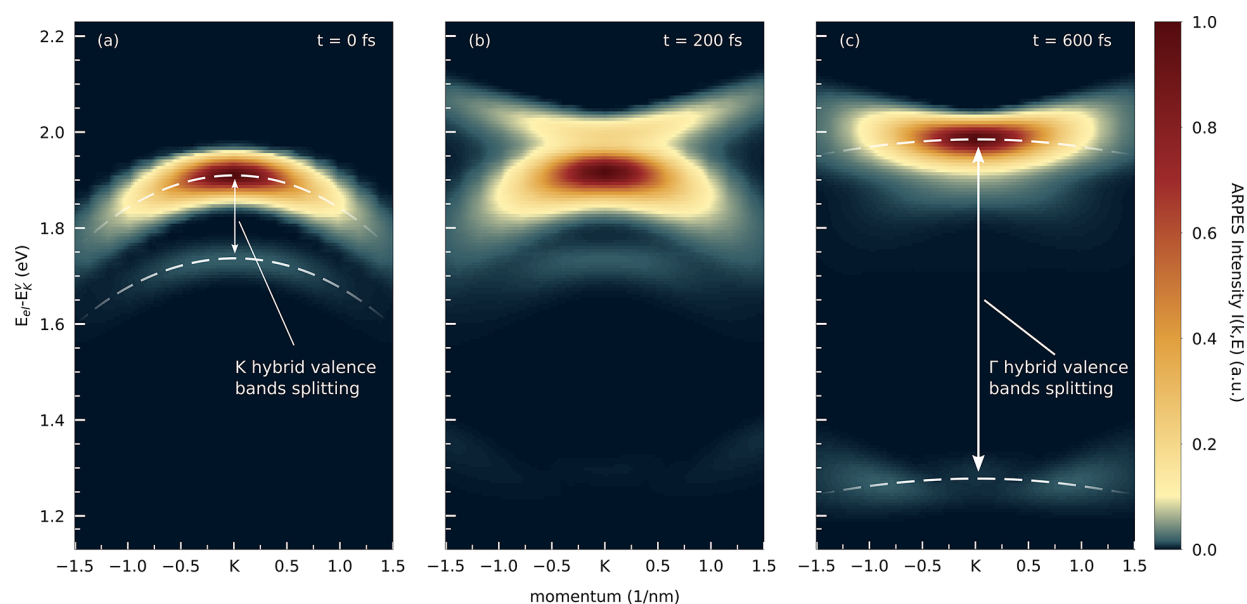


**Figure 3.** Momentum-resolved ARPES map. Hybrid exciton dynamics tracked in a tr-ARPES signal (a) revealing the excitation of the nearly purely intralayer  $K_1K_1$  exciton state (0 fs), (b) the formation of the strongly hybridized  $\Gamma_{\text{hyb}}K_1$  state (200 fs), and (c) the thermalized hybrid exciton distribution (600 fs). The dashed lines show the shifted split valence bands of the hybrid hole at the K point (with the splitting  $\Delta E_K^v$ ) and at the  $\Gamma$  point (with the splitting  $\Delta E_\Gamma^v$ ). The energies are shown with respect to the upper hybrid valence band ( $E_K^v$ ) at the K point (cf. also Figure S2 in the SI).

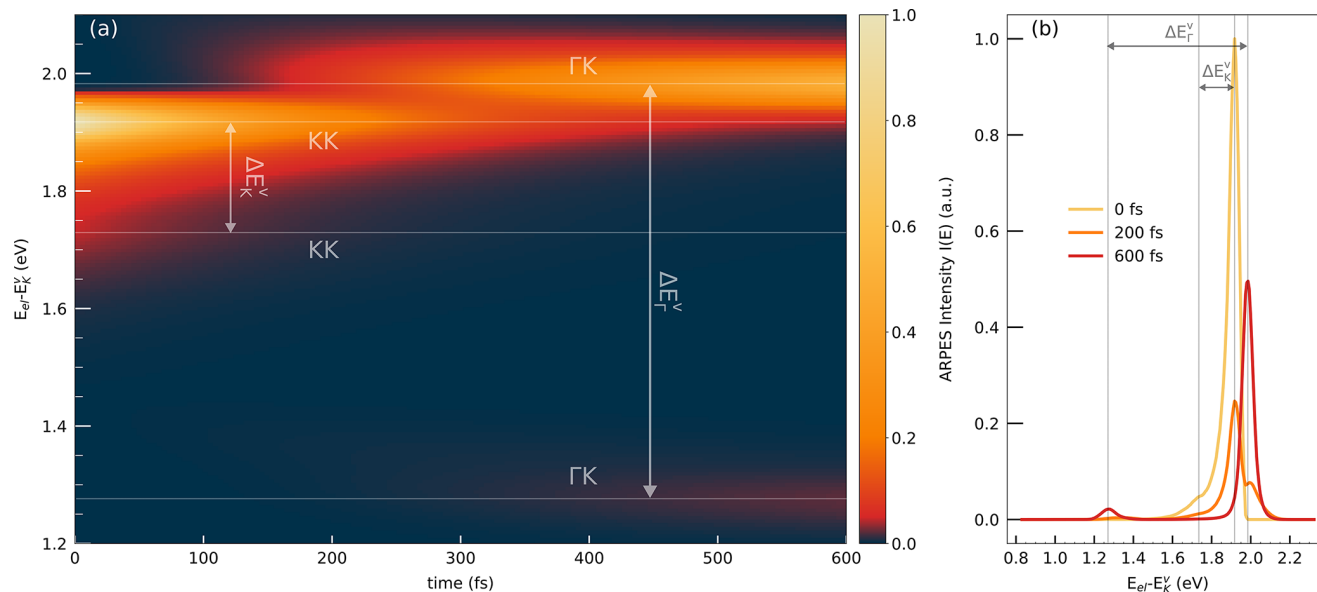


**Figure 4.** Momentum-integrated ARPES map. (a) Energy- and time-resolved ARPES signal, showing the characteristic double-peak structure reflecting the hybrid hole being spread over two valence bands at the K point (initial signal) and at the  $\Gamma$  point (final thermalized signal). (b) ARPES signal at fixed times plotted as a function of energy. The energies are shown with respect to the upper hybrid valence band ( $E_K^v$ ) at the K point as reference.

dispersion, reflecting the curvature of the valence band. This can be observed for the initial occupation of intralayer  $K_1K_1$  excitons in layer 1 (Figure 3a). The phonon-driven exciton relaxation dynamics and the subsequent thermalization bring the system into a thermal equilibrium. At room temperature, this results in a broad exciton distribution over the center-of-mass momentum. For this reason, the shape of the final ARPES signal is reflecting a mixture of the hybrid valence bands (curved downward) and the hybrid exciton parabola (curved upward), cf. Figure 3c). A more detailed discussion on

how the center-of-mass distribution affects the shape of the signal can be found in the SI.

The most important message of our work is the prediction of a double-peak ARPES signal that is characteristic of hybrid exciton states. For the considered  $\text{MoS}_2$  homobilayer, the ARPES signal is governed by the energetically lowest  $\Gamma_{\text{hyb}}K_1$  hybrid exciton. Figure 3c clearly exhibits two peaks that are separated by approximately 0.6 eV. Their position corresponds to the energy of the split hybrid valence bands (illustrated by dashed lines). To explain this observation, we consider the spatial (layer) distribution of the single-particle states

contributing to the entangled electron–hole pair. The two valence bands ( $| \pm \rangle$ ) at  $\Gamma$  are completely delocalized across both layers, i.e.,  $| \pm \rangle = (| 1 \rangle \pm | 2 \rangle) / \sqrt{2}$ , where  $| n \rangle$  indicates the valence band of the pure monolayer  $n$ . Now, the hybrid exciton is formed with an electron that is strongly localized in one of the two layers (at the K point), e.g., layer 1. The Coulomb interaction partially drags the hole into the same layer to reduce the energy, favoring a hole wave function that is mostly in layer 1, too, i.e.  $| 1 \rangle = (| + \rangle + | - \rangle) / \sqrt{2}$ . Consequently, the energetically most favorable two-body state (hX) is built by a superposition of the two hybrid valence bands  $| \pm \rangle$ .

When the  $K_1$  electron from the  $\Gamma_{\text{hyb}}K_1$  hybrid exciton is ejected, a  $\Gamma$  hole is left behind, remaining in the superposition that previously formed the exciton. The conservation of energy and momentum ensures that measuring the energy of the ejected electron, we obtain information about the energy of the hole as well. While the hole within the hybrid exciton is in a quantum mixture of two energy levels, the relative energy between the electron and hole is fixed by the two-particle exciton energy  $E^{\text{X}}$ . This entanglement between electron and hole transfers the superposition of hole energies to the correlated electron, whose energy is consequently undefined as well. Measuring the energy of ejected (initially entangled) electrons therefore allows us to reconstruct the underlying energy distribution of the holes.

To resolve this better, Figure 4 shows the momentum-integrated ARPES signal. At first glance, we observe that the  $\Gamma_{\text{hyb}}K_1$  hybrid exciton has a long lifetime. The ARPES signal remains over picoseconds, since this exciton is the energetically lowest state without any scattering partners at lower energies (cf. the inset of Figure 2). We find that a clear transfer from the initially excited  $K_1K_1$  excitons to the momentum-dark  $\Gamma_{\text{hyb}}K_1$  hybrid excitons occurs on a sub-100 fs time scale. In this time, a double-peaked ARPES signal is formed that is characteristic for a hybrid exciton state and that reflects the splitting  $\Delta E_{\text{K}}^{\text{V}}$  of the hybrid valence bands at the  $\Gamma$  point. Since the single particle states at the K point are strongly layer-polarized, we do not expect to see a well pronounced double-peak ARPES signal for  $K_1K_1$  excitons. However, even this state is weakly hybridized and has a small contribution of an interlayer exciton due to a weak tunneling of holes at the K point. This gives rise to a second signal with low-intensity that is red-shifted by about 200 meV reflecting the splitting of the hybrid valence bands  $\Delta E_{\text{K}}^{\text{V}}$  at the K point, cf. Figure 4b. Note that the ratio of the measured intensity of the double peak signal can be exploited to directly estimate the hole layer polarization (see SI for a detailed discussion).

In summary, our work demonstrates how hybrid excitons can be identified in the tr-ARPES spectra. The investigated  $\text{MoS}_2$  homobilayer is an exemplary case and the developed approach can be applied to a much larger class of exciton-dominated materials.

## CONCLUSION

Based on a microscopic and material-specific theory, we predict pronounced signatures of hybrid excitons in tr-ARPES spectra. We investigate the exemplary case of a  $\text{MoS}_2$  homobilayer in the naturally available  $H_i^h$  stacking and find a characteristic double-peak ARPES signal arising from the split hybrid valence bands at the  $\Gamma$  point where the left-behind hole is located. This double-peaked signal can be considered as a clear fingerprint for the existence of hybrid exciton states, and

should be experimentally accessible with the current experimental limits for the energy resolution ( $\approx 200$  meV).<sup>21</sup> In particular, materials with an efficient interlayer tunneling resulting in a large spectral splitting of the hybrid valence bands are favorable, as the double-peak signal is then easy to resolve in the experiment. Furthermore, the presence of energetically lowest dark hybrid exciton states is of advantage, as they exhibit a long lifetime facilitating the experimental observation. Although the choice of  $\text{MoS}_2$  homobilayer is favorable for these reasons, the hybridization of the hole (50%/50%) is similar to the exciton hybridization giving rise to the predicted relatively small double-peak intensity ratio. Heterostructures exhibiting a considerably different degree of hybridization for holes and excitons should give rise to larger intensity ratios that are more easily accessible in ARPES experiments. Overall, our work provides a concrete recipe for how to directly visualize hybrid exciton states in ARPES measurements and will trigger new experimental studies in atomically thin semiconductors and related materials.

## ASSOCIATED CONTENT

### Supporting Information

The Supporting Information is available free of charge at <https://pubs.acs.org/doi/10.1021/acsp Photonics.3c00599>.

Details on the derivation of the main equations and additional discussion on the thermal equilibrated hybrid exciton distribution (PDF)

## AUTHOR INFORMATION

### Corresponding Author

Giuseppe Meneghini – Department of Physics, Philipps University of Marburg, 35037 Marburg, Germany; [orcid.org/0000-0002-1889-2380](https://orcid.org/0000-0002-1889-2380); Email: [giuseppe.meneghini@physik.uni-marburg.de](mailto:giuseppe.meneghini@physik.uni-marburg.de)

### Authors

Marcel Reutz – I Physikalisches Institut, Georg-August-Universität Göttingen, 37073 Göttingen, Germany; [orcid.org/0000-0002-1085-2931](https://orcid.org/0000-0002-1085-2931)

Stefan Mathias – I Physikalisches Institut, Georg-August-Universität Göttingen, 37073 Göttingen, Germany; [orcid.org/0000-0002-1255-521X](https://orcid.org/0000-0002-1255-521X)

Samuel Brem – Department of Physics, Philipps University of Marburg, 35037 Marburg, Germany; [orcid.org/0000-0001-8823-1302](https://orcid.org/0000-0001-8823-1302)

Ermin Malic – Department of Physics, Philipps University of Marburg, 35037 Marburg, Germany

Complete contact information is available at: <https://pubs.acs.org/doi/10.1021/acsp Photonics.3c00599>

### Funding

This project has received funding from Deutsche Forschungsgemeinschaft via CRC 1083 and the Project 512604469 as well as from the European Unions Horizon 2020 research and innovation program under Grant Agreement No. 881603 (Graphene Flagship).

### Notes

The authors declare no competing financial interest.

## REFERENCES

- (1) He, K.; Kumar, N.; Zhao, L.; Wang, Z.; Mak, K. F.; Zhao, H.; Shan, J. Tightly bound excitons in monolayer  $\text{WSe}_2$ . *Phys. Rev. Lett.* **2014**, *113*, 026803.
- (2) Chernikov, A.; Berkelbach, T. C.; Hill, H. M.; Rigosi, A.; Li, Y.; Aslan, B.; Reichman, D. R.; Hybertsen, M. S.; Heinz, T. F. Exciton binding energy and nonhydrogenic rydberg series in monolayer  $\text{WS}_2$ . *Phys. Rev. Lett.* **2014**, *113*, 076802.
- (3) Wang, G.; Chernikov, A.; Glazov, M. M.; Heinz, T. F.; Marie, X.; Amand, T.; Urbaszek, B. Colloquium: Excitons in atomically thin transition metal dichalcogenides. *Rev. Mod. Phys.* **2018**, *90*, 021001.
- (4) Mueller, T.; Malic, E. Exciton physics and device application of two-dimensional transition metal dichalcogenide semiconductors. *npj 2D Materials and Applications* **2018**, *2*, 1–12.
- (5) Rivera, P.; Schaibley, J. R.; Jones, A. M.; Ross, J. S.; Wu, S.; Aivazian, G.; Klement, P.; Seyler, K.; Clark, G.; Ghimire, N. J.; Yan, J.; Mandrus, D. G.; Yao, W.; Xu, X. Observation of long-lived interlayer excitons in monolayer  $\text{MoSe}_2$ - $\text{WSe}_2$  heterostructures. *Nat. Commun.* **2015**, *6*, 1–6.
- (6) Miller, B.; Steinhoff, A.; Pano, B.; Klein, J.; Jahnke, F.; Holleitner, A.; Wurstbauer, U. Long-lived direct and indirect interlayer excitons in van der waals heterostructures. *Nano Lett.* **2017**, *17*, S229–S237.
- (7) Kunstmann, J.; Mooshammer, F.; Nagler, P.; Chaves, A.; Stein, F.; Paradiso, N.; Plechinger, G.; Strunk, C.; Schuller, C.; Seifert, G.; Reichman, D. R.; Korn, T. Momentum-space indirect interlayer excitons in transition-metal dichalcogenide van der waals heterostructures. *Nat. Phys.* **2018**, *14*, 801–805.
- (8) Jin, C.; Regan, E. C.; Yan, A.; Iqbal Bakti Utama, M.; Wang, D.; Zhao, S.; Qin, Y.; Yang, S.; Zheng, Z.; Shi, S.; Watanabe, K.; Taniguchi, T.; Tongay, S.; Zettl, A.; Wang, F. Observation of moiré excitons in  $\text{WSe}_2/\text{WS}_2$  heterostructure superlattices. *Nature* **2019**, *567*, 76–80.
- (9) Tran, K.; Moody, G.; Wu, F.; Lu, X.; Choi, J.; Kim, K.; Rai, A.; Sanchez, D. A.; Quan, J.; Singh, A.; et al. Evidence for moiré excitons in van der waals heterostructures. *Nature* **2019**, *567*, 71–75.
- (10) Seyler, K. L.; Rivera, P.; Yu, H.; Wilson, N. P.; Ray, E. L.; Mandrus, D. G.; Yan, J.; Yao, W.; Xu, X. Signatures of moiré-trapped valley excitons in  $\text{MoSe}_2/\text{WSe}_2$  heterobilayers. *Nature* **2019**, *567*, 66–70.
- (11) Alexeev, E. M.; Ruiz-Tijerina, D. A.; Danovich, M.; Hamer, M. J.; Terry, D. J.; Nayak, P. K.; Ahn, S.; Pak, S.; Lee, J.; Sohn, J. I.; Molas, M. R.; Koperski, M.; Watanabe, K.; Taniguchi, T.; Novoselov, K. S.; Gorbachev, R. V.; Shin, H. S.; Fal'ko, V. I.; Tartakovskii, A. I. Resonantly hybridized excitons in moiré superlattices in van der waals heterostructures. *Nature* **2019**, *567*, 81–86.
- (12) Ruiz-Tijerina, D. A.; Fal'ko, V. I. Fal'ko, "Interlayer hybridization and moiré superlattice minibands for electrons and excitons in heterobilayers of transition-metal dichalcogenides. *Phys. Rev. B* **2019**, *99*, 125424.
- (13) Sigl, L.; Troue, M.; Katzer, M.; Selig, M.; Sigger, F.; Kiemle, J.; Brotons-Gisbert, M.; Watanabe, K.; Taniguchi, T.; Gerardot, B. D.; Knorr, A.; Wurstbauer, U.; Holleitner, A. W. Optical dipole orientation of interlayer excitons in mose 2- wse 2 heterostacks. *Phys. Rev. B* **2022**, *105*, 035417.
- (14) Holler, J.; Selig, M.; Kempf, M.; Zipfel, J.; Nagler, P.; Katzer, M.; Katsch, F.; Ballottin, M. V.; Mitioglu, A. A.; Chernikov, A.; Christianen, P. C. M.; Schuller, C.; Knorr, A.; Korn, T. Interlayer exciton valley polarization dynamics in large magnetic fields. *Phys. Rev. B* **2022**, *105*, 085303.
- (15) Ciarrocchi, A.; Unuchek, D.; Avsar, A.; Watanabe, K.; Taniguchi, T.; Kis, A. Polarization switching and electrical control of interlayer excitons in two-dimensional van der waals heterostructures. *Nat. Photonics* **2019**, *13*, 131–136.
- (16) Sun, Z.; Ciarrocchi, A.; Tagarelli, F.; Gonzalez Marin, J. F.; Watanabe, K.; Taniguchi, T.; Kis, A. Excitonic transport driven by repulsive dipolar interaction in a van der waals heterostructure. *Nat. Photonics* **2022**, *16*, 79–85.
- (17) Hagel, J.; Brem, S.; Malic, E. Electrical tuning of moiré excitons in mose 2 bilayers. *2D Mater.* **2023**, *10*, 014013.
- (18) Deilmann, T.; Thygesen, K. S. Interlayer excitons with large optical amplitudes in layered van der waals materials. *Nano Lett.* **2018**, *18*, 2984.
- (19) Brem, S.; Lin, K.-Q.; Gillen, R.; Bauer, J. M.; Maultzsch, J.; Lupton, J. M.; Malic, E. Hybridized intervalley moiré excitons and flat bands in twisted wse 2 bilayers. *Nanoscale* **2020**, *12*, 11088–11094.
- (20) Hagel, J.; Brem, S.; Linderalv, C.; Erhart, P.; Malic, E. Exciton landscape in van der waals heterostructures. *Physical Review Research* **2021**, *3*, 043217.
- (21) Schmitt, D.; Bange, J. P.; Bennecke, W.; AlMutairi, A.; Meneghini, G.; Watanabe, K.; Taniguchi, T.; Steil, D.; Luke, D. R.; Weitz, R. T.; Steil, S.; Jansen, G. S. M.; Brem, S.; Malic, E.; Hofmann, S.; Reutzel, M.; Mathias, S. Formation of moiré interlayer excitons in space and time. *Nature* **2022**, *608*, 499–503.
- (22) Wallauer, R.; Perea-Causin, R.; Munster, L.; Zajusch, S.; Brem, S.; Gudde, J.; Tanimura, K.; Lin, K.-Q.; Huber, R.; Malic, E.; Hofer, U. Momentum-resolved observation of exciton formation dynamics in monolayer  $\text{ws}_2$ . *Nano Lett.* **2021**, *21*, S867–S873.
- (23) Christiansen, D.; Selig, M.; Malic, E.; Ernstorfer, R.; Knorr, A. Theory of exciton dynamics in time-resolved arpes: Intra- and intervalley scattering in two-dimensional semiconductors. *Phys. Rev. B* **2019**, *100*, 205401.
- (24) Madeo, J.; Man, M. K. L.; Sahoo, C.; Campbell, M.; Pareek, V.; Wong, E. L.; Al-Mahboob, A.; Chan, N. S.; Karmakar, A.; Mariserla, B. M. K.; Li, X.; Heinz, T. F.; Cao, T.; Dani, K. M. Directly visualizing the momentum-forbidden dark excitons and their dynamics in atomically thin semiconductors. *Science* **2020**, *370*, 1199–1204.
- (25) Dong, S.; Puppini, M.; Pincelli, T.; Beaulieu, S.; Christiansen, D.; Hubener, H.; Nicholson, C. W.; Xian, R. P.; Dendzik, M.; Deng, Y.; Windsor, Y. W.; Selig, M.; Malic, E.; Rubio, A.; Knorr, A.; Wolf, M.; Rettig, L.; Ernstorfer, R. Direct measurement of key exciton properties: Energy, dynamics, and spatial distribution of the wave function. *Natural sciences* **2021**, *1*, No. e10010.
- (26) Kormanyos, A.; Burkard, G.; Gmitra, M.; Fabian, J.; Zolyomi, V.; Drummond, N. D.; Fal'ko, V. k-p theory for two-dimensional transition metal dichalcogenide semiconductors. *2D Materials* **2015**, *2*, 022001.
- (27) Ferreira, F.; Magorrian, S. J.; Enaldiev, V. V.; Ruiz-Tijerina, D. A.; Fal'ko, V. I. Band energy landscapes in twisted homobilayers of transition metal dichalcogenides. *Appl. Phys. Lett.* **2021**, *118*, 241602.
- (28) Brem, S.; Linderalv, C.; Erhart, P.; Malic, E. Tunable phases of moiré excitons in van der waals heterostructures. *Nano Lett.* **2020**, *20*, 8534–8540.
- (29) Merkl, P.; Mooshammer, F.; Brem, S.; Girnghuber, A.; Lin, K.-Q.; Weigl, L.; Liebich, M.; Yong, C.-K.; Gillen, R.; Maultzsch, J.; Lupton, J. M.; Malic, E.; Huber, R. Twist-tailoring coulomb correlations in van der waals homobilayers. *Nat. Commun.* **2020**, *11*, 1–7.
- (30) Meneghini, G.; Brem, S.; Malic, E. Ultrafast phonon-driven charge transfer in van der waals heterostructures. *Natural Sciences* **2022**, *2*, No. e20220014.
- (31) Damascelli, A.; Hussain, Z.; Shen, Z.-X. Angle-resolved photoemission studies of the cuprate superconductors. *Reviews of modern physics* **2003**, *75*, 473.
- (32) Weinelt, M.; Kutschera, M.; Fauster, T.; Rohlfling, M. Dynamics of exciton formation at the si (100) c ( $4 \times 2$ ) surface. *Physical review letters* **2004**, *92*, 126801.
- (33) Rustagi, A.; Kemper, A. F. Photoemission signature of excitons. *Phys. Rev. B* **2018**, *97*, 235310.

# Hybrid exciton signatures in ARPES spectra of van der Waals materials

## Supplementary Information

Giuseppe Meneghini,<sup>1,\*</sup> Marcel Reutzler,<sup>2</sup> Stefan Mathias,<sup>2</sup> Samuel Brem,<sup>1</sup> and Ermin Malic<sup>1</sup>

<sup>1</sup>*Department of Physics, Philipps University of Marburg, 35037 Marburg, Germany*

<sup>2</sup>*I. Physikalisches Institut, Georg-August-Universität Göttingen, Göttingen, Germany*

### THEORETICAL APPROACH

#### Bandstructure and Dynamics

In order to track the tr-ARPES signal in our work we use the theoretical framework based on a density matrix formalism<sup>1-3</sup>. First, we set up an excitonic Hamiltonian for a TMD bilayer system, including exciton-phonon and exciton-light interactions yielding

$$\begin{aligned}
 H_X &= \sum_{\mu\mathbf{Q}} E_{\mathbf{Q}}^{\mu} X_{\mathbf{Q}}^{\mu\dagger} X_{\mathbf{Q}}^{\mu} + \sum_{\mu\nu\mathbf{Q}} \mathcal{T}_{\mu\nu} X_{\mathbf{Q}}^{\mu\dagger} X_{\mathbf{Q}}^{\nu} \\
 H_{X-ph} &= \sum_{j,\mathbf{Q},\mathbf{q},\mu,\nu} \tilde{\mathcal{D}}_{j,\mathbf{q},\mathbf{Q}}^{\nu\mu} X_{\mathbf{Q}+\mathbf{q}}^{\nu\dagger} X_{\mathbf{Q}}^{\mu} b_{j,\mathbf{q}} + h.c. \\
 H_{X-l} &= \sum_{\sigma,\mathbf{Q},\mu} \mathbf{A} \cdot \mathcal{M}_{\mathbf{Q}\sigma}^{\mu} X_{\mathbf{Q}}^{\mu} + h.c.
 \end{aligned} \tag{1}$$

with the exciton energy  $E_{\mathbf{Q}}^{\mu} = \hbar^2 \mathbf{Q}^2 / (2M_{\mu}) + E_{\mu}^g + E_{\mu}^b$  at the center-of-mass momentum  $\mathbf{Q}$  with  $E_{\mu}^g$  energy gap between valence and conduction band and  $E_{\mu}^b$  binding energy, obtained from solving the Wannier equation, containing the free exciton energy and the monolayer energies extracted from DFT calculations shifted by the layer polarization-induced alignment potential<sup>4</sup>, and with the exciton annihilation (creation) operators  $X^{(\dagger)}$ . The appearing excitonic tunnelling matrix elements  $\mathcal{T}_{\mu\nu} = \langle \mu | V_0 + V_1 | \nu \rangle$ , where  $V_{0/1}$  are the effective electrostatic potential created by the nuclei and core electrons of layer 0/1 and  $|\mu/\nu\rangle$  excitonic wave functions<sup>2,5</sup>. Furthermore, the exciton-phonon and the exciton-light matrix elements are defined as

$$\begin{aligned}
 \tilde{\mathcal{D}}_{j,\mathbf{q},\mathbf{Q}}^{\nu\mu} &= D_{j,\mathbf{q}}^{\zeta_{\mu}^e \zeta_{\nu}^e} \delta_{\zeta_{\mu}^h \zeta_{\nu}^h} \delta_{\zeta_{\nu}^e - \zeta_{\mu}^e, \zeta_j^{ph}} \delta_{L_{\nu}^e, L_j^{ph}} \delta_{L_{\nu}^e, L_{\mu}^e} \mathcal{F}^{\mu\nu} (\tilde{m}_h^{\nu} [\mathbf{q}]) + \\
 &\quad - D_{j,\mathbf{q}}^{\zeta_{\mu}^h \zeta_{\nu}^h} \delta_{\zeta_{\mu}^e \zeta_{\nu}^e} \delta_{\zeta_{\nu}^h - \zeta_{\mu}^h, \zeta_j^{ph}} \delta_{L_{\nu}^h, L_j^{ph}} \delta_{L_{\nu}^h, L_{\mu}^h} \mathcal{F}^{\mu\nu} (-\tilde{m}_e^{\nu} [\mathbf{q}]) \\
 \mathcal{F}^{\mu\nu} (\mathbf{q}) &= \sum_{\mathbf{k}} \psi^{\mu*} (\mathbf{k} + \mathbf{q}) \psi^{\nu} (\mathbf{k}) \\
 \mathcal{M}_{\mathbf{Q}\sigma}^{\mu} &= \frac{e_0}{m_0} \delta_{\zeta_{\mu}^e \zeta_{\mu}^h, \mathbf{K}\mathbf{K}} \mathbf{M}_{\mathbf{Q}\sigma}^{c\nu} \sum_{\mathbf{k}} \psi^{\mu*} (\mathbf{k})
 \end{aligned} \tag{2}$$

with the electron-phonon coupling  $D_{j,\mathbf{q}}^{\zeta_{\mu}^e \zeta_{\nu}^e}$  for electron/hole in the conduction or valence bands  $\lambda = c/v$  taken from DFPT calculations<sup>6</sup>. The coefficients  $\tilde{m}_{e/h} = m_{e/h} / (m_e + m_h)$  take into account the electron-hole mass asymmetry. The main high-symmetry points are labeled by  $\zeta$  and  $L$  denotes the layer index, where we use the suffix  $e/h/ph$  for electrons, holes, or phonons, respectively. Furthermore,  $\mathbf{M}_{m\nu,\sigma}^{c\nu} = -i\hbar \langle n_{\nu} | \nabla | m_c \rangle$  denotes the optical matrix element in electron-hole picture and contains the optical selection rules with  $\sigma$  describing the polarization and  $\mathbf{A}$  the vector potential of the light pulse.

We diagonalize the excitonic Hamiltonian in Eq. (1) by introducing a new set of operators  $Y_{\mathbf{Q}}^{\eta} = \sum_{\mu} c_{\mu}^{\eta} (\mathbf{Q}) X_{\mathbf{Q}}^{\mu}$  describing hybrid excitons, with the mixing coefficients  $c_{\mu}^{\eta} (\mathbf{Q})$  and the new quantum num-

ber  $\eta$  defining the hybrid-exciton bands. We obtain the final form of the hybrid exciton Hamiltonian

$$\begin{aligned}
H_Y &= \sum_{\eta} \mathcal{E}_{\mathbf{Q}}^{\eta} Y_{\mathbf{Q}}^{\eta\dagger} Y_{\mathbf{Q}}^{\eta} \\
H_{Y-ph} &= \sum_{j, \mathbf{Q}, \mathbf{q}, \eta, \xi} \mathcal{D}_{j, \mathbf{q}, \mathbf{Q}}^{\xi \eta} Y_{\mathbf{Q}+\mathbf{q}}^{\xi\dagger} Y_{\mathbf{Q}}^{\eta} b_{j, \mathbf{q}} + h.c. \quad \text{with} \quad \mathcal{D}_{j, \mathbf{q}, \mathbf{Q}}^{\xi \eta} = \sum_{\mu, \nu} c_{\mu}^{\eta*}(\mathbf{Q}) c_{\nu}^{\xi}(\mathbf{Q} + \mathbf{q}) \tilde{\mathcal{D}}_{j, \mathbf{q}}^{\nu \mu} \\
H_{Y-l} &= \sum_{\sigma, \mathbf{Q}, \eta} \mathbf{A} \cdot \tilde{\mathcal{M}}_{\mathbf{Q}\sigma}^{\eta} Y_{\mathbf{Q}\parallel}^{\eta} + h.c. \quad \text{with} \quad \tilde{\mathcal{M}}_{\sigma\mathbf{Q}}^{\eta} = \sum_{\mu} c_{\mu}^{\eta*}(\mathbf{Q}) \mathcal{M}_{\mathbf{Q}\sigma}^{\mu}
\end{aligned} \tag{3}$$

with the corresponding hybrid-exciton energies  $\mathcal{E}_{\mathbf{Q}}^{\eta}$ .

We use the derived Hamiltonian to compute the equation of motion for the hybrid exciton densities  $N_{\mathbf{Q}}^{\eta} = \delta N_{\mathbf{Q}}^{\eta} + |P_{\mathbf{Q}}^{\eta}|^2$  with the coherent polarization  $P_{\mathbf{Q}}^{\eta} = \langle Y_{\mathbf{Q}}^{\eta\dagger} \rangle$  and the incoherent exciton density  $\delta N_{\mathbf{Q}}^{\eta} = \langle Y_{\mathbf{Q}}^{\eta\dagger} Y_{\mathbf{Q}}^{\eta} \rangle - \langle Y_{\mathbf{Q}}^{\eta\dagger} \rangle \langle Y_{\mathbf{Q}}^{\eta} \rangle$ . Solving the Heisenberg equation, we obtain the following equations of motion<sup>7,8</sup>

$$\begin{aligned}
i\hbar \partial_t P_0^{\eta} &= -(\mathcal{E}_0^{\eta} + i\Gamma_0^{\eta}) P_0^{\eta} - \tilde{\mathcal{M}}_0^{\eta} \cdot \mathbf{A}(t) \\
\delta \dot{N}_{\mathbf{Q}}^{\eta} &= \sum_{\xi} W_{0\mathbf{Q}}^{\xi \eta} |P_0^{\eta}|^2 + \sum_{\xi, \mathbf{Q}'} \left( W_{\mathbf{Q}'\mathbf{Q}}^{\xi \eta} \delta N_{\mathbf{Q}'}^{\xi} - W_{\mathbf{Q}\mathbf{Q}'}^{\eta \xi} \delta N_{\mathbf{Q}}^{\eta} \right)
\end{aligned} \tag{4}$$

where 0 refers to the vanishing center-of-mass momentum  $\mathbf{Q} = 0$  due to the condition that the laser pulse only creates hybrid excitons around  $\mathbf{Q} = 0$  at the K valley. The appearing scattering rates are related via  $2\Gamma_{\mathbf{Q}}^{\eta}/\hbar = \sum_{\mathbf{Q}'\xi} W_{\mathbf{Q}\mathbf{Q}'}^{\xi \eta}$  with

$$W_{\mathbf{Q}\mathbf{Q}'}^{\eta \xi} = \frac{2\pi}{\hbar} \sum_{j, \pm} \left| \mathcal{D}_{j, \mathbf{Q}'-\mathbf{Q}}^{\eta \xi} \right|^2 \left( \frac{1}{2} \pm \frac{1}{2} + n_{j, \mathbf{Q}'-\mathbf{Q}}^{ph} \right) \delta \left( \mathcal{E}_{\mathbf{Q}'}^{\xi} - \mathcal{E}_{\mathbf{Q}}^{\eta} \mp \hbar \Omega_{j, \mathbf{Q}'-\mathbf{Q}} \right)$$

where  $n_{j, \mathbf{Q}'-\mathbf{Q}}^{ph}$  is the Boltzmann distribution for phonons<sup>9</sup>.

### Modelling the ARPES signal

We introduce the basic steps for the derivation of an equation describing ARPES measurements. The starting point of our result is the three-step model<sup>10</sup> with the main contribution to the ARPES signal stemming from Fermis-Golden rule:

$$\mathcal{I}(\mathbf{k}, h\nu; t) \propto \sum_{i, f} |\langle f\mathbf{k} | H_{int} | i \rangle|^2 N_i(t) \delta(E_{f\mathbf{k}} - E_i - h\nu) \tag{5}$$

where  $|i/f\rangle$  are the initial/final state of the system where we consider eigenstates of the two-body Hamiltonian with initial/final eigenenergies  $E_{i/f}$ . The energy of the photon is denoted by  $h\nu$  and the initial state occupation by  $N_i(t)$ . The initial states in our system are hybrid excitons, while the final state consists of an ejected free electron and a left-behind hole in a hybridized valence band of the bilayer. We proceed in evaluating the above expectation value by expressing the initial and final states in electronic operators of pure monolayer eigenstates. The final state can be described by the product of a free electron and a hybrid hole, where the latter is obtained by solving the eigenvalue problem for the following bilayer Hamiltonian

$$H = \sum_{\mathbf{k}l\lambda} \mathcal{E}_{\lambda l\mathbf{k}} a_{\lambda\mathbf{k}l}^{\dagger} a_{\lambda\mathbf{k}l} + \sum_{\mathbf{k}ll'\lambda} \mathcal{T}_{\lambda ll'} a_{\lambda\mathbf{k}l'}^{\dagger} a_{\lambda\mathbf{k}l} \tag{6}$$

with  $\lambda = c, v$  indicating the band index and  $a_{\lambda\mathbf{k}l}^{(\dagger)}$  conduction/valence band annihilation(creation) operators and  $\mathcal{T}_{\lambda ll'}$  band-dependent tunnelling strength between the two layers  $ll'$ . The solution of the eigenvalue problem leads us to a set of hybridized valence and conduction bands

$$E_{\mathbf{k}\gamma}^{\lambda} = \frac{1}{2} (\mathcal{E}_{\lambda, 1\mathbf{k}} + \mathcal{E}_{\lambda, 2\mathbf{k}}) \pm \frac{1}{2} \sqrt{(\mathcal{E}_{\lambda, 1\mathbf{k}} - \mathcal{E}_{\lambda, 2\mathbf{k}})^2 + 4|\mathcal{T}_{\lambda, 12}|^2} \tag{7}$$

with  $\gamma = (\pm, \xi)$  labeling the two new states ( $\pm$  solutions) and the valley index  $\xi$ . The corresponding eigenvectors are obtained from the same 2x2 eigenvalue problem which we write as a superposition of the old monolayer states as

$$|\gamma\lambda\mathbf{p}\rangle = \sum_l g_{l\mathbf{p}}^\gamma a_{l\mathbf{p}\xi}^\dagger |0\rangle$$

with the mixing coefficients  $g_l^\gamma$ . Since in the final state the two particles are not bound by the Coulomb interaction, we can describe the final state as a product of a free electron state ( $a_{f\mathbf{k}}^\dagger$ ) and the above derived hybrid holes,

$$|f\rangle = |\mathbf{k}, \gamma v\mathbf{p}\rangle = \sum_l g_{l\mathbf{p}}^\gamma a_{f\mathbf{k}}^\dagger a_{vl\mathbf{p}\xi_h} |0\rangle \quad (8)$$

with free electron operator  $a_{f\mathbf{k}}^\dagger$ .

We now proceed in expressing the initial state in terms of monolayer electrons. To do so we start from the hybrid exciton state  $|\eta\mathbf{Q}\rangle$  and perform a series of backward transformation from hybrid exciton operators to exciton operators arriving finally to electron operators  $Y^\dagger \rightarrow X^\dagger \rightarrow a^\dagger a$ , obtaining

$$|i\rangle = |\eta\mathbf{Q}\rangle = Y_{\eta\mathbf{Q}}^\dagger |0\rangle = \sum_\mu \mathbf{c}_\mu^{\eta*}(\mathbf{Q}) X_{\mu\mathbf{Q}}^\dagger |0\rangle = \sum_{\mu\mathbf{k}} \mathbf{c}_\mu^{\eta*}(\mathbf{Q}) \psi^{\mu*}(\mathbf{k}) a_{c,\mathbf{k}+\tilde{m}_e\mathbf{Q},\mu_e}^\dagger a_{v,\mathbf{k}-\tilde{m}_h\mathbf{Q},\mu_h} |0\rangle$$

with the compound index  $\eta = (n, \xi)$  describing the hybrid degrees of freedom,  $\mathbf{c}_\mu^{\eta*}(\mathbf{Q})$  excitonic mixing coefficients,  $\mu = (L, \xi)$  describing the excitonic degrees of freedom, with  $L = (l_e, l_h)$  and  $\xi = (\xi_e, \xi_h)$ , and we use the notation  $\mu_{e/h}$  to refer the quantum numbers inside  $\mu$  labelled by  $e/h$ . Note that we include only the lowest 1s excitonic states. Inserting the initial and final states in Eq. (5) we obtain

$$\mathcal{I}(\mathbf{k}, h\nu) \propto \sum_{\substack{\eta\gamma \\ \mathbf{p}\mathbf{Q}}} |\langle \mathbf{k}, \gamma v\mathbf{p} | H_{int} | \eta\mathbf{Q} \rangle|^2 \cdot N_{\mathbf{Q}}^\eta(t) \delta(E_{\mathbf{k}}^e - E_{\gamma,\mathbf{p}}^v - E_{\eta,\mathbf{Q}}^X - h\nu) \quad (9)$$

where  $\mathbf{p}$  is the hole momentum,  $N_{\mathbf{Q}}^\eta(t)$  denotes the hybrid exciton time-dependent occupation for the hX state  $\eta$  at the center-of-mass momentum  $\mathbf{Q}$ , relative to the valley. Moreover,  $E_{\mathbf{k}}^e$  corresponds to the free electron energy,  $E_{\gamma,\mathbf{p}}^v$  to the hybrid valence band energy,  $E_{\eta,\mathbf{Q}}^X$  to the hybrid exciton energy. The electron-light Hamiltonian reads

$$H_{int} = \sum_{\mathbf{p}\mathbf{k}\gamma} \mathcal{M}_{\mathbf{p}\mathbf{k}\xi_e} a_{f\mathbf{p}}^\dagger a_{c\mathbf{k}}^\gamma = \sum_{\mathbf{p}\mathbf{k}\gamma l} g_{l\mathbf{k}}^\gamma \mathcal{M}_{\mathbf{p}\mathbf{k}\xi_e} a_{f\mathbf{p}}^\dagger a_{c\mathbf{k}l\xi_e} \quad (10)$$

with the optical matrix element  $\mathcal{M}_{\mathbf{p}\mathbf{k}\xi_e}$  containing the optical selection rules. In the hybrid exciton basis, we find

$$\langle \mathbf{k}, \gamma v\mathbf{p} | H_{int} | \eta\mathbf{Q} \rangle = \langle 0 | \sum_{l_h} g_{l_h\mathbf{p}}^{\gamma*} a_{v,\mathbf{p},l_h\xi_h}^\dagger a_{f\mathbf{k}} \sum_{\substack{\mathbf{p}'\mathbf{k}' \\ \gamma'l_e}} g_{l_e\mathbf{k}'}^{\gamma'} \mathcal{M}_{\mathbf{p}'\mathbf{k}'\xi_e} a_{f,\mathbf{p}'}^\dagger a_{c,\mathbf{k}',l_e\xi_e} \cdot \sum_{\mu\mathbf{q}} \mathbf{c}_\mu^{\eta*}(\mathbf{Q}) \psi^{\mu*}(\mathbf{q}) a_{c,\mathbf{q}+\tilde{m}_e\mathbf{Q},l'_e\xi'_e}^\dagger a_{v,\mathbf{q}-\tilde{m}_h\mathbf{Q},l'_h\xi'_h} |0\rangle.$$

By considering the expectation value of these operators we have

$$\langle 0 | a_{v,\mathbf{p},l_h\xi_h}^\dagger a_{f,\mathbf{k}} a_{f,\mathbf{p}'}^\dagger a_{c,\mathbf{k}',l_e\xi_e} a_{c,\mathbf{q}+\tilde{m}_e\mathbf{Q},l'_e\xi'_e}^\dagger a_{v,\mathbf{q}-\tilde{m}_h\mathbf{Q},l'_h\xi'_h} |0\rangle = \delta_{\mathbf{p},\mathbf{q}-\tilde{m}_h\mathbf{Q}} \delta_{\mathbf{k},\mathbf{p}'} \delta_{\mathbf{k}',\mathbf{q}+\tilde{m}_e\mathbf{Q}} \delta_{l_h,l'_h} \delta_{l_e,l'_e} \delta_{\xi_h,\xi'_h} \delta_{\xi_e,\xi'_e}$$

For the photo-emission process, we claim conservation of the total electron momentum and neglect all other momentum dependencies,

$$\mathcal{M}_{\mathbf{p}\mathbf{k}\xi} = \tilde{\mathcal{M}} \delta_{\mathbf{p}\parallel, \mathbf{k}+\xi}$$

we can rewrite the total ARPES signal as follows

$$\mathcal{I}(\mathbf{k}, h\nu; t) \propto \sum_{\eta,\gamma,\mathbf{p}} |\mathcal{G}_{\mathbf{p}\mathbf{k}}^{\eta\gamma}|^2 N_{\mathbf{k}-\mathbf{p}}^\eta(t) \delta(E_{\mathbf{k}}^e - E_{\gamma,\mathbf{p}}^v - E_{\eta,\mathbf{k}-\mathbf{p}}^X - h\nu) \quad (11)$$

with

$$\mathcal{G}_{\mathbf{pk}}^{\eta\gamma} = \sum_{\mu} g_{l_h, \mathbf{p}}^{\gamma*} \tilde{\mathcal{M}} \mathbf{c}_{\mu}^{\eta*}(\tilde{\mathbf{k}} - \mathbf{p}) \psi^{\mu*}(\tilde{m}_e \mathbf{p} + \tilde{m}_h \tilde{\mathbf{k}}) \cdot \delta_{\xi_h^{\gamma}, \xi_h^{\mu}}. \quad (12)$$

where we used  $\tilde{\mathbf{k}} = \mathbf{k} - \xi_e$ . The new coupling  $\mathcal{G}_{\mathbf{pk}}^{\eta\gamma}$  contains the momentum dependence of the ARPES signal, i.e. superposition of the excitonic wavefunctions weighted by the mixing coefficients and the hole hybridization coefficients. Note that ARPES signals stemming from different electron valleys are additionally weighted by different photoemission matrix elements  $\mathcal{M}$ , which is neglected here.

### HYBRID EXCITON FINGERPRINT

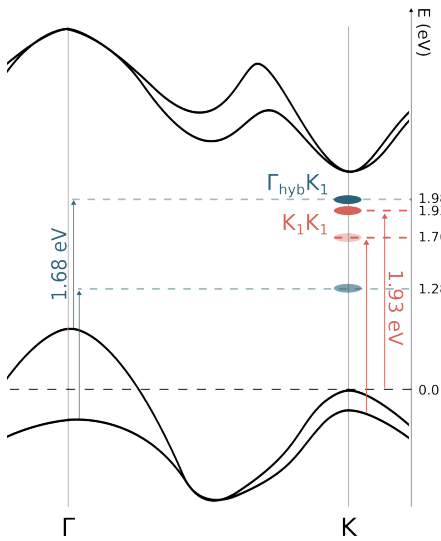


Fig. S1: Schematic of the electronic band structure of the MoS<sub>2</sub> homobilayer, highlighting the position of the main ARPES signals from the main text. The reference point is the highest valence band at the K point. Signals arising from the K<sub>1</sub>K<sub>1</sub> and  $\Gamma_{hyb}K_1$  hybrid state are red and blue, respectively.

In the main text we have discussed the differences between ARPES signals stemming from pure excitonic and hybrid excitonic states. We predict the appearance of a double-peaked ARPES signal that is characteristic for hybrid exciton states. Here, we discuss in more detail the position and the shape of the ARPES signals. FigureS1 illustrates the expected position of ARPES signals assuming the highest valence band at the K point as reference. We mentioned in the main text that the shape of the ARPES signal is linked to the center-of-mass momentum distribution of the hybrid excitons occupation. We show here how considering very narrow initial distributions, we can see in a much more pronounced way the negative curvature of the ARPES signal reflecting the dispersion of the involved valence bands. Another interesting point is the role of the  $\Gamma_{hyb}\Lambda_{hyb}$  states. In some studies<sup>11</sup>, the conduction band at the  $\Lambda$  and K points are almost degenerate, resulting in the  $\Gamma_{hyb}\Lambda_{hyb}$  hybrid exciton being the energetically lowest state. As a consequence, this state would carry the most occupation in equilibrium. This would result in an additional relaxation step from the  $\Gamma_{hyb}K_1$  to the  $\Gamma_{hyb}\Lambda_{hyb}$  hybrid exciton. As the latter state is also characterized by a hybrid hole at the  $\Gamma$  point, the predicted ARPES signal would be qualitatively the same, however, the signal would be monitored at the  $\Lambda$  point. In Fig. S2 we performed a static computation neglecting the dynamics of excitons. Instead, we use an extremely narrow Gaussian exciton density distribution in Eq. (5). By centering the distribution for each hybrid state separately we obtain the ARPES signals shown in Figs. S2(a,b,c). We observe nicely the negative curvature of the signals. For the case of the  $\Gamma_{hyb}\Lambda_{hyb}$  state we predict the same behaviour as for the  $\Gamma_{hyb}K$  state, since the two state share the same type of hybrid hole valley. The only differences are the momentum and the exact energy position of the ARPES signals.

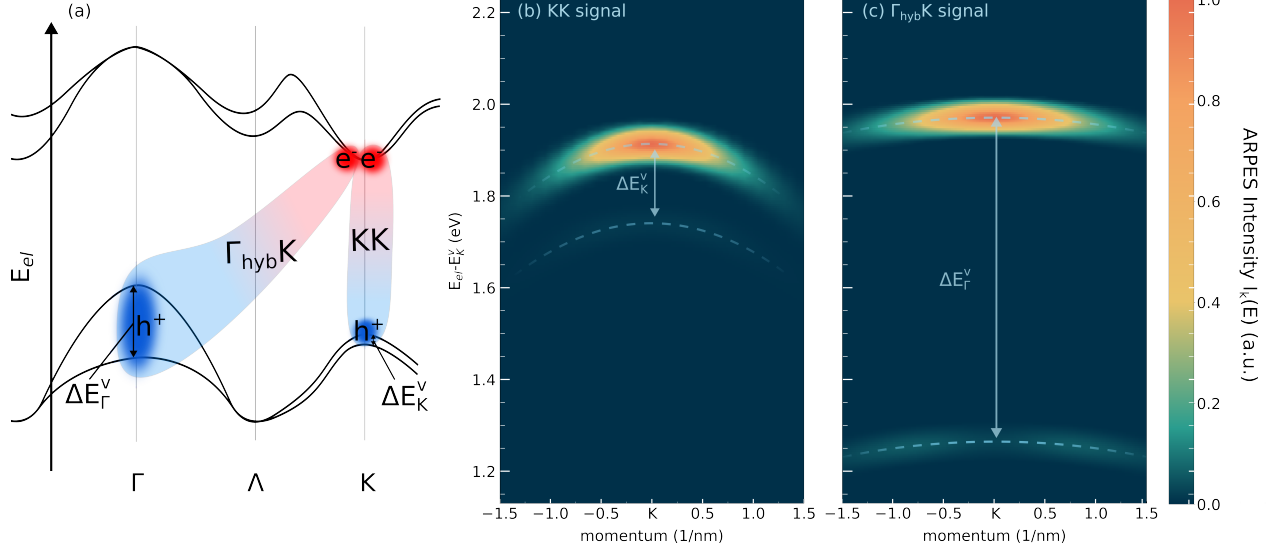


Fig. S2: Hybrid excitons ARPES fingerprints. (a) Sketch of the MoS<sub>2</sub> electronic band structure, highlighting the possible hybrid excitonic species contributing to the relaxation dynamics. (b,c,d) ARPES signal in the case that the population is placed in different hybrid exciton states (KK,  $\Gamma$ K,  $\Gamma\Lambda$ ), with a very narrow momentum distribution around each excitonic valley. The signal reflects the curvature of the hybrid valence band (dashed lines). In the case of hybrids excitons, we find the characteristic two-peaked ARPES signal reflecting the splitting in the hybrid valence bands.

### PEAKS INTENSITY RATIO AND HOLE LAYER POLARIZATION

The characteristic presence of the double peak signal provides experimental access to the inner quantum structure of the hybrid exciton. The intensity ratio between these peaks is intrinsically linked to the hole layer polarization, as explained in the following. If we consider the maximum intensity of the momentum-integrated ARPES signal for the one of the peaks stemming from the hybrid state, we can write, by exploiting Eq. 11,

$$I(E_{max}^{\gamma}) := I_{\gamma} = \sum_{\mathbf{p}, \mathbf{k}} |\mathcal{G}_{\mathbf{p}\mathbf{k}}^{\gamma}|^2 N_{\mathbf{k}-\mathbf{p}} \delta(E_{\mathbf{k}}^e - E_{\gamma, \mathbf{p}}^v - E_{\mathbf{k}-\mathbf{p}}^X - E_{max}^{\gamma})$$

where we use  $\gamma = \uparrow / \downarrow$  for the upper and lower valence bands at  $\Gamma$  (arising from the layer hybridization). We omit the index  $\eta = \Gamma\mathbf{K}$ , since both contributions of the double peak signal arise from the same hybrid exciton. For the stationary state in the low temperature limit we can approximate  $N_{\mathbf{Q}} = N_{\mathbf{Q}} \delta_{\mathbf{Q},0}$ . Using Eq. 12 where  $g_{l_h \mathbf{p}}^{\gamma*} = g_{l_h}^{\gamma*}$ , we can rewrite the equation for the APRES intensity in terms of CoM ( $\mathbf{Q}$ ) and relative ( $\mathbf{q}$ ) momenta

$$\begin{aligned} I_{\gamma} &= \sum_{\mathbf{Q}, \mathbf{q}} \left| \sum_{\mu} g_{l_h}^{\gamma*} \mathbf{c}_{\mu}^*(\mathbf{Q}) \psi^{\mu*}(\mathbf{q}) \right|^2 N_{\mathbf{Q}} \delta_{\mathbf{Q},0} \delta(E_{\mathbf{q}+\tilde{m}_e \mathbf{Q}}^e - E_{\gamma, \mathbf{q}-\tilde{m}_h \mathbf{Q}}^v - E_{\mathbf{Q}}^X - E_{max}^{\downarrow}) \\ &= \sum_{\mathbf{q}} \left| \sum_{\mu} g_{l_h}^{\gamma*} \mathbf{c}_{\mu}^*(0) \psi^{\mu*}(\mathbf{q}) \right|^2 N_0 \delta(E_{\mathbf{q}}^e - E_{\gamma, \mathbf{q}}^v - E_0^X - E_{max}^{\gamma}). \end{aligned}$$

Using the specific form for the hybrid valence band coefficients ( $|\gamma\rangle = 1/\sqrt{2}(|0\rangle \pm |1\rangle)$ ) and choosing as a base the layer of the hole ( $|l_h\rangle$ ) and for the excitonic mixing coefficients ( $\Gamma\mathbf{K}$  made mainly of  $|\mathbf{c}_{intra}\rangle^2 \simeq 39\%$  and  $|\mathbf{c}_{inter}\rangle^2 \simeq 61\%$ ), we obtain

$$\begin{aligned} I_{\gamma} &= \sum_{\mathbf{q}} |\mathbf{c}_{intra}^* \psi_{intra}^*(\mathbf{q}) \pm \mathbf{c}_{inter}^* \psi_{inter}^*(\mathbf{q})|^2 N_0 \delta(E_{\mathbf{q}}^e - E_{\gamma, \mathbf{q}}^v - E_0^X - E_{max}^{\gamma}) \\ &= N_0 |\mathbf{c}_{intra}^* \psi_{intra}^*(0) \pm \mathbf{c}_{inter}^* \psi_{inter}^*(0)|^2. \end{aligned}$$

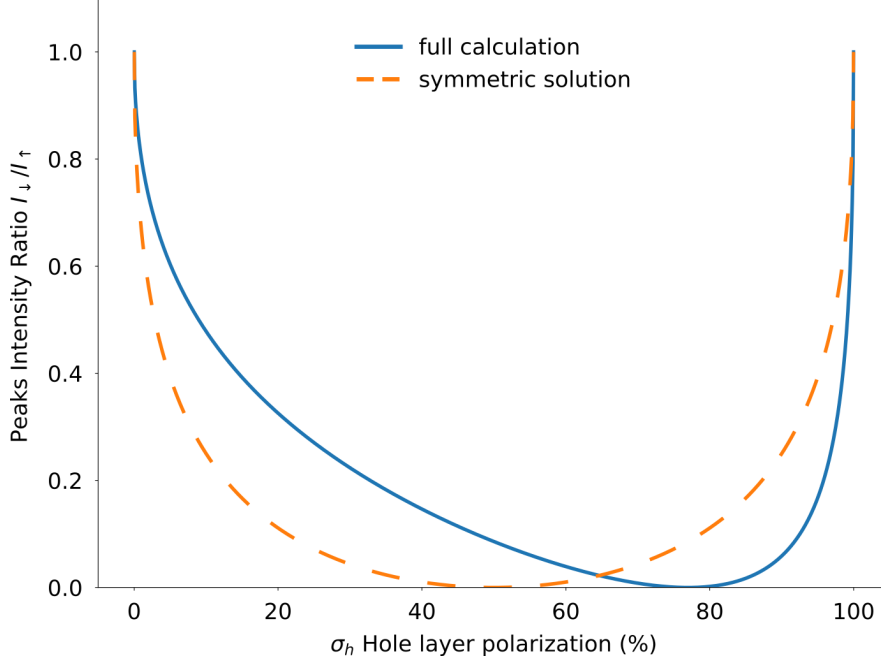


Fig. S3: Ratio of the maximum ARPES intensity of the two peaks arising from the hybrid  $\Gamma$ K exciton as a function of the hole layer polarization. The dashed orange line shows the artificial case in which we neglect the excitonic intra-interlayer wavefunction difference, while the solid blue shows the full calculation.

where the delta function in energy fixes the exciton's relative momentum  $\hbar^2 \mathbf{q}^2 / (2m_e) + \hbar^2 \mathbf{q}^2 / (2m_h) - E_{\gamma,0}^v - E_0^X - E_{max}^\gamma = 0 \implies \mathbf{q} = 0$ . Finally using the completeness of the mixing coefficients, we have  $|\mathbf{c}_{intra}^*|^2 = 1 - |\mathbf{c}_{inter}^*|^2$ . We can interpret  $|\mathbf{c}_{inter}^*|^2$  as the degree of hole layer polarization induced by the exciton bound state. Thus, we define the hole exciton-induced polarization as  $\sigma_h = |\mathbf{c}_{inter}^*|^2$ , where  $\sigma_h = 0$  stands for hole in the same layer of the electron and  $\sigma_h = 1$  in the opposite. Inserting this in the previous equation we find

$$I_\gamma = N_0 |\sqrt{1 - \sigma_h} \psi_{intra}^*(0) - \sigma_h \psi_{inter}^*(0)|^2.$$

Now considering the ratio of  $I_\gamma$  for the two different hybrid valence bands, i.e.  $I_\downarrow / I_\uparrow$ , we obtain an equation with the ratio of the maximum intensity of the momentum-integrated ARPES signal as a function of the hole layer polarization:

$$\frac{I_\downarrow}{I_\uparrow} = \frac{|\sqrt{1 - \sigma_h} \psi_{intra}^*(0) - \sigma_h \psi_{inter}^*(0)|^2}{|\sqrt{1 - \sigma_h} \psi_{intra}^*(0) + \sigma_h \psi_{inter}^*(0)|^2}$$

Figure S3 shows the intensity ratio at the maximum energy for the two peaks as function of the hole layer polarization. We compare the artificial symmetric case neglecting the intra- and interlayer wavefunction difference with the full calculation taking the dependence on wavefunctions into account. Without the presence of a light excitation, the energetically favorable state for the hole would be the highest hybrid valence band, i.e. a 50%-50% mixture of the two layers' ground states. In the presence of optical excitation, the electron-hole bound state (exciton) induces a symmetry breaking of this mixture, inducing a polarization of the hole. If the exciton hybridization would not break the symmetry, keeping the hole in a 50%-50% mixture the expected intensity ratio would be zero (hole polarization  $\simeq 0.5$  corresponds to a ratio  $\simeq 0$ , as can be seen from the dashed orange line in fig.S3), meaning that only one peak ( $I_\uparrow$ ) would be visible in the ARPES signal (Figs. 4/5 in the main text). Only when the exciton state breaks the symmetry of the homobilayer, attracting the hole closer to one of the two layers, the hole has to form a superposition of single particle states to minimize the energy, resulting in the appearance of contributions from both hybrid valence bands. Considering the difference between intra- and interlayer wavefunctions, we obtain the expected non-symmetric dependence (cf. the solid blue line in Fig.S3), where a "measured" ratio of  $\simeq 0.15$  corresponds to a hole polarization of  $\simeq 40\%$ .

---

\* giuseppe.meneghini@physik.uni-marburg.de

- [1] Samuel Brem, Christopher Linderålv, Paul Erhart, and Ermin Malic, “Tunable phases of moiré excitons in van der waals heterostructures,” *Nano letters* **20**, 8534–8540 (2020).
- [2] Samuel Brem, Kai-Qiang Lin, Roland Gillen, Jonas M Bauer, Janina Maultzsch, John M Lupton, and Ermin Malic, “Hybridized intervalley moiré excitons and flat bands in twisted wse 2 bilayers,” *Nanoscale* **12**, 11088–11094 (2020).
- [3] Florian Katsch, Malte Selig, Alexander Carmele, and Andreas Knorr, “Theory of exciton-exciton interactions in monolayer transition metal dichalcogenides,” *Physica Status Solidi (b)* **255**, 1800185 (2018).
- [4] Fábio Ferreira, SJ Magorrian, VV Enaldiev, DA Ruiz-Tijerina, and VI Fal’ko, “Band energy landscapes in twisted homobilayers of transition metal dichalcogenides,” *Applied Physics Letters* **118**, 241602 (2021).
- [5] Joakim Hagel, Samuel Brem, Christopher Linderålv, Paul Erhart, and Ermin Malic, “Exciton landscape in van der waals heterostructures,” *Physical Review Research* **3**, 043217 (2021).
- [6] Jin Z, Li X, Mullen J T, and Kim K W, “Intrinsic transport properties of electrons and holes in monolayer transition-metal dichalcogenides,” *Phys. Rev. B* **90**, 045422 (2014).
- [7] Samuel Brem, Malte Selig, Gunnar Berghäuser, and Ermin Malic, “Exciton relaxation cascade in two-dimensional transition metal dichalcogenides,” *Scientific reports* **8**, 1–8 (2018).
- [8] Malte Selig, Gunnar Berghäuser, Marten Richter, Rudolf Bratschitsch, Andreas Knorr, and Ermin Malic, “Dark and bright exciton formation, thermalization, and photoluminescence in monolayer transition metal dichalcogenides,” *2D Materials* **5**, 035017 (2018).
- [9] Giuseppe Meneghini, Samuel Brem, and Ermin Malic, “Ultrafast phonon-driven charge transfer in van der waals heterostructures,” *Natural Sciences* **2**, e20220014 (2022).
- [10] Andrea Damascelli, Zahid Hussain, and Zhi-Xun Shen, “Angle-resolved photoemission studies of the cuprate superconductors,” *Reviews of modern physics* **75**, 473 (2003).
- [11] Andor Kormányos, Viktor Zólyomi, Vladimir I Fal’ko, and Guido Burkard, “Tunable berry curvature and valley and spin hall effect in bilayer mos 2,” *Physical Review B* **98**, 035408 (2018).

---

Paper 5

---

# Excitonic Thermalization Bottleneck in Twisted TMD Heterostructures

Giuseppe Meneghini,\* Samuel Brem, and Ermin Malic



Cite This: *Nano Lett.* 2024, 24, 4505–4511



Read Online

ACCESS |



Metrics & More



Article Recommendations



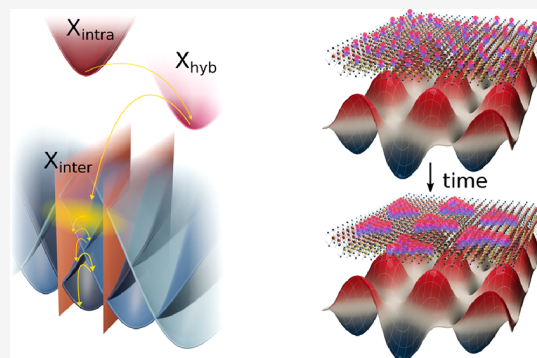
Supporting Information

**ABSTRACT:** Twisted van der Waals heterostructures show intriguing interface exciton physics, including hybridization effects and emergence of moiré potentials. Recent experiments have revealed that moiré-trapped excitons exhibit remarkable dynamics, where excited states show lifetimes that are several orders of magnitude longer than in monolayers. The origin of this behavior is still under debate. Based on a microscopic many-particle approach, we investigate the phonon-driven relaxation cascade of non-equilibrium moiré excitons in the exemplary  $\text{MoSe}_2$ – $\text{WSe}_2$  heterostructure. We track exciton relaxation pathways across different moiré mini-bands and identify the phonon-scattering channels assisting the spatial redistribution of excitons into low-energy pockets of the moiré potential. We unravel a phonon bottleneck in the flat band structure at low twist angles preventing excitons from fully thermalizing into the lowest state, explaining the measured enhanced emission intensity and lifetime of excited moiré excitons. Overall, our work provides important insights into the exciton relaxation dynamics in flat-band exciton materials.

**KEYWORDS:** *van der Waals heterostructures, moiré excitons, exciton dynamics, relaxation bottleneck*

Van der Waals heterostructures consisting of monolayers of transition metal dichalcogenides (TMDs) have been intensively studied in the past years.<sup>1–4</sup> The type-II heterostructure facilitates the emergence of interlayer excitons, where the Coulomb-bound electrons and holes are spatially separated in opposite layers.<sup>4–7</sup> These states are characterized by a long lifetime and exhibit a permanent out-of-plane dipole moment, making them promising for technological applications.<sup>8–10</sup> In addition, the presence of a strong tunneling between the layers allows the existence of layer-hybridized states, in which the intra- and interlayer nature can be controlled by electrical fields.<sup>11,12</sup> Hybrid excitons have been shown to play a key role for the charge transfer process in these materials<sup>13–15</sup> as well as for the transport behavior.<sup>12</sup> The possibility of introducing a twist angle between two vertically stacked TMD layers has opened the door to fascinating physical phenomena that are governed by periodic moiré potentials.<sup>16,17</sup> In the range of small twist angles ( $\leq 2^\circ$ ), long-lived moiré-trapped exciton states have been demonstrated, resulting in a multi-peaked structure in photoluminescence (PL) spectra.<sup>18–20</sup> The microscopic origin of the moiré-peak series can be traced back to the radiative recombination of excitons located in different moiré sub-bands. The latter are flat at small twist angles, reflecting their localization in real space.

A thorough microscopic understanding of moiré exciton physics is highly interesting for fundamental science and also of key importance for the technological application potential of



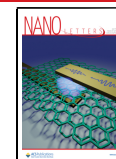
van der Waals heterostructures.<sup>21–23</sup> The strong localization and the nontrivial band topology give rise to remarkable quantum many-body effects,<sup>24,25</sup> varying from spin-liquid states<sup>26,27</sup> to Mott insulating states<sup>28–30</sup> and even superconductivity.<sup>31,32</sup> Several models have studied these exotic states, applying the common approach of mapping the system to Hubbard-like models.<sup>26,28,33–35</sup> The starting point and common assumption for these models are that all carriers occupy the lowest mini-band/localized orbital. However, in typical experiments, excitation with a laser creates a population of hot excitons that first have to dissipate their thermal energy to reach the ground state. A microscopic modeling of the relaxation cascade of hot excitons along the moiré sub-band structures that consists of many flat bands is a challenging task. Experimental observations hint at the presence of nonthermal exciton distributions resulting in long-lived excited states. Several experimental studies have demonstrated that their lifetime is on the order of nanoseconds in marginally twisted van der Waals heterostructures.<sup>18,36,37</sup> PL spectra show that the optical response of excited states can be much brighter

**Received:** January 26, 2024

**Revised:** April 2, 2024

**Accepted:** April 3, 2024

**Published:** April 5, 2024



compared to the ground state, indicating a strong non-equilibrium exciton distribution.<sup>18</sup> Although these experiments clearly hint at an unconventional relaxation dynamics in the presence of a moiré potential, there is still little known about the underlying microscopic processes.

In this work, we study the phonon-driven relaxation cascade of hot interlayer excitons in the exemplary twisted MoSe<sub>2</sub>–WSe<sub>2</sub> heterostructure. We focus on the low twist angle regime characterized by moiré-trapped excitons and a flat moiré sub-band structure.<sup>18,19,38,39</sup> Our study is based on a microscopic many-particle approach and allows us to track the phonon-driven relaxation pathway of excitons from an initial hot exciton distribution toward the ground state. We conduct a temperature-, momentum- and time-dependent study of the exciton relaxation dynamics identifying the presence of a pronounced relaxation bottleneck for small twist angles ( $\simeq 1^\circ$ ) and low temperatures (<100 K), in particular preventing excitons to efficiently scatter from the first and second excited states to the ground state. We calculate the time-dependent PL and show that the bottleneck effect manifests in a significant occupation of excited states and results in their unexpectedly high emission—in excellent qualitative agreement with observations in experimental PL spectra.<sup>18</sup> Based on our theoretical framework, we find a microscopic explanation for the experimental observations of long-lived excited moiré exciton states and their unexpected bright emission in PL spectra. Unraveling the origin of the highly nonthermal moiré exciton distribution based on the pronounced relaxation bottleneck has a major impact on exciton transport in twisted TMD heterostructures.

To microscopically understand the exciton dynamics in twisted van der Waals heterostructures, we first need to derive the key equations describing the motion of excitons in the presence of a periodic moiré potential. We start from the general Hamilton operator for TMD bilayers within the effective mass approximation. We include the energy of intra- and interlayer excitons and their interaction with phonons using a valley-local approach within the Einstein–Debye approximation of the phonon dispersion<sup>40,41</sup> yielding

$$H = \sum_{\mu} \mathcal{E}_{\mathbf{Q}}^{\mu} X_{\mathbf{Q}}^{\mu\dagger} X_{\mathbf{Q}}^{\mu} + \sum_{\mu\nu j \mathbf{q}} D_{j\mathbf{q}\mathbf{Q}}^{\mu\nu} X_{\mathbf{Q}+\mathbf{q}}^{\nu\dagger} X_{\mathbf{Q}}^{\mu} b_{j\mathbf{q}} + h.c.$$

with  $\mathcal{E}_{\mathbf{Q}}^{\mu}$  as the free excitonic energy,  $D_{j\mathbf{q}\mathbf{Q}}^{\mu\nu}$  as the exciton–phonon matrix element, and  $b_{j\mathbf{q}}$  as the phonon annihilation operator labeled by the phonon mode  $j$  and the momentum transfer  $\mathbf{q}$ . The Hamiltonian includes  $X_{\mathbf{Q}}^{\mu\dagger}$  as the exciton creation/annihilation operator with  $\mathbf{Q}$  as the center-of-mass momentum of the electron–hole pair and  $\mu$  as the compound index containing the excitonic quantum numbers  $\mu = n, \xi_e, \xi_h, l_e$  and  $l_h$ , where  $n$  denotes the series of Rydberg-like states,  $\xi_{e/h}$  is the electron and hole valley index, and  $l_{e/h}$  is the layer index. Further details on the bilayer Hamiltonian can be found in the [Supporting Information](#). Since our goal is to understand the exciton relaxation cascade in the presence of a moiré potential, we focus on the lowest interlayer exciton series of states that are known to be located at the K point in the MoSe<sub>2</sub>–WSe<sub>2</sub> heterostructure investigated here. Note that one can neglect the hybridization of intra- and interlayer exciton states as here the wave function overlap is known to be small, while the energetic detuning is large.<sup>41–44</sup>

The presence of a twist angle can be included within a tight-binding approach in terms of an effective potential, arising

from the spatially dependent atomic local alignment,<sup>19</sup> denoted as moiré potential  $V_M = \sum_{\mathbf{g}} M_{\mathbf{g}} X_{\mathbf{Q}+\mathbf{g}}^{\dagger} X_{\mathbf{Q}}$ . Here, we have introduced  $\mathbf{g} = s_1 \mathbf{G}_1^M + s_2 \mathbf{G}_2^M$ , with  $\mathbf{G}_{1/2}^M$  as reciprocal moiré lattice vectors and  $s_{1/2}$  as integers and  $M_{\mathbf{g}}$  refers to the effective exciton potential generated by the local displacement of the two twisted layers (more details can be found in the [Supporting Information](#)). By changing into a moiré exciton basis and introducing creation and annihilation operators for moiré excitons  $Y_{\mathbf{Q}}^{\eta} = \sum_{\mathbf{g}} \omega_{\mathbf{g}}^{\eta}(\mathbf{Q}) X_{\mathbf{Q}+\mathbf{g}}$  with the mixing coefficient  $\omega_{\mathbf{g}}^{\eta}(\mathbf{Q})$  corresponding to the Bloch wave function, we transform the Hamilton operator described above into<sup>19</sup>

$$\tilde{H} = \sum_{\eta} E_{\mathbf{Q}}^{\eta} Y_{\mathbf{Q}}^{\eta\dagger} Y_{\mathbf{Q}}^{\eta} + \sum_{\eta \xi j, \mathbf{Q} \mathbf{q}} \tilde{\mathcal{D}}_{\mathbf{Q} \mathbf{q}}^{\eta \xi} Y_{\mathbf{Q}}^{\xi\dagger} Y_{\mathbf{Q}}^{\eta} b_{\mathbf{q}, -\mathbf{Q}+\mathbf{g}}^j + h.c.$$

with  $\tilde{\mathcal{D}}_{\mathbf{Q} \mathbf{q}}^{\eta \xi}$  as the exciton–phonon coupling tensor in the new basis containing the overlap of initial and final moiré states. Now, we use this moiré exciton Hamiltonian to solve the Heisenberg equation of motion for the exciton occupation  $N_{\mathbf{Q}}^{\eta} = \langle Y_{\mathbf{Q}}^{\eta\dagger} Y_{\mathbf{Q}}^{\eta} \rangle$ . Within the second-order Born–Markov approximation, we obtain a Boltzmann scattering equation describing the phonon-mediated relaxation dynamics of the exciton occupation<sup>45–48</sup>

$$\dot{N}_{\mathbf{Q}}^{\eta}(t) = \sum_{\xi \mathbf{Q}'} [\mathcal{W}_{\mathbf{Q} \mathbf{Q}'}^{\xi \eta} N_{\mathbf{Q}'}^{\xi}(t) - \mathcal{W}_{\mathbf{Q} \mathbf{Q}}^{\eta \xi} N_{\mathbf{Q}}^{\eta}(t)] \quad (1)$$

with the scattering tensor  $\mathcal{W}_{\mathbf{Q} \mathbf{Q}'}^{\xi \eta}$  containing the microscopically calculated transition rates between different exciton states driven by emission and absorption of optical and acoustic phonons. Here, we include a collisional broadening (third-order terms) to take into account a self-consistent temperature-dependent broadening that softens the energy conservation (more details can be found in the [Supporting Information](#)). Note that we focus on the low-density regime without doping, where exciton–exciton processes (such as Auger-type scattering) and more involved Coulomb complexes (such as biexcitons and trions) can be neglected.<sup>49</sup> This equation allows us to track the relaxation cascade of excitons from an initially created hot distribution toward the ground state resolved in time and momentum.

In the following, we focus on the analysis of the time evolution of momentum-integrated exciton occupation  $N^{\eta}(t) = \sum_{\mathbf{Q}} N_{\mathbf{Q}}^{\eta}(t)$  and energy- and momentum-resolved occupation  $N(E, \mathbf{Q}, t) = \sum_{\eta} N_{\mathbf{Q}}^{\eta}(t) \delta(E - E_{\mathbf{Q}}^{\eta})$ . In addition, we introduce the density of in-scattering states  $\text{DO}\Gamma_{\text{in}}^{\eta}(E, t) = \sum_{\xi \mathbf{Q}'} \mathcal{W}_{\mathbf{Q}, \mathbf{Q}=0}^{\xi \eta}(t) \delta(E - E_{\mathbf{Q}}^{\xi})$ , quantifying the density of states contributing the most to the influx of excitons to a specific state  $\eta$ . To perform a quantitative analysis and be able to compare our predictions with experiments, we compute the time- and energy-dependent photoluminescence intensity  $I_{\text{PL}}(E, t)$  using<sup>50</sup>

$$I_{\text{PL}}(E, t) \propto \sum_{\eta, \sigma} \gamma_{\sigma}^{\eta} N_{\mathbf{Q}=0}^{\eta}(t) \mathcal{L}_{\Gamma^{\eta}}(E_{\mathbf{Q}=0}^{\eta} - E) \quad (2)$$

with  $\gamma_{\sigma}^{\eta}$  containing the optical selection rules for moiré excitons and  $\mathcal{L}_{\Gamma^{\eta}}$  denoting the Cauchy–Lorentz distribution. The width  $\Gamma^{\eta} = \hbar/2 \sum_{\xi, \mathbf{Q}'} \mathcal{W}_{\mathbf{Q}=0, \mathbf{Q}}^{\eta \xi}$  is determined by evaluating the exciton scattering tensor at  $\mathbf{Q} = 0$ . To be able to quantify the efficiency of the relaxation process, we introduce the relaxation time  $\tau_{\eta \rightarrow \xi} = 1/(\tilde{\Gamma}^{\eta \rightarrow \xi})$  (where

$\Gamma_{\mathbf{Q}}^{\eta \rightarrow \xi} = \hbar/2 \sum_{\mathbf{Q}'} \mathcal{W}_{\mathbf{Q}\mathbf{Q}'}^{\eta\xi}$  and  $\bar{\Gamma}$  represents the momentum average) describing the scattering efficiency from the state  $\eta$  to  $\xi$ . Further details on the theoretical approach can be found in the [Supporting Information](#).

We now apply the theoretical framework described above and numerically evaluate eq 1 for the specific case of the twisted MoSe<sub>2</sub>–WSe<sub>2</sub> heterostructure, focusing on small twist angles ( $\approx 1^\circ$ ) and low temperatures ( $\approx 40$  K). Our aim is to study the relaxation cascade of injected hot interlayer excitons in the presence of a periodic moiré potential ([Figure 1a](#)).

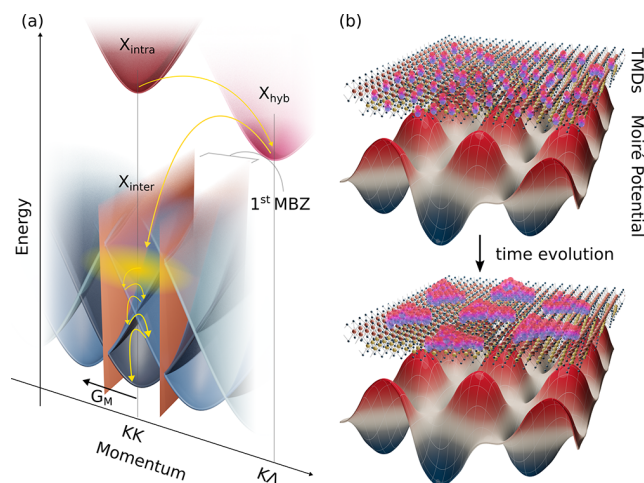


**Figure 1.** Sketch of exciton dynamics in a twisted TMD heterostructure. (a) After optical excitation of intralayer excitons ( $X_{\text{intra}}$ ) in one of the layers, exciton population relaxes to the energetically lowest states (interlayer excitons  $X_{\text{inter}}$  in the case of MoSe<sub>2</sub>–WSe<sub>2</sub> investigated here) via momentum-dark hybrid excitons  $X_{\text{hyb}}$ . We focus here on microscopic modeling the relaxation cascade of hot interlayer excitons. We depict the exemplary case of parabolic bands, in which a new periodicity ( $G_M$  reciprocal lattice moiré vector) arises. In the case of small twist angles, there is, in addition to the new periodicity, a change in the band curvature, resulting in flat bands. This modifies drastically the allowed scattering channels. (b) Exciton relaxation in momentum space is reflected by the change of exciton localization in real space: the thermalization process brings the exciton population (purple dots) from a delocalized phase to the most favorable configuration of trapped states.

Typically in heterostructures with a high degree of hybridization, intralayer excitons are optically excited in one of the two layers and they then scatter down to the energetically lower interlayer exciton states.<sup>14,15</sup> Here, the excess energy is different from zero, and the last step of the dissipation process requires an intravalley phonon-mediated cascade in the range of energies heavily affected by the moiré potential. In this work, we focus on the final stage of this dynamics, i.e., the relaxation cascade within the series of interlayer moiré minibands. Atomic reconstruction is typically more important at smaller twist angles and has thus been neglected here.<sup>51</sup>

We start our analysis by investigating how the presence of a moiré potential modifies the interlayer exciton landscape in the twisted MoSe<sub>2</sub>–WSe<sub>2</sub> heterostructure. The energy landscape is obtained by solving the eigenvalue problem including the angle-dependent moiré potential. This gives us access to the new eigenenergies of the system,  $E_{\mathbf{Q}}^{\eta}$ , as shown in [Figure 2](#). We can distinguish nearly flat bound states ( $X_{0,1,2,3}$ ), characterized by wave functions localized around minima of the moiré

potential, and free states ( $X_{\text{free}}$ ) which show a more delocalized wave function.<sup>19</sup> After having calculated the exciton energy landscape, our first goal is to reveal the microscopic origin of the measured long lifetimes of the excited moiré state.<sup>36,32</sup> To address this question, we analyze the phonon-driven transition rates and the relaxation time from the excited states ( $X_{1,2}$ ) to the ground state  $X_0$ .

We first investigate the time evolution of the exciton occupation  $N(E, \mathbf{Q})$  that we plot superimposed on the moiré exciton band structure in [Figure 2](#). This way, we can directly track the relaxation pathway of excitons. We start with an initial exciton distribution in the energy range of free states, specifically around 40–50 meV away from the ground interlayer exciton state ([Figure 2a](#)). The subsequent thermalization of moiré excitons can be described in terms of two competing processes, driven by emission of optical and acoustic phonons, respectively. Scattering with acoustic phonons, characterized by a small transfer of energy and momentum, populates the adjacent energy bands, i.e., the intermediate states  $X_3$ . The scattering with optical phonons makes excitons dissipate faster and relax further down to the first excited states  $X_{1,2}$  (cf. the arrows in [Figure 2b](#)).

To better understand the relaxation path of excitons, we show in [Figure 2b,c](#) the density of in-scattering states  $\text{DO}\Gamma_{\text{in}}^{\eta}$  for the ground state  $\mu = 0$  and for the first excited states  $\mu = 1, 2$ . This quantity discloses the energy window of initial states contributing the most to the population of the final state  $\mu$ . Considering the case of the first excited states, we find that the energy window including the free states that have been initially populated contributes the most ([Figure 2b](#)). On the other hand, the ground state is mostly populated from the in-scattering from the intermediate states  $X_3$  ([Figure 2c](#)). As a result, the occupation of  $X_{1,2}$  that is driven by emission of optical phonons occurs on a much faster time scale of a few tens of femtoseconds compared to the population of the ground state on a time scale of hundreds of fs. For the latter to be filled, excitons have first to relax via acoustic phonons to the intermediate states  $X_3$ . [Figure 2d](#) illustrates that, interestingly, even for longer times of a few picoseconds, the occupation of the ground state remains clearly lower than the one of the first excited states, in contrast to what we would expect from a thermalized distribution. This indicates the emergence of a pronounced relaxation bottleneck that keeps the exciton occupation out of thermal equilibrium.

Note that the initial condition chosen for the study is based on the observation of the  $\text{DO}\Gamma_{\text{in}}^1(E)$ . In order to obtain the strongest out-of-equilibrium distribution of excitons, one has to excite in an energy window in which the population is scattering faster to  $X_{1,2}$  than to  $X_3$ . Exciting in a different energy window changes the quantitative distribution of the excitonic occupation of  $X_0$  and  $X_{1,2}$ , but our key result, i.e. the emergence of a relaxation bottleneck giving rise to nonthermal exciton distributions at low temperatures, remains unaffected. A more detailed discussion can be found in the [Supporting Information](#), where we explicitly show the impact of different initial conditions on the relaxation dynamics of moiré excitons.

To be able to compare our predictions with experiments, we determine the consequences of the predicted nonequilibrium exciton occupation on time-dependent PL spectra by evaluating eq 2. We find a clearly higher emission from the first excited state  $X_{1,2}$  than from the ground state  $X_0$  ([Figure 3](#)), reflecting directly the higher occupation of  $X_{1,2}$  shown in [Figure 2d](#). This finding is in excellent qualitative agreement

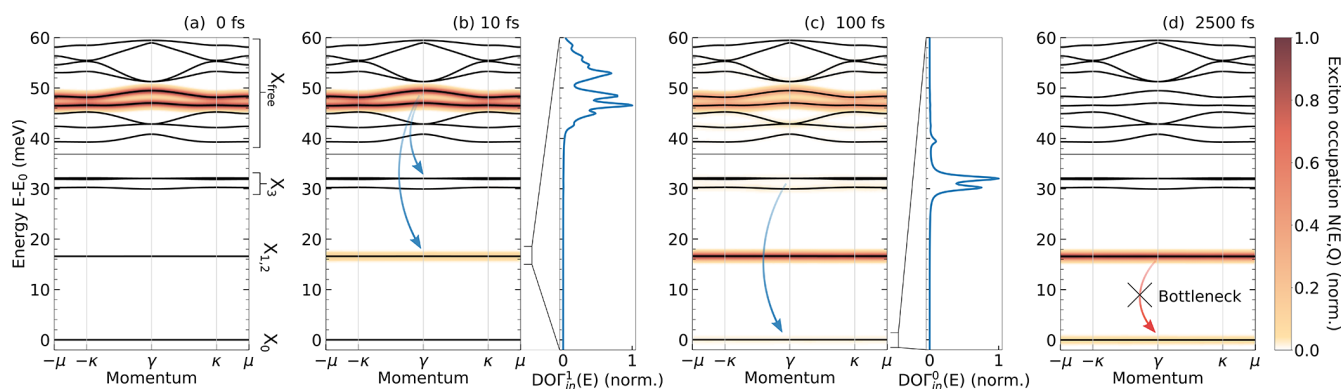


**Figure 2.** Interlayer exciton energy landscape of the MoSe<sub>2</sub>-WSe<sub>2</sub> heterostructure (with a 1° twist angle) consisting of bound states ( $X_{0,1,2}$ ), intermediate states ( $X_3$ ), and free states ( $X_{\text{free}}$ ). All energies are plotted with respect to the ground state ( $E_0$ ). We show superimposed on the bands the energy- and momentum-resolved exciton occupation (red-orange shaded) at subsequent steps of the dynamics at 40 K. (a) We start at 0 fs with an initial hot distribution of excitons (created through scattering from optically excited intralayer exciton states, cf. Figure 1a). (b) At an early stage of the dynamics (10 fs), the emission of optical phonon drives the population predominantly to the first degenerate excited states  $X_{1,2}$ . (c)  $X_0$  is occurring at a much slower speed, driven by the filling of intermediate states  $X_3$  due to the scattering with acoustic phonons (100 fs). This different energy dependence in the relaxation becomes clear by analyzing the density of in-scattering states  $\text{DO}\Gamma_{\text{in}}^0(E)$  (see the text for the definition) for  $X_0$  and  $X_{1,2}$ , illustrating which energy window contributes the most to the increase of the exciton population of these lower states. (d) In the final stage of the dynamics on the time scale of a few ps, we observe a bottleneck effect, i.e. the scattering to the ground state is almost completely suppressed. This results in a strong out-of-equilibrium exciton distribution, where excited states show a higher occupation than the ground state.

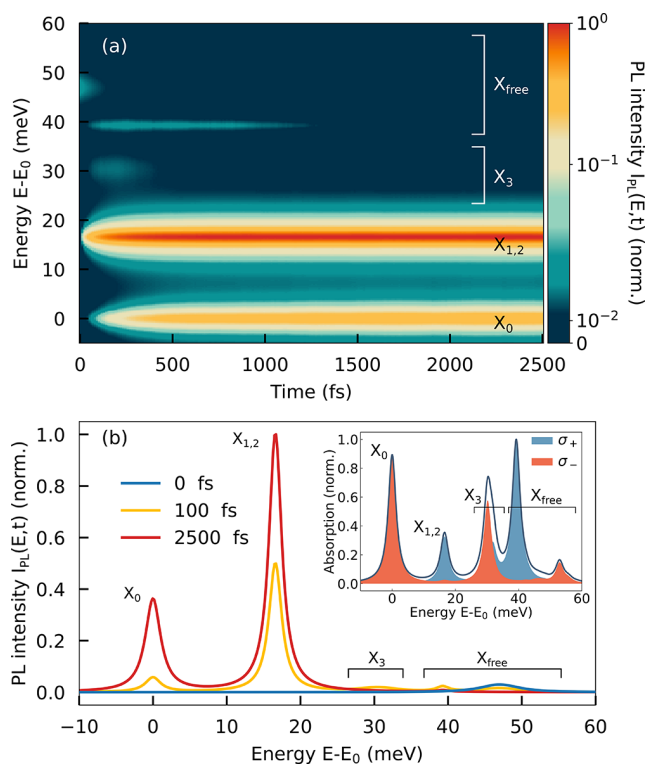


**Figure 3.** (a) Photoluminescence spectrum as a function of energy and time and (b) at different fixed time cuts. We include the absorption spectrum as an inset in (b) to highlight the optical selection rules of different states. Here, the solid gray line shows the total absorption, while red and blue lines denote the contribution of the  $\sigma_-$  and  $\sigma_+$  circularly polarized light, respectively.

with experimental measurements.<sup>18</sup> According to eq 2, the PL intensity depends on the exciton occupation in a certain state weighted by its optical matrix element. The latter describes the oscillator strength of the states and can be directly accessed in a linear absorption spectrum (cf. inset to Figure 3b). We find that the absorption peak of  $X_{1,2}$  has half intensity with respect

to the ground state  $X_0$  and that only one of the two degenerate states  $X_{1,2}$  is optically active.<sup>19</sup> For these reasons, a higher PL peak of  $X_{1,2}$  means that its occupation has to be significantly larger than the one of  $X_0$ , which is only the case for a highly nonequilibrium exciton distribution emerging as a consequence of a pronounced relaxation bottleneck. Note that the predicted excited state peaks can be well differentiated from other multiexcitonic features in temperature- and power-dependent studies.

To further characterize the relaxation bottleneck effect, we performed a temperature-dependent study of the exciton relaxation dynamics. A suitable quantity to track the emergence of the bottleneck is the relaxation time from the first excited states to the ground state,  $\tau_{1 \rightarrow 0}$ . We directly compare the momentum-integrated time-dependent exciton occupation at 40 and 300 K (cf. Figure 4). We find qualitatively different exciton dynamics: in the low-temperature case, we observe a strong out-of-equilibrium distribution of excitons, with excited states  $X_{1,2}$  containing a roughly 8 times larger population than the ground state  $X_0$  (Figure 4a). This behavior is not seen at room temperature, where the initially hot excitons dissipate all their excess energy, reaching a Boltzmann distribution on a subpicosecond time scale (cf. the solid and dashed lines in Figure 4b). This hints at a temperature-dependent activation of the bottleneck effect and is further confirmed by analyzing the temperature-dependent relaxation time  $\tau_{1 \rightarrow 0}$ , shown in Figure 4b. Here, we find a huge variation of several orders of magnitude in  $\tau_{1 \rightarrow 0}$ : for temperatures lower than 100 K, the transition from  $X_{1,2}$  to  $X_0$  becomes drastically slowed down, resulting in an extremely large relaxation time  $\tau_{1 \rightarrow 0}$  being on a time scale comparable to or even longer than the recombination time of interlayer excitons of typically  $\approx 10^2$ – $10^3$  ps.<sup>53</sup> In addition to the temperature dependence, we show in the inset of Figure 4c a twist-angle-dependent study for a fixed temperature of 40 K. This analysis clearly reveals that in addition to the temperature-dependent activation of the bottleneck, also the twist angle plays a crucial role. Moving from the small ( $\leq 2^\circ$ ) to the large ( $\geq 3^\circ$ ) twist angle limit, we observe the same behavior found in the temperature-

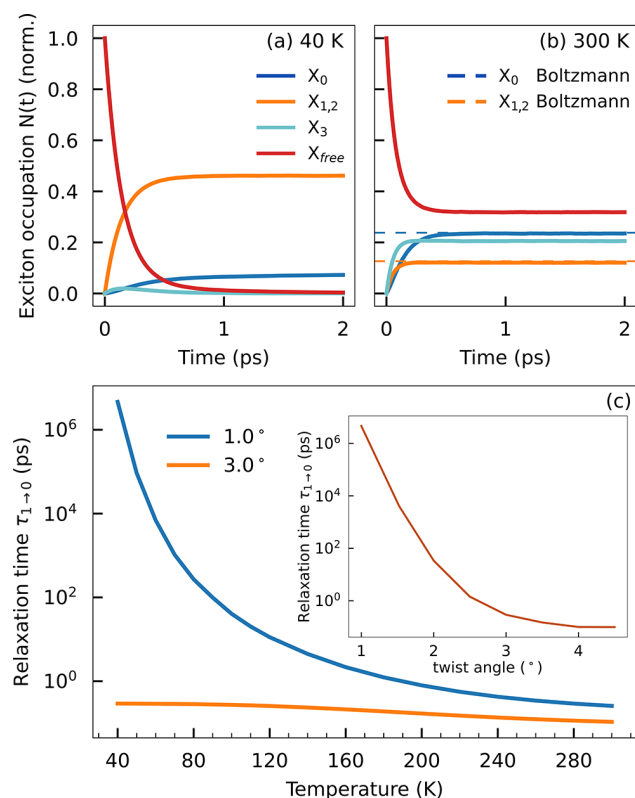


**Figure 4.** Momentum-integrated exciton dynamics at (a) 40 K and (b) 300 K. At low temperatures, we observe a much larger stationary occupation of the first excited states  $X_{1,2}$ , highlighting the importance of the relaxation bottleneck leading to a strong deviation from a thermal distribution. In contrast, at higher temperatures, the exciton occupation clearly relaxes into a Boltzmann distribution (dashed lines). (c) The relaxation time  $\tau_{1 \rightarrow 0}$  from the first excited state to the ground state as a function of temperature, showing that the bottleneck effect becomes significantly strong at temperatures smaller than approximately 100 K, leading to recombination times in the ns or even  $\mu$ s range. In the inset, we plot the relaxation time  $\tau_{1 \rightarrow 0}$  as a function of the twist angle at a fixed temperature of 40 K, showing the strongly pronounced bottleneck effect in the low twist angle limit ( $\leq 2^\circ$ ).

dependent analysis, i.e. a variation of several orders of magnitude in the relaxation time.

These temperature and twist angle studies help us reveal the microscopic origin of the bottleneck effect. This can be understood in terms of exciton energies and the center-of-mass momenta. The conservation of energy contained in  $\tilde{D}_{\mathbf{Q}\mathbf{Q}'}^{\eta_j^i}$ , in combination with the flatness of the bands appearing in the small twist angle limit, impose a strong boundary condition to the available scattering partners for this transition. Given the excitonic flat dispersion for both the initial ( $X_{1,2}$ ) and the final state ( $X_0$ ), the energy conservation plays the key role. The energy difference between  $X_{1,2}$  and  $X_0$  is  $\approx 16$  meV. Acoustic phonons, given their linear dispersion, would require a huge momentum transfer to be able to dissipate this amount of energy. The momentum required is larger than 10 mini Brillouin zones (mBZs), where the exciton–phonon matrix element becomes negligibly small, as the overlap of the moiré exciton wave functions of the involved states is mostly localized in the first mBZ.<sup>19</sup> In contrast, optical phonons exhibit an energy of  $\approx 20$ – $25$  meV that is closer to the energy condition

required for the transition. The activation of this channel is explained in terms of temperature-dependent broadening of the phonon-induced dephasing.

Given the energetic arguments presented above, the key quantities for the emergence of the bottleneck are the dispersion of the first excited state and the ground state and the energy gap between them. Increasing the twist angle significantly modifies the dispersion of exciton bands toward a regular parabolic shape. At the same time, the gap between the bands becomes smaller, allowing for more scattering partners for both acoustic and optical phonon-driven scattering. A direct consequence is the decreasing importance of the relaxation bottleneck at the larger twist angles. The relaxations dynamics for  $3^\circ$  is shown and further discussed in the [Supporting Information](#).

The moiré exciton relaxation dynamics discussed so far in the momentum space also has a consequence in real space, modifying the equilibrium moiré exciton distribution within the moiré trap. A detailed analysis can be found in the [Supporting Information](#).

In this study, we have investigated the relaxation dynamics of interlayer excitons in a twisted  $\text{MoSe}_2$ – $\text{WSe}_2$  heterostructure exhibiting flat moiré bands. Based on a microscopic model including the twist-angle-dependent moiré potential, we demonstrate the relaxation cascade of an initial hot distribution of interlayer excitons and identify a pronounced relaxation bottleneck at low temperatures and low twist angles. This drastically slows the thermalization of excitons, resulting in quasi-stationary exciton occupations far away from the Boltzmann distribution. A direct consequence is a higher occupation of excited exciton states explaining their larger emission compared to the ground state, in excellent qualitative agreement with experimental observations in photoluminescence spectra of twisted TMD heterostructures. Furthermore, we studied the temperature-dependent activation of the relaxation bottleneck, tracing back its microscopic origin to a combination of the energy separation and the flatness of the involved moiré exciton sub-bands. Overall, our study provides important microscopic insights into the exciton relaxation behavior in the presence of flat moiré bands in twisted van der Waals heterostructures.

## ■ ASSOCIATED CONTENT

### Supporting Information

The Supporting Information is available free of charge at <https://pubs.acs.org/doi/10.1021/acs.nanolett.4c00450>.

Derivation of the main Hamiltonian in the moiré exciton formalism, definition of the scattering tensors and details on the quantities introduced in the main text, and additional studies on the self-consistent out-scattering rate, initial excitation conditions, twist angle dependence of the bottleneck effect, and moiré exciton distribution in real space ([PDF](#))

## ■ AUTHOR INFORMATION

### Corresponding Author

Giuseppe Meneghini – Department of Physics, Philipps University of Marburg, 35037 Marburg, Germany;  
[orcid.org/0000-0002-1889-2380](https://orcid.org/0000-0002-1889-2380);  
 Email: [giuseppe.meneghini@physik.uni-marburg.de](mailto:giuseppe.meneghini@physik.uni-marburg.de)

## Authors

Samuel Brem – Department of Physics, Philipps University of Marburg, 35037 Marburg, Germany; [orcid.org/0000-0001-8823-1302](https://orcid.org/0000-0001-8823-1302)

Ermin Malic – Department of Physics, Philipps University of Marburg, 35037 Marburg, Germany

Complete contact information is available at:

<https://pubs.acs.org/10.1021/acs.nanolett.4c00450>

## Notes

The authors declare no competing financial interest.

## ACKNOWLEDGMENTS

This project has received funding from the Deutsche Forschungsgemeinschaft via CRC 1083 and the project 512604469.

## REFERENCES

- (1) Liu, Y.; Weiss, N. O.; Duan, X.; Cheng, H.-C.; Huang, Y.; Duan, X. Van der waals heterostructures and devices. *Nature Reviews Materials* **2016**, *1*, 1–17.
- (2) Li, C.; Cao, Q.; Wang, F.; Xiao, Y.; Li, Y.; Delaunay, J.-J.; Zhu, H. Engineering graphene and tmds based van der waals heterostructures for photovoltaic and photoelectrochemical solar energy conversion. *Chem. Soc. Rev.* **2018**, *47*, 4981–5037.
- (3) Wilson, N. P.; Yao, W.; Shan, J.; Xu, X. Excitons and emergent quantum phenomena in stacked 2d semiconductors. *Nature* **2021**, *599*, 383–392.
- (4) Hagel, J.; Brem, S.; Linderalv, C.; Erhart, P.; Malic, E. Exciton landscape in van der waals heterostructures. *Physical Review Research* **2021**, *3*, No. 043217.
- (5) Rivera, P.; Schaibley, J. R.; Jones, A. M.; Ross, J. S.; Wu, S.; Aivazian, G.; Klement, P.; Seyler, K.; Clark, G.; Ghimire, N. J.; Yan, J.; Mandrus, D. G.; Yao, W.; Xu, X. Observation of long-lived interlayer excitons in monolayer mose<sub>2</sub>-wse<sub>2</sub> heterostructures. *Nat. Commun.* **2015**, *6*, 6242.
- (6) Kojima, K.; Lim, H. E.; Liu, Z.; Zhang, W.; Saito, T.; Nakanishi, Y.; Endo, T.; Kobayashi, Y.; Watanabe, K.; Taniguchi, T.; Matsuda, K.; Maniwa, Y.; Miyauchi, Y.; Miyata, Y. Restoring the intrinsic optical properties of cvd-grown mos<sub>2</sub> monolayers and their heterostructures. *Nanoscale* **2019**, *11*, 12798–12803.
- (7) Merkl, P.; Mooshammer, F.; Steinleitner, P.; Girnguber, A.; Lin, K.-Q.; Nagler, P.; Holler, J.; Schuller, C.; Lupton, J. M.; Korn, T.; Ovesen, S.; Brem, S.; Malic, E.; Huber, R. Ultrafast transition between exciton phases in van der waals heterostructures. *Nature materials* **2019**, *18*, 691–696.
- (8) Ross, J. S.; Rivera, P.; Schaibley, J.; Lee-Wong, E.; Yu, H.; Taniguchi, T.; Watanabe, K.; Yan, J.; Mandrus, D.; Cobden, D.; Yao, W.; Xu, X. Interlayer exciton optoelectronics in a 2d heterostructure p–n junction. *Nano Lett.* **2017**, *17*, 638–643.
- (9) Jin, C.; Regan, E. C.; Wang, D.; Iqbal Bakti Utama, M.; Yang, C.-S.; Cain, J.; Qin, Y.; Shen, Y.; Zheng, Z.; Watanabe, K.; Taniguchi, T.; Tongay, S.; Zettl, A.; Wang, F. Identification of spin, valley and moiré quasi-angular momentum of interlayer excitons. *Nat. Phys.* **2019**, *15*, 1140–1144.
- (10) Tan, Q.; Rasmita, A.; Li, S.; Liu, S.; Huang, Z.; Xiong, Q.; Yang, S. A.; Novoselov, K. S.; Gao, W.-b. Layer-engineered interlayer excitons. *Science Advances* **2021**, *7*, No. eabh0863.
- (11) Erkensten, D.; Brem, S.; Perea-Causin, R.; Hagel, J.; Tagarelli, F.; Lopriore, E.; Kis, A.; Malic, E. Electrically tunable dipolar interactions between layer-hybridized excitons. *Nanoscale* **2023**, *15*, 11064.
- (12) Tagarelli, F.; Lopriore, E.; Erkensten, D.; Perea-Causin, R.; Brem, S.; Hagel, J.; Sun, Z.; Pasquale, G.; Watanabe, K.; Taniguchi, T.; Malic, E.; Kis, A. Electrical control of hybrid exciton transport in a van der waals heterostructure. *Nat. Photonics* **2023**, *17*, 1–7.
- (13) Jin, C.; Ma, E. Y.; Karni, O.; Regan, E. C.; Wang, F.; Heinz, T. F. Ultrafast dynamics in van der waals heterostructures. *Nature Nanotechnol.* **2018**, *13*, 994–1003.
- (14) Meneghini, G.; Brem, S.; Malic, E. Ultrafast phonon-driven charge transfer in van der waals heterostructures. *Natural Sciences* **2022**, *2*, No. e20220014.
- (15) Schmitt, D.; Bange, J. P.; Bennecke, W.; AlMutairi, A.; Meneghini, G.; Watanabe, K.; Taniguchi, T.; Steil, D.; Luke, D. R.; Weitz, R. T.; Steil, S.; Jansen, G. S. M.; Brem, S.; Malic, E.; Hofmann, S.; Reutzel, M.; Mathias, S. Formation of moiré interlayer excitons in space and time. *Nature* **2022**, *608*, 499–503.
- (16) Mak, K. F.; Shan, J. Semiconductor moiré materials. *Nat. Nanotechnol.* **2022**, *17*, 686–695.
- (17) Andrei, E. Y.; Efetov, D. K.; Jarillo-Herrero, P.; MacDonald, A. H.; Mak, K. F.; Senthil, T.; Tutuc, E.; Yazdani, A.; Young, A. F. The marvels of moiré materials. *Nature Reviews Materials* **2021**, *6*, 201–206.
- (18) Tran, K.; Moody, G.; Wu, F.; Lu, X.; Choi, J.; Kim, K.; Rai, A.; Sanchez, D. A.; Quan, J.; Singh, A.; Embley, J.; Zepeda, A.; Campbell, M.; Autry, T.; Taniguchi, T.; Watanabe, K.; Lu, N.; Banerjee, S. K.; Silverman, K. L.; Kim, S.; Tutuc, E.; Yang, L.; MacDonald, A. H.; Li, X. Evidence for moiré excitons in van der waals heterostructures. *Nature* **2019**, *567*, 71–75.
- (19) Brem, S.; Linderalv, C.; Erhart, P.; Malic, E. Tunable phases of moiré excitons in van der waals heterostructures. *Nano Lett.* **2020**, *20*, 8534–8540.
- (20) Huang, D.; Choi, J.; Shih, C.-K.; Li, X. Excitons in semiconductor moiré superlattices. *Nat. Nanotechnol.* **2022**, *17*, 227–238.
- (21) Choi, W.; Choudhary, N.; Han, G. H.; Park, J.; Akinwande, D.; Lee, Y. H. Recent development of two-dimensional transition metal dichalcogenides and their applications. *Mater. Today* **2017**, *20*, 116–130.
- (22) Yu, H.; Liu, G.-B.; Tang, J.; Xu, X.; Yao, W. Moiré excitons: From programmable quantum emitter arrays to spin-orbit-coupled artificial lattices. *Science advances* **2017**, *3*, No. e1701696.
- (23) Tran, K.; Choi, J.; Singh, A. Moiré and beyond in transition metal dichalcogenide twisted bilayers. *2D Materials* **2021**, *8*, No. 022002.
- (24) Shimazaki, Y.; Schwartz, I.; Watanabe, K.; Taniguchi, T.; Kroner, M.; Imamoglu, A. Strongly correlated electrons and hybrid excitons in a moiré heterostructure. *Nature* **2020**, *580*, 472–477.
- (25) Wang, L.; Shih, E.-M.; Ghiotto, A.; Xian, L.; Rhodes, D. A.; Tan, C.; Claassen, M.; Kennes, D. M.; Bai, Y.; Kim, B.; Watanabe, K.; Taniguchi, T.; Zhu, X.; Hone, J.; Rubio, A.; Pasupathy, A. N.; Dean, C. R. Correlated electronic phases in twisted bilayer transition metal dichalcogenides. *Nature materials* **2020**, *19*, 861–866.
- (26) Wu, F.; Lovorn, T.; Tutuc, E.; MacDonald, A. H. Hubbard model physics in transition metal dichalcogenide moiré bands. *Physical review letters* **2018**, *121*, No. 026402.
- (27) Kiese, D.; He, Y.; Hickey, C.; Rubio, A.; Kennes, D. M. TMDs as a platform for spin liquid physics: A strong coupling study of twisted bilayer WSe<sub>2</sub>. *APL Materials* **2022**, *10*, No. 031113.
- (28) Tang, Y.; Li, L.; Li, T.; Xu, Y.; Liu, S.; Barmak, K.; Watanabe, K.; Taniguchi, T.; MacDonald, A. H.; Shan, J.; Mak, K. F. Simulation of hubbard model physics in wse<sub>2</sub>/ws<sub>2</sub> moiré superlattices. *Nature* **2020**, *579*, 353–358.
- (29) Regan, E. C.; Wang, D.; Jin, C.; Bakti Utama, M. I.; Gao, B.; Wei, X.; Zhao, S.; Zhao, W.; Zhang, Z.; Yumigeta, K.; Blei, M.; Carlstrom, J. D.; Watanabe, K.; Taniguchi, T.; Tongay, S.; Crommie, M.; Zettl, A.; Wang, F. Mott and generalized wigner crystal states in wse<sub>2</sub>/ws<sub>2</sub> moiré superlattices. *Nature* **2020**, *579*, 359–363.
- (30) Li, T.; Jiang, S.; Li, L.; Zhang, Y.; Kang, K.; Zhu, J.; Watanabe, K.; Taniguchi, T.; Chowdhury, D.; Fu, L.; Shan, J.; Mak, K. F. Continuous mott transition in semiconductor moiré superlattices. *Nature* **2021**, *597*, 350–354.
- (31) Shi, W.; Ye, J.; Zhang, Y.; Suzuki, R.; Yoshida, M.; Miyazaki, J.; Inoue, N.; Saito, Y.; Iwasa, Y. Superconductivity series in transition metal dichalcogenides by ionic gating. *Sci. Rep.* **2015**, *5*, No. 12534.

- (32) Qiu, D.; Gong, C.; Wang, S.; Zhang, M.; Yang, C.; Wang, X.; Xiong, J. Recent advances in 2d superconductors. *Adv. Mater.* **2021**, *33*, No. 2006124.
- (33) Pan, H.; Wu, F.; Das Sarma, S. Quantum phase diagram of a moiré-hubbard model. *Phys. Rev. B* **2020**, *102*, No. 201104.
- (34) Gotting, N.; Lohof, F.; Gies, C. Moiré-bose-hubbard model for interlayer excitons in twisted transition metal dichalcogenide heterostructures. *Phys. Rev. B* **2022**, *105*, No. 165419.
- (35) Xu, Y.; Kang, K.; Watanabe, K.; Taniguchi, T.; Mak, K. F.; Shan, J. A tunable bilayer hubbard model in twisted wse2. *Nat. Nanotechnol.* **2022**, *17*, 934–939.
- (36) Choi, J.; Florian, M.; Steinhoff, A.; Erben, D.; Tran, K.; Kim, D. S.; Sun, L.; Quan, J.; Claassen, R.; Majumder, S.; Hollingsworth, J. A.; Taniguchi, T.; Watanabe, K.; Ueno, K.; Singh, A.; Moody, G.; Jahnke, F.; Li, X. Twist angle-dependent interlayer exciton lifetimes in van der waals heterostructures. *Phys. Rev. Lett.* **2021**, *126*, No. 047401.
- (37) Li, Z.; Lu, X.; Cordovilla Leon, D. F.; Lyu, Z.; Xie, H.; Hou, J.; Lu, Y.; Guo, X.; Kaczmarek, A.; Taniguchi, T.; Watanabe, K.; Zhao, L.; Yang, L.; Deotare, P. B. Interlayer exciton transport in mose2/wse2 heterostructures. *ACS Nano* **2021**, *15*, 1539–1547.
- (38) Jin, C.; Regan, E. C.; Yan, A.; Iqbal Bakti Utama, M.; Wang, D.; Zhao, S.; Qin, Y.; Yang, S.; Zheng, Z.; Shi, S.; Watanabe, K.; Taniguchi, T.; Tongay, S.; Zettl, A.; Wang, F. Observation of moiré excitons in wse2/ws2 heterostructure superlattices. *Nature* **2019**, *567*, 76–80.
- (39) Brem, S.; Malic, E. Bosonic delocalization of dipolar moiré excitons. *Nano Lett.* **2023**, *23*, 4627–4633.
- (40) Ovesen, S.; Brem, S.; Linderalv, C.; Kuisma, M.; Korn, T.; Erhart, P.; Selig, M.; Malic, E. Interlayer exciton dynamics in van der waals heterostructures. *Communications Physics* **2019**, *2*, 1–8.
- (41) Brem, S.; Lin, K.-Q.; Gillen, R.; Bauer, J. M.; Maultzsch, J.; Lupton, J. M.; Malic, E. Hybridized intervalley moiré excitons and flat bands in twisted wse 2 bilayers. *Nanoscale* **2020**, *12*, 11088–11094.
- (42) Cappelluti, E.; Roldan, R.; Silva-Guillen, J. A.; Ordejon, P.; Guinea, F. Tight-binding model and direct-gap/indirect-gap transition in single-layer and multilayer mos 2. *Phys. Rev. B* **2013**, *88*, No. 075409.
- (43) Gillen, R.; Maultzsch, J. Interlayer excitons in MoSe<sub>2</sub>/WSe<sub>2</sub> heterostructures from first principles. *Phys. Rev. B* **2018**, *97*, No. 165306.
- (44) Merkl, P.; Mooshammer, F.; Brem, S.; Girnguber, A.; Lin, K.-Q.; Weigl, L.; Liebich, M.; Yong, C.-K.; Gillen, R.; Maultzsch, J.; Lupton, J. M.; Malic, E.; Huber, R. Twist-tailoring coulomb correlations in van der waals homobilayers. *Nat. Commun.* **2020**, *11*, 1–7.
- (45) Thränhardt, A.; Kuckenburg, S.; Knorr, A.; Meier, T.; Koch, S. W. Quantum theory of phonon-assisted exciton formation and luminescence in semiconductor quantum wells. *Phys. Rev. B* **2000**, *62*, 2706.
- (46) Haug, H.; Koch, S. W. *Quantum theory of the optical and electronic properties of semiconductors*; World Scientific: 2009).
- (47) Selig, M.; Berghauser, G.; Richter, M.; Bratschitsch, R.; Knorr, A.; Malic, E. Dark and bright exciton formation, thermalization, and photoluminescence in monolayer transition metal dichalcogenides. *2D Materials* **2018**, *5*, No. 035017.
- (48) Brem, S.; Selig, M.; Berghauser, G.; Malic, E. Exciton relaxation cascade in two-dimensional transition metal dichalcogenides. *Sci. Rep.* **2018**, *8*, 1–8.
- (49) Erkensten, D.; Brem, S.; Wagner, K.; Gillen, R.; Perea-Causin, R.; Ziegler, J. D.; Taniguchi, T.; Watanabe, K.; Maultzsch, J.; Chernikov und, A.; Malic, E. Dark exciton-exciton annihilation in monolayer transition-metal dichalcogenides. *Phys. Rev. B* **2021**, *104*, No. L241406.
- (50) Rossi, F.; Kuhn, T. Theory of ultrafast phenomena in photoexcited semiconductors. *Rev. Mod. Phys.* **2002**, *74*, 895.
- (51) Weston, A.; Zou, Y.; Enaldiev, V.; Summerfield, A.; Clark, N.; Zolyomi, V.; Graham, A.; Yelgel, C.; Magorrian, S.; Zhou, M.; Zultak, J.; Hopkinson, D.; Barinov, A.; Bointon, T. H.; Kretinin, A.; Wilson, N. R.; Beton, P. H.; Fal'ko, V. I.; Haigh, S. J.; Gorbachev, R. Atomic reconstruction in twisted bilayers of transition metal dichalcogenides. *Nat. Nanotechnol.* **2020**, *15*, 592–597.
- (52) Tan, Q.; Rasmita, A.; Zhang, Z.; Novoselov, K. S.; Gao, W.-b. Signature of cascade transitions between interlayer excitons in a moiré superlattice. *Phys. Rev. Lett.* **2022**, *129*, No. 247401.
- (53) Jiang, Y.; Chen, S.; Zheng, W.; Zheng, B.; Pan, A. Interlayer exciton formation, relaxation, and transport in tmd van der waals heterostructures. *Light: Science & Applications* **2021**, *10*, 72.

# Excitonic thermalization bottleneck in twisted TMD heterostructures

## Supplementary Information

Giuseppe Meneghini,<sup>1,\*</sup> Samuel Brem,<sup>1</sup> and Ermin Malic<sup>1</sup>

<sup>1</sup>*Department of Physics, Philipps University of Marburg, 35037 Marburg, Germany*

### THEORETICAL APPROACH

In this section we introduce a detailed derivation of the equations of motion shown in the main text.

#### Exciton bandstructure and dynamics

First, we introduce the change of basis to obtain the moiré Hamilton operator. The starting point is the Hamiltonian in second quantization describing a TMD bilayer system<sup>1,2</sup>, where we include the free exciton energy and the exciton-phonon interaction yielding

$$H = \sum_{\mu\mathbf{Q}} \mathcal{E}_{\mathbf{Q}}^{\mu} X_{\mathbf{Q}}^{\mu\dagger} X_{\mathbf{Q}}^{\mu} + \sum_{j\mathbf{Q}\mathbf{q}\mu\nu} \tilde{\mathcal{D}}_{j\mathbf{q}\mathbf{Q}}^{\mu\nu} X_{\mathbf{Q}+\mathbf{q}}^{\nu\dagger} X_{\mathbf{Q}}^{\mu} b_{j,\mathbf{q}} + h.c. \quad (1)$$

Here, we use a valley-local approach including the exciton quantum number  $\mu = (n^{\mu}, \zeta_e^{\mu}, \zeta_h^{\mu}, l_e^{\mu}, l_h^{\mu})$ , where  $n$  describes the series of Rydberg-like states determining the relative electron-hole motion. Furthermore,  $\zeta_{e/h}$  and  $l_{e/h} = 0, 1$  correspond to the electron/hole valley and the layer index, respectively. We use also in the case of phonons a compound mode index  $j = (\kappa_j, \zeta_j^{ph}, l_j^{ph})$ , where  $\kappa$  is the phonon mode,  $\zeta$  and  $l$  phonon valley and layer respectively. Moreover, we have introduced the exciton annihilation (creation) operators  $X^{(\dagger)}$  and the exciton energy  $\mathcal{E}_{\mathbf{Q}}^{\mu} = \hbar^2 \mathbf{Q}^2 / (2M_{\mu}) + E_{\mu}^g + E_{\mu}^b$  at the center-of-mass momentum  $\mathbf{Q}$  with the mass  $M^{\mu} = m_e^{\mu} + m_h^{\mu}$  ( $m_{e/h}$  electron/hole mass). Here,  $E_{\mu}^g$  corresponds to the energy gap between the valence and the conduction band and  $E_{\mu}^b$  denotes the exciton binding energy, obtained from solving the Wannier equation.

For the exciton-phonon contribution, we have introduced the exciton-phonon coupling element  $\tilde{\mathcal{D}}_{j\mathbf{q}\mathbf{Q}}^{\nu\mu}$  reading

$$\begin{aligned} \tilde{\mathcal{D}}_{j,\mathbf{q},\mathbf{Q}}^{\mu\nu} = & D_{j,\mathbf{q}}^{\zeta_{\mu}^e \zeta_{\nu}^e c} \delta_{\zeta_{\mu}^h \zeta_{\nu}^h} \delta_{\zeta_{\nu}^e - \zeta_{\mu}^e, \zeta_j^{ph}} \delta_{l_{\nu}^e, l_j^{ph}} \delta_{l_{\nu}^e, l_{\mu}^e} \mathcal{F}^{\mu\nu} \left( \frac{m_h^{\nu}}{M^{\nu}} [\mathbf{q} + s_{\mu\nu} \mathbf{Q}] \right) + \\ & - D_{j,\mathbf{q}}^{\zeta_{\mu}^h \zeta_{\nu}^h v} \delta_{\zeta_{\mu}^e \zeta_{\nu}^e} \delta_{\zeta_{\nu}^h - \zeta_{\mu}^h, \zeta_j^{ph}} \delta_{l_{\nu}^h, l_j^{ph}} \delta_{l_{\nu}^h, l_{\mu}^h} \mathcal{F}^{\mu\nu} \left( -\frac{m_e^{\nu}}{M^{\nu}} [\mathbf{q} + s_{\mu\nu} \mathbf{Q}] \right). \end{aligned} \quad (2)$$

Here, we use the subscript  $ph$  to label phonon quantum numbers, and the terms  $\delta_{\zeta_{\mu}^e/h \zeta_{\nu}^e/h} \delta_{\zeta_{\nu}^h/e - \zeta_{\mu}^h/e, \zeta_j^{ph}}$  fix the momentum conservation of the scattering process with the phonon momentum  $\tilde{\mathbf{q}} = \zeta_j^{ph} + \mathbf{q}$ . In addition we have introduced the form factors  $\mathcal{F}^{\mu\nu}(\mathbf{q}) = \sum_{\mathbf{k}} \psi^{\mu*}(\mathbf{k}) \psi^{\nu}(\mathbf{k} + \mathbf{q})$  with the excitonic eigenfunction  $\psi^{\mu}(\mathbf{k})$ ,  $s_{\mu\nu} = 1 - M_{\nu}/M_{\mu}$ , and  $D_{j,\mathbf{q}}^{\zeta_m^{\lambda} \zeta_n^{\lambda}}$  as the electron/hole-phonon coupling element for TMD monolayers, taken from first-principle calculations<sup>3</sup>, yielding

$$\begin{aligned} D_{j,\mathbf{q}}^{\zeta_m^{\lambda} \zeta_n^{\lambda}} & \approx \sqrt{\frac{\hbar}{2\rho_{l_j^{ph}} A \Omega_{j\mathbf{q}}}} \tilde{D}_{j,\mathbf{q}}^{\zeta_m^{\lambda} \zeta_n^{\lambda}} \\ \text{with } \tilde{D}_{j,\mathbf{q}}^{\zeta_m^{\lambda} \zeta_n^{\lambda}} & = \begin{cases} \tilde{D}_{\zeta^{\lambda} \mathbf{q}}^{\lambda} & \text{if } \zeta_m^{\lambda} = \zeta_n^{\lambda} = \zeta \quad \text{and } \kappa_j = TA, LA \\ \tilde{D}_{\zeta_m^{\lambda} \zeta_n^{\lambda}}^{\lambda} & \text{else} \end{cases} \\ \text{and } \Omega_{j\mathbf{q}} & = \begin{cases} v_j \mathbf{q} & \text{if } \kappa_j = TA, LA \\ \Omega_j & \text{else.} \end{cases} \end{aligned} \quad (3)$$

Here,  $\lambda = c, v$  corresponds to the electronic band index,  $TA, LA$  to the acoustic transversal and longitudinal phonon modes, and with the "else" we refer to the optical modes and intervalley contributions. Furthermore,  $A$  denotes the area of the system,  $\rho_{l_j^{ph}}$  the surface mass density in the specific phonon layer  $l_j^{ph}$ , and  $v_j$  the sound velocity in the TMD layer. For our study, we focus only on low-energy excitations close to the ground state. Therefore, we can neglect the tunnelling-induced mixing of intra- and interlayer states, since the ground state in the investigated MoSe<sub>2</sub>-WSe<sub>2</sub> heterostructure is a KK interlayer exciton and the electron/hole tunneling is negligible around the K valley<sup>4</sup>. In this context, we treat the effect of the twist angle as an effective potential, the so-called moiré potential reading<sup>2</sup>

$$V_M = \sum_{\mathbf{Q}\tilde{\mathbf{g}}\mathbf{g}} \mathcal{M}_{\tilde{\mathbf{g}}\mathbf{g}} X_{\mathbf{Q}\tilde{\mathbf{g}}}^\dagger X_{\mathbf{Q}\mathbf{g}} \quad (4)$$

where the exciton quantum number  $\mu$  is fixed to be the exciton ground state and thus omitted in the following. Furthermore,  $\mathbf{Q} \in 1^{st}$  MBZ and  $\mathbf{g} = s_1 \mathbf{G}_1^M + s_2 \mathbf{G}_2^M$  with  $\mathbf{G}_{1/2}^M$  as the reciprocal moiré lattice vector and  $s_{1/2}$  as integers (where we use MBZ to refer to the moiré Brillouin zone accounting for the new periodicity arising from the moiré potential). The moiré matrix elements are defined as follows

$$\begin{aligned} \mathcal{M}_{\tilde{\mathbf{g}}\mathbf{g}} = & \Theta \left( \delta_{s_1, \tilde{s}_1 + (-1)^{l_e} \delta_{s_2, \tilde{s}_2} + \delta_{s_1, \tilde{s}_1} \delta_{s_2, \tilde{s}_2 + (-1)^{l_e}} + \delta_{s_1, \tilde{s}_1 + (-1)^{l_e} \delta_{s_2, \tilde{s}_2 + (-1)^{l_e}} \right) + \\ & + \Theta^* \left( \delta_{s_1, \tilde{s}_1 - (-1)^{l_e} \delta_{s_2, \tilde{s}_2} + \delta_{s_1, \tilde{s}_1} \delta_{s_2, \tilde{s}_2 - (-1)^{l_e}} + \delta_{s_1, \tilde{s}_1 - (-1)^{l_e} \delta_{s_2, \tilde{s}_2 - (-1)^{l_e}} \right) \end{aligned} \quad (5)$$

where  $\Theta = v_{l_e}^c \mathcal{F}(\frac{m_h}{M} \mathbf{g}_0) - v_{l_h}^{v*} \mathcal{F}(\frac{m_e}{M} \mathbf{g}_0)$  with  $v_{l_e/h}^{c/v} = \gamma_1^{c/v} + \gamma_2^{c/v} e^{2\pi i/3}$  as the effective atomic potentials for the conduction and the valence bands in the neighbouring layer. The parameters  $\gamma_{1/2}^{c/v}$  are obtained from first-principle calculations, and  $\mathbf{g}_n = C_3^{n-1}(\mathbf{G}_1^1 - \mathbf{G}_1^0)$ , where  $G_m^l$  refers to the  $m = 1, 2$  reciprocal lattice vector for layer  $l = 0, 1$ . By introducing the moiré potential and using the new periodicity of the system we can rewrite the free exciton Hamiltonian for the ground state in the presence of moiré potential in the following way<sup>2</sup>

$$H_M = \sum_{\mathbf{Q}\mathbf{g}} \mathcal{E}_{\mathbf{Q}\mathbf{g}} X_{\mathbf{Q}\mathbf{g}}^\dagger X_{\mathbf{Q}\mathbf{g}} + \sum_{\mathbf{Q}\tilde{\mathbf{g}}\mathbf{g}} \mathcal{M}_{\tilde{\mathbf{g}}\mathbf{g}} X_{\mathbf{Q}\tilde{\mathbf{g}}}^\dagger X_{\mathbf{Q}\mathbf{g}} \quad (6)$$

where we decompose the total center-of-mass momentum in terms of the new moiré reciprocal lattice vector  $\tilde{\mathbf{Q}} = \mathbf{Q} + \mathbf{g}$  with the new quantum number  $\mathbf{g}$ . This Hamiltonian is diagonal for moiré excitons, i.e.  $Y_{\mathbf{Q}}^{\eta(\dagger)} = \sum_{\mathbf{g}} \omega_{\mathbf{g}}^{\eta(*)}(\mathbf{Q}) X_{\mathbf{Q}\mathbf{g}}^{(\dagger)}$ , when the momentum-mixing coefficients  $\omega_{\mathbf{g}}^{\eta(*)}(\mathbf{Q})$  fulfill the eigenvalue problem

$$\mathcal{E}_{\mathbf{Q}\mathbf{g}} \omega_{\mathbf{g}}^{\eta}(\mathbf{Q}) + \sum_{\tilde{\mathbf{g}}} \mathcal{M}_{\tilde{\mathbf{g}}\mathbf{g}} \omega_{\tilde{\mathbf{g}}}^{\eta}(\mathbf{Q}) = E_{\mathbf{Q}}^{\eta} \omega_{\mathbf{g}}^{\eta}(\mathbf{Q}). \quad (7)$$

Using these states to perform a change of basis in the full Hamiltonian in Eq. (1) leads us to the final Hamilton operator

$$\tilde{H} = \sum_{\eta} E_{\mathbf{Q}}^{\eta} Y_{\mathbf{Q}}^{\eta\dagger} Y_{\mathbf{Q}}^{\eta} + \sum_{\substack{\eta\xi j \\ \mathbf{Q}\mathbf{Q}'\mathbf{g}}} \tilde{D}_{\mathbf{Q}\mathbf{Q}'\mathbf{g}}^{\eta\xi j} Y_{\mathbf{Q}}^{\xi\dagger} Y_{\mathbf{Q}}^{\eta} b_{\mathbf{Q}'-\mathbf{Q}+\mathbf{g}}^j + h.c. \quad (8)$$

where the moiré exciton-phonon coupling elements are defined as follows

$$\tilde{D}_{\mathbf{Q}\mathbf{Q}'\mathbf{g}}^{\eta\xi j} = \sum_{\mathbf{g}'\tilde{\mathbf{g}}} \tilde{D}_{j\mathbf{Q}'-\mathbf{Q}+\mathbf{g}, \mathbf{Q}} \omega_{\tilde{\mathbf{g}}}^{\eta*}(\mathbf{Q}) \omega_{\mathbf{g}'}^{\xi}(\mathbf{Q}') \delta_{\mathbf{g}, \mathbf{g}' - \tilde{\mathbf{g}}}. \quad (9)$$

These are expressed in terms of exciton-phonon coupling elements  $\tilde{D}_{j\mathbf{Q}'-\mathbf{Q}+\mathbf{g}, \mathbf{Q}}$  defined in Eq. (2).

With the full Hamiltonian, we solve the Heisenberg equation of motion for moiré excitons occupation  $N_{\mathbf{Q}}^{\eta} = \langle Y_{\mathbf{Q}}^{\eta\dagger} Y_{\mathbf{Q}}^{\eta} \rangle$ , truncating the Martin-Schwinger hierarchy using a second-order Born-Markov approximation, obtaining<sup>5,6</sup>

$$\dot{N}_{\mathbf{Q}}^{\eta} = \sum_{\xi\mathbf{Q}'} \left( \mathcal{W}_{\mathbf{Q}'\mathbf{Q}}^{\xi\eta} N_{\mathbf{Q}'}^{\xi} - \mathcal{W}_{\mathbf{Q}\mathbf{Q}'}^{\eta\xi} N_{\mathbf{Q}}^{\eta} \right). \quad (10)$$

The phonon-mediated scattering tensor, including emission and absorption processes ( $\pm$ ), reads

$$\mathcal{W}_{\mathbf{Q}\mathbf{Q}'}^{\eta\xi} = \sum_{j\pm\mathbf{g}} \left| \tilde{D}_{\mathbf{Q}'\mathbf{Q}\mathbf{g}}^{\eta\xi j} \right|^2 \left( \frac{1}{2} \pm \frac{1}{2} + n_{j\mathbf{Q}'-\mathbf{Q}+\mathbf{g}}^B \right) \delta \left( \Delta_{\mathbf{Q}\mathbf{Q}'\mathbf{g}}^{\eta\xi\pm} \right) \quad (11)$$

with the energy conservation  $\Delta_{\mathbf{Q}\mathbf{Q}'\mathbf{g}}^{\eta\xi\pm} = E_{\mathbf{Q}'}^{\xi} - E_{\mathbf{Q}}^{\eta} \pm \Omega_{j\mathbf{Q}'-\mathbf{Q}+\mathbf{g}}$ , where  $n_{j\mathbf{Q}'-\mathbf{Q}+\mathbf{g}}^B$  is the Bose-Einstein distribution for phonons with the mode  $j$ , the momentum  $\mathbf{Q}' - \mathbf{Q} + \mathbf{g}$ , and the energy  $\Omega_{j\mathbf{Q}'-\mathbf{Q}+\mathbf{g}}$ . Using the scattering tensor we can define the density of in-scattering states for the specific moiré exciton state  $\eta$ , yielding

$$\text{DO}\Gamma_{in}^{\eta}(E) = \sum_{\xi\mathbf{Q}'} \mathcal{W}_{\mathbf{Q}',\mathbf{Q}=\mathbf{0}}^{\xi\eta} \delta \left( E - E_{\mathbf{Q}'}^{\xi} \right). \quad (12)$$

This quantifies the density of states contributing the most to the influx of excitons to a specific state  $\eta$ . Additionally, an important quantity to monitor how the optical selection rules of interlayer excitons are influenced by the moiré potential is the absorption reading<sup>2</sup>

$$\begin{aligned} \alpha(E) &= \sum_{\eta\sigma} |\gamma_{\sigma}^{\eta}|^2 \mathcal{L}_{\Gamma\eta}(E_{\mathbf{Q}=\mathbf{0}}^{\eta} - E) \\ \text{with } \gamma_{\sigma}^{\eta} &= \sum_{\mathbf{g}} \omega_{\mathbf{g}}^{\eta}(\mathbf{Q} = \mathbf{0}) \tilde{\gamma}_{\sigma}(\mathbf{g}) \\ \text{with } \tilde{\gamma}_{\sigma}(\mathbf{q}) &= \Omega_L \sum_{n=0}^2 e^{-i2n\pi/3} \delta_{\mathbf{q},\mathbf{g}_n} \frac{C_3^{n-1}(\mathbf{K}_l)}{|\mathbf{K}_l|} \cdot \mathbf{e}_{\sigma} \end{aligned} \quad (13)$$

with  $\Omega_L \propto \sum_{\mathbf{k}} \psi_L(\mathbf{k})$  and  $L = (l_e, l_h)$ . All equations are evaluated at  $\mathbf{Q} = \mathbf{0}$  corresponding to the minimum of the moiré exciton dispersion. This means that in the case of intralayer excitons the zero would be exactly at  $\mathbf{Q} = \mathbf{0}$ , since the relative momentum displacement of electrons and holes is zero. In contrast, for interlayer excitons the equations are evaluated at  $Q = \kappa$  (K point of the MBZ), reflecting the mismatch of the Brillouin zones of the two layers.

### Self-consistent dephasing rate, photoluminescence intensity, and relaxation time

Equation (11) is derived by using a second-order Born-Markov approximation<sup>5-8</sup>, thus obtaining fixed resonances from the energy conservation described by the delta function. A more general approach can be used to include a self-consistent temperature-dependent broadening. The latter can be obtained by continuing the correlation expansion taking into account two-particle correlations and considering only the imaginary part of the self-energy (neglecting polaron renormalization terms)<sup>9</sup>. Considering only the phonon contribution, we can define the dephasing rate as follows

$$\Gamma_{\mathbf{Q}}^{\eta\xi} = \frac{\hbar}{2} \sum_{j\pm\mathbf{Q}'\mathbf{g}} \left| \tilde{D}_{\mathbf{Q}'\mathbf{Q}\mathbf{g}}^{\eta\xi j} \right|^2 \left( \frac{1}{2} \pm \frac{1}{2} + n_{j\mathbf{Q}'-\mathbf{Q}+\mathbf{g}}^B \right) \mathcal{L}_{\Gamma_{\mathbf{Q}}^{\eta} + \Gamma_{\mathbf{Q}'}^{\xi}} \left( \Delta_{\mathbf{Q}\mathbf{Q}'\mathbf{g}}^{\eta\xi\pm} \right) \quad (14)$$

resulting in a system of coupled equations that can be solved self-consistently. Here,  $\mathcal{L}_{\Gamma}$  corresponds to the Cauchy/Lorentz distribution with the width  $\Gamma$ . We directly compare a self-consistent calculation of the out-scattering rate from the first excited states to the ground state including the temperature-dependent broadening with a calculation based on a fixed width  $\Gamma = 1$  meV of the Cauchy/Lorentz distribution (chosen to be close to the value of the lowest temperature of the self-consistent treatment), cf. Fig. S1. We find an out-scattering that is by orders of

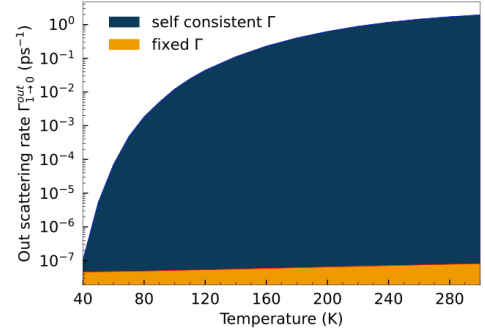


Fig. S1. Comparison of the temperature dependent out-scattering rate from the first excited states to the ground state using the self-consistent approach and a fixed width of the Cauchy/Lorentz distribution in Eq. (14).

magnitude more pronounced at enhanced temperatures for the self-consistent treatment reflecting the softening of the strict energy conservation. Finally, we use Eq. (14) to determine the time- and energy-dependent photoluminescence intensity  $I_{PL}(E, t)$  for moiré excitons<sup>2,10</sup> reading

$$I_{PL}(E, t) \propto \sum_{\eta, \sigma} |\gamma_{\sigma}^{\eta}|^2 N_{\mathbf{Q}=\mathbf{0}}^{\eta} \mathcal{L}_{\Gamma^{\eta}}(E_{\mathbf{Q}=\mathbf{0}}^{\eta} - E). \quad (15)$$

In addition, we define the relaxation time  $\tau_{\eta \rightarrow \xi}$  quantifying the scattering from the moiré exciton state  $\eta$  to the state  $\xi$  yielding

$$\tau_{\eta \rightarrow \xi} = \frac{1}{\tilde{\Gamma}_{\eta\xi}}. \quad (16)$$

with  $\tilde{\Gamma}_{\eta\xi}$  being the momentum-average of the previously defined  $\Gamma_{\mathbf{Q}}^{\eta\xi}$ . We use this equation in the main text to characterize the relaxation bottleneck effect and study its temperature dependence. There, we highlighted the predominant impact of the bottleneck effect and attributed it to optical phonons, which are usually responsible for the fast relaxation due to their higher energy. To better justify this, we present in Fig. S2 the out-scattering rate  $\Gamma_{1 \rightarrow 0}^{out}$  decomposed in its acoustic and optical phonon contributions. We find clearly that the most efficient contribution to exciton thermalization arises from optical phonons, being at least one order of magnitude larger than the scattering with acoustic phonons.

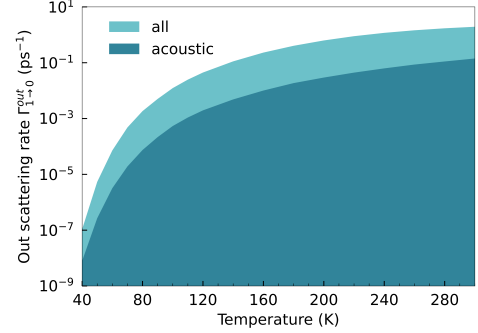


Fig. S2. Out-scattering rate  $\Gamma_{1 \rightarrow 0}^{out}$  from the first excited states to the ground state (inverse of  $\tau_{1 \rightarrow 0}$ ) as a function of temperature. We identify the different contributions of acoustic and optical phonons, showing the predominant role of the latter for the relaxation dynamics.

## DEPENDENCE ON THE INITIAL EXCITATION CONDITIONS

In the main text we have briefly discussed that the specific ratio of exciton occupation distributed between the ground state and the first excited states is strongly influenced by the initial excitation condition, more specifically on the excitation energy window. We show in this section that, although the specific output of the dynamics can be dependent on the initial condition, the general physical result is still valid, i.e. the final distribution of excitons at low temperatures and low twist angles deviates from a Boltzmann distribution due to the emergence of a relaxation bottleneck effect. In particular, we vary the initial exciton energy distribution  $E_i = 55, 62, 70$  meV, and calculate the final steady-state exciton distribution, cf. Fig. S3. The top row in Fig. S3 shows different time cuts of the momentum-integrated energy-resolved moiré exciton occupation. A common aspect of the exciton dynamics is the very fast initial dissipation of energy that brings the initial distribution of excitons to intermediate states. Focusing on the 1000 fs time cut, we see that the dynamics has already reached a stationary solution, and we find a clear deviation states from the thermal Boltzmann distribution at 40 K (dashed line). The quantitative percentage of deviation depends on the initial condition: if excitons can emit optical phonons during the dissipation process to reach efficiently intermediate states ( $X_3$  states), the occupation of the ground state becomes greater than the first excited states. This is the case for initial exciton occupations at 62 and 70 meV and is explained in terms of the  $X_3$  states scattering efficiently to the ground state, cf. Fig. S3 (b,c). In contrast, states at energies around 55 meV scatter more efficiently to the first excited states, cf. Fig. S3 (a). The larger occupation of the ground state is accompanied by a brighter response of  $X_0$  in PL spectra, cf. the lower panels in Fig. S3.

## TWIST ANGLE DEPENDENCE OF THE RELAXATION BOTTLENECK

In the main text we focus on analyzing the small twist angle regime, pointing out that the appearance of flat bands has a key role for the emergence of the relaxation bottleneck during the exciton thermalization process.

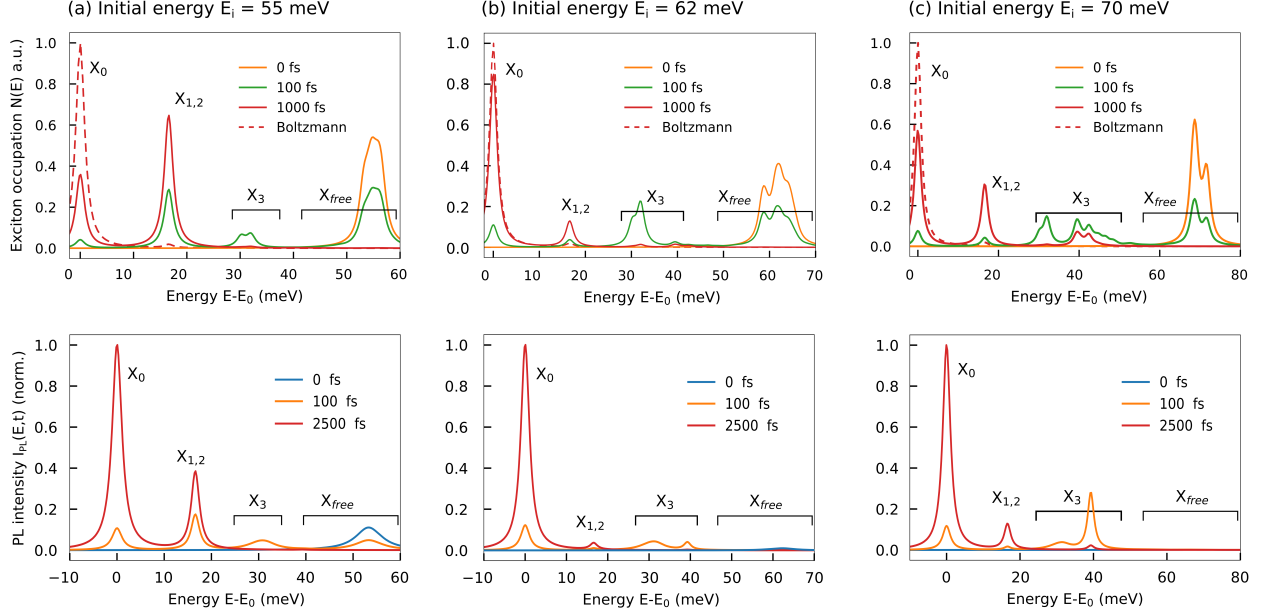


Fig. S3. Study of the moiré exciton dynamics at 40 K for different initial conditions. We initialize the system with a uniform energy distribution of excitons centered at (a)  $E_i = 55$  meV, (b)  $E_i = 62$  meV and (c)  $E_i = 70$  meV. In the top row we show energy-resolved and momentum-integrated exciton occupation at different time cuts with the red dashed line corresponding to the Boltzmann distribution. In the bottom row, we show photoluminescence spectra as a function of energy at different fixed time cuts.

To better emphasize this we have conducted a twist-angle-dependent study (inset of Fig. 4 in the main text). We find that for twist angles  $\leq 2^\circ$ , where the moiré-induced deformation of the exciton bandstructure is significant, the relaxation time increases rapidly leading to the activation of the bottleneck effect. Here, we show an intermediate twist angle ( $\simeq 3^\circ$ ), where exciton bands are not entirely flat any longer but present flat regions in the dispersion of the first excited state, cf. Fig. S4(a). To understand better the peculiar dynamics for this specific case, we conduct the same characterization performed in the main manuscript. To be consistent with the study in the main text, we choose an initial condition for the excitation in the same energy window ( $\simeq 48$  meV from the ground state minimum). Following the time evolution and conducting the same temperature-dependent study, we determine the relaxation time  $\tau_{1 \rightarrow 0}$  that is now strongly momentum-dependent. We can clearly observe that although the general definition of  $\tau_{1 \rightarrow 0}$  adapted to the twist angle comparison in Fig.4 in the main text suggests a faster relaxation, we observe a still quite pronounced bottleneck effect. This difference can be explained in terms of two competing processes: (i) intraband scattering leading to the relaxation towards the minima of the band (flat regions of  $X_1$  in S4), and (ii) scattering to the ground state. Although excitons occupying higher energy regions of the  $X_1$  miniband would scatter faster to the ground state than excitons in the flat regions (due to the energy condition of the optical phonons responsible for the bottleneck), intraband relaxation turns out to be much faster and traps excitons in the flat regions, creating again a relaxation bottleneck. To better grasp the effective timescale of the process we compute the local relaxation time  $\tau_{1 \rightarrow 0}$  around the minima of  $X_1$ , obtaining in this way a better insight of the dynamics. We show the exciton dynamics at 40 K and 300 K in Figs. S4(b)-(c). We directly compare  $\tau_{1 \rightarrow 0}$  in the small (red line) and the large (blue line) twist angle regime, cf. Fig.S4(d). The largest difference in the relaxation time is found at low temperatures. The slowed-down relaxation process at  $1^\circ$  can be traced back to flat exciton bands and the restricted scattering efficiency due to the energy conservation. This is pronounced, in particular, at low temperatures, where the broadening of states is small and thus a strict energy conservation needs to be fulfilled. The effect is much less pronounced at  $3^\circ$  exhibiting parabolic bands, where the number of possible scattering partners is much higher than in the case of flat bands at  $1^\circ$ . As the temperature increases the relaxation time at both twist angles starts to merge leading to a comparable relaxation time at room temperature. As can be understood from this analysis, intermediate twist angles exhibit a peculiar bottleneck effect, and in this case the definition of the relaxation time used in

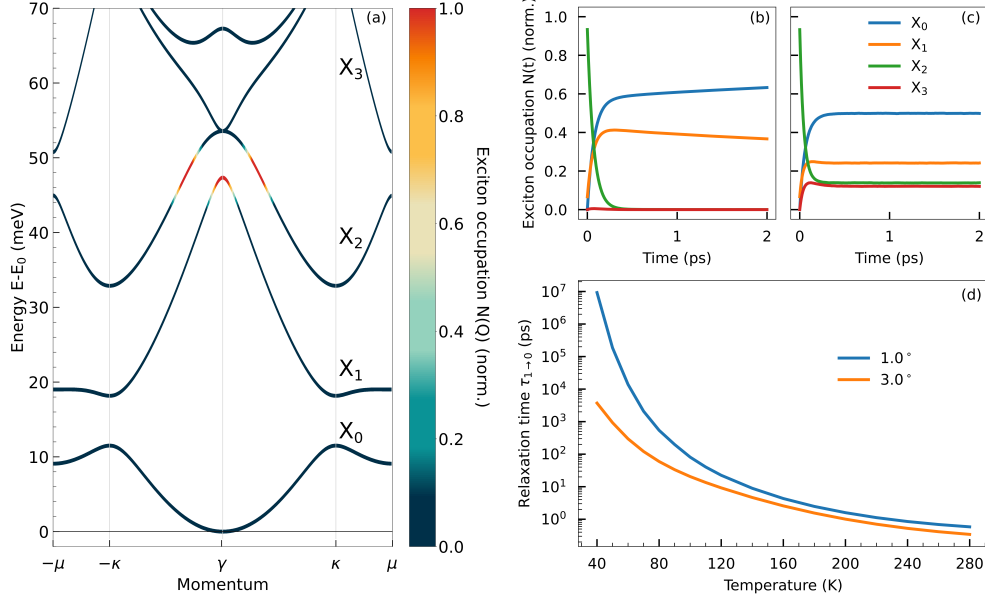


Fig. S4. Relaxation dynamics at the larger twist angle of  $3^\circ$ . (a) Moiré exciton band structure, where the initial momentum-dependent occupation is highlighted with a color scheme. We plot the momentum-integrated and time-dependent exciton occupation for each band relevant for the relaxation process at (b) 40 K and (c) 300 K. (d) Direct comparison of the temperature-dependent relaxation time at  $1^\circ$  and  $3^\circ$  showing that the  $X_1 \rightarrow X_0$  transition is slow even for  $3^\circ$ , but still several orders of magnitude faster than at  $1^\circ$ , where the flat bands strongly restrict the number of possible scattering states.

the general twist-angle-dependent study of Fig.4 in the main text, needs to be interpreted as a lower bound of the relaxation time.

Overall, we can conclude that the key ingredient for the emergence of the relaxation bottleneck is the peculiar flat bandstructure of moiré excitons. The results obtained, although specifically calculated for the exemplary  $\text{MoSe}_2\text{-WSe}_2$  heterostructure, are applicable to other TMD heterostructures. We predict the appearance of a relaxation bottleneck in all the materials, where the moiré potential leads to flat subbands with an energetic separation between the first excited and ground state that is larger than the energy of the optical phonons dominating the thermalization process.

### MOIRÉ EXCITON DISTRIBUTION IN REAL SPACE

In the main text we briefly state that the relaxation bottleneck also influences the real space distribution of excitons - depending on which state is mostly occupied at equilibrium. This is in particular valid for small twist angles, where the ground state and the first excited states exhibit very different excitonic wavefunctions. While the ground state wavefunction is of an s-type character, the first excited states are rather p-type-like<sup>2</sup>. We investigate the change in the exciton distribution in the real space for a twist angle of  $1^\circ$  (i) for an initial exciton occupation in the energy window of 40-50 meV resulting in highly occupied excited states (Fig. S5(a)) and (ii) for an initial exciton occupation around 62 meV resulting in a highly occupied ground state (Fig. S5(b)). In the first case, we find that excitons have a p-type shape around each moiré trap in real space, while in the second case the exciton distribution has the characteristic s-type shape centered at each moiré trap. As p-type orbitals have a broader profile in real space, this results in a larger overlap of the excitonic wavefunctions of neighbouring traps, thus affecting the tunneling rate between them.

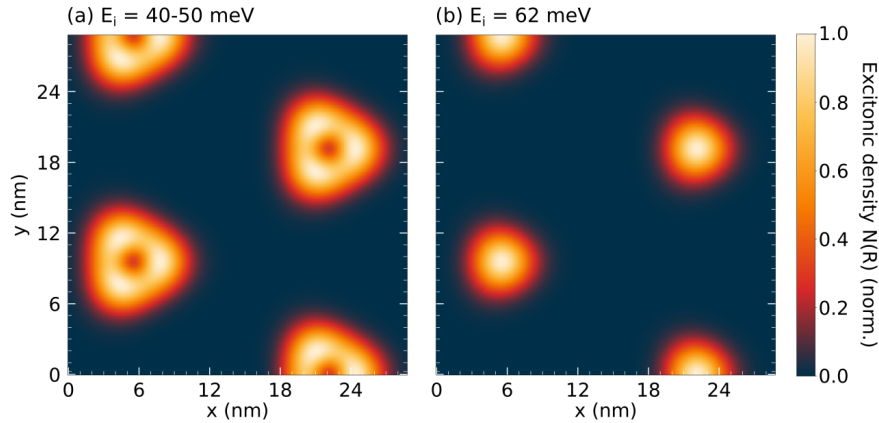


Fig. S5. Equilibrium moiré exciton distribution in real space, highlighting the different situation in the case of (a) highly occupied excited states with a p-type orbital character (obtained for initial exciton occupations in the energy window of 40-50 meV) and (b) highly occupied ground state with an s-type orbital character (obtained for an initial exciton occupation around 62 meV).

\* giuseppe.meneghini@physik.uni-marburg.de

- [1] Simon Ovesen, Samuel Brem, Christopher Linderälv, Mikael Kuisma, Tobias Korn, Paul Erhart, Malte Selig, and Ermin Malic, “Interlayer exciton dynamics in van der waals heterostructures,” *Communications Physics* **2**, 1–8 (2019).
- [2] Samuel Brem, Christopher Linderälv, Paul Erhart, and Ermin Malic, “Tunable phases of moiré excitons in van der waals heterostructures,” *Nano letters* **20**, 8534–8540 (2020).
- [3] Jin Z, Li X, Mullen J T, and Kim K W, “Intrinsic transport properties of electrons and holes in monolayer transition-metal dichalcogenides,” *Phys. Rev. B* **90**, 045422 (2014).
- [4] Joakim Hagel, Samuel Brem, Christopher Linderälv, Paul Erhart, and Ermin Malic, “Exciton landscape in van der waals heterostructures,” *Physical Review Research* **3**, 043217 (2021).
- [5] Samuel Brem, Malte Selig, Gunnar Berghäuser, and Ermin Malic, “Exciton relaxation cascade in two-dimensional transition metal dichalcogenides,” *Scientific reports* **8**, 1–8 (2018).
- [6] Malte Selig, Gunnar Berghäuser, Marten Richter, Rudolf Bratschitsch, Andreas Knorr, and Ermin Malic, “Dark and bright exciton formation, thermalization, and photoluminescence in monolayer transition metal dichalcogenides,” *2D Materials* **5**, 035017 (2018).
- [7] Hartmut Haug and Stephan W Koch, *Quantum theory of the optical and electronic properties of semiconductors* (World Scientific Publishing Company, 2009).
- [8] A Thränhardt, S Kuckenburger, A Knorr, T Meier, and SW Koch, “Quantum theory of phonon-assisted exciton formation and luminescence in semiconductor quantum wells,” *Physical Review B* **62**, 2706 (2000).
- [9] Fausto Rossi and Tilmann Kuhn, “Theory of ultrafast phenomena in photoexcited semiconductors,” *Reviews of Modern Physics* **74**, 895 (2002).
- [10] SW Koch, M Kira, G Khitrova, and HM Gibbs, “Semiconductor excitons in new light,” *Nature materials* **5**, 523–531 (2006).